Imaging cold atoms with shot-noise and diffraction limited holographic microscopy

James Paul Sobol

July 19, 2015

Submitted to Swansea University in fulfilment of the requirements for the Degree of Doctor of Philosophy.

Prifysgol Abertawe
Swansea University

Abstract

In-line holographic microscopy promises lensless phase and amplitude sensitive imaging at high numerical aperture, and has seen application in a number of fields including biology. In spite of the benefits promised by in-line holography for imaging cold atoms including, sensitive 3D off-resonant imaging, its application to imaging laser cooled atoms has been limited. The lack of application can be attributed to two major sources of noise; the twin and DC images, and speckle noise. This thesis presents the theoretical and experimental development of a holographic microscope, for diffraction and shot-noise limited microscopy of cold atoms. The wavefront scattered by laser cooled ^{87}Rb atoms is extracted from a hologram, and using simple algorithms the twin and DC problems are eliminated, whilst speckle noise is substantially suppressed. With NA = 0.16, diffraction and shot-noise limited retrievals of the wavefronts scattered by sub-millimetre sized clouds, located in a glass cell with no anti-reflection coating, are consistently demonstrated, at various probe detunings and with signal-to-noise ratio of up to SNR = 41. The microscope simultaneously retrieves the probe phase shift and sample optical depth with sensitivities that outperform the expected shot-noise limited sensitivities in absorption and phase-contrast imaging by a factor of 8 in this experiment. This holographically enhanced sensitivity is attributed to a commonly overlooked property of holographic microscopy, that permits near optimal signal collection using a camera with limited dynamic range. In exploring this enhancement toward single atom sensitivity, experimental retrievals of the samples column density infer an atom number sensitivity per resolution area of $\delta N_{\mathrm{atom}} = 0.75$. In a proposed NA = 0.7 atom chip integrated microscope, single atom resolution is expected when probing with a detuning equal to eight times the natural linewidth. The technique is proposed for precise phase imaging of dense atomic gases, and off-resonant probing of atoms in optical lattices sites with multiple atom occupancies.

Declarations and statements

Declaration

This work has not previously been accepted in substance for any degree and is not being concurrently submitted in candidature for any degree.

Signed: _____ (James P. Sobol) Date: July, 2015

Statement 1

This thesis is the result of my own investigations, except where otherwise stated. Other sources are acknowledged by giving explicit references within the appended bibliography.

Signed: _____ (James P. Sobol) Date: July, 2015

Statement 2

I hereby give consent for this thesis, if accepted, to be available for photocopying and for inter-library loan, and for the title and summary to be made available to outside organisations.

Signed: _____ (James P. Sobol) Date: July, 2015

Contents

Acknowledgements

I first express my gratitude in particular to my supervisor Prof. Saijun Wu, who I am grateful to have had the opportunity to work with, and extremely fortunate to have learned from his extensive knowledge. I am particularly thankful for his patience, and his willingness to make time for my questions, no matter how trivial. His input and ideas form the foundation of this work, which without his guidance would have been impossible to accomplish.

I thank Dr Will Bryan for his supervision during the latter stages of this project and his guidance through the write up of this thesis; Dr Aled Isaac for helpful discussions and advice relating to the project and the write up of this thesis; and Dr Stefan Eriksson for useful discussions we have had during his role as the project assessor.

I would also like to acknowledge the contribution from; Ben Knight-Gregson for his part in the collective development of an understanding of holographic microscopy whilst undertaking a Masters project; Mark Worsfold for his contribution during a summer project to the design of the Zeeman slower used in this work; And to Robert James for his work toward processing holographic reconstructions on graphics processing units.

To my friends and colleges including, Daniel Edwards, Rhys Jenkins, Alexander Bainbridge, Adam Williams, Alex Alampounti and Christopher Barnett, who have all made a meaningful contribution to the work presented in this thesis during extended discussions over tea and coffee, I give my sincere appreciation.

My gratitude is extended to the staff within the department, including Hugh Thomas, Julian Kivell, Mr Philip Hopkins, Jonathan Woodman-Ralph, Gill Oliver, Liz Davies and David Payne, without whom the Physics department would not function.

I acknowledge and appreciate the immense emotional and financial contributions made by my family during the expanse of this project, including my mother, father, gran, auntie Kristine and uncle Robert, to name but a few.

I express particular gratitude to the contribution made by my wife Cara during this project. Not only has she had to support me financially and and emotionally, but has also had to deal with my extended working hours that leave precious little time for us to spend together.

Physical constants

Symbol	Description
$\hbar = 1.0546 \times 10^{-34}$ Js	Reduced Planck constant
$h = 6.626 \times 10^{-34}$ Js	Planck constant
$e = 1.6022 \times 10^{-19}$ C	Electronic charge
$k_B = 1.3807 \times 10^{-23}$ JK^{-1}	Boltzmann's constant
$\epsilon_0 = 8.854 \times 10^{-12}$ Fm^{-1}	Electric permittivity of free space
$\mu_B = 9.274 \times 10^{-24}$ JT^{-1}	Bohr magneton
$\mu_0 = 4\pi \times 10^{-7}$ Hm^{-1}	Magnetic permeability of free space
$c = 2.9979 \times 10^{8}$ ms^{-1}	Speed of light
$m_{\mathrm{Rb}} = 1.443 \times 10^{-25}$ kg	Mass of ^{87}Rb

Commonly used symbols

Symbol	Description
ω	Optical frequency
ω_0	Transition resonant frequency
Δ	Detuning from resonance
Ω	Rabi frequency
Γ	Excited state decay rate
ν	Detuning in units of Γ
λ	Wavelength
s_0	Resonant saturation parameter
s	Saturation parameter
k	Wavenumber
x, y, z	Cartesian coordinates
B,$\mathbf{B}$	Magnetic field
$\mathbf{E}$	Electric field
ρ_c	Column density
ϕ	Phase shift
OD	Optical depth

List of Figures

List of Tables

Chapter 1

Introduction

Since the development of laser cooling techniques [1–3], research in the field of cold atom physics has received a great deal of attention. Experiments with cold neutral atoms rely on the interaction between atoms and light, not only for cooling and trapping, but also to extract information from the atomic sample. In laser cooling, the kinetic energy of atoms is reduced thanks to the absorption and subsequent spontaneous emission, as demonstrated in early experiments in atomic beam slowing [4] and the optical molasses [5]. Trapping was later combined with the optical molasses cooling technique via the addition of an inhomogeneous magnetic field in a scheme known as the magneto-optical trap (MOT) [6]. Many cold atom experiments use the MOT as a starting point, since it can deliver large numbers of atoms with high density and low temperatures ($\sim 10\ \mu$K). The pre-cooled atomic sample can be more efficiently loaded into optical and/or magnetic traps, where other cooling mechanisms can achieve Bose-Einstein condensation (BEC) [7–10] and degenerate Fermi gases [11]. Coherent matter waves permit high precision matter wave interferometry [12] of cold atoms. A MOT is often used as a source of cold atoms for accurate definition of the second using atomic fountain clocks [13, 14]. In loading atoms from a MOT into an optical lattice, the accuracy of atomic clocks can be improved significantly, as demonstrated in optical lattice clocks [15].

Much of the developed knowledge in cold atom physics has arisen from observing the interaction of light with atoms. This is why breakthroughs in cold atom research are often preceded or accompanied by improved imaging techniques [16–18]. Quantum gas microscopy [19–22] permits site resolved detection of atoms trapped in an optical lattice over long exposure times, and opens the doorway to study of strongly correlated bosonic [19, 20], and fermionic [21, 22] gases in unprecedented detail.

In this work, a novel double point source in-line holographic microscope for phase shift and absorption sensitive imaging of cold atom samples at the shot-noise and diffraction limits is theoretically and experimentally developed. In spite of the potential benefits of holographic microscopy for cold atoms such as lens-free 3D imaging with arbitrary probe detuning, the application of holography to cold atoms is limited [23–25]. This can be attributed to two major challenges; the first are the well known twin [26–29] and DC [30–33] image noises, and the second is the speckle noise problem [34–37] inherent to all cold atom imaging to varying degrees of severity. Taking advantage of the unique properties of double source holographic microscopy, in particular the increased probe wavefront complexity yielding more twin image information, the twin, DC and speckle noise problems can be addressed. With the major obstacles to cold atom holographic microscopy alleviated, diffraction and shot-noise limited holographic microscopy of cold atoms (see chapter 5) with simultaneous retrieval of the probe phase-shift and absorption is demonstrated for the first time to the author's knowledge.

An ultimate goal of this work is to go beyond a rudimentary demonstration of holographic microscopy for cold atoms, and progress the holographic technique toward high numerical aperture and shot-noise-limited number resolving phase imaging of cold atoms. It is well known that near-resonant imaging methods encounter difficulty, since light assisted collisions leading to atoms being lost in pairs from optical lattice sites [19–22, 38], resonant dipole-dipole interactions and multiple photon scattering in dense gases inhibit simple retrieval of the probe absorption by dense clouds via Beer's law [39], and lead to a deviation in the expected absorption cross-section [40–42]. With these effects reduced with a detuned probe beam, phase sensitive holographic microscopy may provide a solution [34] for precise phase imaging of dense atomic samples. The idea of single atom resolved holographic microscopy is motivated by an important but somewhat neglected advantage of holographic microscopy for cold atoms; the point source geometry permits optimal collection of the high spatial frequency interference using the entire CCD chip, thus allowing phase shift and absorption measurements that display a holographically enhanced sensitivity over traditional in-focus cold atom imaging techniques such as absorption and phase-contrast imaging (see chapters 6 and 7). This enhancement, combined with the benefit of simultaneous retrieval of probe phase shift and attenuation, is exploited for precise phase shift and absorption retrieval from holograms (see chapter 6) and toward single atom sensitivity with holographic microscopy (see chapter 7).

1.1 Thesis outline

Chapter 2

A selection of the theoretical background of laser cooling and the optical detection of neutral atoms that is relevant to the work described in this thesis is discussed. Starting from the Schrödinger equation, the interaction of light with a two level atom with no spontaneous emission will be investigated. A dissipative term is introduced, with the result yielding the optical Bloch equations. Using the steady sate solution to the optical Bloch equations, expressions for an optical probes absorption and phase shift upon interaction with a single atom is derived. A review is then conducted of the established imaging techniques for laser cooled atoms. The challenges that each are subject to are explained and evaluated. Particular attention is paid to absorption and phase-contrast imaging, since they are the most common absorption and phase sensitive imaging schemes for cold atoms.

Chapter 3

The in-line holographic microscope, first proposed by Dennis Gabor [43–45], is introduced to highlight the key concepts and techniques in digital in-line holographic microscopy (DIHM). In analysing the in-line geometry, the well known twin image problem is discussed along with a selection of the developed solutions to the problem. The difficulties associated with direct application of DIHM to imaging cold atom samples are exposed, and the rewards that could be reaped if the difficulties are addressed such as high numerical aperture (e.g. NA = 0.7) lens-free phase and amplitude sensitive microscopy of cold atom samples are discussed.

The second part of this chapter is devoted to the theoretical development of a novel double point source in-line holographic microscope (DSHM) to simultaneously address the well known twin image and DC noise problems associated with direct application of DIHM to imaging cold atoms. Taking advantage of the double source geometries effect on the twin image, an iterative technique is developed to simultaneously remove the twin and DC image problems. The expected shot-noise-limited signal to noise ratio is derived, and methods are developed to extract the atomic clouds optical properties. Finally, the prospects for using this double source holographic microscope for imaging cold atoms is discussed.

Chapter 4

In this chapter the design and construction of an experimental system for preparing and delivering cold atoms is presented. Furthermore, the design and construction of

two versions of the double source holographic microscope are presented. One version achieves NA = 0.07 and the other an improved NA = 0.16.

Chapter 5

The performance of the twin and DC noise removal procedure in the double source geometry is evaluated against reconstructions from idealised holograms and those from the single source in-line geometry. It is confirmed by comparison with the theoretical prediction of the shot-noise level that experimental reconstructions can approach the shot-noise limit consistently for optically thin samples. By analysis of density modulated images of atomic samples, diffraction limited imaging is confirmed. Furthermore, a speckle noise suppression algorithm is developed that consists of including the point-like sources of speckle noise into the reference field estimation for reconstruction.

Chapter 6

A method is presented for extraction of the probe absorption and phase shift with double source holographic microscopy. The absorption and phase shift sensitivities in the reconstructed images are measured and shown to be better than those expected in the established absorption or phase-contrast imaging by a factor of more than 8 in this particular work. Then the reasons behind the observed holographically enhanced sensitivity inherent to point source holography is discussed in detail. Finally, to demonstrate the ability of double source holographic microscopy for precision retrieval of phase shift and absorption, their detuning dependence is measured across an atomic resonance, both in absence and in presence of the dressing MOT lasers. The agreement between the measured detuning dependence of phase shift and absorption confirms the validity of the proposed retrieval.

Chapter 7

The holographically enhanced sensitivity is theoretically explored toward single atom detection with double source holographic microscopy. Then the experimental efforts conducted in this project toward achieving single atom sensitive holography are presented. With an NA= 0.07 holographic microscope and a probe near the atomic resonance, a sensitivity to atom number per resolution above the single atom level is demonstrated. Images reconstructed from an upgraded NA= 0.16 imaging system are then presented. With a probe near-resonance a sensitivity to atom number per resolution area at the boundary of the single atom level is demonstrated. A pre-requisite for number resolving detection of cold atoms is then demonstrated, by

probing the laser cooled atoms continuously for an extended exposure time at the shot-noise limit.

In the latter part of this chapter suggestions are made for future work on the double source holographic microscope. Future improvements to the set-up are suggested, that should permit single atom sensitive imaging with detuned probing ($\Delta = 8\Gamma$) with a numerical aperture as large as NA = 0.7, and reduce the amount of speckle noise recorded in holograms as a result the spatial filtering awarded by pinhole sources.

Chapter 8

Here the conclusions from the work described in this thesis are drawn and the developed double source holographic microscope is evaluated. The possible extension of this work for precise phase imaging of dense atomic gases, and for off-resonant probing of multiple atoms in optical lattices is discussed.

Published work

To date a single paper has been published from the work conducted during this project.

- Imaging cold atoms with shot-noise and diffraction limited holography,
  J. P. Sobol and Saijun Wu,
  New Journal of Physics 16 093064 (2014).

The work published in this paper can also be found in this thesis. In particular large parts of chapters 3 and 5 to 7, which discuss the design and results of the developed double source holographic microscope published in this paper.

Chapter 2

Laser cooling and optical imaging of atoms

In this chapter the basic theoretical background of laser cooling and the detection of neutral atoms via observation of the scattered light is discussed. Furthermore, a review of the established imaging techniques for cold atoms is conducted.

The effect of electromagnetic radiation on the internal states of an atom is fundamental to laser cooling and imaging atoms using laser light. In section 2.1 a brief analytical investigation of the interaction of atoms with light will be conducted, then by including a damping term, the optical Bloch equations which describe the dynamics of the system interacting with the radiation field are derived. A two-level atom picture is considered for simplicity. Using the steady state solutions to the optical Bloch equations, the coherence is calculated. Then the electric field induced atomic dipole moment is used to derive an expression for the complex susceptibility $\tilde{\chi}$ (see section 2.1.4) of an atomic cloud with a certain number density ρ. Following on, an expression for the complex refractive index n is reached (section 2.1.5). Then the effect of a static cloud of cold atoms on the amplitude and phase of an optical probe will be derived.

Cooling techniques for atoms (see section 2.2) require a source of atoms with velocity below the capture velocity of the technique. To deliver slow atoms, methods of slowing atomic beams from "hot" sources are commonly used (see sections 2.2.1 and 2.2.1). An array of more sophisticated three dimensional cooling schemes including Doppler cooling techniques such as the optical molasses (see section 2.2.2) and the MOT (see section 2.2.3) are used to achieve temperatures $T \sim 100\mu$K, for alkali atoms such as Rubidium. A derivation of the force that arises in both of these

Doppler cooling schemes is given. Dipole and magnetic traps that allow atoms to be confined for long time periods are briefly discussed in sections 2.2.4 and 2.2.5.

In most cold atom experiments the observable being measured is the final distribution of atoms, in real, velocity, or internal state space. The most convenient way to measure is through high-fidelity and highly sensitive imaging methods. In this chapter the commonly used imaging techniques in cold atom experiments are categorised into incoherent (see section 2.3.1) and coherent (see sections 2.3.2 and 2.3.3) methods, and their principles of operation and their individual limitations are reviewed. These discussions will be referred to in comparison with holographic technique described in chapter 3. In particular, it is pointed out that outstanding problems inherent to near-resonant imaging techniques, such as the resonant dipole-dipole interaction induced atom losses and the multiple scattering induced signal deviations, can be resolved with off-resonant imaging. Though phase sensitive techniques such as phase-contrast imaging have been developed, they encounter difficulty at high NA. It is concluded that there remains a demand for an alternative capable of sensitive high numerical aperture imaging of atoms at arbitrary detunings and at the diffraction and shot-noise limits.

2.1 Interaction of atoms with light

Neglecting spontaneous emission, the interaction of an atom with a monochromatic electromagnetic wave, see fig. 2.1, is governed by the time dependent Schrödinger equation,

$$\mathrm{i}\hbar\dot{\Psi}\left(\mathbf{r},t\right)=\hat{H}\Psi\left(\mathbf{r},t\right), \tag{2.1}$$

where $\mathbf{r}$ is the relative displacement between the electron and the nucleus. The Hamiltonian $\hat{H}$ has two parts, $\hat{H}_0$ gives eigenvalues and eigenfunctions corresponding to the unperturbed atomic energy levels $\hbar\omega_n$ and wave functions $\psi_n\left(\mathbf{r}\right)=\langle\mathbf{r}|n\rangle$ respectively, and $\hat{H}_I\left(t\right)=-\mathbf{D}\cdot\mathbf{E}\left(\mathbf{r}_{\mathrm{CM}},t\right)$, with $\mathbf{D}$ the electric dipole moment operator, describes the perturbation by the oscillatory radiation field $\mathbf{E}\left(\mathbf{r}_{\mathrm{CM}},t\right)$ with amplitude $\mathbf{E}_0$ and frequency ω on an atom with centre of mass location $\mathbf{r}_{\mathrm{CM}}$. For an electric field linearly polarized along the direction of $\mathbf{r}$, the Hamiltonian for a two level atom interacting with the radiation can be written as

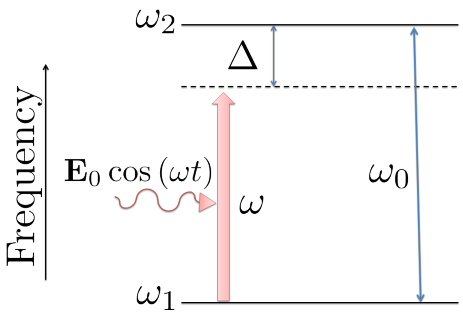

Figure 2.1: Displayed is a schematic of a two level atom with ground state energy $\hbar\omega_1$ and excited state energy $\hbar\omega_2$. The incoming radiation with frequency ω has a detuning $\Delta = \omega - \omega_0$ from the transition resonant frequency $\omega_0 = \omega_2 - \omega_1$.

$$\hat{H}_0 |n\rangle = \hbar\omega_n |n\rangle , \tag{2.2}$$

$$\hat{H}_I(t) = -e\mathbf{r} \cdot \mathbf{E}_0 \cos(\omega t) , \tag{2.3}$$

$$\hat{H} = \hat{H}_0 + \hat{H}_I(t) \overset{n=2}{\Longrightarrow} \begin{pmatrix} \hbar\omega_1 & -e\mathbf{r} \cdot \mathbf{E}_0 \cos(\omega t) \\ -e\mathbf{r} \cdot \mathbf{E}_0 \cos(\omega t) & \hbar\omega_2 \end{pmatrix} , \tag{2.4}$$

with $-e$ the charge on the electron. Considering the general solution of eq. (2.1), the atomic wave function can be expressed at any instant of time in terms of ω_n and the time dependent coefficients c_n (normalisation requires that $\sum_n |c_n|^2 = 1.$),

$$\Psi(\mathbf{r}, t) = \sum_n c_n |n\rangle \, \mathrm{e}^{-\mathrm{i}\omega_n t} \overset{n=2}{\Longrightarrow} \begin{pmatrix} c_1 \mathrm{e}^{-\mathrm{i}\omega_1 t} \\ c_2 \mathrm{e}^{-\mathrm{i}\omega_2 t} \end{pmatrix} . \tag{2.5}$$

The spatial variation of $\mathbf{E}(\mathbf{r}_{\mathrm{CM}}, t)$ can be neglected over the region of the spatial integral of $\hat{H}_I(t)$, since the optical wavelength $\lambda \gg |\mathbf{r}|$, thus the electric field has almost uniform amplitude over the atomic wavefunction so $\mathbf{E}_0$ can be taken outside the integral. This is the well known electric dipole approximation . Invoking the electric dipole approximation, the Rabi frequency [46–48] is defined as

$$\Omega = \frac{-e \langle 2| \mathbf{r} \cdot \mathbf{E}_0 |1\rangle}{\hbar} = \frac{-\mathrm{d}_{21} \cdot \mathbf{E}_0}{\hbar}, \tag{2.6}$$

where $\mathrm{d}_{mn} = e \langle m| \mathbf{r} |n\rangle$ is the transition dipole matrix element. By substituting eq. (2.5) into the time dependent Schrödinger equation (eq. (2.1)) and using eq. (2.6) and the transition resonant frequency $\omega_0 = \omega_2 - \omega_1$, an expression for the

time derivatives of the c_n coefficients can be found

$$\mathrm{i}\begin{pmatrix}\dot{c}_1\\ \dot{c}_2\end{pmatrix} = \begin{pmatrix}0 & \frac{\Omega^*}{2}\left(\mathrm{e}^{\mathrm{i}(\omega-\omega_0)t}+\mathrm{e}^{-\mathrm{i}(\omega+\omega_0)t}\right)\\ \frac{\Omega}{2}\left(\mathrm{e}^{\mathrm{i}(\omega+\omega_0)t}+\mathrm{e}^{-\mathrm{i}(\omega-\omega_0)t}\right) & 0\end{pmatrix}\begin{pmatrix}c_1\\ c_2\end{pmatrix}. \tag{2.7}$$

For most cases of interest in laser cooling, the perturbing radiation has a frequency close to resonance $\omega \sim \omega_0$ (e.g. in an optical molasses for ^{87}Rb where $|\omega - \omega_0| \sim 10$ MHz $\ll \omega \sim 100$ THz.). The terms with $\omega + \omega_0 \sim 2\omega_0$ rotate much faster than the frame of reference, thus average to zero over time scales meaningful to most applications in laser cooling. This rotating wave approximation [46–48] and the definition of the detuning from resonance $\Delta = \omega - \omega_0$ are used to simplify eq. (2.7), thus

$$\mathrm{i}\begin{pmatrix}\dot{c}_1\\ \dot{c}_2\end{pmatrix} = \frac{1}{2}\begin{pmatrix}0 & \Omega^*\mathrm{e}^{\mathrm{i}\Delta t}\\ \Omega\mathrm{e}^{-\mathrm{i}\Delta t} & 0\end{pmatrix}\begin{pmatrix}c_1\\ c_2\end{pmatrix}. \tag{2.8}$$

Making a rotating frame transformation where $\tilde{c}_1 = c_1\mathrm{e}^{-\mathrm{i}\Delta t/2}$ and $\tilde{c}_2 = c_2\mathrm{e}^{\mathrm{i}\Delta t/2}$ and using eq. (2.8), the time derivatives of the transformed $\tilde{c}_n$ are

$$\mathrm{i}\begin{pmatrix}\dot{\tilde{c}}_1\\ \dot{\tilde{c}}_2\end{pmatrix} = \frac{1}{2}\begin{pmatrix}\Delta & \Omega^*\\ \Omega & -\Delta\end{pmatrix}\begin{pmatrix}\tilde{c}_1\\ \tilde{c}_2\end{pmatrix}. \tag{2.9}$$

2.1.1 Light shift

The interaction of the atom with the radiation field not only affects the coefficients but also the energy levels. This light shift of the energy levels corresponds to the eigenvalues Λ of eq. (2.9),

$$\begin{vmatrix}\Delta/2-\Lambda & \Omega/2\\ \Omega^*/2 & -\Delta/2-\Lambda\end{vmatrix} = \Lambda^2 - \left(\frac{\Delta}{2}\right)^2 - \left(\frac{|\Omega|}{2}\right)^2 = 0. \tag{2.10}$$

The quadratic expression (eq. (2.10)) has two solutions for the eigenvalues $\Lambda = \pm\left(\Delta^2 + |\Omega|^2\right)^{1/2}/2$. When there is no radiation field ($|\Omega| = 0$), the eigenvalues $\Lambda = \pm\Delta/2$ correspond to two levels separated by Δ. One is the exited state and the other is the ground state plus one photon energy from the radiation field, also known as a dressed state [49]. Light shifts are important in dipole traps [50] when there is a large detuning from resonance $\Omega \ll |\Delta|$. A series expansion under this condition reveals the eigenvalues as $\Lambda \simeq \pm\left(\Delta/2 + |\Omega|^2/4\Delta\right)$. The states are shifted from their

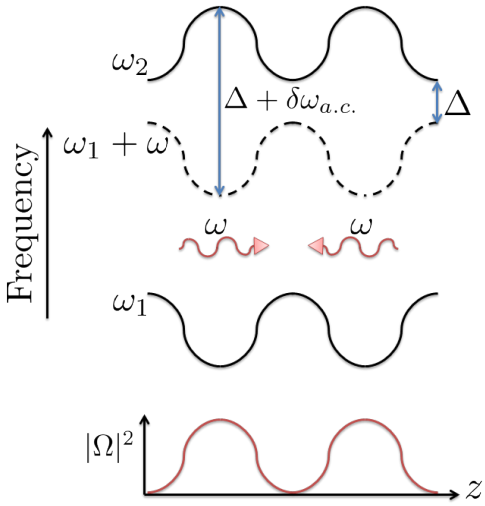

Figure 2.2: The effect of the varying intensity $I \propto |\Omega|^2$ on the ground and excited state frequencies (solid black lines), and on the ground dressed state frequency (dashed black line). When $\Omega > 0$ the states are shifted by $\delta\omega_{\mathrm{AC}}$.

unperturbed eigenfrequencies by the light shift (or AC Stark shift),

$$\delta\omega_{\mathrm{AC}} = \frac{|\Omega|^2}{4\Delta}. \tag{2.11}$$

The energy of the ground state is shifted upward for positive detuning and downward for negative detuning [46]. The shift is proportional to the light intensity, as depicted in fig. 2.2, which is often inhomogeneous and spatially dependant. The force $F \simeq -\hbar\nabla\delta\omega_{\mathrm{AC}}$ exerted on the atoms is known as the dipole force, which accounts for the conservative part of the light force. To fully account for both the conservative and dissipative parts, spontaneous emission (see appendix B) must be included in the two-level model. The dipole force is used when trapping atoms, and the dependence of the force on the sign of the detuning has important consequences for these traps [50], by deciding whether the force is an attractive or repulsive one.

2.1.2 Optical Bloch equations

The density matrix formalism [47, 51] is introduced to allow the description of systems of mixed states, and allows introduction of the effect of spontaneous emission. For the two level atom the density matrix is given by

$$\hat{\rho} = \begin{pmatrix} |c_1|^2 & c_1 c_2^* \\ c_2 c_1^* & |c_2|^2 \end{pmatrix} = \begin{pmatrix} \rho_{11} & \rho_{12} \\ \rho_{21} & \rho_{22} \end{pmatrix}. \tag{2.12}$$

A transformation to the rotating frame can be made for the elements of the density matrix as with the $\tilde{c}_n$ coefficients. Finding the time derivatives of the elements of the density matrix (i.e. with $\dot{\tilde{\rho}}_{12} = \dot{\tilde{c}}_1\tilde{c}_2^* + \tilde{c}_1\dot{\tilde{c}}_2^*$ etc...) and using eq. (2.9) the following compact set of equations are reached;

$$\dot{\rho}_{11} = \frac{\mathrm{i}}{2}\left(\Omega\tilde{\rho}_{12} - \Omega^*\tilde{\rho}_{21}\right), \tag{2.13}$$

$$\dot{\rho}_{22} = \frac{\mathrm{i}}{2}\left(\Omega^*\tilde{\rho}_{21} - \Omega\tilde{\rho}_{12}\right), \tag{2.14}$$

$$\dot{\tilde{\rho}}_{12} = \frac{\mathrm{i}\Omega^*}{2}\left(\rho_{11} - \rho_{22}\right) - \mathrm{i}\Delta\tilde{\rho}_{12}, \tag{2.15}$$

$$\dot{\tilde{\rho}}_{21} = \frac{\mathrm{i}\Omega}{2}\left(\rho_{22} - \rho_{11}\right) + \mathrm{i}\Delta\tilde{\rho}_{21}. \tag{2.16}$$

To include spontaneous emission in a simple way, it is assumed that the ground state has a negligible decay rate. Furthermore it is assumed that the exited state decay is purely radiative with a rate Γ. This decay of the excited state population also effects the coherences (ρ_{21} and ρ_{12}), resulting in a transverse relaxation rate of $\Gamma/2$. A decay of population from the exited state results in an increase of population in the ground state. Considering this, eqs. (2.13) to (2.16) can be re-written to include the effect of spontaneous emission from the exited state, thus;

$$\dot{\rho}_{11} = \frac{\mathrm{i}}{2}\left(\Omega\tilde{\rho}_{12} - \Omega^*\tilde{\rho}_{21}\right) + \Gamma\rho_{22}, \tag{2.17}$$

$$\dot{\rho}_{22} = \frac{\mathrm{i}}{2}\left(\Omega^*\tilde{\rho}_{21} - \Omega\tilde{\rho}_{12}\right) - \Gamma\rho_{22}, \tag{2.18}$$

$$\dot{\tilde{\rho}}_{12} = \frac{\mathrm{i}\Omega^*}{2}\left(\rho_{11} - \rho_{22}\right) - \left(\mathrm{i}\Delta + \Gamma/2\right)\tilde{\rho}_{12}, \tag{2.19}$$

$$\dot{\tilde{\rho}}_{21} = \frac{\mathrm{i}\Omega}{2}\left(\rho_{22} - \rho_{11}\right) + \left(\mathrm{i}\Delta - \Gamma/2\right)\tilde{\rho}_{21}. \tag{2.20}$$

These are known as the optical Bloch equations (this derivation does not take into account the cases where cold atom collisions become important, in such cases the decay of the populations and coherences are described by different parameters [47, 52].).

In the work conducted in this project, the laser light was applied to the atoms for a time that is much longer than the lifetime of the excited state $\tau_\mathrm{e} = 1/\Gamma$, thus it is the steady state solutions to eqs. (2.17) to (2.20) that are important. The steady state solutions are found by setting the time derivatives to zero and utilizing the conservation of population $\rho_{11} + \rho_{22} = 1$, the population difference $w = \rho_{11} - \rho_{22}$ and coherence conjugation $\rho_{12} = \rho_{21}^*$. By defining the saturation parameter s, the

on-resonance saturation parameter s_0 along with the saturation intensity I_s,

$$s \equiv \frac{|\Omega|^2/2}{\Delta^2 + \Gamma^2/4} \equiv \frac{s_0}{1 + (2\Delta/\Gamma)^2}, \tag{2.21}$$

$$s_0 \equiv \frac{2|\Omega|^2}{\Gamma^2} \equiv \frac{I}{I_s}, \tag{2.22}$$

$$I_s \equiv \frac{2\pi^2 \hbar c \Gamma}{3\lambda^3}, \tag{2.23}$$

concise steady state solutions for the populations and the coherences can be found. An expression for the population difference w is found using eqs. (2.17) and (2.18). Then solutions for the coherences and the excited sate population $\tilde{\rho}_{12}$ and ρ_{22} are found using w,

$$w = \frac{1}{1+s}, \tag{2.24}$$

$$\tilde{\rho}_{12} = \frac{\mathrm{i}\Omega^* \left(\frac{\Gamma}{2} - \mathrm{i}\Delta\right)}{2|\frac{\Gamma}{2} - \mathrm{i}\Delta|^2 (1+s)} = \frac{\mathrm{i}\Omega^* \left(\frac{\Gamma}{2} - \mathrm{i}\Delta\right)}{2\left(\Delta^2 + \Gamma^2/4 + |\Omega|^2/2\right)}, \tag{2.25}$$

$$\rho_{22} = \frac{1-w}{2} = \frac{s}{2(1+s)} = \frac{s_0/2}{1 + s_0 + (2\Delta/\Gamma)^2}. \tag{2.26}$$

Looking at eq. (2.26) and considering light fields such that $s \gg 1$, the excited state population saturates and approaches a value of $\rho_{22} \to 1/2$. The population is equally distributed between the ground and excited state and $w \to 0$. The interaction of atoms with electromagnetic radiation results in a force that is composed of a conservative and a dissipative part (see appendix B). The conservative part is used to trap atoms, whilst the dissipative part is often used for cooling.

2.1.3 Scattering rates

Imaging techniques rely on the detection of scattered photons from the sample [23, 25, 53–58]. For the two level atom, the total scattering rate of photons out of a probe beam Γ_{tot} is given by the product of the excited state rate Γ and the probability of the atom being in the excited state,

$$\Gamma_{\mathrm{tot}} = \Gamma \rho_{22} = \frac{\Gamma s}{2(1+s)}. \tag{2.27}$$

This total scattering rate is composed of both the scattering rates of the coherent and incoherent photons, $\Gamma_{\mathrm{tot}} = \Gamma_{\mathrm{coh}} + \Gamma_{\mathrm{inc}}$. These scattering rates can be found

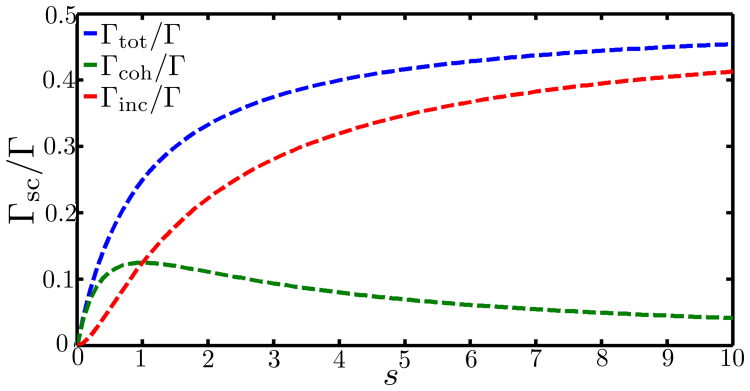

Figure 2.3: The graph displays the coherent (Γ_{coh}), incoherent (Γ_{inc}) and the total (Γ_{tot}) scattering rates in units of the excited state decay rate Γ, plotted against the unitless saturation parameter s.

by writing the dipole operator as a sum of its average value and its instantaneous difference from the average [53, 54, 59], a derivation is beyond the scope of this work, but the result is

$$\Gamma_{coh} = \frac{\Gamma_{tot}}{(1+s)} = \frac{\Gamma s}{2\,(1+s)^2}, \tag{2.28}$$

$$\Gamma_{inc} = \frac{s\Gamma_{tot}}{(1+s)} = \frac{\Gamma s^2}{2\,(1+s)^2}. \tag{2.29}$$

The three scattering rates eqs. (2.27) to (2.29) are plotted (in units of the excited state decay rate $\Gamma sc/\Gamma$, where Γsc is the scattering rate) against the unitless saturation parameter s in fig. 2.3. For $s \ll 1$, coherent scattering dominates the total scattering rate, whilst for $s \gg 1$ the total scattering is dominated by the incoherent part.

2.1.4 Complex susceptibility

The polarisation density $\mathbf{P}$ of a dielectric medium such as a cold atom gas under the influence of a perturbing electric field $\mathbf{E}$, is related to the field via the complex susceptibility $\tilde{\chi}$ of the medium [60],

$$\mathbf{P} = \epsilon_0 \tilde{\chi} \mathbf{E} = \frac{\epsilon_0}{2}\left(\tilde{\chi}\mathbf{E}_0 e^{i\omega t} + \tilde{\chi}^* \mathbf{E}_0^* e^{-i\omega t}\right), \tag{2.30}$$

where ϵ_0 is the permittivity of free space, ω the optical angular frequency, $\mathbf{E}_0$ the electric field amplitude and t the time . With the electric displacement $\mathbf{D} = \epsilon_0 \mathbf{E} + \mathbf{P}$, which using eq. (2.30) can be written as $\mathbf{D} = \epsilon_0 (1 + \tilde{\chi})\,\mathbf{E}$, the relative permittivity

of the medium is the term in the brackets,

$$\epsilon_r = 1 + \tilde{\chi}. \tag{2.31}$$

A sample containing N cold atoms within a volume V has a number density $\rho = N/V$. If the dipole moment $\mathbf{d} = e \cdot \mathbf{r}$, then this ensemble has a macroscopic polarisation density $\mathbf{P}$ given by

$$\mathbf{P} = \rho\langle\mathbf{d}\rangle = \rho \,\mathrm{Tr}\left(\hat{\rho}\mathbf{d}\right) = \rho\left(\mathrm{d}_{12}\rho_{21} + \mathrm{d}_{21}\rho_{12}\right), \tag{2.32}$$

where d_{mn} is the transition dipole matrix element [61]. It is convenient at this point to make a transformation to a frame that rotates with the perturbing electric field, such that $\rho_{12} = \tilde{\rho}_{12}\mathrm{e}^{-\mathrm{i}\omega t}$. Equating the two expressions (eqs. (2.30) and (2.32)) for $\mathbf{P}$ gives,

$$\rho\left(\mathrm{d}_{12}\tilde{\rho}_{21}\mathrm{e}^{\mathrm{i}\omega t} + \mathrm{d}_{21}\tilde{\rho}_{12}\mathrm{e}^{-\mathrm{i}\omega t}\right) = \frac{\epsilon_0}{2}\left(\tilde{\chi}\mathbf{E}_0\mathrm{e}^{\mathrm{i}\omega t} + \tilde{\chi}^*\mathbf{E}_0^*\mathrm{e}^{-\mathrm{i}\omega t}\right). \tag{2.33}$$

Equating the coefficients of $\mathrm{e}^{\mathrm{i}\omega t}$ in eq. (2.33), acting upon both sides of the equation with d_{21}, and using eq. (2.6) yields an expression for the complex susceptibility,

$$\tilde{\chi} = -\frac{2\rho|\mathrm{d}_{12}|^2\tilde{\rho}_{21}}{\epsilon_0\hbar\Omega}. \tag{2.34}$$

A substitution for ρ_{21} using the complex conjugate of eq. (2.25), and with $|\mathrm{d}_{12}|^2 = 3\pi\Gamma\epsilon_0\hbar c^3/\omega^3$, the resonant scattering cross-section $\sigma_0 = 3\lambda^2/2\pi$ and the detuning dependant scattering cross-section $\sigma = \sigma_0/\left(1 + s_0 + 4\nu^2\right)$ [47], the complex susceptibility can be expressed as,

$$\tilde{\chi} = \frac{\rho\sigma}{k}\left(\mathrm{i} - 2\nu\right) = \frac{\rho\tilde{\sigma}}{k}, \tag{2.35}$$

where $\nu = \Delta/\Gamma$ is the detuning in units of the excited state natural linewidth and $\tilde{\sigma} = \sigma_{Re} + \mathrm{i}\sigma_{Im} = \sigma\left(\mathrm{i} - 2\nu\right)$ is the complex absorption cross-section. The susceptibility of a dielectric material determines the response of the polarisation of a medium to an electric field.

2.1.5 Refractive index

The refractive index n of a homogeneous medium is simply the ratio of the speed of light in vacuum to the speed of light within the medium. In vacuum, the speed of light $c = 1/\sqrt{\epsilon_0\mu_0}$, where μ_0 is the permeability of free space. Other media may

have a different permittivity ϵ and permeability μ. In such media the speed of light is $u = 1/\sqrt{\epsilon\mu}$, and the refractive index of the medium is,

$$\mathrm{n} = \frac{c}{u} = \sqrt{\frac{\epsilon\mu}{\epsilon_0\mu_0}}. \tag{2.36}$$

In most non-ferromagnetic materials, including a dilute atomic cloud, with an electric field at optical frequencies, $\mu \simeq \mu_0$ and $\mathrm{n} \simeq \sqrt{\epsilon/\epsilon_0} = \sqrt{\epsilon_r}$ [60]. Assuming a dilute gaseous media with $\mathrm{n} \simeq 1$ and using eq. (2.31), the refractive index can be expressed as

$$\mathrm{n} = \sqrt{1+\tilde{\chi}} \simeq 1 + \frac{\tilde{\chi}}{2}. \tag{2.37}$$

Using eqs. (2.35) and (2.37), the refractive index n can be split into its real n_{Re} and imaginary n_{Im} components,

$$\mathrm{n}_{Re} = 1 + \frac{\rho\sigma_{Re}}{2k}, \tag{2.38}$$

$$\mathrm{n}_{Im} = \frac{\rho\sigma_{Im}}{2k}. \tag{2.39}$$

2.1.6 Phase shift and optical depth

Assuming the atomic sample is thin enough that transverse propagation of light inside the sample can be ignored, the phase shift (ϕ) of the light and the optical depth (OD) of the sample are determined relative to the light travelling an equivalent distance through vacuum. With the integral of the refractive index along the propagation direction $\int \mathrm{n}\, \mathrm{d}z$, the probing field amplitude can be written as

$$\mathbf{E}_r = \mathbf{E}_0 \mathrm{e}^{\mathrm{i}\left(k\int \mathrm{n}\mathrm{d}z - \omega t\right)}. \tag{2.40}$$

In vacuum the atomic number density $\rho = 0$, thus $\mathrm{n} = \mathrm{n}_{Re} + \mathrm{i}\mathrm{n}_{Im} = 1$. In this scenario $\int \mathrm{n}\, \mathrm{d}z = z$, and eq. (2.40) reduces to $\mathbf{E}_r = \mathbf{E}_0 \mathrm{e}^{\mathrm{i}(kz-\omega t)}$. This method of representing $\mathbf{E}_r$ as in eq. (2.40) will become useful for defining the optical depth OD and phase shift ϕ. Using this notation the wave travelling through an atomic sample with a non uniform complex refractive index n can be easily expressed as

$$\mathbf{E}_r + \mathbf{E}_s = \mathbf{E}_0 \mathrm{e}^{-k\int \mathrm{n}_{Im}\mathrm{d}z} \mathrm{e}^{\mathrm{i}\left(k\int \mathrm{n}_{Re}\mathrm{d}z - \omega t\right)}, \tag{2.41}$$

where $\mathbf{E}_s$ is the scattered wavefront from the sample. Limits can be placed on the integration that cover the extent of the object along the propagation direction. The

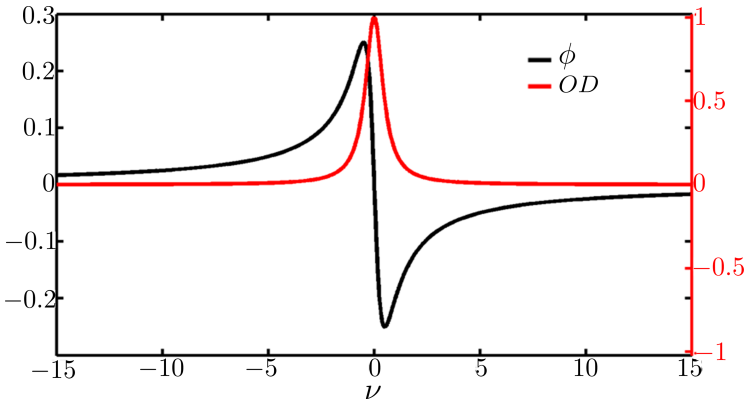

Figure 2.4: Displayed is a plot of the phase shift (ϕ, black line) and optical depth (OD, red line) in units of the resonant optical depth ($OD\,(\nu = 0)$), versus the detuning in units of the excited state decay rate $\nu = \Delta/\Gamma$, plotted for $s \ll 1$ so there is negligible power broadening. For $|\nu| \ll 1$ the graph displays anomalous dispersion, and there is a sharp transition between a positive and negative phase shift.

interaction with the sample phase shifts and attenuates the phase and amplitude of the probing wavefront $\mathbf{E}_r$ respectively. Then using eq. (2.40) the wavefront exiting the sample can then be written in terms of an attenuation and a phase shift ϕ of the wave propagating through vacuum,

$$\mathbf{E}_r + \mathbf{E}_s = \mathbf{E}_r \mathrm{e}^{-k\int \mathrm{n}_{Im}\mathrm{d}z} \mathrm{e}^{\mathrm{i}k\int(\mathrm{n}_{Re}-1)\mathrm{d}z} = \mathbf{E}_r \mathrm{e}^{-\frac{OD}{2}+\mathrm{i}\phi}. \tag{2.42}$$

Then an expression for the wavefront scattered by the atoms can be obtained from eq. (2.42) as,

$$\mathbf{E}_s = \mathbf{E}_r \left(\mathrm{e}^{-\frac{OD}{2}+\mathrm{i}\phi} - 1\right). \tag{2.43}$$

With the column density defined as the integral of the number density along the line of sight $\rho_c = \int \rho \, \mathrm{d}z$, and the expressions for the real and imaginary parts of the refractive index (eqs. (2.38) and (2.39)) and eq. (2.42), its easy to show that,

$$\phi = k\int(\mathrm{n}_{Re}-1)\mathrm{d}z = \frac{\rho_c\sigma_{Re}}{2} = -\rho_c\sigma\nu, \tag{2.44}$$

$$OD = 2k\int \mathrm{n}_{Im}\mathrm{d}z = \rho_c\sigma_{Im} = \rho_c\sigma. \tag{2.45}$$

In fig. 2.4, the normalised phase shift and optical depth (normalised with respect to the resonant optical depth $OD\,(\nu = 0)$ (eq. (2.45)).) are plotted against ν. Near

the atomic resonance ($\nu = 0$) the graph displays anomalous dispersion, since the refractive index of the medium increases with decreasing detuning. For negative detuning ($\nu < 0$), the phase shift is positive, thus indicating that n < 1 and the wave phase velocity is greater than the speed of light in vacuum.

2.2 Laser cooling and trapping

It could be said that modern cold atom physics started with the slowing of atomic atomic beams [1, 4, 62–66]. Nowadays, methods to slow down an atomic beam from an oven is still a critical step for efficient loading many atoms to a ultra-high vacuum (UHV) environment for cold atom experiments.

The forces that arise as a consequence of the interaction of an electromagnetic field with atoms (see appendix B) can be utilised to trap and cool the atoms. In this section a review of standard methods in laser cooling and trapping relevant to this project will be reviewed. In particular, methods of slowing atomic beams in one dimension are presented in section 2.2.1, whilst more sophisticated three dimensional cooling schemes including the optical molasses and magneto-optical trap are discussed in sections 2.2.2 and 2.2.3 respectively. Optical (see section 2.2.4) and magnetic (see section 2.2.5) traps that permit cooling schemes such as evaporative cooling for BEC formation are briefly discussed.

2.2.1 Slowing atomic beams

Atoms thermally evaporated from a typical oven travel at velocities of a few hundred meters per second, too high to achieve efficient capture into a trap for cooling. An ^{87}Rb atom with mass $m_{\mathrm{Rb}} = 1.441 \times 10^{-25}$ kg leaving an oven with a temperature of $T = 370$ K, has a most probable velocity $v_p = \sqrt{2k_B T/m_{\mathrm{Rb}}} \simeq 266$ ms^{-1} [67]. Considering that the scattering force saturates, there is a maximum force F_{max} acting on the ^{87}Rb atom in a travelling wave opposing the atom's motion, thus there is a maximum deceleration associated with it of $a_{\mathrm{max}} = F_{\mathrm{max}}/m_{\mathrm{Rb}}$. Typically half the maximum value is used for calculation to ensure that atoms are not left behind as a consequence of the random nature of the force [46]. Assuming the light frequency remains resonant as the atom is decelerated, the stopping distance can be estimated as $L_0 = v_p^2/a_{\mathrm{max}} = 0.76$ m, which is typical for all of the alkali metals. For an atom leaving the oven with velocity v_0 under constant deceleration, the velocity $v(z)$ at a distance z is

$$v(z) = v_0\sqrt{1 - z/L_0}. \tag{2.46}$$

For monochromatic laser light, the assumption that the frequency remains resonant as the atoms slow is poor. Atoms that are resonant will be decelerated, thus the change in Doppler shift takes them out of resonance with the slowing laser. Chirped slowing [46, 47, 64] keeps the atoms resonant as they slow by linearly varying the laser frequency to compensate the Doppler shift. This laser frequency shift can be achieved using electro-optic modulators or by directly scanning the frequency of a diode laser. However, a more efficient approach is to instead vary the atomic resonant frequency using a Zeeman shift in a so-called Zeeman slower [1, 4, 65, 66]. In weak fields such that the interaction with the external field is weaker than the hyperfine interaction [46] the frequency shift $\delta\omega_{\text{ze}}$ is related to the magnetic field strength B via

$$\delta\omega_{\text{ze}} = g\mu_B MB/\hbar, \tag{2.47}$$

with μ_B the Bohr magneton, M the projection of the angular momentum along B, and g the Landé g-factor. Using a varying field solenoid to produce a magnetic field $B(z)$, the atoms can remain resonant with the laser light if $\omega_0 + \mu_B B(z)/\hbar = \omega + kv(z)$ is satisfied. Here it is assumed that the transition used for slowing is the $5^2S_{1/2}$ to $5^2P_{3/2}$ in ^{87}Rb, in particular the transition between the hyperfine levels $(F = 2, M_F = \pm 2 \rightarrow F' = 3, M_F = \pm 3)$ (a diagram of the D_2 transition in ^{87}Rb is given in fig. 4.4.). From eq. (2.46) the field profile required to compensate the Doppler shift with the Zeeman shift is

$$B(z) = B_0\sqrt{1 - z/L_0} + B_{\text{bias}} \tag{2.48}$$

with $B_0 = \hbar k v_0/\mu_B$, and B_{bias} a bias field that can allow use of a slowing laser with a detuning from resonance at $v = 0$ and $B = 0$. In practice B_{bias} and ω are tuned such that atoms have a non zero end velocity, so they can continue on to an experiment or trap [46]. Such a device permits efficient slowing, since at some point along the slower any atoms with $v < v_0$ will come into resonance and be slowed. The Zeeman shift of the ground and excited states must be different so that there is a shift in the atomic resonant frequency. Alternative techniques to slowing atoms include changing the resonant frequency using a strong and varying electric field [68, 69], and slowing using high power broadband light [70, 71] so that atoms at a range of velocities are resonant with the slowing light.

During this project an attempt was made to combine the Zeeman slowing scheme with broadband/chirped beam slowing (see appendix E). However, due to the lack of success with this attempt, only the Zeeman part is utilised in practice.

2.2.2 Optical molasses

Deceleration of an atom beam only reduces the velocity and its spread in one dimension, whereas the random fluctuation of the scattering force heats up the atoms in all three dimensions. The objective of cooling is to reduce the temperature of cold atom samples in all three dimensions. The optical molasses was the first three dimensional laser cooling technique applied to atomic samples [5]. It consists of three orthogonal standing waves constructed by placing two counter propagating beams along each dimension that overlap at a central point. The six beams derive from a single laser source and each have an equal negative detuning Δ from the rest frame atomic resonance ω_0. It will be assumed that the beam intensities are weak such that $s_0 \ll 1$. Atoms at rest in the standing wave feel no net force, however considering an atom with a non-zero velocity, there will be an imbalance in the force exerted on the atom by the two beams (fig. 2.5). An atom travelling with velocity v_z travels toward a beam with a frequency that is Doppler shifted $\omega + kv_z$ nearer to the atomic resonance, whilst it travels away from a beam that is shifted further from the resonance $\omega - kv_z$ [46]. This Doppler shift increases the probability of scattering from the beam the atom is moving toward, thus resulting in a net force which is given by the net effect of the scattering force from the two counter propagating beams $F_{\mathrm{OM},z} = F_{\mathrm{scat}}(\Delta - kv_z) - F_{\mathrm{scat}}(\Delta + kv_z)$. Using $f(x + dx) \simeq f(x) + f'(x)\,dx$, an expression for this force can be derived as,

$$F_{\mathrm{OM},z} \simeq -2\frac{\partial F_{\mathrm{scat}}}{\partial \omega} kv_z = -\alpha v_z. \tag{2.49}$$

The same result is obtained when considering the other two dimensions. The light exerts a damping force on the atoms with damping coefficient α, which by differentiation of eq. (B.4) with s_0 negligible in the denominator is

$$\alpha = 4\hbar k^2 s_0 \frac{-2\Delta/\Gamma}{\left(1 + (2\Delta/\Gamma)^2\right)^2}. \tag{2.50}$$

For this force to oppose the atomic velocity, the detuning must be negative or the force will be a driving force and tend to increase velocity. Considering the z-axis,

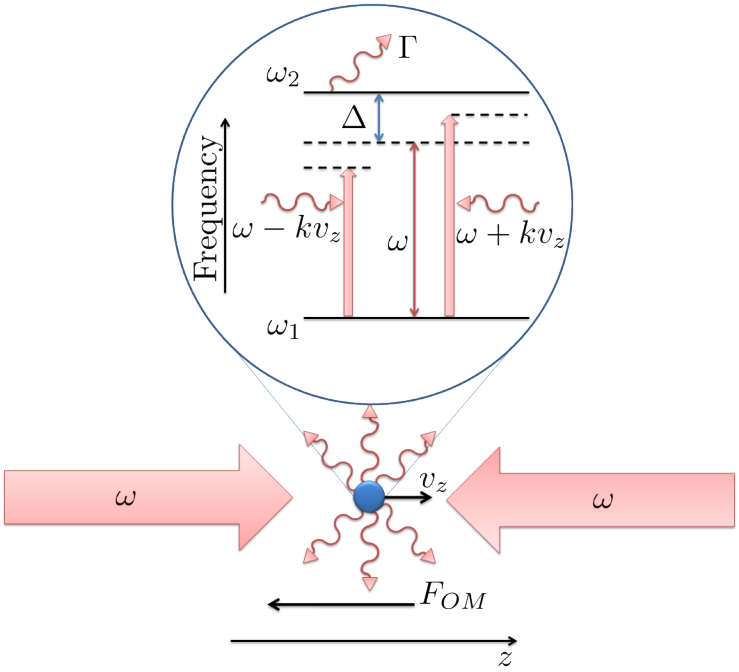

Figure 2.5: An atom is illuminated by two equal but opposing waves with frequency ω and negative detuning $\Delta < 0$, the atom has a velocity v_z toward one of the beams. The resultant Doppler shift (kv_z) makes the beam the atom is travelling toward closer to resonance whilst the beam it travels away from is moved further from resonance. The imbalance in the scattering force from the beams produces a net force F_{OM} that opposes the atomic velocity.

the rate of change in the atomic kinetic energy due to $F_{\mathrm{OM},z}$ is

$$\frac{1}{2}m\frac{\partial v_z^2}{\partial t} = -\alpha v_z^2. \tag{2.51}$$

In steady state, the force seems to reduce the kinetic energy to zero. This is a physically unrealistic result, since the force cannot reduce the atomic velocity to zero due to fluctuations in the force that have not been taken into account in the derivation. By including the fluctuations a limit to the temperature can be found known as the Doppler temperature, which minimised at $\Delta = \Gamma/2$ and is given by $T_{\mathrm{D}} = \hbar\Gamma/2k_B$ which was long believed to be the lower limit to the optical molasses technique. The Doppler limit was soon seen as an inadequate limit for laser cooling of cold atoms when a temperature of 43 ± 20 μK was measured in an optical molasses of Sodium atoms [72] using the time of flight technique (see appendix A), well below the predicted Doppler limit of $T_D \approx 240$ μK. This observation led to the discovery of new Sisyphus cooling mechanisms to explain the low temperature (see appendix B.0.2).

2.2.3 The magneto-optical trap

The magneto-optical trap (MOT) uses a combination of laser light and magnetic fields to trap and cool atomic samples [6]. Similar to the optical molasses in section 2.2.2, the MOT is composed of standing waves formed by counter propagating beams along each of the three dimensions with frequency ω tuned below the atomic resonance. In the MOT, a magnetic field is introduced via coils in the anti-Helmholtz configuration (fig. 2.6). The field orientation is such that the zero coincides with the overlap region of the three standing waves (it is noted here that the field produced by anti-Helmholtz coils is twice as strong along the central axis (z-axis here) than that of the radial directions, and the separation of the coils is ideally equal to the coil radius.). Atoms that move away from the field zero see a magnetic field that lifts the degeneracy of the magnetic sub-levels, thus the state with $J = 1$ is split into three sub-levels with $M_J = \pm 1, 0$. In order for the radiation to excite a transition to one of the sub-levels, the photon needs to carry the correct angular momentum with respect to the quantization axis, which is defined by the magnetic field direction. A circularly polarized photon with $+1$ unit of angular momentum is known as a σ^+ photon and can only excite a $\delta M_J = M_{J,\mathrm{excited}} - M_{J,\mathrm{ground}} = 1$ transition. The opposite is true for a σ^- photon and a photon carrying no angular momentum can only excite a transition with $\delta M_J = 0$. In the MOT standing waves are formed with

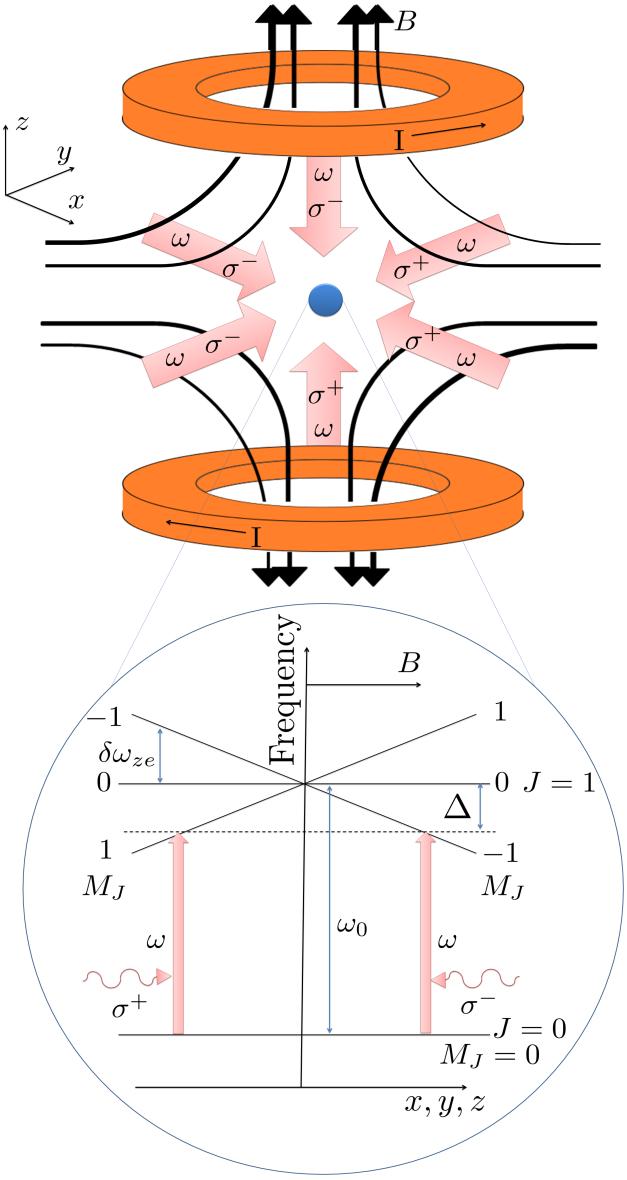

Figure 2.6: Displayed is a schematic of the set-up of the coils and laser beams in a MOT. The coils are arranged in the anti-Helmholtz configuration with a current I in opposing directions for each coil. The black lines represent the field lines from the coils. Along each spatial dimension there are a pair of counter-propagating beams with negative detuning $\Delta < 0$ and opposing σ^+ and σ^- polarisation. (Inset) A schematic displaying the effect of atomic position along the z-axis on the magnetic M_J sub-levels. Atoms that are positioned at $\pm z$ see the $M_J = \mp 1$ sub-level Zeeman-shifted nearer to resonance.

counter propagating beams with opposing circularly polarized light. Similar to the optical molasses, an atom in the MOT moving with a velocity v toward a beam sees its frequency Doppler shifted nearer to resonance, whilst the beam it travels away from is shifted further from resonance, thus resulting in a reduction of the velocity (see section 2.2.2).

There is another effect caused by the magnetic field and the polarisation of the radiation. As the atoms position reaches $+z$ from the field zero, the M_J sub-level is Zeeman shifted nearer to resonance with the σ^- radiation. Then there is preferential scattering from the σ^- beam when the atoms position moves toward it, thus pushing the atoms back toward the field zero , see fig. 2.6.

The force on an atom in a MOT can be computed in a similar fashion to that of the optical molasses in eq. (2.49). With $\beta = \partial\left(\delta\omega_{\mathrm{ze}}\right)/\partial z$, the force along the z-axis is $F_{\mathrm{MOT}} = F_{\mathrm{scat}}^{\sigma^+}\left(\Delta - kv_z - \beta z\right) - F_{\mathrm{scat}}^{\sigma^-}\left(\Delta + kv_z + \beta z\right)$. Using ω_0 as a constant so that the detuning is only a function of ω and using $f\left(x + dx\right) \simeq f\left(x\right) + f'\left(x\right)dx$ the force on atoms in a MOT is

$$F_{\mathrm{MOT}} \simeq -2\frac{\partial F_{\mathrm{scat}}}{\partial \omega}\left(kv_z + \beta z\right) = -\alpha v_z - \frac{\alpha\beta}{k}z. \tag{2.52}$$

The force is made up of two components, the first is the same velocity dependant force as that in the optical molasses and results in a reduction in the atomic velocity cooling the atoms. The second is a position dependant trapping force that pushes the atoms toward the field zero where the beams overlap. Atoms undergo a damped harmonic motion, where the amplitude of the motion decays as $A_0 \exp\left(-t/\tau_{\mathrm{d}}\right)$ with damping constant $\tau_{\mathrm{d}} = 2m/\alpha$. The combination of trapping and cooling makes the MOT convenient when compared to the optical molasses as the preparatory stage in laser cooling experiments as it can cool more atoms for a longer time as they do not diffuse out of the trap so easily, thus giving a larger yield of cold atoms. Once a satisfactory number of cold atoms have accumulated in the MOT, the field can be switched off and other cooling schemes such as Sisyphus cooling [73, 74] can be implemented (see appendix B.0.2).

2.2.4 Dipole trapping

Cold atoms can be confined within spatially dependant conservative potentials that arise as a consequence of light and/or Zeeman shifts. In the first demonstration of a dipole trap for atoms [75] a single focused laser beam was used to generate the trapping potential, and atoms were loaded into the trap after pre-cooling using

the optical molasses technique (section 2.2.2). The trapping force is related to the gradient of the light shift (appendix B) and so the spatial variation in the intensity of a focused laser beam produces a spatially varying light shift across the beam waist, and along the beam propagation direction. The trap depth is increased with beam intensity. This is accompanied with an increased scattering, thus resulting in heating. To reduce the heating, a large detuning ($|\Delta| \gg \Gamma$) for the trap beam can be chosen. Under this condition the scattering rate and the dipole potential depth become

$$R_{\text{scat}} \simeq \frac{\Gamma^3 s_0\left(x, y, z\right)}{8\Delta^2}, \tag{2.53}$$

and

$$U_{\text{dip}} \simeq \frac{\hbar\Gamma^2 s_0\left(x, y, z\right)}{8\Delta} \tag{2.54}$$

respectively. Proper choice of the detuning can yield a significant trapping potential with negligible scattering. As the dipole force is dependant on detuning, in order to trap atoms at the focus of a beam a negative detuning must be chosen. The dipole force is conservative, hence when there is negligible scattering the total energy is conserved. As atoms move within the trap volume, they must be cooled into the potential in order to be captured by the trap. The shape of a trap formed by the focal point of a laser beam is a cigar, since the intensity changes more rapidly across the beam waist than longitudinally. The dipole force can be utilised in standing waves to form more complex trapping potentials such as in optical lattices [76, 77].

2.2.5 Magnetic trapping

The Stern-Gerlach experiment demonstrated the force that is felt by a neutral atom with magnetic moment $\boldsymbol{\mu}$ in a magnetic field $\boldsymbol{B}$, $F_{\text{mag}} = \nabla\left(\boldsymbol{\mu} \cdot \boldsymbol{B}\right)$, and this force has been used to trap cold atoms [78]. Magnetic trapping is often used after an initial stage of laser cooling with an optical molasses and/or MOT, thus atoms that are to be trapped move slowly. Slow atoms are able to adiabatically follow the field direction, thus the dipole moment of the atom and the field direction stay aligned. Under this adiabatic condition the Zeeman shift (see section 2.2.1) is dependant on the magnitude of the magnetic field, and using eq. (2.47) the force can be written as

$$F_{\text{mag}} = -g\mu_B M \frac{dB}{dz}. \tag{2.55}$$

Due to Earnshaw's theorem, there can be no magnetic field maximum for a static field in 3D, but there can be a field minimum, which can be used to trap weak-field seeking atoms. A quadrupole field [47], generated by a pair of anti-Helmholtz coils as in the MOT, see fig. 2.6, forms a field minimum at its centre, thus one can use the MOT coils to generate the trapping field. The field from a pair of anti-Helmholtz coils is $\mathbf{B} = B_x, B_y, -2B_z$, near the centre the field increases linearly in the radial direction $r = \sqrt{x^2 + y^2}$. The trap attracts atoms in a low-field seeking state ($gM > 0$) (M is the projection of the angular momentum along B.), to the trap centre whilst repelling atoms in a high field seeking state ($gM < 0$). At the centre of the trap where $|B| = 0$, different M states mix together and an atom can transfer into a different M state that may not be low-field seeking. The atoms that undergo such a transition will be expelled from the trap. This loss mechanism is inconvenient for trapping atoms for long periods of time (e.g. ~ 10 s), other traps have been devised to counteract the problem such as the Ioffe-Pritchard magnetic trap [46, 47]. Despite the loss mechanism, in this work the quadrupole trap was used to confine atoms as the long trapping times required for evaporative cooling are unnecessary and so discussion of magnetic traps is limited to the quadrupole case. For an ^{87}Rb atom in the $5^2S_{1/2}, F = 2, M_F = \pm 2$ state, the field gradient required in a MOT (~ 10 Gcm^{-1}), imparts a magnetic force $F_{mag} \approx 3.7 \times 10^{-24}$ N, that is just enough to support atoms against gravity $F_{grav} \approx 1.4 \times 10^{-24}$ N. However to use the MOT coils as a magnetic trap to tightly confine atoms, the current in the coils needs to be increased, and the heat generated from this current increase must be dissipated by cooling the coils. This can be achieved with air or water cooling.

The use of magnetic traps for atoms in conjunction with evaporative cooling [79] is a common method for achieving BEC, where the magnetic potential well depth is reduced to allow the atoms with the largest thermal energy to escape the trap. The atoms left behind in the trap re-thermalise to a lower temperature. This powerful cooling method can achieve much cooler temperatures than optical cooling relying on spontaneous emission, although a large fraction of the atomic sample is lost to achieve the low temperatures.

2.3 Traditional ways of imaging cold atoms

In this section a review is conducted of the established imaging techniques for cold atoms. To this end, the methods are categorised into either incoherent or coherent schemes. The example given of an incoherent approach is the popular

fluorescence imaging (see section 2.3.1), in which the nearly isotropic fluorescence from atoms is imaged in-focus with a camera. Coherent imaging methods for cold atoms fall into two groups, techniques that record an in-focus image of the sample transmission (see section 2.3.2) and approaches that image the out-of-focus diffraction (see section 2.3.3). The difference between detecting the fluorescence and the coherent samples scattered wavefront $\mathbf{E}_s$ from the atoms have implications for the diffraction limited resolution, as is discussed in section 3.1.2, whilst the difference between recording the in-focus and out-of-focus diffraction has implications for the sensitivity (see section 6.1.2).

In addition, aberration and speckle noise are two further issues of practical importance for most imaging techniques. Although complex optical arrangements can be utilised to minimise aberration in fluorescence and absorption imaging (see section 2.3.2), it is highlighted that the aberration in phase-contrast (see section 2.3.2) and dark-ground (see section 2.3.2) imaging is practically unavoidable at high NA, thus limiting their application in high precision off-resonant imaging.

Speckle noise affects all methods of imaging cold atoms [35], since the narrow atomic transitions require a laser with a long coherence length $L_{\text{coh}} = \lambda^2/\delta\lambda$, where λ is the average wavelength output of the laser and $\delta\lambda$ is the laser linewidth. Increasing the linewidth, as is commonly used in holographic imaging outside of cold atom research to suppress speckle noise [80], is inadequate for cold atoms, which typically requires the linewidth to be smaller than the detuning. Speckle noise can impose difficulties for subtracting away the background light in incoherent or in-focus coherent imaging, since at high spatial frequency it is sensitive to vibration. When imaging the out-of-focus diffraction as in diffractive imaging, speckle noise can generate severe artefacts. In section 5.4 a method is presented for suppressing speckle noise in the holographic method developed in this work.

2.3.1 Incoherent imaging: fluorescence imaging

Possibly the simplest imaging technique applied to cold atom imaging, in fluorescence imaging, a near-resonant probe with known intensity and detuning illuminates the sample. Then a proportion of the nearly isotropic spontaneous scattering is collected by a lens, and imaged to a detector, see fig. 2.7. The probe light is normally retro-reflected and passed twice through a $\lambda/4$ waveplate to balance the radiation pressure during imaging, the balanced MOT cooling beams themselves can be used as the probe light (section 2.2.3).

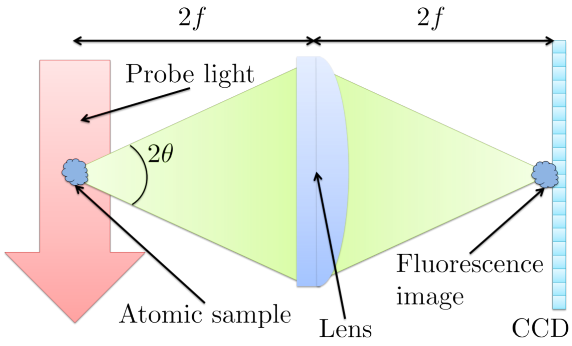

Figure 2.7: Shown is a schematic of a fluorescence imaging set-up in the $2f$-$2f$ lens configuration. A near-resonant probe beam with known detuning Δ and intensity I illuminates the sample, but is not collected by the imaging lens. The probe can be a single beam, or even the MOT cooling beams themselves section 2.2.3. The lens collects the fluorescence from the sample and images it onto a detector.

The light collected by the lens subtends an angle 2θ, resulting in a numerical aperture $\mathrm{NA} = \mathrm{n}\sin\theta$ (for vacuum $\mathrm{n} = 1.$), and a solid angle subtended by the lens of $\bar{\Omega} = 2\pi\,(1 - \cos\theta)$. For a camera with an exposure time τ_{exp}, and quantum efficiency Q, the total number of photon counts detected by the camera N_{ph} is given by (assuming that one detected photon corresponds to one detector count.),

$$N_{ph} = \left(\frac{\bar{\Omega}_s}{4\pi}\right)\Gamma_{\mathrm{tot}} N Q \tau_{\mathrm{exp}}, \tag{2.56}$$

where Γ_{tot} is the total scattering rate, see eq. (2.27), N is the number of atoms in the sample and the factor $\left(\bar{\Omega}_s/4\pi\right)$ is the fraction of the 4π solid angle collected by the lens. The atom number can easily be estimated by rearranging eq. (2.56) for N.

The simplicity of fluorescence imaging makes it a convenient diagnostic tool, though for precise determination of atom numbers it requires detectors with high sensitivity and low dark counts. For precision determination of atom number with optically thick atomic samples this method is inadequate. The probe is quickly attenuated by the atomic cloud, changing the probe intensity across the sample, therefore this non-uniform intensity makes the scattering rate difficult to determine accurately. Although the probe attenuation can be alleviated by saturating the atoms with an intense probe [41], such an approach makes it very difficult to image over long exposure times while cooling. Also there is a larger chance of the cloud reabsorbing the fluorescence. Furthermore, with imperfect control of polarisation, coherent counter-propagating beams will interfere, thus producing a spatially varying

intensity across the atomic sample. The combination of these effects tends to inhibit accurate determination of atom number [57], since Γ_{tot} is difficult to define. Accurate number determination with samples of $N \sim 10^3$ atoms has been demonstrated by saturating the atomic fluorescence [81].

In the ideal scenario fluorescence imaging is background free and is nearly free of speckle noise, since it is only picked up by the fluorescence itself. The shot-noise in each pixel of the image is given by the square root of the number of photons detected $\sqrt{N_{ph}}$. This scaling means that maintaining high atom number resolution is more difficult for larger atom numbers [82]. Therefore the precise atom number counting demonstrated with atom numbers $N = 1200$ with a very long exposure time in a molasses [81] is a remarkable achievement.

Although fluorescence imaging is more suited to imaging smaller atomic samples, it encounters difficulties when imaging atoms trapped in optical lattices [19–21, 77]. Lattice sites with more than one atom occupancy per site cannot be imaged with a near-resonant probe as atoms are lost in pairs due to inelastic light assisted collisions [19–22, 38], a limitation shared with all resonant detection techniques.

Precision optics are required for high NA imaging, thus increasing the set-up complexity and inevitably introducing unwanted lens aberrations into images when the field of view is large. In addition, with the depth of field as described by Berek's formula [83, 84] decreasing with an increasing numerical aperture, it is only possible to focus an image at high NA within a small range along the optical axis (~ 1 μm for $\lambda \sim 1$ μm). If attempting to image a sparse 3D optical lattice at high NA, only a narrow planar slice of the lattice is resolvable with a single shot, thus it is impossible to address all of the sites within the lattice. This disadvantage is shared with all of the focal plane detection methods (see section 2.3.2), thus they must be considered as a purely 2D imaging techniques in a single shot, particularly at high NA, if the focal plane is not scanned during the probe.

2.3.2 Coherent imaging I: In-focus image recording

In this section, the group of coherent imaging techniques that use lenses to form an in-focus image at the detector will be discussed. Two of the techniques (absorption and phase-contrast imaging, see sections 2.3.2 and 2.3.2) use lenses to image both the illuminating probe light and the light scattered by the sample, whilst dark-ground imaging (see section 2.3.2) blocks the probe, thus leaving only the image of the scattered light at the camera.

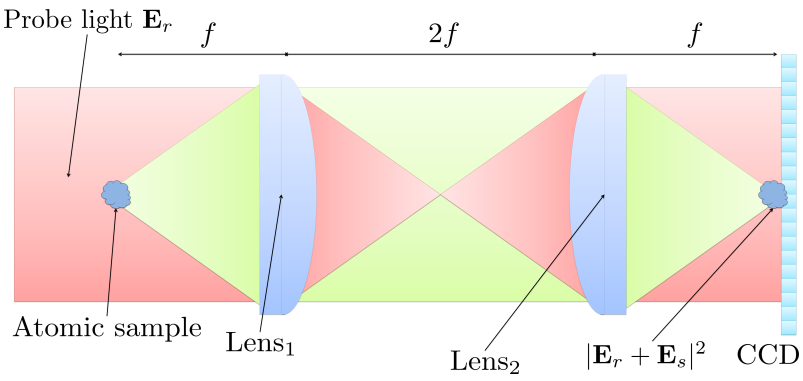

Figure 2.8: Schematic of an absorption imaging set-up in the f-$2f$-f lens configuration. The sample is illuminated with a plane wave probe (red), and the atomic sample is located at the focal point of lens$_1$. The camera is placed at the focal point of lens$_2$, thus the image of the shadow cast by the atomic sample is in-focus at the CCD camera. The green light represents the coherent scattered wavefront $\mathbf{E}_s$ from the sample.

By imaging the probe to the camera, absorption an phase-contrast imaging detect the signal as a variation in the probe light caused by the atomic sample. For these techniques the shot-noise level is proportional to the square root of the probe intensity and is independent of the number of atoms, thus they are more accurate for determining atom number for large atom numbers when compared to fluorescence or dark-ground imaging.

Absorption imaging

The attenuation of light by an atomic cloud is commonly measured in laser cooling labs using absorption imaging [37, 85], where the shadow cast in a probe beam by a cloud of cold atoms is imaged on a detector, as in fig. 2.8. The two lenses in the imaging system can have different focal lengths f_1 and f_2, thus the magnification is given by $M = -f_2/f_1$. Standard detectors, such as complementary metal-oxide semiconductor (CMOS) and charge-coupled device (CCD) cameras are only sensitive to light intensity. Thus using eqs. (2.42) and (2.43) the detector records,

$$|\mathbf{E}_r + \mathbf{E}_s|^2 = |\mathbf{E}_r|^2 \mathrm{e}^{-OD}. \tag{2.57}$$

To extract information such as the column density ρ_c, two images are recorded, one with ($|\mathbf{E}_r + \mathbf{E}_s|^2$) and one without ($|\mathbf{E}_r|^2$) the atomic sample. Then the absorption

is simply given by,

$$\frac{|\mathbf{E}_r + \mathbf{E}_s|^2}{|\mathbf{E}_r|^2} = \mathrm{e}^{-OD}, \tag{2.58}$$

and the OD is extracted as the negative natural logarithm of the absorption [85],

$$OD = -\ln\left(\frac{|\mathbf{E}_r + \mathbf{E}_s|^2}{|\mathbf{E}_r|^2}\right). \tag{2.59}$$

With the scattering cross-section $\tilde{\sigma}$ known, it is easy to determine the column density using eq. (2.45) as $\rho_c = OD/\sigma_{Im}$. Standard cameras are constructed from pixels with size x_{pix} and area $A_p = x_{\mathrm{pix}}^2$. The total number of atoms N in the sample that contribute to the absorption, is found by summing over the pixels,

$$N = \sum_{Pixels} \rho_c A_p / M^2 = \frac{A_p}{M^2 \sigma_{Im}} \sum_{Pixels} OD. \tag{2.60}$$

Imaging is normally conducted near-resonance to maximize the imaginary part of the absorption cross-section, since the technique is sensitive to OD only. As can be seen from fig. 2.4, the optical depth follows a Lorentzian profile and decreases sharply with increasing detuning $|\nu|$. In addition, imaging is ideally conducted with $s \lesssim 1$, so that a large proportion of the scattering is composed of coherent photons.

Absorption imaging is a common technique for probing atomic samples [8–10, 37], and can achieve single atom accuracy [86]. The technique is useful for accurate determination of atom numbers for large atomic samples, since the shot-noise is proportional to the square root of the probe intensity and is insensitive to atom number. However, for a camera with maximum pixel count N_{max} the absorption sensitivity $\delta OD \sim 1/\sqrt{N_{\mathrm{max}}}$ (see section 6.1.2), thus with standard cameras (e.g $N_{\mathrm{max}} \lesssim 10^6$) and unity magnification it is difficult to achieve an absorption sensitivity significantly less than ~ 1 %. Furthermore, the technique encounters difficulties for atomic samples with $OD \gg 1$ due to extinction of the probe light and multiple scattering effects. Furthermore, similar to fluorescence imaging it suffers from light induced atom losses if imaging lattice sites with multiple atom occupancy.

When imaging samples with $OD \gg 1$, the electric field amplitude of a wave travelling through the sample is attenuated by $\mathrm{e}^{-OD/2}$, see eq. (2.42), and the absorption image of such a sample can be "blacked-out" [37, 87], thus extracting ρ_c from the image becomes difficult. The OD can be reduced by off-resonant imaging to faithfully retrieve ρ_c, however with $\Delta \neq 0$ the real part of the refractive index

n_{Re} is non-zero, see eq. (2.38), and the sample can phase shift the probe and act like a lens. The phase shift ϕ refracts the light by an angle approximately given by $\theta_r \simeq 2\lambda\phi/\pi a$, where a is the characteristic width of the sample. The refracted light must be collected by the imaging system or it will result in a false absorption signal. For a diffraction limited imaging system θ_r must be less than the diffraction angle $\theta_r < \lambda/a \rightarrow \phi < \pi/2$. With optimal detuning, imaging clouds with large a is possible, but reducing a increases θ_r, thus imaging small samples becomes problematic. To circumvent the problem the detuning can be further increased, however, since the OD reduces quicker with detuning, the required detuning for small samples results in an OD that is undetectable above the imaging noise [37]. Aside, a reduction in the OD fundamentally results in a loss of signal.

A method of absorption imaging of optically dense samples is to increase the probe intensity so that the central dense region of the cloud does not fully attenuate the probe. The density information from the central region can then be retrieved [41], since the saturated atoms decrease the probe absorption. The coherent scattering rate (eq. (2.28)) reduces with the increasing probe intensity, thus leading to excessive shot-noise in the image, and the information in the tails of the atomic density distribution can be below the shot-noise level. To counteract this problem a second image of the cloud is recorded with a weaker probe so that the tails are observable, but the central region of the distribution then yields unreliable information. The need for multiple images as in this scheme is inconvenient.

The optical density can be reduced by switching off trapping potentials and magnetic fields, thus allowing the atoms to expand for a certain time until the OD is sufficiently low [87]. However for experiments with BECs, the expansion is an irreversible process leading to a loss of information, even if the expansion dynamics were fully understood.

For atomic samples with a high density, such that resonant dipole-dipole interactions between the atoms are no longer negligible, the atoms can no longer be described as non-interacting spheres. In this regime the optical depth obtained via absorption imaging can no longer be described by Beer's law [39]. There is an increased likelihood that photons will be scattered multiple times within the cloud, leading to a reduction in the expected absorption cross-section [40]. Furthermore, similar to fluorescence imaging, near-resonant absorption imaging suffers from atom losses via light assisted collisions [38] if imaging optical lattice sites with multiple atom occupancy.

Finally, similar to the demand in fluorescence imaging, precision optics are required for aberration-free high NA absorption imaging of cold atoms at long distances. Then with the depth of field limited by Berek's formula [83, 84], only a narrow planar slice is resolvable with a single shot, thus it is impossible to address all sites of an optical lattice with a single shot. Then absorption imaging must be considered as a purely 2D imaging technique, particularly at high NA.

Phase-contrast imaging

It is well known that phase sensitive imaging techniques offer solutions to the problem of probe light extinction when using absorption imaging for samples with high optical density. Furthermore, off-resonant imaging could provide a solution to the light induced atom loss and multiple photon scattering issues with near-resonant probing [34].

The technique of phase-contrast imaging (PCI), developed by Fritz Zernike [88, 89], for which he received the Nobel prize in 1953 [90], is a phase sensitive imaging technique, that utilises a phase shift in $\mathbf{E}_r$ or $\mathbf{E}_s$ to produce contrast proportional to the phase shift by an object in the recorded intensity. This technique became important in microscopy, particularly for phase sensitive, and non destructive imaging of biological samples [91]. PCI has been the most widely implemented phase sensitive technique for cold atoms [87, 92–95]. The ability to probe the atomic sample with off-resonant light was important for the observation of dynamic processes in cold atom clouds including: sound propagation through a BEC [92], Feshbach resonances [95], super-fluid flow [96] and vortex nucleation [97].

An example of the PCI set-up is shown in fig. 2.9, where the set-up is similar to absorption imaging, see fig. 2.8, but with a phase plate inserted in the imaging system to phase shift $\mathbf{E}_r$ relative to $\mathbf{E}_s$ so they interfere at the camera. The dimple in the phase plate is typically between ~ 10 μm and ~ 100 μm in diameter and is positioned to minimally affect $\mathbf{E}_s$, whilst providing the phase shift to $\mathbf{E}_r$.

Considering the simple scenario of a weakly phase shifting ($\phi \ll 1$) pure phase object, the scattered wave can be approximated as $\mathbf{E}_s = \mathbf{E}_r e^{i\phi} \approx i\phi \mathbf{E}_r$. Then for a phase plate giving a typical relative phase shift of $\pm\pi/2$ [37], the reference field becomes $\mathbf{E}_r = \mathbf{E}_r e^{\pm i\frac{\pi}{2}} = \pm i\mathbf{E}_r$. Then ignoring terms with ϕ^2, the intensity recorded by the camera is

$$|\mathbf{E}_s + \mathbf{E}_r e^{\pm i\frac{\pi}{2}}|^2 \approx |i\phi\mathbf{E}_r \pm i\mathbf{E}_r|^2 = |\mathbf{E}_r|^2 (1 \pm 2\phi)\,. \tag{2.61}$$

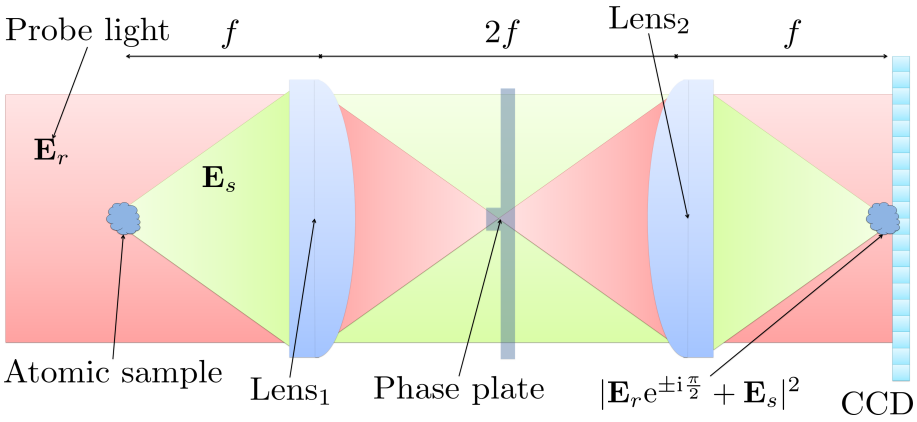

Figure 2.9: Displayed is a schematic of a phase-contrast imaging set-up in the f-$2f$-f lens configuration. The sample is illuminated with a plane wave probe $\mathbf{E}_r$, and the atomic sample is located at the focal point of lens$_1$. The camera is placed at the focal point of lens$_2$, thus the image of $\mathbf{E}_s$ is in-focus at the camera. A phase plate with a bump or dip is used to shift the phase of $\mathbf{E}_r$ after probing the sample by an amount $\pm\pi/2$ relative to the scattered wave $\mathbf{E}_s$, so they interfere at the camera.

Though in practice, for most objects there will be some residual absorption, which affects the imaging accuracy and the sensitivity of PCI [24]. Similar to absorption imaging, the shot-noise in PCI is proportional to the square root of the reference field intensity, thus is can be useful for accurate determination of atom number for larger atomic samples. However, the phase shift sensitivity also scales as $\delta\phi \sim 1/\sqrt{N_{\max}}$, thus it is difficult to achieve a sensitivity below 5 mrad [34] using standard cameras (e.g with $N_{\max} \lesssim 10^6$) with an image magnification near unity (see section 6.1.2)

PCI involves a higher degree of complexity when compared with absorption imaging. The difficulty arises in the alignment of the focused $\mathbf{E}_r$ to the small phase bump/dip in the phase plate, since its effect on the probe is difficult to distinguish from a dust particle. Larger bumps/dips are easier to align, but unintentionally shift more of $\mathbf{E}_s$, thus reducing the signal and introducing unwanted artefacts [91, 98]. Despite the benefits of off-resonant probing, such as alleviating the multiple scattering signal deviation associated with near-resonant probing of optically dense clouds [40], the complexity of PCI is a likely reason that it is less common in laser cooling labs than absorption imaging [24].

Aside from the difficulty in aligning the phase spot, the approximate nature of eq. (2.61) suggests that the information obtained with PCI is approximate. The error comes from the proportion of the scattered wave $\mathbf{E}_s$ that co-propagates with the probe light that is unintentionally phase shifted by the phase plate. At high NA,

this error becomes more severe; imaging requires precision high NA optics which must compensate for aberration, and the imaging lens (lens_1 in fig. 2.9) is required to accomplish two different tasks at once. The lens must collimate the scattered wavefront from the sample, and simultaneously tightly focus the probe light to a point that is smaller than the phase bump/dip. For one of these tasks the lens is in the reverse direction from the ideal orientation, thus it will introduce unnecessary aberration into either $\mathbf{E}_r$ or $\mathbf{E}_s$. At high NA, tight focusing of the probe beam is thus impossible, and this design inadequacy introduces "halo" or "shade-off" artefacts into the image [91, 98]. These artefacts arise in two ways, firstly parts of $\mathbf{E}_r$ that miss the phase bump/dip will not be phase shifted, leading to a reduction in the image contrast, particularly around the edges of the sample. Secondly parts of $\mathbf{E}_s$ that are unintentionally phase shifted by the phase bump/dip lead to a reduction in the contrast at the centre of the image of the sample formed at the detector.

Similar to absorption imaging PCI records an in-focus image, thus it must be considered as a purely 2D imaging technique. Furthermore, PCI suffers from speckle noise, particularly in the reference field (see section 2.3.2). This can be reduced through adjustment of the probe alignment to the atoms and camera. Though adjustment of the probe alignment is inferior to its full removal, as occurs in dark-ground or fluorescence imaging (sections 2.3.1 and 2.3.2 respectively).

Finally, it is also worth mentioning that the phase plates that are required for coherent PCI are not readily commercially available; instead they need to be made using nano-fabrication techniques such as chemical etching or focused ion beam lithography to create a dip in the plate or creating a bump by depositing a layer of phase shifting material on the plate, for example with physical vapour deposition. These fabrication techniques are specialized and can be costly.

Dark-ground imaging

A modification can be made to the phase-contrast imaging geometry by replacing the phase plate with an absorptive mask. The camera then detects the scattered wavefront intensity in an imaging scheme termed dark-ground imaging. Wolfgang Ketterle's group were the first to apply the technique of dark-ground imaging (DGI) to cold atom samples [99], and more recently DGI has been utilised to image a sample with a few tens of atoms [57, 58, 100] and atomic samples with large optical thickness [101]. The technique differs from absorption imaging and PCI in that the technique is sensitive to both OD and ϕ simultaneously.

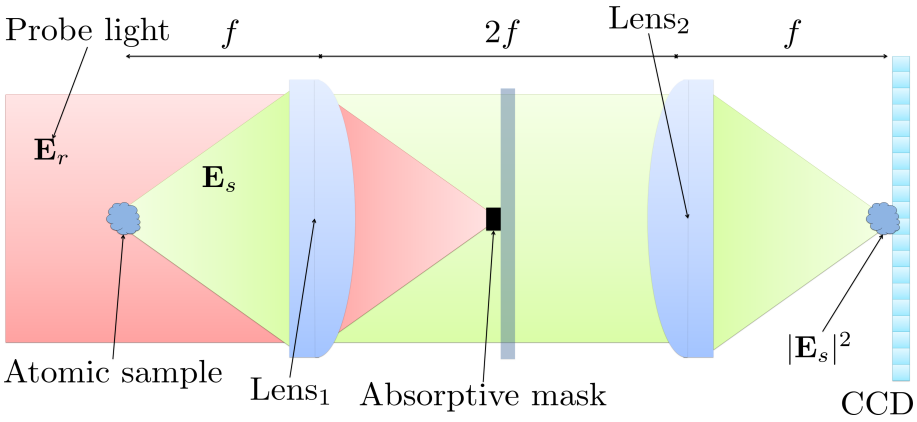

Figure 2.10: Displayed is a schematic of a dark-ground imaging set-up in the f-$2f$-f lens configuration. The sample is illuminated with a plane wave probe $\mathbf{E}_r$, and the atomic sample is located at the focal point of lens$_1$. The camera is placed at the focal point of lens$_2$ so that the image of $\mathbf{E}_s$ is in-focus at the camera. An absorptive mask is used to block the unscattered probe light $\mathbf{E}_r$ after probing the sample, thus $|\mathbf{E}_s|^2$ alone is detected by the camera.

In DGI the reference wave is removed from the imaging system after it has probed the atomic sample by placing an absorptive mask at the Fourier plane of the imaging system, see fig. 2.10. The scattered wavefront is largely unaffected by the mask and continues to propagate to the camera, where an in-focus image of $|\mathbf{E}_s|^2$ is recorded.

For comparison with PCI, a weak ($\phi \ll 1$) pure phase object produces a signal at the detector that is quadratic in ϕ,

$$|\mathbf{E}_s|^2 \approx |\mathrm{i}\phi\mathbf{E}_r|^2 = |\mathbf{E}_r|^2\phi^2. \tag{2.62}$$

Then for small phase shifts $|\phi| \ll 1$, the signal in PCI (eq. (2.61)) is much larger than that of DGI. Though alignment of the $\mathbf{E}_r$ focal spot to the opaque mask in DGI is by far easier than alignment to the phase mask in PCI [24], since standard detectors are sensitive to intensity.

Similar to fluorescence imaging, DGI removes the background light and its associated shot-noise, hence the shot-noise level in DGI is given by the square root of the dark ground signal only. The relation between the dark ground signal and atom number is composed of a coherent term that is proportional to atom number and an incoherent term proportional to the square of the atom number [57]. By blocking the background light, the technique blocks a large amount of the noise that would appear in absorption, phase-contrast or holographic imaging such as laser speckle.

Similar to the "halo" and "shade-off" artefacts in PCI, at high NA it becomes increasingly difficult to fully block the probe light without affecting $\mathbf{E}_s$, thus DGI will suffer from imaging artefacts if the absorptive mask unintentionally blocks too much of $\mathbf{E}_s$, or if it does not fully remove $\mathbf{E}_r$. Stringent demands are placed on the imaging optics for high NA imaging which must also suppress aberration. Also, similar to absorption (see section 2.3.2) and phase-contrast imaging (see section 2.3.2), the technique suffers from a limited depth of field at high NA. A more rigorous comparison of DGI with other imaging techniques is given in [57].

2.3.3 Coherent imaging II: Out-of-focus recording of the diffraction pattern

Holographic imaging techniques for cold atoms extract both the phase and amplitude of the scattered wave $\mathbf{E}_s$ from the interference pattern (hologram) it produces with a coherent reference $\mathbf{E}_r$. These techniques come in the form of either off-axis (see section 2.3.3) or in-line (see section 2.3.3 and chapter 3) holography. Generally holographic techniques extract the out-of-focus $\mathbf{E}_s$, then a numerical propagation to the focal plane permits retrieval of the sample spatial and optical properties. The numerical propagation strictly follows the Maxwell equations, thus is aberration free. However, lenses can be utilised to enhance retrievals resolution. In contrast to in-focus imaging schemes, holographic methods can resolve features along the imaging axis via numerical focusing, so they can be considered three dimensional.

In-line holography consists of illuminating the sample with a probe and recording its interference with the out-of-focus diffraction of $\mathbf{E}_s$. In off-axis interferometers, a separate reference arm traverses an alternate path to the probing field before it is recombined at the detector. Off-axis techniques permit spatial or temporal heterodyning, without which, the phase of $\mathbf{E}_s$ cannot be retrieved from a single hologram, leading to the well known twin image problem [43–45]. Diffraction-contrast imaging (see section 2.3.3) is a type of in-line holography that assumes a monomorphous responsivity (it is assumed that the probe absorption and phase shift are proportional to the column density.) from the atoms to remove the twin image noise. To date diffraction-contrast imaging has been the only demonstration of the in-line technique for imaging cold atoms.

The application of holographic methods to cold atoms is so far limited to a few examples [23–25, 56], primarily due to twin image and speckle noise. In the following, these few examples are summarised and compared with in-focus imaging methods.

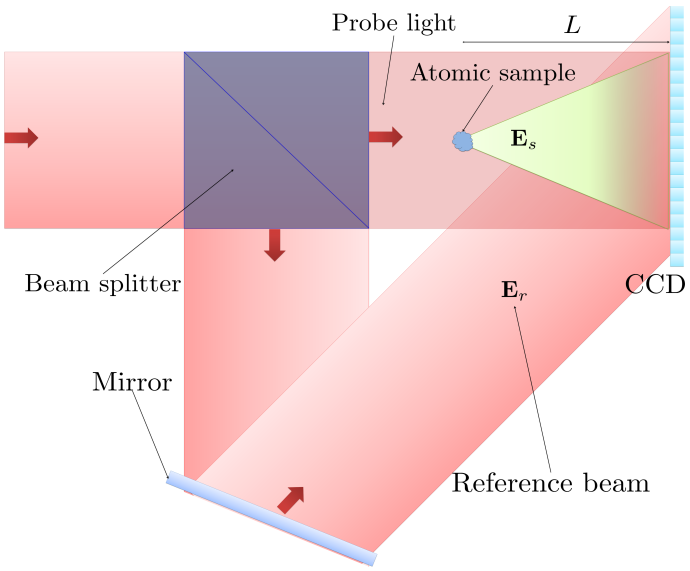

Figure 2.11: Diagram of a set-up for off-axis holography. The probe light is split into two pathways by a beam splitter. The probe beam is absorbed and phase shifted by the atomic sample whilst the reference beam is largely unaffected, apart from scattering of the mirror and other optics that may be used. The reference beam is guided by optics to coincide with the probe beam at an angle at the camera plane where the interference of the probe, the scattered wave from the sample and the reference beam is captured.

A more detailed discussion of the in-line geometry is given in chapter 3, where a novel realisation of an in-line holographic microscope is introduced to solve the twin image, DC and speckle noise problems.

Off-axis holography

A group of separate path interferometers have been proposed [102, 103] and implemented [25, 56] for minimally destructive holographic imaging of cold atom samples. Each follow a general theme whereby the probe beam is split into two separate paths. One beam travels along the probe pathway and interacts with the atomic sample, whilst the reference beam is diverted around the atomic sample. The reference beam is usually diverted outside of the vacuum chamber, or optics are used to steer the beam through a path similar to the probe beam without interacting with the sample. The two beams are recombined at an angle at the plane of the CCD detector where they interfere, see fig. 2.11. What is usually extracted is the wavefront of the probe plus the scattered light from the sample.

A type of off-axis holography, known as spatial heterodyne imaging [25], has been implemented for minimally destructive phase sensitive imaging of cold atoms. The set-up is similar to that of fig. 2.11, but two lenses are inserted into the set-up, one in the probe arm after the atomic sample, and one in the reference arm (see [24, 25] for more detail). The curvatures of the probe and reference beams are matched at the CCD, so that the interference between the two produces straight fringes without the atomic sample. The atomic sample attenuates and phase shifts the probe beam (see section 2.1), which changes the structure of the fringes. A phase shift in the probe displaces the interference fringes from their atomic sample-free positions, whilst an attenuation reduces the fringe contrast. Analysis of the fringes allows extraction of the sample properties.

Spatial heterodyne imaging consists of an elaborate arrangement of optics to steer and image the probe and reference beams to the detector, and the system is highly sensitive to vibration and difficult to align [24]. The use of lenses in the imaging system introduces their unwanted aberration, whilst the use of a reference beam tilted to the probe beam restricts the imaging resolution (see section 3.1.3).

A polarisation-based separate path interferometer has been demonstrated with photon shot-noise limited sensitivity [56]. The set-up of this technique is again a modified version of fig. 2.11, where the probe and reference beams are recombined after the probe interaction with the atomic sample. The combined light is then split into two according to the polarisation of the light using a Wollaston prism, then each beam is detected by a separate CCD [56]. The signal on the both CCDs is analysed to extract the phase and attenuation of the probe beam by the sample. Whilst this method impresses with its photon shot-noise limited sensitivity, the optics to steer the probe and reference beams are complex. The requirement for multiple CCD cameras and an array of optical components makes the technique expensive, susceptible to lens aberration and more difficult to align. The need for multiple optics after the atomic sample increases the distance between the sample and the imaging lenses, thus limiting the numerical aperture available for imaging.

A type of temporal heterodyning known as phase shifting interferometry [104] has been proposed for cold atom imaging [102, 103]. The technique requires multiple exposures of the sample to remove the twin image noise, which can be slow.

A multi exposure technique has been demonstrated for phase shift sensitive imaging of a single ion [55]. A holographic retrieval of the sample phase shift may improve the signal to noise level of reconstructed images.

Diffraction-contrast imaging (In-line holography)

The simplicity of in-line holography is convenient, since all that is required is that the sample be illuminated with a coherent probe and the diffraction pattern imaged with a detector. In such schemes the requirement of imaging lenses is alleviated, thus eliminating lens aberration. A well known issue with the in-line scheme is the formation of a conjugate image that is in-line with the extracted real image $\mathbf{E}_s$ (see section 3.1.3). To aid in the introduction of the microscope developed in this work, a detailed discussion of the in-line holographic geometry is deferred until chapter 3.

All imaging lenses and their unwanted aberrations can be removed using the off-resonant, minimally destructive diffraction-contrast imaging (DCI) [23,24], where the sample is illuminated by the probe and the out-of-focus diffraction pattern is recorded. It is possible to image with plane wave or point source illumination [23]. DCI can be achieved with an absorption imaging system (fig. 2.8), simply by translating the CCD away from the in-focus image of the shadow in the probe beam and recording the diffraction. The increase in flexibility by adapting an absorption imaging system is at the expense of removing lens-less advantage of DCI, since the lenses in the absorption imaging system can introduce aberration into images.

The technique then retrieves the sample column density ρ_c from the reduced contrast $|\mathbf{E}_r + \mathbf{E}_s|^2/|\mathbf{E}_r|^2 - 1$. Retrieval requires the object to have a uniform refractive index, so that the absorption and phase shift are proportional to ρ_c. This monomorphous assumption may explain the lack of widespread use throughout the cold atom research community, since it requires a positive absorption coefficient and inhibits independent retrieval of the probe absorption and phase shift simultaneously (as will be demonstrated by this work in chapter 6).

If the object is phase retarding, the contrast transfer function used for image reconstruction has zeros in it for low spatial frequency, thus rendering the retrieval of ρ_c an ill-posed inverse problem [23]. The Tikhonov method [105] is proposed as a solution to the problem, but whilst it reduces the amplification of image noise, it introduces distortions into the reconstruction [23, 24, 106]. The zeros in the contrast transfer function could be interpreted as an effect of the twin image ($\mathbf{E}_r\mathbf{E}_s^*$) not being fully removed from the diffraction pattern (see section 3.1). Furthermore, DCI does not fully remove the disturbance from the DC noise ($|\mathbf{E}_s|^2$) [34]. Derivation of the contrast transfer function relies on the paraxial approximation, this may render high NA imaging inaccurate [106], an issue that may be addressed by not assuming small angles.

A key advantage of DCI and the holographic techniques (sections 2.3.3 and 3.1) is that they do not require lenses to form an in-focus image at the camera. Therefore they do not suffer from a decreased depth of view at high NA, thus allowing imaging of objects at unknown distances from the detector prior to recording, and allowing imaging of multiple objects at multiple planes with a single recording. This would in principle permit holography to resolve all sites of an optical lattice with a single shot without loss of resolution.

An overlooked advantage of in-line holography with point source illumination is that is permits a larger intensity at the sample plane than at the detector. This allows a longer exposure time before saturating the cameras pixels. This property of point source in-line holography is explored for improving imaging sensitivity in section 6.1.2. These potential benefits of the in-line geometry are dependent on the ability to alleviate the troublesome twin image problem.

2.4 Summary and discussion

The theory presented in this chapter gives a brief insight into and a foundation to the mechanisms used in this work when trapping, cooling and imaging atomic samples. In the review given for established imaging techniques for cold atoms, certain weaknesses are highlighted. Considering the difficulties encountered with near-resonant absorption (see section 2.3.2) and fluorescence imaging (see section 2.3.1), a phase sensitive method is required to push the boundaries of cold atom research beyond its current state. Furthermore, considering the inadequacies of the current array of phase sensitive cold atom imaging techniques (see sections 2.3.2 to 2.3.3), there remains a demand for an off-resonant imaging technique that can image reliably at high numerical aperture at both the shot-noise and diffraction limits. Such a technique may be useful for detecting internal state dynamics such as ground state spin, or for detection of optical lattices with multiple atom occupancy per site.

Chapter 3

Double point source in-line holographic microscopy for cold atoms

Considering the resonant light assisted collision atom losses [38] and multiple scattering induced signal deviation [40] problems in near-resonant fluorescence and absorption imaging (see sections 2.3.1 and 2.3.2), and the difficulties encountered by the currently available phase sensitive methods at high NA, such as imaging artefacts and the CCD dynamic range limiting the phase shift sensitivity, there remains a demand for an off-resonant imaging technique for high NA precision phase microscopy of cold atoms. In this chapter, a novel double point source in-line holographic microscope is proposed as a solution to these problems.

The application of in-line holography to cold atoms is so far limited to diffraction contrast imaging [23, 24], and as of yet, no in-line technique for cold atoms can boast reliable imaging at high NA with diffraction limited resolution and shot-noise limited sensitivity. Similar to the progress made following the implementation of phase-contrast imaging for cold atoms (see section 2.3.2), as a relatively unexplored imaging technique for cold atoms, in-line holographic microscopy may permit imaging of previously unobserved dynamic processes in cold atom gases, and it could extend the range of observables in quantum gas microscopy [19–22, 77].

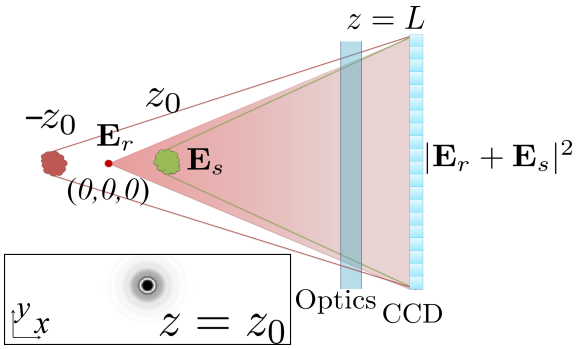

Figure 3.1: Diagram displaying the set-up of an in-line point source holographic microscope. A spherical wave $\mathbf{E}_r$ emanates from the point source (small red point) and interacts with the sample at $z = z_0$ generating a secondary wave $\mathbf{E}_s$. The interference of the two wavefronts is recorded by the CCD camera at $z = L$. The red cloud located at $z = -z_0$ illustrates the twin image, whilst the DC image focuses to the point source. (Inset) A cross sectional view at the $z = z_0$ plane showing interference between the real and twin image that appears in-line with the real image in this geometry. An imaging lens can be used to image the diffraction pattern to the CCD, though this is not needed.

3.1 Gabor's single point source holographic microscope

The first and simplest incarnation of holography, was that proposed by Dennis Gabor in 1949 [43–45], for which he received the Nobel prize in Physics in 1971 [107]. The technique was originally proposed as a way of circumventing the aberrations associated with magnetic electron lenses in electron microscopy [26]. Commonly in optical holographic microscopes, a point source is used as a "perfect lens" to magnify the interference pattern between the point source and the scattering from an object placed in its path. It is known that the wavefront emanating from such a point source, or a pinhole with a sub-wavelength diameter, can be well approximated by a spherical wave,

$$\mathbf{E}_r \simeq \sqrt{\frac{P}{4\pi \mathbf{R}^2}} \mathrm{e}^{ik\mathbf{R}}, \tag{3.1}$$

with $\mathbf{R}$ the wavefronts radial position vector from the source and P the wave power. To distinguish between point source and plane wave illumination, the point source case is often referred to as in-line holographic microscopy, due to the magnification effect of the point source.

3.1.1 Gabor's idea

As is depicted in fig. 3.1, the technique consists of illuminating the sample a distance z_0 away from the source with the spherical reference field $\mathbf{E}_r$. The interaction with the sample generates a secondary wave $\mathbf{E}_s$ emanating from the sample, which as derived in section 2.1.6 is given by eq. (2.43). Digital in-line holographic microscopy (DIHM) can be thought of as a two-step imaging process, where the first is the experimental process of recording the hologram H, and the second is the numerical process of identification of the scattered wavefront $\mathbf{E}_s$ and the subsequent reconstruction of its in-focus image.

The unscattered part of $\mathbf{E}_r$, and $\mathbf{E}_s$ continue to propagate a toward the camera a distance L away from the source. This camera can only measure light intensity, thus records the hologram H as the interference between the two wavefronts. Before digital recording techniques became commonplace, H would have been recorded in a photosensitive film and reconstruction would have been achieved by illuminating the hologram with the reference, hence reconstructing the image optically. Now holograms are commonly recorded with digital CCD/CMOS detectors, and reconstructions are performed numerically on a computer [108, 109].

Although the camera does not directly detect the wavefront phase, it is encoded in the interference fringes of the hologram,

$$H = |\mathbf{E}_r + \mathbf{E}_s|^2 = |\mathbf{E}_r|^2 + \mathbf{E}_r^*\mathbf{E}_s + \mathbf{E}_r\mathbf{E}_s^* + |\mathbf{E}_s|^2. \tag{3.2}$$

From left to right, the terms in eq. (3.2) are referred to as the far field reference intensity, real image, twin image and DC image respectively. Simply recording a hologram with the sample removed $H_0 = |\mathbf{E}_r|^2$ gives the reference intensity. This is particularly quick and simple to achieve for cold atom samples, since atoms can be quickly removed by switching off trapping potentials. If the position of the point source relative to the camera is well known then so is $\mathbf{E}_r$, thus an estimation of the scattered wavefront from the sample at the camera plane can be made,

$$\mathbf{E}_H = \frac{H - H_0}{\mathbf{E}_r^*} = \mathbf{E}_s + \frac{\mathbf{E}_r\mathbf{E}_s^*}{\mathbf{E}_r^*} + \frac{|\mathbf{E}_s|^2}{\mathbf{E}_r^*}. \tag{3.3}$$

However, this estimation remains disturbed by manifestations of the twin image and DC terms. In plane wave illumination, the twin image results in a virtual image, displaced an equal distance from the camera from the real image, but on the opposite

side. In point source holography with $z_0 \ll L$, the real image ($\mathbf{E}_s$) focuses at $z = z_0$. The twin image term in eq. (3.3) appears at $z = -z_0$ as depicted in fig. 3.1, whilst the DC term focuses to the point source at $z = 0$. Both the twin and DC terms appear in-line with the real image, thus at the $z = z_0$ plane, the in-focus real image is disturbed by the out-of-focus twin and DC images. The inset of fig. 3.1 depicts this effect, where a simulated reconstruction of a phase object experiences interference with out-of-focus twin and DC images.

3.1.2 The angular spectrum method

The second stage of digital holographic microscopy encompasses the identification of $\mathbf{E}_s$ via knowledge of $\mathbf{E}_r$ and eq. (3.3), and obtaining an in-focus image at its focal plane $\mathbf{E}_s(z_0)$ from the estimation at the camera, eq. (3.3), by numerical propagation. Approaches to numerical wavefront reconstruction include: reconstruction via the Fresnel approximation [110], reconstruction via a convolution approach [111] and the angular spectrum method [36, 109, 112–114] that is used in this work.

The propagation of a wavefront $\mathbf{E}$ between two dimensional parallel planes is governed by the Helmholtz equation [112],

$$\left(\nabla^2 + k^2\right)\mathbf{E}(x, y, z) = 0. \tag{3.4}$$

The complex electric field is of the form $\mathbf{E}(x, y, z) = \mathrm{e}^{\mathrm{i}\mathbf{k}\cdot\mathbf{R}} = \mathbf{E}(x, y)\,\mathrm{e}^{\mathrm{i}k_z z}$, with $\mathbf{k}^2 = k_x^2 + k_y^2 + k_z^2$. Writing $\mathbf{E}(x, y)$ as a function of its 2D Fourier spectrum $\mathbf{E}(k_x, k_y)$, and using $k_z^2 = \sqrt{k^2 - k_x^2 - k_y^2}$ its easy to show that

$$\mathbf{E}(x, y, z) = \int_{-\infty}^{\infty}\int_{-\infty}^{\infty} \mathbf{E}(k_x, k_y)\,\mathrm{e}^{\mathrm{i}(k_x x + k_y y)}\mathrm{e}^{\mathrm{i}z\sqrt{k^2 - k_x^2 - k_y^2}}\mathrm{d}k_x\mathrm{d}k_y \tag{3.5}$$

is a solution to the Helmholtz equation, eq. (3.4). For ease of notation, $\mathbf{E}(x, y, z)$ may be written only with its z-coordinate $\mathbf{E}(x, y, L) = \mathbf{E}(L)$. Then any wavefront at the camera plane $\mathbf{E}(L)$ can be propagated to any z-plane by taking the 2D Fourier transform, multiplying by the propagation kernel, and taking the inverse Fourier transform

$$\mathbf{E}(z) = \hat{\mathrm{U}}(z - L)\,\mathbf{E}(L) = \mathscr{F}^{-1}\mathrm{e}^{\mathrm{i}(z-L)\sqrt{k^2 - k_x^2 - k_y^2}}\mathscr{F}\mathbf{E}(L). \tag{3.6}$$

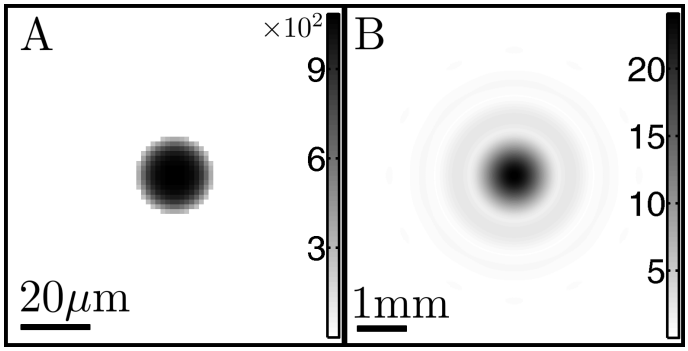

Figure 3.2: (a) Image of the scattered wavefront after propagating the wavefront in (b) via eq. (3.6) to its in-focus image ($|\mathbf{E}_s(z_0)|$). (b) Image of the scattered wavefront from a numerically generated phase object with a characteristic width of 22 μm, at the camera plane (displayed is $|\mathbf{E}_s(L)|$).

This method of wavefront propagation is commonly referred to as the angular spectrum method in the literature [36, 109, 112–114].

The action of eq. (3.6) on a numerically generated scattered wave from a phase object with a diameter of 22 μm is shown in fig. 3.2. It is important to note that this wavefront has been generated in absence of both the twin and DC image noise. At the camera plane the wavefront is spread over a large area of the camera, see fig. 3.2(a), whilst at $z = z_0$ the wavefront is tightly focused, see fig. 3.2(b). For ease of notation, two operators $\hat{\mathrm{U}}_0 = \hat{\mathrm{U}}(z_0 - L)$ and $\hat{\mathrm{U}}_0^{-1} = \hat{\mathrm{U}}(L - z_0)$ are introduced. $\hat{\mathrm{U}}_0$ propagates any wavefront at the camera plane to the object plane and $\hat{\mathrm{U}}_0^{-1}$ does the reverse of $\hat{\mathrm{U}}_0$.

Resolution in coherent and incoherent imaging

The resolution of the microscope determines the size of the smallest features that will be resolvable by the imaging system, and can be defined as the minimum spacing between two points whilst the image of the two points remain resolvable. In this section the resolution for Gabor's coherent in-line holographic technique will be presented and compared with the resolution for incoherent imaging.

In incoherent imaging the fluorescence from a single atom is nearly isotropic, and the light collected by a lens subtends an angle 2θ, as drawn in fig. 2.7. These incoherent photons are then imaged to a detector to form an intensity image. In a medium with refractive index n, the lateral resolution $\tilde{R}_{\mathrm{lat}}$ is given by the spatial frequency of the intensity $|\mathbf{k}_{\mathrm{lat}}| = 2\mathrm{n}|\mathbf{k}|\sin(\theta)$ along the lateral direction, from two focusing light rays with spatial frequency $|\mathbf{k}|$ intersecting at the atom image with

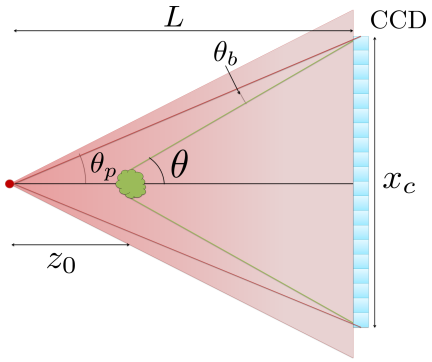

Figure 3.3: Schematic of the point source in-line geometry, highlighting the quantities relevant for determining the microscope resolution. The point source (small red circle) illuminates the sample, the CCD with a width x_c subtends an angle $2\theta_p$ to the source a distance L away, and angle 2θ to the object a distance $L - z_0$ away.

the largest angle (2θ, from opposing edges of the hologram) in the imaging system. Consistent with Abbe's criterion [115], the lateral resolution with $|\mathbf{k}_{\text{lat}}| = 2\pi/R_{\text{lat}}$ is $\tilde{R}_{\text{lat}} = \lambda/2\text{n}\sin(\theta)$.

A commonly overlooked fact in the literature [27, 28] is that the lateral resolution in amplitude measurement-based coherent imaging techniques, including DIHM absorption and phase contrast imaging, is larger than that in intensity measurement based incoherent methods by a factor of two. To understand this, consider a simplified picture where the atomic density is periodically modulated so as to resemble a grating. The Bragg condition (see appendix D.1.1) dictates that for any single ray in the probing light, only one order of diffraction can exist from a single location in the sample at any time. For any coherent imaging technique, no two rays are able to interact with a single location in the sample to simultaneously generate the positive and negative orders of diffraction. Hence considering the case that from a specific location in the sample a $m = 1$ order diffracted ray is such that it intersects the detection plane at its very edge, there will be no corresponding $m = -1$ order diffraction from the same location striking the opposing edge of the camera. Furthermore, with coherent techniques sensitive to the coherent scattered wave complex electric field $\mathbf{E}_s$, the lateral resolution must be determined from the resultant spatial frequency of the wave amplitude and not its intensity. Then it is easy to understand that upon holographic reconstruction of the image, a ray from the edge of the hologram focusing to the image with spatial frequency $|\mathbf{k}|$, will have a lateral component of its spatial frequency given by $|\mathbf{k}_{\text{lat}}| = \text{n}|\mathbf{k}|\sin(\theta)$. Following a

similar argument for the depth component, the minimum imaging resolutions are respectively,

$$R_{\text{lat}} = \frac{\lambda}{\text{n}\sin(\theta)}, \tag{3.7}$$

$$R_{\text{dep}} = \frac{\lambda}{\text{n}(1-\cos(\theta))}. \tag{3.8}$$

The resolution is determined by the wavelength of the illuminating light and the NA of the holographic microscope, and is a factor of two larger than the incoherent fluorescent imaging.

For an object placed along the central imaging axis, it is easy to conclude by looking at fig. 3.3 that the numerical aperture of in-line holographic microscopy is given by

$$\text{NA}_c = \text{n}\sin(\theta) = \text{n}\sin\left(\arctan\left(\frac{x_c}{2(L-z_0)}\right)\right), \tag{3.9}$$

but in digital holography, according to the Whittaker-Shannon sampling theorem [112], an interference fringe period must be larger than at least two pixels to be resolvable without aliasing [112, 116–119]. This condition $\lambda/\sin(\theta_b) \leq 2x_{\text{pix}}$ imposes an upper limit NA_{max} to the achievable NA for a given microscope geometry, which, with $\theta_b = \theta - \theta_p$, is

$$\text{NA}_{\text{max}} = \text{n}\sin\left(\arcsin\left(\frac{\lambda}{2x_{\text{pix}}}\right) + \theta_p\right). \tag{3.10}$$

There is a limited range of valid values of z_0 that an object may be placed at for imaging without aliasing. Assuming that the object is placed at a positive value of z, and if $z_0 \ll L$ and $x_c \ll 2L$, the small angle approximation can be invoked to show that the maximum point-like object-source separation along the z axis is given by

$$z_{0,\text{max}} \approx \frac{\lambda L^2}{\lambda L + x_c x_{\text{pix}}}. \tag{3.11}$$

Then for $z_0 \leq z_{0,\text{max}}$, the numerical aperture is $\text{NA} = \text{NA}_c$ until it reaches a maximum value at $z = z_{0,\text{max}}$ of $\text{NA} = \text{NA}_{\text{max}}$. For $z_0 > z_{0,\text{max}}$ the NA is not well defined, since the detector cannot fully resolve the interference fringes and aliasing will be introduced into the reconstruction.

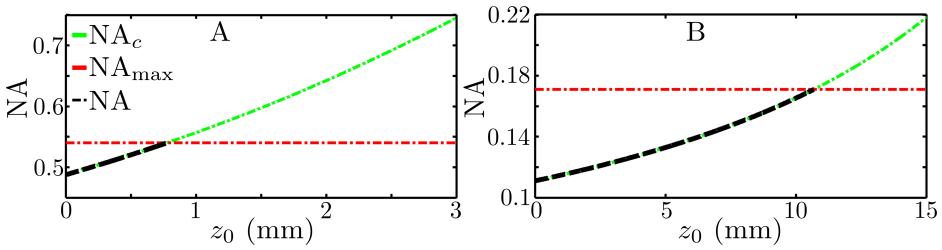

Figure 3.4: Plots displaying the numerical aperture ignoring the Shannon sampling theorem (NA_c), the Shannon limited maximum numerical aperture for the given microscope geometry (NA_{max}) and the resolvable numerical aperture (NA) as a function of the point source-object separation (z_0) for: (a) A high NA$\approx$ 0.55 geometry with source camera separation $L = 6$ mm, and (b) A lower NA$\approx$ 0.15 geometry with source camera separation $L = 30$ mm.

As an example, take a camera of width $x_c = 6.6$ mm and pixel size $x_{pix} = 6.45$ μm. The effect of changing z_0 on the NA is demonstrated for constant source camera separations of $L = 6$ mm, fig. 3.4(a), and $L = 30$ mm, fig. 3.4(b). The graphs displaying NA versus z_0 show the NA increasing until it reaches a limiting value. Using the microscope geometry and eq. (3.11), the value of and $z_{0,max} \approx 10$ mm agrees with the limiting value indicated in fig. 3.4(b), whilst the divergence of the predicted $z_{0,max} \approx 0.6$ mm from the value indicated in fig. 3.4(b) is likely due to the high NA geometry making the small angle approximation invalid. Optimising the microscope resolution without resorting to the use of imaging lenses requires the smallest L possible within the physical constraints of the experiment, and the object to be placed at a large $z_0 \to z_{0,max}$ so that NA $\to$ NA$_{max}$. Design of a microscope with high NA as in [80] is entirely plausible, even for use in laser cooling experiments where the optical access is shared between the imaging and cooling optics.

Sub-pixel resolution

The phase and amplitude information from the light scattered by the object $\mathbf{E}_s$ is fully contained within the interference fringes. Provided that the fringes can be resolved by the detector, the full diffraction limited resolution for the object is recorded within the hologram H. However, often the recorded hologram has a pixel size which is larger than the diffraction limited resolution $x_{pix} > \lambda/\text{NA}$. A simple direct propagation of the recorded hologram using eq. (3.3) and then eq. (3.5) maintains the pixel size of the camera and the final image resolution is limited by x_{pix}. To overcome this problem and achieve sub-pixel size resolution, each of the N $\times$ N pixels in H can be split into T^2 new pixels (a more time consuming option

with little benefit, is to carry out an interpolation of the signal onto a finer grid [36]) with size $x_{\mathrm{pix},T} = x_{\mathrm{pix}}/T$.

The lateral spatial period of the reference field $\mathbf{E}_r$ at the very edge of detector is given by λ/NA. With the Whittaker-Shannon sampling theorem requiring at least two pixels to resolve a single period, supporting a diffraction limited resolution requires that

$$x_{\mathrm{pix},T} \leq \frac{\lambda}{2\mathrm{NA}}. \tag{3.12}$$

Then the final reconstructed image pixel width must be at most half of the imaging resolution.

The expanded hologram has $\mathrm{N}T \times \mathrm{N}T$ pixels. For a typical value for the expansion factor of $T = 5$, a hologram initially recorded with 1000×1000 pixels is reconstructed with 5000×5000 pixels. This increase in pixel number requires a larger memory resource and higher speed processing units, such as a graphics processing units GPU (or a GPU cluster), to maintain the reconstruction speed, since the fast Fourier transforms in eq. (3.5) become slow. Two methods based on the superposition principle of fast Fourier transforms [36, 113] have been presented to counteract the reduction in computation speed for the angular spectrum method. Both methods involve cutting the hologram into tiles, which inevitably introduce a knife edge diffraction effect into the reconstruction from the cut. This should not effect the final image resolution, but for sensitive imaging at the shot-noise limit the added noise is unwanted.

3.1.3 The twin image problem and its solutions

The downfall of in-line holography is the out-of-focus twin image noise, and to a lesser extent the DC noise for optically thick objects (section 3.1). This lead to a vast amount of research in the decades following the proposal of in-line holography into removal of the twin image term in particular. Methods include: subtraction based techniques [120, 121], off-axis spatial heterodyning [122–124], off-axis temporal heterodyning [104, 125, 126] (also known as phase shifting holography), and deterministic [127, 128] and iterative [129–133] phase retrieval. Some twin image removal techniques include the ability to remove the DC noise term, but there are methods that have been developed to remove the DC term alone [30–32]. Of particular importance to this work are the off-axis spatial heterodyning and iterative phase retrieval techniques, see [134, 135] for in depth reviews of twin image removal, whilst a comparison of the iterative phase retrieval algorithms is given in [131].

After the proposal of off-axis spatial heterodyning holography by Leith and Upatnieks [122, 123], it soon became the method of choice for holographic imaging, thanks to its ability to remove the twin image noise. The reference field interferes with the probe arm at an angle to the scattered wave from the object. The introduction of an off-axis reference beam spatially separates the real and twin images at each of their focal planes, and eliminates the twin image noise. However, removing the twin image does come with costs since multiple additional optical elements are required when compared to in-line holography, thus leading to an increase in sources of speckle noise, and making the set-up more susceptible to vibration and temperature fluctuations. Also imaging extended samples requires a large angle between the probe and reference arms, thus decreasing the fringe separation at the camera, and increasing the recording resolution requirement [134]. This problem is exacerbated at high NA, thus a second consequence of the requirement for an increased recording resolution is that it is difficult to achieve high NA imaging with standard CCD detectors. Off-axis holographic techniques have so far rarely been used with cold atoms (see section 2.3.3), mainly because of their increased complexity, but also due to the difficulty in achieving reliable and precise high NA imaging without lenses.

The off-axis phase shifting techniques (section 2.3.3) require multiple images recorded with a phase shift introduced to the $\mathbf{E}_r$ or $\mathbf{E}_s$ wavefront between each capture. The shifts can be achieved with a wave plate or by mechanical extension of a mirror [104, 134]. Phase shifting holography has been proposed for cold atom imaging [102, 103], but these set-ups are complex compared to the in-line geometry, require many more optics and multiple, typically long exposures.

Iterative phase retrieval techniques with in-line holography require propagation between two different image planes whilst satisfying constraints placed on the object at each iteration. After each iteration the technique converges nearer to the ideal $\mathbf{E}_s$, but this convergence is often highly reliant on the initial conditions and the constraints imposed [134]. Some of the constraints can be very restrictive to the types of objects that can be imaged; requiring the object to be purely amplitude [136] or absorbing [137], place constraints on the recorded intensity [138], or on both the recording and image planes [139]. More advanced algorithms [140, 141] place less restrictive constraints on the object, however they require no gain from the sample which may be unsuitable in some experiments with atomic samples. A technique based upon the constraint that the object be contained within a finite support [132, 133] is capable of reconstructing complex objects, and does not place

any constraint on the objects refractive index. A finite support means that the real image has a finite spatial extent and a support or mask can be used to exclude the real image. This method may be favourable for general use with imaging atomic samples, as the laser cooling and trapping techniques (see chapter 2) naturally spatially constrain atomic samples. The iterative twin image removal algorithm developed in this work (see section 3.2.3) is an extension of this method based on objects located within a finite support.

The convergence speed of twin image removal algorithms based on objects located within a finite support [132, 133] depend on the spreading of the twin image due to diffraction relative to the in-focus real image at the real image plane. The diffraction effect a distance z away from an object with a characteristic size a, can be characterised with the dimensionless Fresnel number,

$$N_f = \frac{a^2}{\lambda z}. \tag{3.13}$$

It is worth noting that although the twin image and DC noise terms impose tough challenges for imaging with in-line holography, there are situations where both are negligible. When imaging a weakly interacting sample, whose characteristic size is much smaller than $2z_0\lambda$ (e.g. a single trapped atom placed at a value of z_0 such that $\mathrm{NA} \to \mathrm{NA}_{\max}$, as discussed in section 3.1.2), imaging is said to be in the "holographic regime" [26–28], thus it has a small Fresnel number $N_f \ll 1$, and the DC term is negligible $|\mathbf{E}_s|^2 \ll |\mathbf{E}_r|^2$. Even at high $\mathrm{NA} = 0.7$, the distance between the real and twin image focal points $z = 2z_0$, can be sufficiently large that $N_f \ll 1$, and the approximate spherical wave amplitude from the twin image is so out-of-focus at the real image plane that it contributes negligibly to the background [27, 28, 142]. High NA twin image and DC noise free imaging of single atoms (or multiple atoms in a sparse optical lattice [19–22, 77]) may be possible with point source in-line holography, without the need for any twin or DC image noise removal procedure.

3.1.4 The strengths of in-line holography and the obstacles to its implementation for cold atoms

It remains to justify the pursuit of a holographic imaging technique for cold atoms, and to outline the difficulties that need to be overcome for such a technique to come to fruition.

The simple set-up as discussed in section 3.1.3, consists of fewer optical components than all of the techniques discussed in section 2.3, bar fluorescence imaging (though fluorescence imaging does require an imaging lens.). The expected diffraction limited resolution in DIHM is equivalent to that in the coherent methods described in section 2.3, which is a factor of two larger than the intensity measurement based fluorescence imaging.

The removal of the need for an imaging lens can make point source in-line holography free of lens aberration even at high NA, particularly if $\mathbf{E}_r$ is accurately known. If the set-up does not permit a small enough sample to camera separation, then the NA in holographic microscopy can be increased with auxiliary lenses. In comparison with focal plane imaging (see sections 2.3.1 and 2.3.2), holographic microscopy aided by lenses gives the opportunity for accurate numerical aberration correction, since the complex scattered wavefront is extracted. In addition, for a point-like object, and for $z_0 \ll L$, the object is located near to the point source, thus light from the point source and the point-like object traverse a similar optical path. Any aberration experienced by $\mathbf{E}_r$ will be mutually experienced by $\mathbf{E}_s$, thus the resultant interference fringes will be minimally effected by the aberration. With very close source to object distances $z_0 \ll L$, the common wavefront curvature for $\mathbf{E}_r$ and $\mathbf{E}_s$ results in a larger interference fringe spacing at the camera than would be possible when spatial heterodyning with off-axis holographic techniques [122, 123]. The object-source separation z_0 can be tuned so the fringes are resolvable by the detector (see section 3.1.2), and in doing so, the method has achieved high NA $= 0.8$ lensless imaging [80].

In fluorescence imaging (see section 2.3.1), the photon shot-noise increases with the square root of atom number. This is advantageous for detection of atom shot-noise when the sample contains small atom numbers $N \lesssim 10^3$, but is less favourable for detecting larger samples. As a coherent imaging technique, holographic microscopy offers a solution to this, since similar to absorption and phase-contrast imaging, the shot-noise level is independent of the atom number.

As a phase sensitive imaging technique, holography can overcome the problems with absorption imaging, outlined in section 2.3.2. For dense samples $OD \gg 1$, the problem of "blacked out" absorption images [37, 87] can be alleviated by reducing the absorption coefficient with a detuned probe. Resonant van der Waals interactions [39] and probe photons scattering multiple times [39] in dense samples, make faithful retrieval of atomic density information simply via Beer's law impossible. These effects

are reduced with off-resonant probing, and imaging optically dense samples would not require multiple exposures of the sample at different probe intensities [41] (see section 2.3.2). Off-resonant imaging reduces the scattering rate of the probe when imaging compared to resonant absorption imaging and in turn reduces the heating, which is easier to counteract with cooling schemes. As a consequence, similar to phase-contrast imaging, off-resonant holography can be used for in-situ minimally destructive imaging of atomic samples, or even permit imaging of optical lattice sites with multiple atom occupancy [34] where fluorescence imaging fails [19–22, 38].

The advantages associated with coherent off-resonant probing are not exclusive to holography but common to all coherent phase sensitive imaging techniques for cold atoms (section 2.3). However, it is important to note that due to the holographically enhanced sensitivity (see section 6.1.2), holographic microscopy should be capable of detecting a smaller phase shift or absorption than phase-contrast imaging or absorption imaging, if an identical camera is used with unity magnification. Furthermore, a simple high NA holographic microscope with 3D field of view and free of imaging artefacts, is in sharp contrast to high NA phase-contrast and dark-ground imaging.

There remain two obstacles to the implementation of point source holographic microscopy with cold atoms. The first, as discussed in section 3.1.3 is the development of a suitable twin and DC image removal procedure, preferably one that does not impose significant constraints on the atomic refractive index. A solution that assists the phase retrieval technique based on the finite support constraint [132, 133], would be suitable provided that the set-up complexity is not significantly increased. Though as is argued in section 3.1.3, the twin image is not a problem for objects with small Fresnel numbers $N_f \ll 1$. The second is the speckle noise problem inherent to all atomic imaging techniques to varying degrees of severity. Adjusting the probe alignment to reduce speckle noise in the image as in absorption or PCI (see section 2.3.2), is less effective in DIHM, since the diffraction makes efficient use of the full camera, as does the speckle noise. A technique to suppress the speckle noise would significantly enhance the applicability of holography for cold atom imaging. To a lesser extent, the DC noise remains a problem for the implementation of DIHM, though it is negligible in certain situations ($\mathbf{E}_s \ll \mathbf{E}_r$), and there are various methods of removing its effects [30–32].

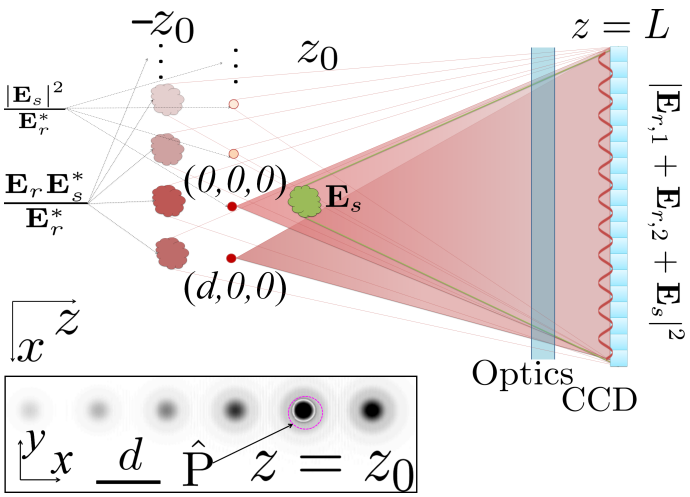

Figure 3.5: Schematic of the double source holographic microscope with source power ratio $\eta < 1$. The CCD camera, placed a distance $z = L$ away from the two point sources (red circles), records the three wavefront interference from the light scattered by the atoms $\mathbf{E}_s$ and the double reference field $\mathbf{E}_{r,1} + \mathbf{E}_{r,2}$ in the hologram $H = |\mathbf{E}_{r,1} + \mathbf{E}_{r,2} + \mathbf{E}_s|^2$. A one-step reconstruction via $\hat{\mathrm{U}}_0\mathbf{E}_H$ results in an in-focus image of $\mathbf{E}_s\,(z_0)$ and multiple out-of-focus copies of the twin $(\mathbf{E}_r\mathbf{E}_s/\mathbf{E}_r^*)$ and DC $(|\mathbf{E}_s|^2/\mathbf{E}_r)$ images, each separated by the source separation d. Optics such as a vacuum window or a lens may be placed before the camera. (Inset) A cross sectional view at the $z = z_0$ plane showing in-focus real image and multiple copies of the twin images. The purple circle illustrates a typical mask $\hat{\mathrm{P}}$ that may be used for twin image removal via eqs. (3.24) and (3.27).

3.2 The double source holographic microscope

To address the twin image and DC noise problems preventing cold atom research from exploiting the benefits promised by in-line holography, a novel double point source geometry is introduced. The idea is motivated by the ability of iterative phase retrieval based on the finite support constraint [132, 133] to remove the twin image noise. The convergence of such phase retrieval algorithms depends on the amount of out-of-focus twin image energy that is located outside of the boundary of the real image. In this section, the increased spreading of the twin image term thanks to the introduction of a second point source into the DIHM geometry is taken advantage of to make efficient use of such phase retrieval algorithms.

3.2.1 The simple double source scheme

To increase the spreading of the twin image energy over the image plane, and to improve the phase retrieval convergence, a second point source can be introduced

into the in-line microscope geometry, thus increasing the complexity of the reference field $\mathbf{E}_r = \mathbf{E}_{r,1} + \mathbf{E}_{r,2}$. In fig. 3.5, a schematic of the double source geometry is shown. Similar to the in-line geometry (section 3.1), the in-line point source at spatial coordinate $\mathbf{r}_1 = (0, 0, 0)$ with power P_1 illuminates the sample, thus generating a wavefront $\mathbf{E}_s$ originating from the object location. A second source $\mathbf{E}_{r,2}$ with power $P_2 = \eta P_1$, coherent with $\mathbf{E}_{r,1}$ originates from $\mathbf{r}_2 = (d, 0, 0)$. The interference between the three wavefronts is captured in the hologram H at the camera plane,

$$H = |\mathbf{E}_{r,1} + \mathbf{E}_{r,2} + \mathbf{E}_s|^2. \tag{3.14}$$

The addition of the second point source in double source holographic microscopy (DSHM) effects the hologram in the same way as a point-like source of speckle noise, producing an intensity modulation to the hologram that would be expected in pure DIHM. To create the point sources, pinholes with sub-wavelength diameter can be fabricated into absorptive substrates with nano-fabrication techniques such as focused ion beam lithography (FIB) or by focusing two laser beams to diffraction limited focal points with a single lens (see sections 4.4.2 and 7.3.1).

With the separation of the two point sources $|\mathbf{r}_2 - \mathbf{r}_1| = d$ pre-measured so that the source-camera separation can be calibrated (see section 6.1.1), and the source diameters $\sim \lambda$ (e.g. when using a sub-wavelength diameter pinhole illumination source, as described in section 7.3.1) so that $\mathbf{E}_r$ is well described by a spherical wave (see section 3.1), an estimation of the reference field is easy to generate numerically. Then with a reference intensity $H_0 = |\mathbf{E}_{r,1} + \mathbf{E}_{r,2}|^2$ recorded without the atomic sample, the initial estimation of $\mathbf{E}_s$ at the camera plane is,

$$E_H = \frac{H - H_0}{\mathbf{E}_r^*} = \mathbf{E}_s + \frac{\mathbf{E}_{r,1} + \mathbf{E}_{r,2}}{\mathbf{E}_{r,1}^* + \mathbf{E}_{r,2}^*}\mathbf{E}_s^* + \frac{|\mathbf{E}_s|^2}{\mathbf{E}_{r,1}^* + \mathbf{E}_{r,2}^*}. \tag{3.15}$$

The more complex reference field leaves the real image term unaffected by the addition of the second point source when compared to DIHM, eq. (3.3), and is expected to form a real image at $z = z_0$. However the twin image and DC terms differ from those of DIHM, since they are manifestations the product of $\mathbf{E}_s^*$ and $|\mathbf{E}_s|^2$ with the modified reference field respectively. The effect that the addition of $\mathbf{E}_{r,2}$ has on the twin image and DC terms depends on whether the source power ratio $\eta < 1$ or $\eta > 1$. To better understand this effect on the twin image term when $\eta < 1$, a series

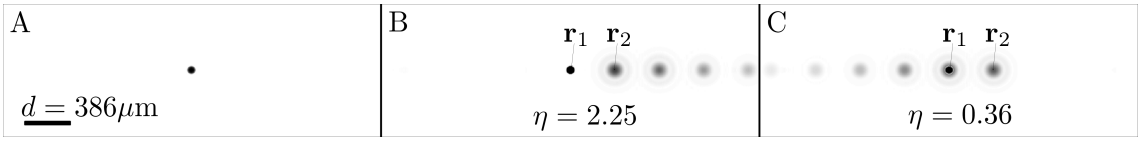

Figure 3.6: Holographic reconstructions of $|\mathbf{E}_s(z_0)|$ for a simulated phase object using DSHM. (a) The ideal $|\mathbf{E}_s(z_0)|$ free of twin image and DC noise. (b) Reconstruction $|\mathbf{E}_s(z_0)|$ with $\eta = 2.25$. $\mathbf{r}_1$ and $\mathbf{r}_2$ indicate the x, y coordinate of the $\mathbf{E}_{r,1}$ and $\mathbf{E}_{r,2}$ point sources respectively. The out-of-focus twin image copies start at the $\mathbf{r}_2$ x, y coordinate and are repeated to the right, resulting in no in-line twin image at the $\mathbf{r}_1$ x, y coordinate. (c) Reconstruction with $\eta = 0.36$, the out-of-focus twin image copies start at the $\mathbf{r}_2$ x, y coordinate and are repeated to the left, thus the in-line twin image interferes with the real image.

expansion reveals that the manifestation of the twin image term becomes

$$\frac{\mathbf{E}_r}{\mathbf{E}_r^*}\mathbf{E}_s^* \approx \frac{\mathbf{E}_{r,1}}{\mathbf{E}_{r,1}^*}\mathbf{E}_s^*\left(1 - \frac{\mathbf{E}_{r,2}^*}{\mathbf{E}_{r,1}^*} + \frac{\mathbf{E}_{r,2}^{*2}}{\mathbf{E}_{r,1}^{*2}} - \dots\right) + \frac{\mathbf{E}_{r,2}}{\mathbf{E}_{r,1}^*}\mathbf{E}_s^*\left(1 - \frac{\mathbf{E}_{r,2}^*}{\mathbf{E}_{r,1}^*} + \frac{\mathbf{E}_{r,2}^{*2}}{\mathbf{E}_{r,1}^{*2}} - \dots\right). \quad (3.16)$$

The addition of $\mathbf{E}_{r,2}$ with $\eta < 1$ into the in-line microscope geometry results in multiple copies of the twin image term, each taking a proportion of the total twin image energy. The $\mathbf{E}_s^*\mathbf{E}_{r,1}/\mathbf{E}_{r,1}^*$ term in eq. (3.16) is the same twin image term expected in the pure in-line geometry, and focuses at $\mathbf{r} = (0, 0, -z_0)$. Although not present in eq. (3.16), an $\mathbf{E}_s^*\mathbf{E}_{r,2}/\mathbf{E}_{r,2}^*$ term would be the same as the expected twin image in the pure off-axis geometry, which is located at $\mathbf{r} = (2d, 0, -z_0)$. It is then easy to understand that a $\mathbf{E}_s^*\mathbf{E}_{r,2}/\mathbf{E}_{r,1}^*$ term results in a copy of the twin image term located exactly half way $\mathbf{r} = (d, 0, -z_0)$ between the pure in-line and off-axis twin image locations. Each subsequent multiplication by $\mathbf{E}_{r,2}^{*n}/\mathbf{E}_{r,1}^{*n}$ translates the focal point of the first order twin image term by $\mathbf{r} = (-nd, 0, 0)$. This effect of addition of $\mathbf{E}_{r,2}$ is depicted in fig. 3.6(c) for reconstruction of $|\mathbf{E}_s(z_0)|$ from a hologram of a simulated phase object with $d = 386$ μm and $\eta = 0.36$. The multiple copies of the out-of-focus twin image terms at $z = z_0$ are visible and are each separated by a distance d.

To gain a full understanding of the double source geometry, the effect of the dual reference field on the DC image must be considered. In a similar fashion to the twin

image term, a series expansion with $\eta < 1$ reveals that,

$$\frac{|\mathbf{E}_s|^2}{\mathbf{E}_r} \approx \frac{|\mathbf{E}_s|^2}{\mathbf{E}^*_{r,1}} \left(1 - \frac{\mathbf{E}^*_{r,2}}{\mathbf{E}^*_{r,1}} + \frac{\mathbf{E}^{*2}_{r,2}}{\mathbf{E}^{*2}_{r,1}} - \dots\right). \tag{3.17}$$

The near uniformly distributed $|\mathbf{E}_s|^2$ intensity at the camera plane creates a wavefront after division by the reference field $|\mathbf{E}_s|^2/\mathbf{E}^*_{r,1}$ that originates from a small DC image that is in-focus at $\mathbf{r} \approx \mathbf{r}_1$. And similar to the twin image term, each subsequent multiplication by $\mathbf{E}^{*n}_{r,2}/\mathbf{E}^{*n}_{r,1}$ translates the focal point of the first order DC image by $\mathbf{r} = (-nd, 0, 0)$, thus resulting in multiple copies each separated by a distance d.

For completeness, the effect on the twin image and DC terms for $\eta > 1$ can be analysed in a similar way to $\eta < 1$. A series expansion reveals that the twin image term becomes,

$$\frac{\mathbf{E}_r}{\mathbf{E}^*_r}\mathbf{E}^*_s \approx \frac{\mathbf{E}_{r,1}}{\mathbf{E}^*_{r,2}}\mathbf{E}^*_s \left(1 - \frac{\mathbf{E}^*_{r,1}}{\mathbf{E}^*_{r,2}} + \frac{\mathbf{E}^{*2}_{r,1}}{\mathbf{E}^{*2}_{r,2}} - \dots\right) + \frac{\mathbf{E}_{r,2}}{\mathbf{E}^*_{r,2}}\mathbf{E}^*_s \left(1 - \frac{\mathbf{E}^*_{r,1}}{\mathbf{E}^*_{r,2}} + \frac{\mathbf{E}^{*2}_{r,1}}{\mathbf{E}^{*2}_{r,2}} - \dots\right). \tag{3.18}$$

The $\mathbf{E}_{r,1}\mathbf{E}^*_s/\mathbf{E}^*_{r,2}$ term is the same that arises in eq. (3.16) and appears half way between the expected real and twin image location $\mathbf{r} = (d, 0, -z_0)$. The effect of addition of $\mathbf{E}_{r,2}$ for $\eta > 1$, differs from the case where $\eta < 1$. Each subsequent multiplication by $\mathbf{E}^{*n}_{r,1}/\mathbf{E}^{*n}_{r,2}$ translates the focal location of the twin image by $\mathbf{r} = (nd, 0, 0)$, the reverse direction to eq. (3.16). Notice here that the pure off-axis twin image $\mathbf{E}^*_s\mathbf{E}_{r,2}/\mathbf{E}^*_{r,2}$ is present, whilst there is no in-line twin image as can be seen in fig. 3.6(b). Then DSHM with $\eta > 1$ achieves full real and twin image separation, but in a non optimal way as will be discussed shortly.

In a similar fashion the DC term for $\eta > 1$ is,

$$\frac{|\mathbf{E}_s|^2}{\mathbf{E}_r} \approx \frac{|\mathbf{E}_s|^2}{\mathbf{E}^*_{r,2}} \left(1 - \frac{\mathbf{E}^*_{r,1}}{\mathbf{E}^*_{r,2}} + \frac{\mathbf{E}^{*2}_{r,1}}{\mathbf{E}^{*2}_{r,1}} - \dots\right). \tag{3.19}$$

The $|\mathbf{E}_s|^2/\mathbf{E}^*_{r,2}$ operation focuses the near uniform $|\mathbf{E}_s|^2$ to $\mathbf{r} \approx \mathbf{r}_2$, and each subsequent $\mathbf{E}^{*n}_{r,1}/\mathbf{E}^{*n}_{r,2}$ multiplication translates the DC image by $\mathbf{r} = (nd, 0, 0)$. Then for $\eta > 1$, the twin image and DC noise is fully spatially separated from the real image, provided that the sample is illuminated with $\mathbf{E}_{r,1}$ alone. Otherwise the pure off-axis twin

image and DC terms in eqs. (3.18) and (3.19) respectively, will interfere with the real image.

Convenient as full separation of the twin and DC image may be, imaging with $\eta > 1$ is not ideal for optimisation of the SNR. The SNR of holographic reconstructions scales with the square root of the number of coherent scattered photons N_s from the sample (see section 3.2.2). With the sample being probed by $\mathbf{E}_{r,1}$ alone to remove the twin and DC terms, there is no increase in N_s with an increase in the power of the $\mathbf{E}_{r,2}$ reference field. Any increase in signal by increasing $\mathbf{E}_{r,2}$ is balanced equally by an increase in the shot-noise level. Furthermore, optimisation of the imaging sensitivity (see sections 6.1.2 and 7.1) requires that optimal use is made of the cameras bit depth. Then to reduce the fringe contrast to make better use of the cameras bit depth whilst optimising the SNR imaging must be conducted with $\eta \ll 1$. In this scenario there remains some twin image and DC noise disturbance, with the twin image that is in-line with the sample taking a fractional energy of $(1-\eta)^2$. To achieve sensitive and precise imaging of samples with $\eta \ll 1$, a method of removing the remaining twin and DC noise must be implemented.

3.2.2 Shot-noise limited signal-to-noise ratio

To permit comparison of DSHM with the established imaging techniques discussed in section 2.3, the signal-to-noise ratio (SNR) of the method when imaging cold atoms is examined. To achieve this the RMS shot-noise level in the focal plane electric field is calculated and compared to the signal expected at the focal plane. For simplicity in this discussion, DSHM with $\eta \ll 1$ is considered so that the geometry closely resembles that of DIHM.

Noise

The RMS (root mean square) photon shot-noise level in H and H_0, is proportional to the square root of the photon counts $N_H = HA_pQ\tau_{\text{exp}}/\hbar\omega$, where the RMS shot-noise levels in H and H_0 in units of intensity are $\delta_H = \sqrt{N_H}\hbar\omega/A_pQ\tau_{\text{exp}}$ and $\delta_{H_0} = \sqrt{N_{H_0}}\hbar\omega/A_pQ\tau_{\text{exp}}$ respectively (here A_p, Q and τ_{exp} are the pixel area, detector quantum efficiency and exposure time respectively). With $|\mathbf{E}_r| = \sqrt{H_0}$, and for weak objects such that $H \approx H_0$, the associated shot-noise $\delta\mathbf{E}_H$ in the approximation of $\mathbf{E}_s$ (eq. (3.3)) has an RMS level of

$$\delta_{\mathbf{E}_H} = \sqrt{2\hbar\omega/A_pQ\tau_{\text{exp}}}, \tag{3.20}$$

at the camera plane $z = L$. To determine the expected RMS level of the shot-noise field at the atomic image focal plane $\delta_{\mathbf{E}(z_0)}$, the shot-noise pattern that is random pixel by pixel but has a uniform intensity contribution at each pixel $|\hat{\mathrm{U}}_0 \delta\mathbf{E}_H|^2$ at $z = L$ is evaluated and summed to give the intensity of $\delta\mathbf{E}(z_0)$. The shot-noise wavefront $\delta\mathbf{E}_H$, contained on a grid of pixels individually restricting each proportion of the wavefront to an area A_p is approximated as spherical waves propagating toward the point source. The noise level near the source can be calculated using Kirchhoff's diffraction theorem and a 2D integration of the intensity contribution over the pixels,

$$\delta_{\mathbf{E}_s(z\approx 0)} = \sqrt{2\hbar\omega/\tilde{A}_r Q \tau_{\mathrm{exp}}} \tag{3.21}$$

where $\tilde{A}_r = \lambda^2/(4\mathrm{NA}_p \arctan(\mathrm{NA}_p))$, and $\mathrm{NA}_p = x_c/\sqrt{x_c^2 + 4L^2}$ is the numerical aperture spanned by the camera to the point source. With a sample placed near the point source ($z_0 \ll L$), the RMS noise level near the atomic sample with $\delta_{\mathbf{E}(z_0)} \approx \delta_{\mathbf{E}_s(z\approx 0)}$ and $\tilde{A}_r \approx \lambda^2/4\mathrm{NA}^2 = A_r$ is,

$$\delta_{\mathbf{E}(z_0)} \approx \sqrt{2\hbar\omega/A_r Q \tau_{\mathrm{exp}}}, \tag{3.22}$$

which is equivalent to the electric field amplitude for two photons.

Signal

The number of coherent scattered photons contributing to the signal over an area A_r is $N_s = \langle |\mathbf{E}_s(z_0)|^2 \rangle A_r Q\tau/\hbar\omega$. Then with the signal to noise ratio over the area A_r given by $\left(\left\langle |\mathbf{E}_s(z_0)/\delta_{\mathbf{E}(z_0)}|^2 \right\rangle\right)^{1/2}$ it can be expressed as

$$\mathrm{SNR} = \sqrt{N_s/2}. \tag{3.23}$$

In agreement with previous work [25,143–146], the SNR is decided only by the number of coherent scattered photons from the sample N_s. Then in off-axis holography, increasing the power in a reference arm that does not interact with the atomic sample has no effect on the SNR of the reconstruction if the technical noise is negligible.

In comparison with standard absorption or phase-contrast imaging (see section 2.3.2), where the signal is twice that of DSHM and the shot-noise limited SNR= $\sqrt{2N_s}$ [25, 143–145], the SNR for shot-noise limited holography is only expected to be a factor two less. In holographic microscopy the SNR is expected to be insensitive to a change in L, a feature that could be explored for image resolving

along the imaging axis, whilst in standard imaging $L \approx z_0$ within the depth of view, and the SNR becomes sensitive to L, particularly at large NA.

3.2.3 Iterative twin and DC image removal

The spreading of the twin image energy into multiple copies by the addition of $\mathbf{E}_{r,2}$ reduces the interfering in-line twin image energy (see section 3.2.1). As a consequence, the out-of-focus twin image energy outside of the boundary of the real object is increased. The increased separation of the real and twin image energy at $z = z_0$ can be utilised to aid in removal of the twin image and DC noise. The convergence of iterative phase retrieval techniques (see section 3.1.3) based on objects being constrained to a finite support [132,133] depends on the amount of out-of-focus twin image energy outside of the object support. With DSHM providing an increase in the spreading of the twin image energy, and with laser cooling techniques naturally spatially containing atomic samples, pursuing an iterative technique based on a finite support for the object is well justified.

To remove the remaining twin image energy in DSHM with $\eta < 1$, an iterative technique is developed based on the constraint that the object is contained within a finite support. The method differs from those discussed in references [132] and [133] as it does not require edge detection techniques to define the object support. Furthermore, in this work additional steps are added to eliminate the DC noise term. The amount of twin image energy outside the boundary of the real image is maximized at the real image focal plane $z = z_0$. To collect the real image energy at $z = z_0$, an aperture operator $\hat{\mathrm{P}}$ with characteristic diameter a that must be at least as large as the sample is introduced. Using eq. (3.3), the camera to focal plane propagation operator $\hat{\mathrm{U}}_0$ (see section 3.1.2) and the conjugation operator $\hat{\mathrm{C}}\mathbf{E} = \mathbf{E}^*\mathbf{E}_r/\mathbf{E}_r^*$ that converts any wavefront at the camera plane into its twin, the twin image is removed and the real $\mathbf{E}_s(z_0)$ approximated iteratively with the following algorithm,

$$\begin{aligned} \mathbf{E}_s^{(0)} &= \hat{\mathrm{U}}_0 \mathbf{E}_H, \\ \mathbf{E}_s^{(n+1)} &= \hat{\mathrm{U}}_0 \hat{\mathrm{C}} \hat{\mathrm{U}}_0^{-1} \left(\mathbf{E}_s^{(0)} - \hat{\mathrm{P}} \mathbf{E}_s^{(n)} \right). \end{aligned} \tag{3.24}$$

The action of eq. (3.24) follows the operator convention. Then with $\mathbf{E}_s^{(n)} = \mathbf{E}_s(z_0) + \delta\mathbf{E}_s^{(n)}$, the error $\delta\mathbf{E}_s^{(n)}$ in the estimation is expected to converge toward zero. The

residual energy fraction is defined as,

$$r = \frac{\int |\mathbf{E}_s^{(n)} - \mathbf{E}_s(z_0)|^2 \mathrm{d}x\mathrm{d}y}{\int |\mathbf{E}_s(z_0)|^2 \mathrm{d}x\mathrm{d}y}, \tag{3.25}$$

and is shown to decay with a characteristic constant $N_0 = -1/\log(\epsilon)$ (see section 5.2). The quantity ϵ is the fraction of the out-of-focus twin image energy $\hat{\mathrm{U}}_0\hat{\mathrm{C}}\hat{\mathrm{U}}_0^{-1}\hat{\mathrm{P}}\mathbf{I}$ (with $\mathbf{I} = 1$ a 2D uniform wavefront) of the aperture itself that is contained within the aperture $\hat{\mathrm{P}}$ at $z = z_0$,

$$\epsilon = \frac{\int |\hat{\mathrm{P}}\hat{\mathrm{U}}_0\hat{\mathrm{C}}\hat{\mathrm{U}}_0^{-1}\hat{\mathrm{P}}\mathbf{I}|^2 \mathrm{d}x\mathrm{d}y}{\int |\hat{\mathrm{U}}_0\hat{\mathrm{C}}\hat{\mathrm{U}}_0^{-1}\hat{\mathrm{P}}\mathbf{I}|^2 \mathrm{d}x\mathrm{d}y}. \tag{3.26}$$

With the characteristic size a of the aperture $\hat{\mathrm{P}}$ having to be at least as large as the sample, ϵ can characterise the amount of overlap between the real and twin image energies. The speed of twin image removal can be improved with a reduction in ϵ.

The algorithm can be applied to images recorded using DIHM (see section 3.1). Large samples often require an aperture $\hat{\mathrm{P}}$ with Fresnel number $N_f > 1$, eq. (3.13), and $\epsilon \approx 1$. In such a scenario the algorithm is shown to not converge within even $\sim 10^3$ iterations (see section 5.2) of eq. (3.24), and is likely to be dominated by numerical errors introduced during iteration before the algorithm can remove the twin image. In contrast, in DSHM even for objects with $N_f \gg 1$ the in-line twin image only takes a fractional energy $(1-\eta)^2$, thus the overlap of the real and twin image energies $\epsilon \approx (1-\eta)^2$ can still be small with appropriate choice of η. As is shown in section 5.2, the algorithm converges quickly in DSHM even for an object with $N_f = 28$, where DIHM fails.

The algorithm presented in eq. (3.24) does not cause a reduction of the DC noise term, thus is only applicable if $|\mathbf{E}_s|^2 \ll |\mathbf{E}_r|^2$ for every pixel on the recording camera. For scenarios where the DC noise is significant, eq. (3.24) can be modified to remove it by adding a step into eq. (3.24) that estimates the DC term at each iteration and subtracts it away. The modified algorithm is,

$$\begin{aligned}
\mathbf{E}_s^{(0)} &= \hat{\mathrm{U}}_0\mathbf{E}_H, \\
\tilde{\mathbf{E}}_s^{(0,n)} &= \hat{\mathrm{U}}_0\left(\mathbf{E}_H - |\hat{\mathrm{U}}_0^{-1}\hat{\mathrm{P}}\mathbf{E}_s^{(n)}|^2/\mathbf{E}_r^*\right), \\
\mathbf{E}_s^{(n+1)} &= (1-\vartheta)\,\hat{\mathrm{P}}\mathbf{E}_s^{(n)} + \vartheta\hat{\mathrm{U}}_0\hat{\mathrm{C}}\hat{\mathrm{U}}_0^{-1}\left(\tilde{\mathbf{E}}_s^{(0,n)} - \hat{\mathrm{P}}\mathbf{E}_s^{(n)}\right),
\end{aligned} \tag{3.27}$$

with the DC term $|\mathbf{E}_s(L)|^2/\mathbf{E}_r^* \approx |\hat{\mathrm{U}}_0^{-1}\hat{\mathrm{P}}\mathbf{E}_s^{(n)}|^2/\mathbf{E}_r^*$, and a parameter ϑ introduced to control the speed of the algorithm convergence. Due to the non-linear nature of eq. (3.27), it can become unstable for large $\mathbf{E}_s \sim \mathbf{E}_r$, and adjustment of ϑ improves the algorithms stability. For simplicity in following discussions, it is assumed that reconstruction follows eq. (3.24).

The performance and convergence of the twin and DC image removal algorithms presented in eqs. (3.24) and (3.27) respectively, are analysed in section 5.2 for simulated phase objects and for real experimental data. Convergence speeds in DIHM and DSHM are compared for objects with different values of N_f and η.

Microscope field of view with iterative twin image removal

As an imaging technique that records interference fringes, the field of view in DIHM is determined by the maximum distance $d_{\max}$ that two point sources can be separated by whilst their interference fringes remain resolvable by the detector without aliasing. Assuming that both point sources are placed in the $z = 0$ plane, with one placed at $\mathbf{r}_1$ and the other placed at $\mathbf{r}_2$, the largest angular separation between two waves exiting from each of the points occurs at a position on the CCD half way between $\mathbf{r}_1$ and $\mathbf{r}_2$. The angle that the two beams intersect is given by θ, and for $|\mathbf{r}_2 - \mathbf{r}_1| = d << 2L$, the small angle approximation can be invoked, thus giving $\theta \approx d/2L$. Then the interference fringe separation can be written as $d_f \approx 2\lambda L/d$.

According to the Whittaker-Shannon sampling theorem [112], two CCD pixels are required to detect an interference fringe without aliasing ($2x_c \leq d_f$). Then to resolve an interference fringe the separation of the two sources must obey,

$$d \leq d_{\max} = \frac{\lambda L}{x_c}, \tag{3.28}$$

then in DIHM at the $z = z_0$ plane, the field of view is given by the area of a circle with a radius $d_{\max}$.

In DSHM without twin image removal, the shape of the field of view is difficult to define analytically, the interference between the two point sources and an object must be resolvable, and the maximum separation between each of the three sources cannot exceed $d_{\max}$ along the $z = 0$ plane. Along the central imaging axis ($x = y = 0$), the maximum $z_0 \approx z_{0,\max}$ which determines the $\mathrm{NA}_{\max}$ in section 3.1.2. Schematics are shown in fig. 3.7 displaying the expected shape of the field of view in the $z = 0$ (fig. 3.7(a)), $y = 0$ (fig. 3.7,(b)) and $x = 0$ (fig. 3.7(c)) planes for DSHM without twin image removal. At the $z = 0$ plane, the field of view is determined by the overlap

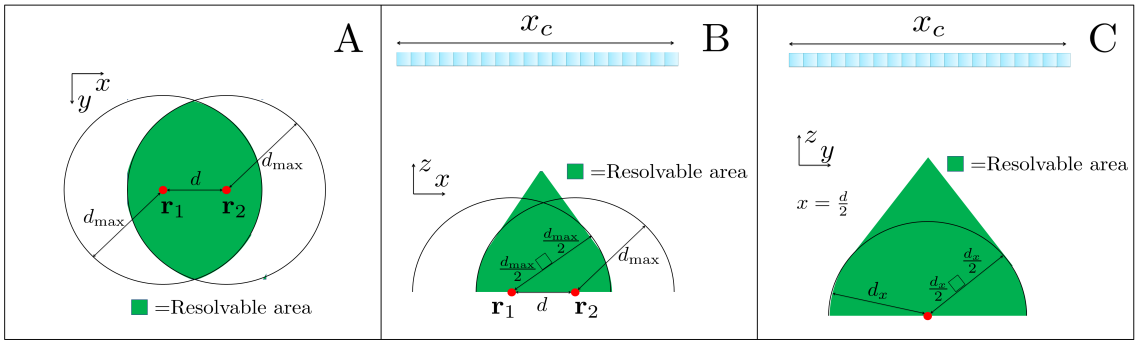

Figure 3.7: Schematics displaying the field of view in DSHM (assuming $d \ll x_c$, the diagrams are not drawn to scale). (a). The source plane where $z = 0$ (b). The $y = 0$ plane (c) the $x = d/2$ plane. The green shaded area indicates the region where the fringes from a point-like object and the two source will be resolvable by the camera.

region of two circles, both with radius given by $d_{\max}$, and with centres located at $\mathbf{r}_1$ and $\mathbf{r}_2$ respectively, the green coloured area in fig. 3.7(a) highlights this area. The field of view along the $y = 0$ plane is more difficult to define, but the outer bounds of the field of view will follow a curve with radius of curvature $d_{\max}$, centred at $\mathbf{r}_1$ or $\mathbf{r}_2$ for small values of z. The outer bounds will continue to follow this curve, until such a value of z that the smallest fringes produced by the two points is only resolvable by the very edge of the camera. After such a value of z, the outer bounds follows the tangent line of the curve for smaller values of z, until it intersects with the tangent line relating to the opposing source/camera edge, see fig. 3.7(b). Similar to the $y = 0$ plane, the field of view will follow a similar form at the at the $x = d/2$ plane, see fig. 3.7(c), but with a maximum separation between the points for small values of z given by $d_x = \sqrt{d_{\max}^2 - d^2/4}$ replacing $d_{\max}$.

A consequence of the iterative twin image removal is that the field of view becomes proportional to the source separation d. To understand this, consider the multiple twin image copies that are present in eq. (3.16). For a particular point-like twin image, whose location is at $\mathbf{r} = (-nd, 0, -z_0)$, alone its conjugate image would be expected to come into focus at $\mathbf{r} = (nd, 0, z_0)$. Instead, the cumulative effect of all of the twin image terms in eq. (3.16) results in a constructive effect that leaves only the real image $\mathbf{E}_s(z_0)$ after a $\hat{\mathrm{U}}_0\hat{\mathrm{C}}\hat{\mathrm{U}}_0^{-1}$ operation on all of the multiple twin images alone (i.e. without the real and DC terms present). In eq. (3.24) a mask $\hat{\mathrm{P}}$ is used

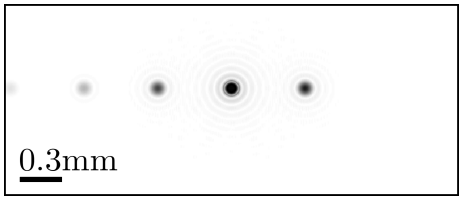

Figure 3.8: Displayed is an image showing the multiple copies of the real image $|\hat{\mathrm{U}}_0\hat{\mathrm{C}}\hat{\mathrm{U}}_0^{-1}\hat{\mathrm{P}}\mathbf{E}_s(z_0)^*|$ at the real image focal plane. The blocking of a proportion of the in-line twin image by $\hat{\mathrm{P}}$ during the $\hat{\mathrm{U}}_0\hat{\mathrm{C}}\hat{\mathrm{U}}_0^{-1}\hat{\mathrm{P}}\mathbf{E}_s(z_0)^*$ operation lifts a destructive interference effect on the multiple copies, making them visible.

to block the real image, but in doing so a proportion of the in-line twin image is also blocked if $\eta < 1$. This blocking reduces the constructive effect and does not leave only $\mathbf{E}_s(z_0)$ after a $\hat{\mathrm{U}}_0\hat{\mathrm{C}}\hat{\mathrm{U}}_0^{-1}\hat{\mathrm{P}}$ operation. The destructive effect suppressing the images that would be expected to form at $\mathbf{r} = (nd, 0, z_0)$ is lifted. This results in multiple copies of the real image at $z = z_0$ separated by d as depicted in fig. 3.8.

The consequence of the multiple real image copies after a $\hat{\mathrm{U}}_0\hat{\mathrm{C}}\hat{\mathrm{U}}_0^{-1}\hat{\mathrm{P}}$ operation restricts the allowable characteristic size a of the mask $\hat{\mathrm{P}}$. If during iteration, one of the in-focus copies of the real image encroaches into the mask, the algorithm will fail to converge, hence for for the algorithm to converge, $a \leq d$. However with the maximum possible field of view given by $d_{\max}$, a proper choice of d approaching $d_{\max}$ allows almost full recovery of the allowable field of view.

Noise increase from twin image removal

To determine the effect of twin image removal on the shot-noise limited noise level near the atomic sample $\delta\mathbf{E}(z_0)$, the input of eq. (3.24) can be modified to $\tilde{\mathbf{E}}_s^{(0)} = \mathbf{E}_s^{(0)} + \delta\mathbf{E}(z_0)$. With the DC term negligible, and $N_f \lesssim 100$ so that $\hat{\mathrm{U}}_0\hat{\mathrm{C}}\hat{\mathrm{U}}_0^{-1}\delta\mathbf{E}(z_0) \approx \delta\mathbf{E}(z_0)$, as eq. (3.24) converges to $\tilde{\mathbf{E}}_s = \mathbf{E}_s(z_0) + \delta\mathbf{E}_s$ the noise level is

$$\delta\mathbf{E}_s = \delta\mathbf{E}(z_0) + \hat{\mathrm{U}}_0\hat{\mathrm{C}}\hat{\mathrm{U}}_0^{-1}\hat{\mathrm{P}}\delta\mathbf{E}_s. \tag{3.29}$$

To aid calculation of the final shot-noise level $\delta\mathbf{E}_s$, an object-free hologram of pure shot-noise is generated at the camera plane by generation of a random number at each pixel that obeys Poisson statistics for both H and H_0. After division by the conjugate reference field as in eq. (3.15), the shot-noise background $\delta\mathbf{E}(L)$ can be propagated to $z = z_0$ via $\delta\mathbf{E}(z_0) = \hat{\mathrm{U}}_0\delta\mathbf{E}(L)$. In fig. 3.9, images are shown that illustrate the process described in eq. (3.29), with $\eta = 0.16$ and a mask such that $N_f \sim 1$. The initial shot-noise level near the atomic location $\delta\mathbf{E}(z_0)$ and the

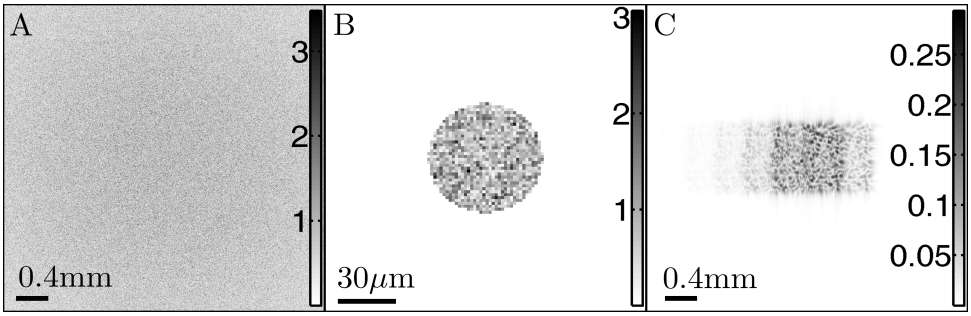

Figure 3.9: (a) Image of the shot-noise background $|\delta\mathbf{E}(z_0)|$ at the focal plane. (b) Image of the apertured shot-noise $|\hat{\mathrm{P}}\delta\mathbf{E}(z_0)|$. (c) The out-of-focus twin image of the apertured shot-noise at the focal plane $|\hat{\mathrm{U}}_0\hat{\mathrm{C}}\hat{\mathrm{U}}_0^{-1}\hat{\mathrm{P}}\delta\mathbf{E}(z_0)|$, the filtered noise is no longer correlated with $\delta\mathbf{E}(z_0)$.

apertured shot-noise $\hat{\mathrm{P}}\delta\mathbf{E}(z_0)$ are displayed in fig. 3.6(a,b) respectively. After one iteration, the twin image of the apertured shot-noise $\hat{\mathrm{U}}_0\hat{\mathrm{C}}\hat{\mathrm{U}}_0^{-1}\hat{\mathrm{P}}\delta\mathbf{E}(z_0)$ no longer appears as a random shot-noise pattern at the real image plane, see fig. 3.6(c), and is no longer correlated with $\delta\mathbf{E}(z_0)$. Then $\hat{\mathrm{P}}\delta\mathbf{E}_s$ is a uniform shot-noise pattern inside the aperture $\hat{\mathrm{P}}$, and its twin image $\hat{\mathrm{U}}_0\hat{\mathrm{C}}\hat{\mathrm{U}}_0^{-1}\hat{\mathrm{P}}\delta\mathbf{E}_s$ is not correlated with $\delta\mathbf{E}(z_0)$, hence the noise contributions can be summed in quadrature,

$$\delta^2_{\mathbf{E}_s} = \delta^2_{\mathbf{E}(z_0)} + \xi^2\delta^2_{\mathbf{E}_s}, \tag{3.30}$$

where ξ is the ratio of the RMS levels $\hat{\mathrm{U}}_0\hat{\mathrm{C}}\hat{\mathrm{U}}_0^{-1}\hat{\mathrm{P}}\delta\mathbf{E}_s/\delta\mathbf{E}_s$. With a substitution for $\delta_{\mathbf{E}(z_0)}$ using eq. (3.22) and rearranging eq. (3.30), the final shot-noise level after iteration of the twin image removal algorithm (eq. (3.24)) is

$$\delta_{\mathbf{E}_s} \approx \frac{\sqrt{2\hbar\omega/A_rQ\tau_{\mathrm{exp}}}}{\sqrt{1-\xi^2}}. \tag{3.31}$$

In comparison, $\xi_{\mathrm{inline}} = 1/\left(1+(2x_c/L)/(a/z_0)\right)$ (determined by considering the area ratio of the apertured shot-noise i.e. the area of $\hat{\mathrm{P}}$ and its NA limited shadow at the twin image plane.) in the in-line geometry with $z_0 \ll L$. In DSHM $\xi = (1-\eta)\,\xi_{\mathrm{inline}}$ and can be significantly smaller if $\eta \ll 1$. Then the noise increase due to twin image removal is expected to be less in DSHM with $\eta < 1$ than if utilised in DIHM.

To demonstrate the noise increase due to iteration in DSHM with a known $\mathbf{E}_r$, holograms containing only shot-noise are numerically generated with differing values

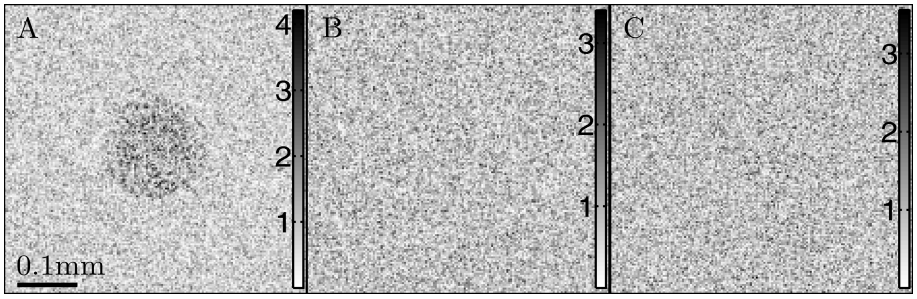

Figure 3.10: Images displaying $|\delta\mathbf{E}_s(z_0)|$ near the location of the mask $\hat{\mathrm{P}}$ after 110 iterations (the algorithm has converged within 110 iterations) of the twin image removal algorithm (eq. (3.24)). (a) The noise background after iteration with a mask $\hat{\mathrm{P}}$ with Fresnel number $N_f = 118$ and source power ratio $\eta = 0.16$, the noise within the mask has increased by $\delta\mathbf{E}_s/\delta\mathbf{E}(z_0) \approx 1.25$. (b) The noise background after iteration with a mask with $N_f = 118$ and $\eta = 0.80$, the noise increase is $\delta\mathbf{E}_s/\delta\mathbf{E}(z_0) \approx 1$. (c) The noise background after iteration with a mask with $N_f = 3$ and $\eta = 0.16$, displaying a negligible noise increase $\delta\mathbf{E}_s/\delta\mathbf{E}(z_0) \approx 1$.

of η. The shot-noise is propagated to $z = z_0$ using eq. (3.15) and the $\hat{\mathrm{U}}_0$ operator, where a mask can be generated with any desired N_f. After generation of the aperture operator $\hat{\mathrm{P}}$, the action of eq. (3.24) is performed for 110 iterations on the shot-noise background alone, so that the final shot-noise level after iteration can be shown. The noise level after iteration for $\eta = 0.16$ and a mask such that $N_f = 118$ is displayed in fig. 3.10(a). The increased level of shot-noise inside the circular aperture $\hat{\mathrm{P}}$ via eq. (3.31) is visible, thus highlighting the apertures location. In fig. 3.10(b) and (c), the final noise level after 110 iterations for $\eta = 0.8$, $N_f = 118$ and $\eta = 0.16$, $N_f = 3$ are shown respectively. As expected, there is negligible noise increase after iteration for both scenarios in fig. 3.10(b) and (c), as indicated by the formula for ξ, the noise increase due to iteration is expected to be small except when both $a/z_0 \gg \mathrm{NA}$ and $\eta \ll 1$. Such a situation is easy to avoid in DSHM since z_0 and η can be independently tuned.

To verify that the noise increase follows that described by eq. (3.31), the RMS noise level within $\hat{\mathrm{P}}$, from object free holograms of shot-noise, can be measured before ($\delta_{\mathbf{E}(z_0)}$) and after ($\delta_{\mathbf{E}_s}$) convergence of eq. (3.24). In fig. 3.11 the ratio of the RMS noise after and before 100 iterations $\delta_{\mathbf{E}_s}/\delta_{\mathbf{E}(z_0)}$ (the algorithm has converged within 100 iterations.) is plotted against $1/\sqrt{1-\xi^2}$ for $\eta = 0.16$. Due to the random nature, each point on the graph is the average of ten holograms for each value of ξ. More accurate data could be retrieved by averaging over larger numbers of holograms, however due to the significant computation time required to simulate the

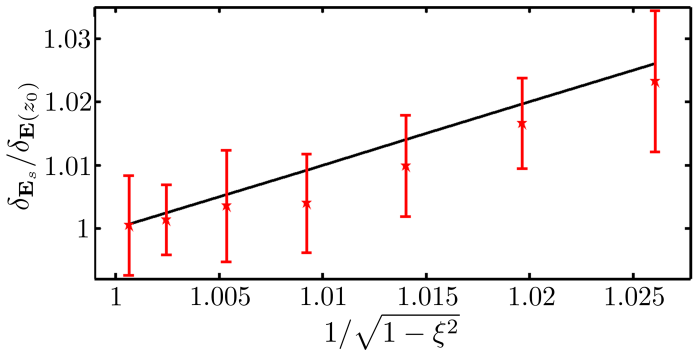

Figure 3.11: Plot of the noise ratio after and before 100 iterations of eq. (3.24) ($\delta\mathbf{E}_s/\delta\mathbf{E}(z_0)$ versus $1/\sqrt{1-\xi^2}$). The black line is the theoretical prediction that follows a straight line with gradient of 1. The data points are the mean of ten repeats, and the error bars are given by the standard error.

reconstruction of so many holograms a compromise has been made. As expected, the plot follows a straight line with gradient ≈ 1 within the error bars, indicating an increase that follows eq. (3.31). For large values of $\xi \sim 1$, the plot of $\delta_{\mathbf{E}_s}/\delta_{\mathbf{E}(z_0)}$ versus $1/\sqrt{1-\xi^2}$ is expected to deviate from the theory since the assumption used to derive eq. (3.31) that $\hat{\mathrm{U}}_0\hat{\mathrm{C}}\hat{\mathrm{U}}_0^{-1}\hat{\mathrm{P}}\delta\mathbf{E}_s$ is not correlated with $\delta\mathbf{E}(z_0)$ becomes invalid. The values of a and z_0 are chosen so that the mask is contained within the microscope field of view (see section 3.2.3) and aliasing does not disturb the noise estimation, since with smaller values of ξ aliasing becomes more prominent and can result in a deviation from that expected by the theory. Furthermore, it is ensured that $a/z_0 < \mathrm{NA}$ so the geometric shadow of $\hat{\mathrm{P}}$ at the camera plane is contained within the camera.

The RMS noise level after convergence of the twin image removal is expected to be larger when used in DIHM as opposed to DSHM for an object with a given N_f. To show this, in fig. 3.12 the ratio of the RMS noise after and before convergence of eq. (3.24) ($\delta\mathbf{E}_s/\delta\mathbf{E}(z_0)$), is plotted against the ratio of the RMS levels in the in-line geometry ξ_{inline} for object free holograms of shot-noise. The parameter ξ_{inline} is changed using a range of masks $\hat{\mathrm{P}}$ with differing N_f in DIHM ($\eta = 0$), and in DSHM ($\eta = 0.6$). Each data point is the mean of 10 simulations, and within the error the data points agree with the theoretical predictions (dashed lines), thus verifying that the increase in DIHM compared to DSHM is given by $\sqrt{1-\xi^2}/\sqrt{1-\xi_{\mathrm{inline}}^2}$. Similar to the data shown in fig. 3.11, more accurate data could be achieved by averaging the reconstructions from more holograms. Furthermore, for larger values of ξ_{inline}

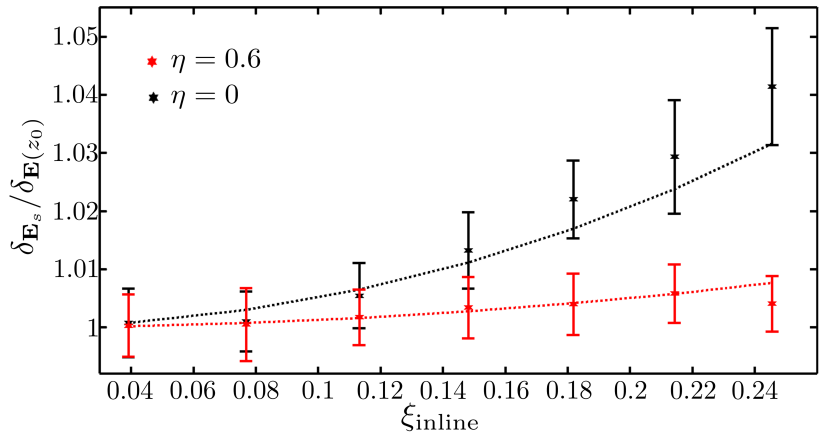

Figure 3.12: Plots of the noise ratio before and after convergence of eq. (3.24) $\delta\mathbf{E}_s/\delta\mathbf{E}\,(z_0)$ versus ξ, for DIHM ($\eta = 0$) and DSHM ($\eta = 0.6$).

than are shown in fig. 3.12, the assumption used to derive eq. (3.31) becomes invalid, since $\hat{\mathrm{U}}_0\hat{\mathrm{C}}\hat{\mathrm{U}}_0^{-1}\hat{\mathrm{P}}\delta\mathbf{E}_s$ is becoming correlated with $\delta\mathbf{E}\,(z_0)$.

3.2.4 Recovering atomic optical properties

Finding the optical depth OD, probe light phase shift ϕ and the column density ρ_c in holographic imaging requires knowledge of the reference field at the sample location $\mathbf{E}_r\,(z_0)$. With the probe field well known at the camera plane, a simple propagation via $\mathbf{E}_r\,(z_0) = \hat{\mathrm{U}}_0\mathbf{E}_r\,(L)$ gives the focal plane reference, as discussed in section 6.1.1. Then in holography with $\mathbf{E}_s\,(z_0)$ given by eq. (2.43) at the sample plane the optical depth and phase shift are respectively,

$$OD = 2\mathrm{Re}\left[\ln\left(1 + \frac{\mathbf{E}_s}{\mathbf{E}_r}\right)\right], \tag{3.32}$$

$$\phi = \mathrm{Im}\left[\ln\left(1 + \frac{\mathbf{E}_s}{\mathbf{E}_r}\right)\right]. \tag{3.33}$$

In chapter 6, the fractional absorption $\alpha_f = |1 + \frac{\mathbf{E}_s}{\mathbf{E}_r}|^2 - 1 \approx -OD$ is used for displaying images of samples with $OD \ll 1$.

With knowledge of the complex absorption cross section $\tilde{\sigma}$ for the atomic sample, the column density ρ_c can be calculated in holography via,

$$\rho_c = \frac{|\ln\left(1 + \frac{\mathbf{E}_s}{\mathbf{E}_r}\right)|}{|\tilde{\sigma}|}. \tag{3.34}$$

Extracting the total number of atoms N from a hologram with sub-pixel sized resolution (see section 3.1.2) is achieved by summing the column density over the split pixels,

$$N = \sum_{\text{Pixels}} \rho_c x_{\text{pix},T}^2, \tag{3.35}$$

where $x_{\text{pix},T} = x_{\text{pix}}/T$, and T^2 is the number of sub-pixels each original camera pixel is divided into.

Straight propagation via $\mathbf{E}_r(z_0) = \hat{\mathrm{U}}_0 \mathbf{E}_r(L)$ to obtain the focal plane reference field can however be problematic. The non-periodic signal at the camera plane results in boundary artefacts in the 2D Fourier transform. Upon propagation, the boundary artefacts act like diffraction from a knife edge which can distort the estimation of $\mathbf{E}_r(z_0)$. To counteract this problem, with prior knowledge of the microscope geometry and a spherical reference field, a smooth $\mathbf{E}_r(z_0)$ can be numerically generated using eq. (3.1), however as discussed in chapter 6 this ignores structure such as speckle noise in the probing wavefront. Alternatively an approach involving inserting $\mathbf{E}_r(L)$ into a larger grid at the camera with a 2D Gaussian fit to suppress the edge effects, as outlined in section 6.1.1, can be used. Both approaches do not retrieve an accurate estimation of the object plane reference field, but as is discussed in more detail in chapter 6, the consistency in the estimation of the reference field at the camera plane for extraction of $\mathbf{E}_s$ and the reference field used for estimation of $\mathbf{E}_r$ is believed to result in a common mode rejection of the errors, thus allowing accurate retrievals of ϕ and OD.

3.3 Removing obstructions to holography with cold atoms

Aided by the addition of a second point source, a method capable of removing the twin image and DC noise associated with DIHM has been proposed. In removing the twin image noise, DSHM overcomes the major obstacle to the development of a holographic technique for cold atoms. The proposed solution retains the advantages promised by DIHM over the established imaging techniques, as outlined in section 3.1.4, with the cost being limited to a small increase in the set-up complexity and a moderate image reconstruction time.

DSHM can in principle be simpler than absorption imaging (section 2.3.2) since the need for imaging lenses is removed. DSHM is one of the simplest twin image free, phase sensitive techniques, with a simpler set-up than that of PCI (section 2.3.2),

DGI (section 2.3.2) and pure off-axis techniques (section 2.3.3). As with DIHM, lens aberration can be eliminated by removing the requirement for an imaging lens. Furthermore, the heavy requirements imposed upon the imaging lenses in PCI and DGI, resulting in "halo" and "shade off" artefacts [91, 98] can be removed.

With a frequency detuned probe, DSHM can overcome the difficulties encountered with absorption imaging of optically dense samples (see section 3.1.4), such as resonant dipole-dipole interactions resulting in the atomic density being poorly described by Beer's law. With minimal heating to the sample, minimally destructive imaging should be possible. The reduction in light assisted collisions with detuned probing could pave the way to imaging of optical lattice sites with multiple atom occupancy per site. For sparse point-like objects, DSHM is expected to be capable of 3D imaging, thus allowing diffraction limited imaging of all occupied sites in a 3D optical lattice with a single shot.

DSHM retains the advantage signal enhancement via collecting the forward scattering, thus DSHM offers a route to detection of atom shot-noise in a sample with large atom numbers $N \gtrsim 1200$ [81], since the shot-noise is proportional to the square root of the mean number of probe photons detected by the camera $\sqrt{N_p}$ and not the number of atoms. This is in sharp contrast to techniques where the noise scales with the square root of the atom number (e.g. fluorescence imaging [19, 38]).

The twin image noise is removed in a single shot, thus alleviating the need for multiple slow exposures as in phase shifting holography (see section 2.3.3). With no conditions imposed on the atomic refractive index, the technique is capable of simultaneous phase and absorption retrieval, and detecting atomic samples with negative probe detuning, overcoming these problems associated with DCI (section 2.3.3). DSHM can image reliably if there is probe gain from the sample, which would be impossible using alternative phase retrieval techniques (see section 3.1.3).

The addition of $\mathbf{E}_{r,2}$ causes an intensity modulation at the detection plane. This intensity modulation reduces the mean number of photons that can be detected by the camera. With a uniform wave at the camera, N_p can approach the maximum pixel count of the camera $N_{\max}$, but with a modulated intensity pattern N_p is reduced to avoid pixel saturation. The reduction depends on source power ratio η and is at a maximum of a factor of two less when $\eta = 1$. When imaging with $\eta \ll 1$ so that the fringe depth $\ll N_{\max}$, the reduction in N_p can be small $N_p \sim N_{\max}$. For $\eta \ll 1$ the imaging sensitivities are well described by eqs. (6.4) and (6.5), where it is shown that thanks to the ability to record the out-of-focus diffraction, DSHM can display a

greater sensitivity than both absorption and phase-contrast imaging. With the noise increase due to the iterative twin image removal negligible except when $a/z_0 \gg \mathrm{NA}$ and $\eta \ll 1$, imaging with negligible noise increase is easy to achieve with DSHM.

The major disadvantage arises from the use of an iterative technique to remove the twin image noise. The requirement of multiple 2D fast Fourier transforms to propagate the wavefront between the object focal plane and the camera plane requires a modest computation time. The consequence of this is that it is difficult to achieve "live" imaging of atomic gases without significant computational power, such as that awarded by a GPU or a cluster of central processing units (CPU's, or a GPU cluster).

As of yet, the speckle noise problem inherent to all coherent imaging techniques for cold atoms has not been addressed. The ring-like speckle noise fringes at the camera plane caused by the point-like speckle sources are expected to distort $\tilde{\mathbf{E}}_s(L) = \mathbf{E}_s(L) + \mathbf{E}_{\mathrm{speck}}$, by imprinting additional fringes to those naturally present due to the object structure. Under propagation via $\hat{\mathrm{U}}_0\tilde{\mathbf{E}}_s(L)$, the fringes due to speckle noise will deflect a proportion of the energy of $\mathbf{E}_s(z_0)$ into multiple copies displaced by the corresponding distances between the speckle sources and the two point sources at $\mathbf{r}_{1,2}$. The speckle energy is expected to be proportional to the energy of $\mathbf{E}_s$, thus for weakly interacting atomic samples where $|\mathbf{E}_s|^2 \ll |\mathbf{E}_r|^2$, the speckle noise background is likely to be below the shot-noise level. The noise level in detection of weak atomic samples such as single or few atoms may be shot-noise dominated, even if a camera with a large bit depth (e.g. $N_{\mathrm{max}} = 2^{14} - 1$) is used for detection, where it is easier for other noise sources to dominate. To address the speckle noise problem in this work, a method of speckle noise suppression is presented in section 5.4. Similar to the inclusion of a second source into $\mathbf{E}_r$, the approach involves numerical propagation to the point-like sources of speckle noise, their isolation and subsequent inclusion into the reference field for use in eq. (3.15). At the expense of computation time, the speckle noise background for stronger samples can be suppressed to levels approaching the shot-noise limit.

With the twin image, DC and speckle noise sources alleviated, lensless reconstruction with DSHM is expected to approach diffraction limited resolution, provided that the reference field can be well approximated. Furthermore, with efforts to remove background noise sources such as ambient light and unwanted scattering of laser beams from the CCD chip, DSHM can demonstrate shot-noise limited imaging for weak samples, since the speckle noise level, originates from a phase error in the $\mathbf{E}_r$ estimation (see chapter 6), and is expected to be proportional to the signal.

It is expected that DSHM with iterative twin image removal will largely retain the advantages offered by DIHM, apart from a small increase in complexity and a modest increase in reconstruction time. With the theoretical understanding of the microscopes operation presented here, the remaining boundary to the realisation of DSHM is its experimental construction, and the technical challenges associated with delivering cold atoms to the microscope.

Chapter 4

Experiment design and construction

With DSHM largely retaining the advantages offered by DIHM, aside from a modest increase in reconstruction time, its easy to argue the case for pursuing the experimental realisation of the microscope. Technical challenges remain in the way of applying DSHM to imaging cold atoms, in particular delivering cold atoms for the experiment and achieving dual diffraction limited point sources for the microscope.

In this chapter the technical challenges to the application of DSHM for cold atoms will be addressed. In section 4.1 the considerations and challenges encountered during the design and construction of the ultra-high vacuum (UHV) are discussed, including the baking procedure for achieving low pressures of the order $\sim 1 \times 10^{-10}$ torr. The design and construction of electromagnetic coils to facilitate a Zeeman slower, and two MOTs is presented in section 4.2. Then in section 4.3, the detailed atomic structure of the ^{87}Rb D_2 transition used in this work for laser cooling is presented, along with the design of cooling, repump and holographic probe laser systems for addressing the transition. To achieve the diffraction limited point sources for DSHM (section 3.2) a focusing lens array designed using the OSLO [147] optical design software is presented and evaluated in section 4.4.2. The details of a lens systems for a more recent upgrade to the holographic microscope permitting imaging with NA = 0.16 is discussed in section 4.4.3. Although lenses are used in this work to increase the numerical aperture, both to generate the point sources and to image the hologram to the camera in the NA = 0.16 microscope, it is stressed that in principle lenses can be avoided for both the point source generation and the recording of the hologram. Presented in section 4.5 are the experimental timing sequences for

delivering atoms from a main chamber MOT to a glass cell MOT, and for preparation and holographic imaging of the atomic sample.

4.1 Vacuum system

To reduce the background gas pressure, and increase the amount of time that atoms can be trapped by reducing the number of collisions that atoms experience with background gas, experiments with cold atoms are often conducted under UHV conditions. To deliver cold atoms to the experiment, a Zeeman slower has been opted for (other techniques of delivering atoms such as using a getter source [148] and chirped slowing are commonplace, see section 2.2.1.), which consists of a "hot" ($T \approx 370$ K) Rb source in an oven at one end of the slower and the main MOT chamber at the other, that are connected by a one meter long slower tube. In the design of the vacuum chamber this was taken into account, and although unnecessary for testing DSHM, future experiments using the vacuum chamber may require low pressures (e.g. to achieve BEC). A diagram of the entire vacuum system is given in fig. 4.1, displayed with the electromagnetic coils for manipulating the atomic resonance frequency as discussed in section 4.2.

4.1.1 Rb oven and atomic beam collimator

The Rubidium source (Rubidium ingot, 276332-5G , Sigma Aldrich) came in the form of an ingot stored in a glass break-seal ampoule. To minimise oxidisation of the source, the ampoule was broken inside the vacuum chamber at low pressure (1×10^{-7} torr). To achieve this, the Rb oven was fashioned from a flexible coupling (FlexCoupling, 2.75", MDC Vacuum), which was bent to break the glass ampoule when the system was at low pressure, see fig. 4.1. The flexible oven section was wrapped on the outside with heating tape to control its temperature, thus controlling the Rb vapour pressure. A valve (AngleValve, .75"Tube, All Metal, MDC Vacuum) placed on top of the oven section allowed the Rb source to be isolated within the chamber, thus the atomic beam could switched on and off. To help with alignment of the Zeeman slower laser beam, a 6-way cross (2.75"Tube, MDC Vacuum) was inserted between the oven and the slower. Viewports on the 6-way cross allowed optical access to observe the Rb vapour fluorescing under interaction with the Zeeman beam. A 1 cm diameter, 178 mm long, custom made collimation pipe was inserted between the 6-way cross and the slower section to collimate the atomic beam and spatially filter the atoms with large velocities in the x, y plane, thus atoms exiting the collimation pipe have velocity largely along the z-axis ($v_z \gg v_x, v_y$).

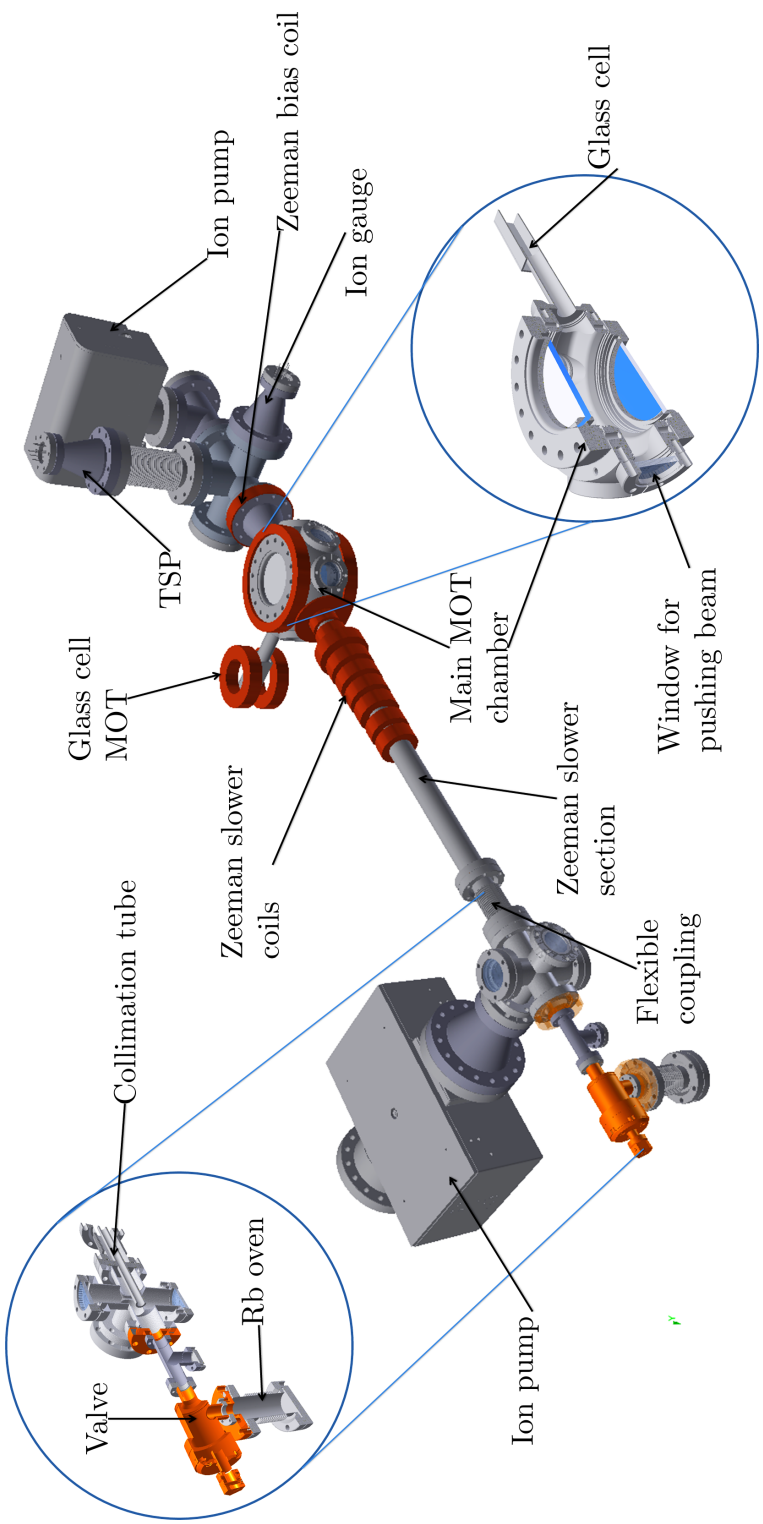

Figure 4.1: Schematic diagram of the vacuum system along with the electromagnetic coils. From the left hand side, a Rb oven was fashioned from a flexible coupling that can be opened or closed with the valve. The inset (top left) gives a cross-section view through the oven section. A collimation tube at the exit of the slower formed a collimated atomic beam with velocity largely along the direction of the Zeeman slower section. At the end of the Zeeman slower section, an octagonal chamber was located to house the main MOT. The second inset (bottom right) shows a cross-sectional view through the main and glass cell MOT chambers. Ion pumps and TSP were used to evacuate the chamber, whilst the Ion gauge monitored the pressure. Coils were arranged to form the magnetic field for a Zeeman slower and two MOTs, whilst a bias coil compensated for the effect of the Zeeman coils on the main MOT field zero.

4.1.2 Zeeman slower and MOT chambers

The typical stopping distance for an alkali atom in a slower is 1 m (see section 2.2.1). For this work, the initial design was to create a hybrid slower consisting of a broadband laser for an initial slowing stage and then a Zeeman slower section for the final slowing stage (see appendix E). For the slower section, a 0.6 m long nipple was used. The broadband slowing could operate in the region between the nipple and the Rb oven ($\approx$ 0.4 m), making the total distance from the oven to the end of the nipple where the main MOT was located $\approx$1 m.

To allow steering of the atomic beam direction along the slowing tube, a second flexible coupling (FlexCoupling, 2.75", MDC Vacuum) was placed between the custom made collimator and the 0.6 m long nipple. The oven location relative to the slower tube could be adjusted by manoeuvring the slower section thanks to the flexible coupling, thus allowing optimal alignment of the atomic beam along the slowing tube.

At the end of the slower, the exit velocity of the atoms could be tuned so that they fall within the MOT capture velocity ($v_c \sim \Delta/k \approx 10$ ms^{-1} [47, 149], for $\Delta \approx 10$ MHz). At this location an octagonal chamber (6.0" Spherical Octagon, Kimball Physics) was placed, see fig. 4.1, which allowed ample optical access to the main MOT.

To undertake lensless holographic microscopy at high NA, short sample to camera distances ($L - z_0 \sim 1$ cm) are required that are difficult to realise within the octagonal chamber. To achieve a short MOT to camera distance, a 25.4 mm by 25.4 mm glass cell vacuum chamber was attached to one of the side ports of the octagon, see fig. 4.1, so that a second MOT could be formed within. A viewport was placed on the port opposite to the glass cell to allow a pushing beam (see sections 4.3.3 and 4.5) to intersect the main MOT and deliver atoms toward the glass cell MOT.

4.1.3 Pumping and baking

To evacuate the chamber, an array of different vacuum pumps designed to operate at different pressures were placed at strategic locations on the vacuum system. The initial pump down stage was conducted using a diaphragm pump, and further a turbo pump [150–152], achieving pressures of the order 1×10^{-7} torr (without baking) Ion pumps [153] were utilized to achieve lower pressures (of the order 1×10^{-10} torr) than those achievable with turbo pumps alone.

To minimize the stray magnetic field from the ion pumps interfering with atoms at the MOT location, two ion pumps were placed at each end of the vacuum system a considerable distance from both MOT locations, see fig. 4.1. The smaller ion pump (Small ion pump 75S, Gamma vacuum) is placed nearer to the octagonal chamber, see fig. 4.1. The larger of the two ion pumps (100L-CV-6S-SC-N-N, Gamma vacuum) is placed nearer to the Rb oven to counteract the increased Rb vapour pressure near the oven.

For achieving and maintaining pressures at 10^{-11} torr, a Titanium sublimation pump (TSP) [154] was positioned such that a large proportion of the vacuum chamber can be coated with Titanium when the TSP is fired, see fig. 4.1.

To permit accurate pressure monitoring near the main MOT, an ionisation gauge [155, 156] (TwinIridiumFilament, 2.75"UHV, MDC Vacuum) was placed near the octagonal chamber, see fig. 4.1. To isolate the chamber, a valve (UHV, All-Metal right angle valve, Agilent) was placed on the flange directly opposite the ionisation gauge. For the initial pumping down of the system, a diaphragm pump and two turbo pumps were connected to the system via a flexible tube connected to the system via the valve.

To achieve the desired UHV pressure, the rate of out-gassing from the vacuum chamber walls was increased by heating the system [152]. To monitor the temperature of the vacuum chamber during baking, a number of thermocouples were placed at various locations along the system. Some were strategically placed at temperature vulnerable locations such as viewports. The heat conductance over the chamber was improved by wrapping the entire vacuum system in a layer of Aluminium foil. Heating tape (Standard type S, Hemi Heating), was evenly wrapped around the whole of the foil coated vacuum chamber. To improve insulation, six layers of Aluminium foil were wrapped around the entire system, above the heating tape. The bake-out procedure was conducted in the following fashion:

1. At room temperature, the chamber was initially evacuated using the diaphragm/turbo pump combination for 10 hours.
2. Using a variac the power supplied to the heating tape was increased to maintain a heating rate of 30 K/h.
3. The power to the heating tape was stabilised to maintain a temperature of 80°C.

4. At 80°C the chamber was continually evacuated for 3 weeks using the turbo pump, whilst the temperature and pressure of the system was continually monitored.
5. The power in the heating tape was reduced to zero and the system was allowed to cool to room temperature at a rate of 30 K/h with the turbo pump remaining on.
6. The ion pumps were switched on, and if desired the system could be isolated by closing the valve connecting the turbo pump.
7. To further reduce the pressure, the TSPs could be fired.

In future work where pressures of 10^{-11} torr may be required, the TSPs may need to be utilised. However, since these low pressures were unnecessary for the purposes of the work discussed in this thesis, the final stage of firing the TSPs was not conducted, thus the final pressure achieved in the system is $\approx 1 \times 10^{-10}$ torr.

4.2 Coil design

The energy levels of an atom can be manipulated utilizing the Zeeman shift, eq. (2.47), induced by the application of an external magnetic field. Weak fields ~ 10 G to ~ 100 G are used to manipulate the resonance frequency of the atomic transitions, and are regularly used in MOTs (section 2.2.3) and Zeeman slowers (section 2.2.1). Stronger fields are often used to trap atoms in magnetic traps (section 2.2.5). Although magnetic fields can be generated using permanent magnets, electromagnetic coils are preferred for the controllability of the field.

To visualise the arrangement of the coils with respect to the vacuum chamber, an Autodesk inventor drawing of the vacuum plus the coil system is displayed in fig. 4.1. With most coils (apart from the glass cell MOT coils) in contact with the vacuum chamber, the chamber its self was used as a heat sink to dissipate the heat from the coils, thus helped in alleviating the need for water cooling. The electromagnetic coils for a Zeeman slower must compensate for the changing Doppler shift as the atoms are slowed (see section 2.2.1). Two separate anti-Helmholtz coils [46] produce the field required for the MOTs (see section 2.2.3). For ease of operation and to minimize cost, a key requirement of the set-up was to avoid the need for cumbersome cooling mechanisms for the coils.

4.2.1 Zeeman coils

The purpose of the magnetic field in a Zeeman slower is to vary the resonance frequency of the atomic transition to compensate for the varying Doppler shift as

the atoms are slowed (see section 2.2.1). The field profile required in the slower to compensate for the varying Doppler shift is as expressed in eq. (2.48). To avoid the slowing light being resonant with atoms that have exited the slower and atoms in the MOT, a scenario known as a reverse slower was chosen [46], so that $\Delta \gg \Gamma$ for atoms with $v = 0$. A secondary advantage of this type of slower is that the large field at the end of the slower follows smoothly into the field required for the main MOT, see fig. 4.2. The Mathematica add-on Radia [157] was used to aid in the design of the coils. As the design was initially to be integrated into a hybrid slower (see appendix E), the Zeeman slower field section was 0.3 m long. The field was designed to slow atoms that travel slower than $v_c = 140$ ms^{-1}, it has B_{bias} such that atoms exit the slower with a with $v = 10$ ms^{-1}.

To match the field described by eq. (2.48), a design was developed consisting of ten separate coils and further a smaller shaping coil (S_c) at the end of the slower to create a sharp transition, see fig. 4.2. The ten coil design consisted of forming the coils with Copper tape that was 25.4 mm wide and 0.2 mm thick insulated with Kapton tape. To shape the field from the coils, each coil needed a different number of turns of the Copper tape when it was wrapped. The number of turns in each of the coils was $n_1 = 2$, $n_2 = 5$, $n_3 = 8$, $n_4 = 11$, $n_5 = 13$, $n_6 = 18$, $n_7 = 20$, $n_8 = 32$, $n_9 = 22$ and $n_{10} = 13$. The first nine of the coils had an inner radius of 29.25 mm, and required a spacer to separate them from the outer surface of the vacuum chamber. Whilst the 10th coil in the slower had an inner radius of 19.25 mm and was wrapped directly against the vacuum chamber.

The shaping coil (S_c in fig. 4.2), was designed to sit on top of the 10th coil and was positioned at the edge nearest to the end of the slower. It had an inner radius of 23.15 mm, was made from Copper tape with a width of 6.4 mm and a thickness of 0.15 mm (Kapton insulated) and had 75 turns of tape.

In optimising the design of the Zeeman slower field to the ideal field given by eq. (2.48) (red line in fig. 4.2), the field from the main MOT and bias coil (see section 4.2.2), were also considered. The spacing between each coil and the currents supplied to the ten slower coils and the shaping coil were altered to optimise the slower field shape. With an equal current of 5.2 A in the ten slower coils and a current of 3.3 A in the shaping coil, the field of the proposed design matched the ideal field, see fig. 4.2. Along the entire section of the Zeeman slower the difference in Zeeman shift produced by the proposed field when compared to the ideal field

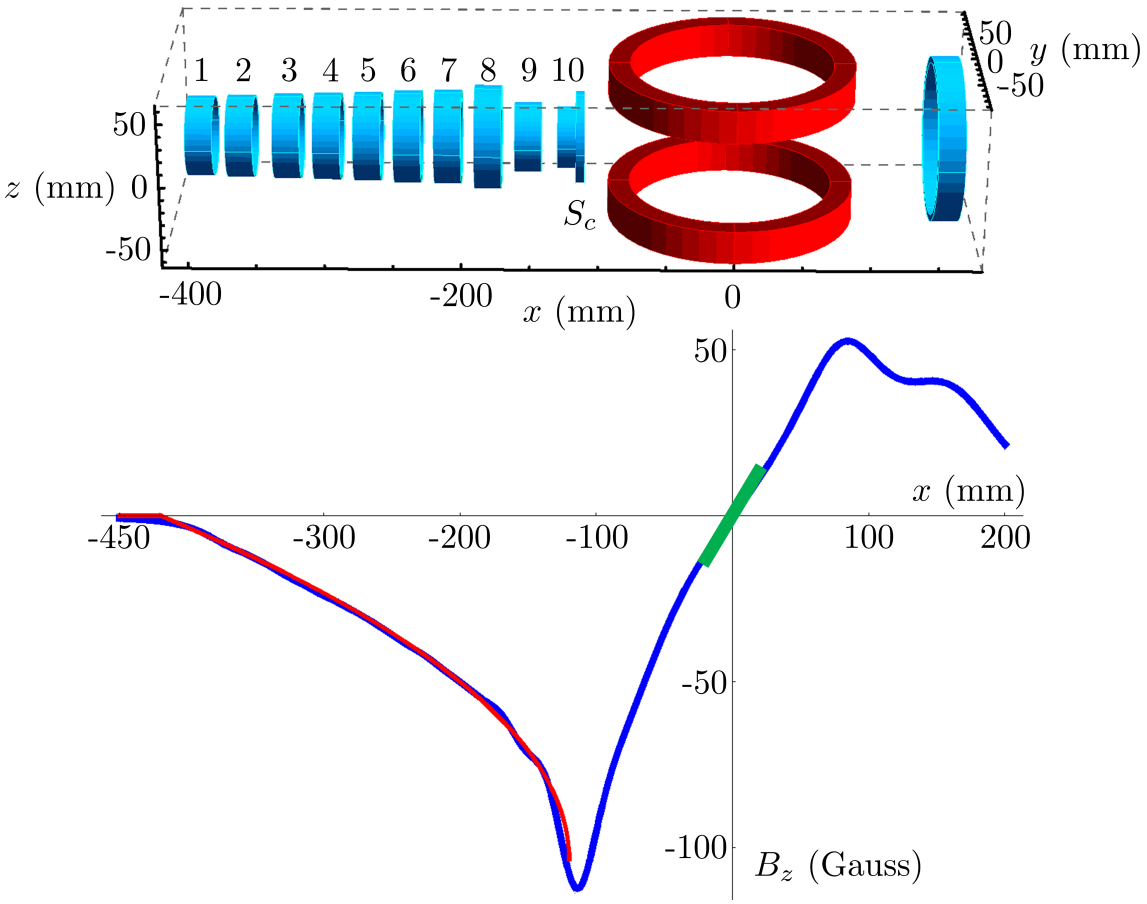

Figure 4.2: Top) Image of the Zeeman slower coils (1 to 10 and S_c), main MOT coils(red) and bias coil (right) design. Bottom) The z field component B_z expected from the coils (blue line) plotted against z, overlaid with the ideal field for the slower (red line) and the ideal 10 Gcm^{-1} MOT field (green line).

never exceeds Γ, thus the slowing laser beam remains on resonance with the slowing atoms along the entire slower length.

The power required to operate the ten coils in the Zeeman slower was calculated to be 1.7 W, and the power required in the shaping coil was 3.4 W. With low power required to operate the slower, air cooling was sufficient, thus no complex water cooling is required.

4.2.2 MOT coils

The simplest way to realise the field required for the MOT, is to arrange two coils in the anti-Helmholtz configuration with a field gradient ≈ 10 Gcm^{-1} near the field zero at the centre [46].

In designing the coils the fact that the physical size of the chamber restricts the size of the coils was taken into account. To minimize the current required to achieve the main MOT field and to aid in heat conduction, the coils were wrapped directly against the outside of the viewports (6.00" Mounting Flange - Viewport, Kimball Physics). The designs for these coils are displayed in fig. 4.2 (red coils). The coils were constructed from the same 25.4 mm by 0.2 mm copper tape as the Zeeman slower coils (section 4.2.1), and had inner radii of 76 mm. To counteract the shift in the MOT field zero along the x-axis when the Zeeman slower field was switched on, a bias coil was located on the opposing side of the anti-Helmholtz coils. The bias coil (the bias coil was made from the same Copper tape as the MOT coils.) was designed to be wrapped against the outside of the main flange of a conical reducer (ConicalReducer, 4.58"x2.75", MDC Vacuum), it had 16 turns of Copper and typically operated with 10 A of current. With 50 turns of Copper and a current of 10 A, the MOT coils were designed to produce the field (B_z) shown in fig. 4.2 with the Zeeman slower and bias fields on accordingly. As indicated in fig. 4.2, a field gradient $\partial B_z/\partial x \approx 10$ Gcm^{-1} was expected near $x = 0$.

The 25.4 mm by 25.4 mm glass cell imposed less of a restriction on the available space to locate coils for the second MOT in the glass cell. To minimize the coil separation, they were located one above and one below the glass cell, ≈ 1 mm from contact with the glass. For stability and heat conduction, the coils were wrapped against a hollow Aluminium tube with an outer diameter 32 mm and an inner diameter of 30 mm. Using the 25.4 mm by 0.2 mm Kapton insulated Copper tape, each coil was wrapped with 90 turns of tape, fig. 4.3(a) displays a schematic of the coil. With a current of 3.5 A, the coils in the anti-Helmholtz configuration

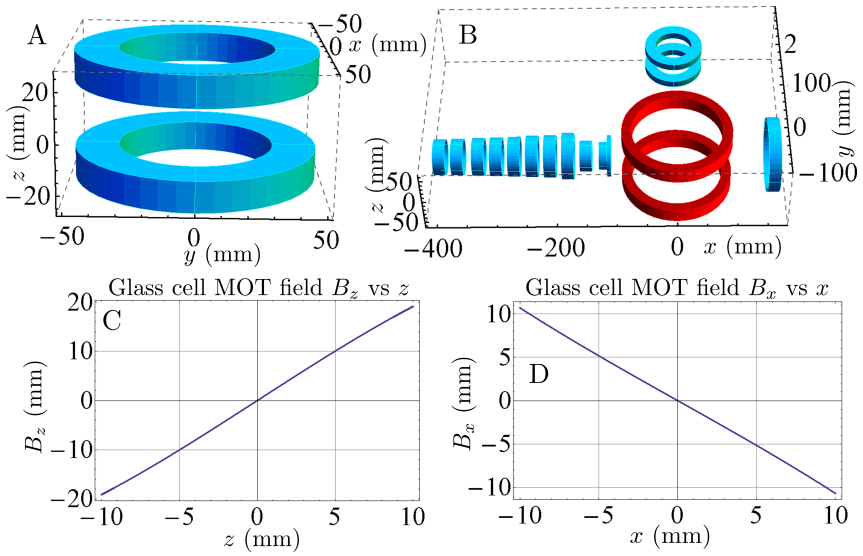

Figure 4.3: (a) Mathematica Radia schematic of the glass cell MOT coil. (b) Schematic of the Glass cell MOT, main MOT, Zeeman slower and bias coils. (c) Designed B_z versus z field profile near the centre of the glass cell MOT anti-Helmholtz coils. (d) Designed B_x versus x field profile near the centre of the glass cell MOT anti-Helmholtz coils, as expected the field gradient is half that in (c).

were designed to produce field gradients of $\partial B_z/\partial z \approx 20$ Gcm^{-1}, fig. 4.3(c), and $\partial B_x/\partial x \approx 10$ Gcm^{-1}, fig. 4.3(d). As an option, operating the glass cell MOT coils with a current of 20 A produced a gradient of $\partial B_z/\partial z = 100$ Gcm^{-1}, which could permit magnetic trapping (see section 2.2.5) of atomic samples.

4.3 Laser system

Laser cooling and detection of atomic samples requires a number of dedicated laser beams at specific frequencies and intensities to manipulate and probe the sample. Knowledge of the atomic structure of the atomic species under study allowed the required laser arrangement for achieving laser cooling and detection of the species to be decided. Using the known structure of the ^{87}Rb (section 4.3.1) D_2 transition (fig. 4.4), optics were arranged to provide light for the Zeeman slower and MOTs (section 4.3.2), and for the repump and probe light (section 4.3.3).

4.3.1 Rubidium 87

Alkali atoms are a popular choice for experiments with laser cooling as they have simple and accessible electronic transitions, and have a similar electronic structure to that of Hydrogen [160]. In particular the Rubidium atom is a popular choice. This

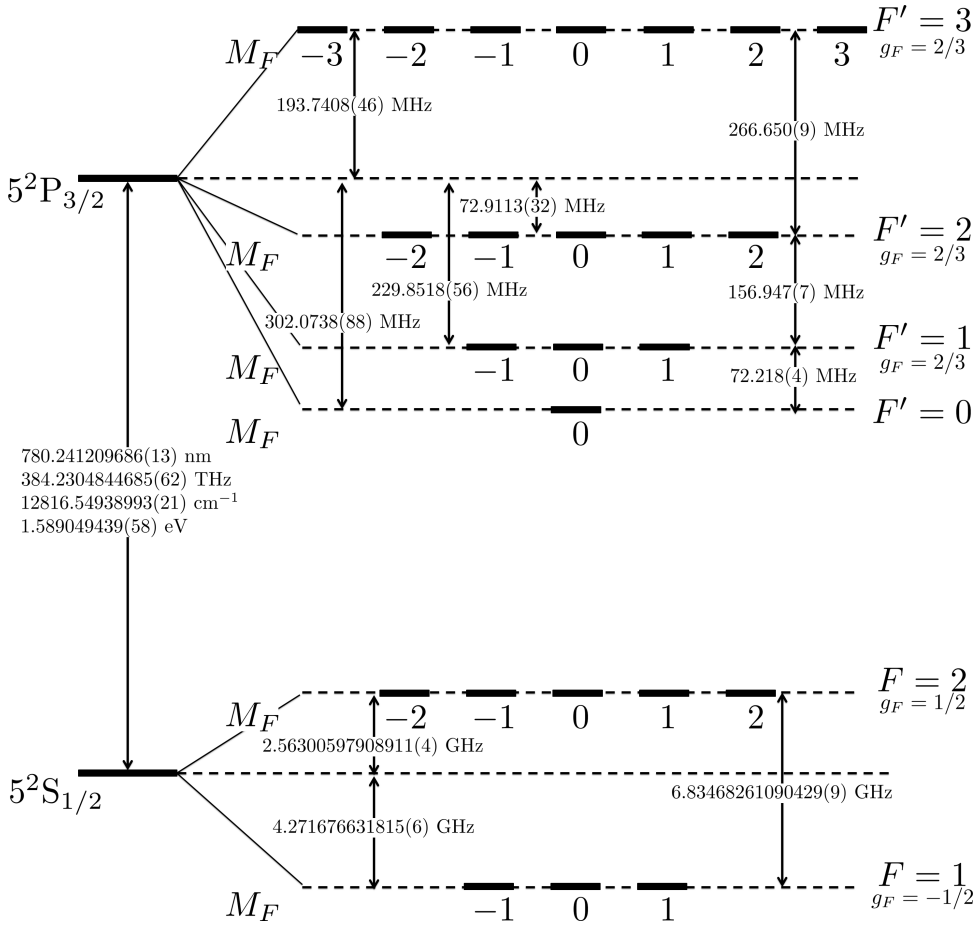

Figure 4.4: A detailed diagram of the ^{87}Rb D_2 transition hyperfine (F/F') and Zeeman (M_F) sublevels, displaying the frequency difference between the hyperfine levels and the approximate Landé g_F-factors. The quoted values are taken from [67], with further affirmation from [158] and [159].

is in part due to the 780 nm D line [67] being close to the readily available 780 nm wavelength of CD burner diode lasers [161] that can be easily tuned and stabilised to the atomic resonance using an external cavity grating [162, 163]. The naturally occurring ^{87}Rb has been widely used for achieving BEC as it has strong mutual scattering that permits efficient evaporative cooling, and a positive scattering length making it mutually repulsive at low temperatures [161].

The species of choice for delivering cold atoms to the holographic microscope in this work was ^{87}Rb. The $5^2S_{1/2} \rightarrow 5^2P_{3/2}$ D_2 transition (fig. 4.4) has a cycling transition ($F = 2 \rightarrow F' = 3$) that is ideal for laser cooling since minimal repump light is needed. The hyperfine structure is further split in to M_F Zeeman sub-levels [46,47] that are degenerate in the absence of an external magnetic field. In a weak magnetic field the degeneracy is lifted, thus each of the M_F sublevels are Zeeman shifted according to eq. (2.47). The shift in stronger fields is described by the Breit-Rabi formula [46, 47].

The D_2 ground and excited levels can be split into 24 separate sublevels, see fig. 4.4. Transitions between the Zeeman sublevels are governed by the electric and magnetic dipole selection rules for electric and magnetic dipole transitions respectively [46]. Transitions driven with $\sigma^{\pm}$ light change the Zeeman sub-level by $\delta M_F = M'_F - M_F = \pm 1$. Transitions driven with π polarised light have $\delta M_F = 0$. Of particular interest are the $F = 2, M_F = \pm 2 \rightarrow F' = 3, M_F = \pm 3$ cooling transitions that require $\sigma^{\pm}$ light. The electric dipole selection rules dictate that the $F' = 3$ state may only decay to the $F = 2$ state, thus this transition is referred to as a cycling transition. These cooling transitions have a stronger coupling with the exciting electromagnetic field than the other transitions within the D_2 manifold in ^{87}Rb [47].

Whilst driving the cooling transition in a MOT, some atoms will undergo a decay into the $F = 1$ ground state, since the polarisation of the light is not guaranteed to be perfectly $\sigma^{\pm}$ polarised, resulting in a $F = 2, M_F = \pm 2 \rightarrow F' = 2, M_F = \pm 2$ transition being excited which can decay to $F = 1, M_F = \pm 1$. This problems is addressed by illuminating the MOT with repump light resonant with either the $F = 1 \rightarrow F' = 1$ or $F = 1 \rightarrow F' = 2$.

There were a number of demands that the laser system needed to meet to achieve cooling and detection of ^{87}Rb atoms. The Zeeman slower with a field directed along the x-axis of fig. 4.2 required $\sigma^{\pm}$ light relative to the field direction to drive the cooling transition. Furthermore, this light needed to be detuned from the $F = 2 \rightarrow F' = 3$ transition to match the capture velocity of the slower. For the MOT, 3 σ^+, and 3 σ^-

beams that counter-propagate with the σ^+ beams were needed that were typically detuned by $\Delta = -13$ MHz from the $F = 2 \rightarrow F' = 3$ transition. A pushing beam resonant to the $F = 2 \rightarrow F' = 3$ transition was needed to transfer atoms from the main MOT to the glass cell MOT. A probe beam with variable detuning from the cycling transition was required for near-resonant and off-resonant holographic probing of the atomic samples. To prevent atoms from falling into a dark state with respect to the cooling light, repump light resonant to either the $F = 1 \rightarrow F' = 1$ or the $F = 1 \rightarrow F' = 2$ was required. In the following subsections (sections 4.3.2 and 4.3.3) the laser set-ups to achieve the light to address these transitions are presented.

4.3.2 Cooling laser

To produce light to address the $F = 2 \rightarrow F' = 3$ transition in ^{87}Rb, an external cavity diode laser (ECDL) [164,165] was dither locked [166] to the atomic resonance in ^{87}Rb via Doppler free saturated absorption spectroscopy (see appendix C). Typically ECDLs have a limited output power, after beam manipulations such as optical isolation or beam shaping, on the order of 10 mW is left [167–169]. To create enough output power to support the multiple beam pathways needed from the cooling laser, a tapered amplifier (TA) [167, 170] was used with a current of 1 A to amplify the 780 nm laser from an input power of 10 mW from an external cavity diode laser to 0.25 W.

Displayed in fig. 4.5 is a detailed schematic of the cooling laser set-up. To minimize optical feedback into the diode, an optical isolator/Faraday rotator (OI) was inserted at the output of the ECDL. The output from the OI was passed through a polarising beam splitter cube (PBS) and the transmitted component sent to a saturated absorption spectroscopy set-up (see appendix C). The reflected beam was combined with light from the repump laser and amplified by the TA together. A $\lambda/2$ waveplate was used to rotate the polarisation of both beams, so that upon entering the TA both had the correct polarisation to be amplified. The frequency of the transmitted component was offset by 200MHz using an acousto optic modulator (AOM) in the double pass configuration (see appendix D). Then the light was passed through a saturated absorption spectroscopy experiment and the laser dither locked [166] to the crossover peak between the $F = 2 \rightarrow F' = 2$ and $F = 2 \rightarrow F' = 3$ transitions. The ECDL output detuning from the $F = 2 \rightarrow F' = 3$ transition was given by the detuning of the crossover resonance plus twice the offset AOM frequency

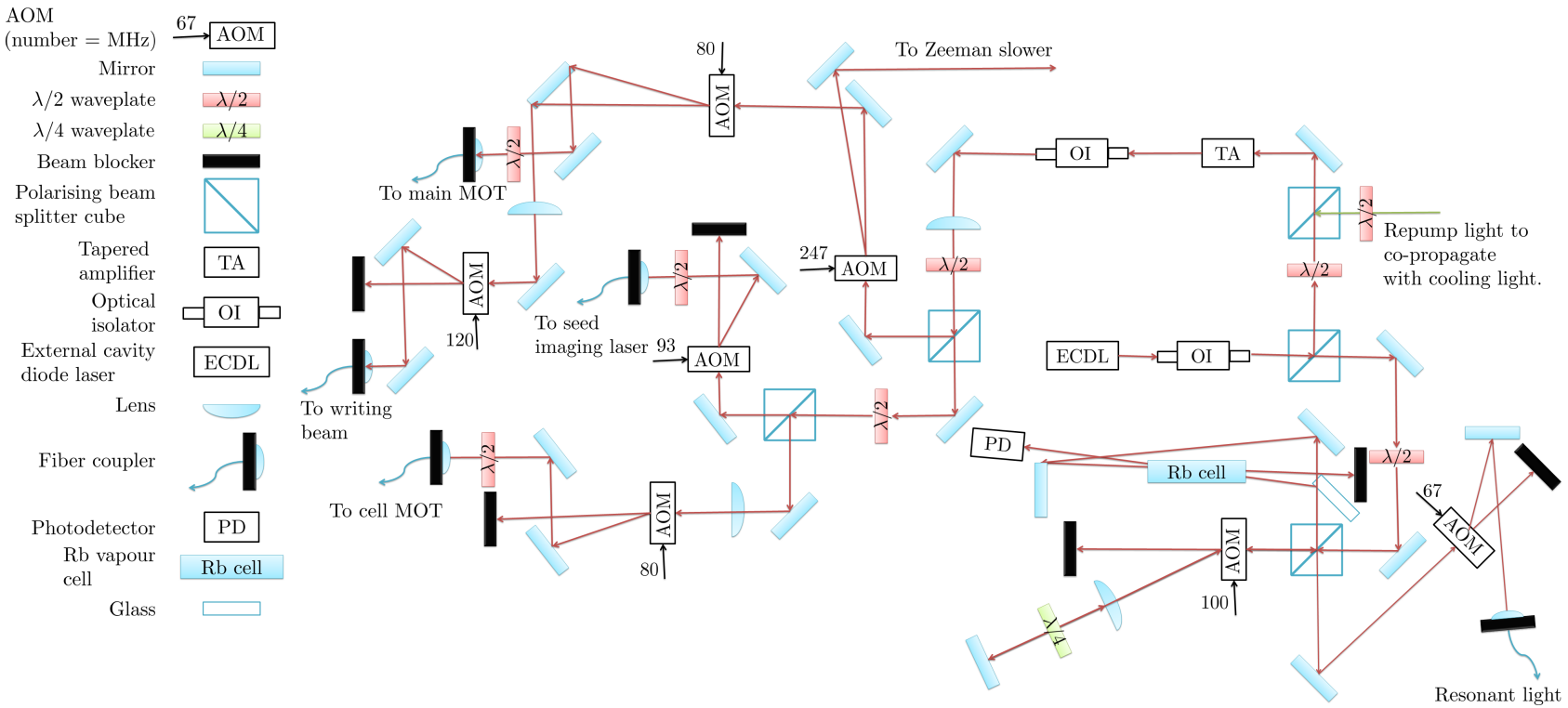

Figure 4.5: Diagram of the cooling laser set-up, with a key to identify each component. The cooling laser beam (red lines) originated from the ECDL and was combined with the repump light (green line), thus providing light for the main MOT, glass cell MOT, Zeeman slower, writing beams and seed light for injection locking the probe laser. Numbers and arrows on the AOMs indicate the input RF (radio frequency) frequency in MHz and the direction of propagation of the sound wave in the AOMs crystal.

88

$\Delta = (2 \times 100) - 133 = 67$ MHz. A small amount of light was separated from the beam line just before the double pass AOM set-up. This light is passed through an AOM driven at 67 MHz, and the $m = -1$ diffraction provided near-resonant light for aiding alignment of beams to atomic samples.

The cooling and repump light that was amplified by the TA passed through an OI before being split into two by a PBS. The reflected pathway provided light for the Zeeman slower, main MOT, and a writing beam that was used to modulate the density of the atomic sample when imaging, whilst the transmitted component provided seeding light for a diode laser and light for the glass cell MOT.

Light for the Zeeman slower was separated from the main beam-line using an AOM driven at 247 MHz. The $m = -1$ diffraction from the AOM was used, thus making the Zeeman beam detuning $\Delta = (67 - 247) = -180$ MHz. The $m = 0$ was further diffracted using an AOM driven at 80 MHz. The $m = -1$ beam was used to provide light for the main MOT at a detuning of $\Delta = (67 - 80) = -13$ MHz. The $m = 0$ beam from the main MOT AOM was passed through another AOM driven at 120 MHz, the $m = 1$ diffraction from this AOM provided light for writing structure to the glass cell MOT at $\Delta = 67 + 120 = 187$ MHz. For output power and polarisation stability, the beams for the MOT and writing beam were coupled into polarisation-maintaining optical fibers, with a $\lambda/2$ waveplate placed before the input to align the input polarisation to the fiber.

The light for the glass cell MOT at $\Delta = 67 - 80 = -13$ MHz, was provided by the $m = -1$ diffraction from an AOM driven at 80 MHz, see fig. 4.5. A beam with $\Delta = 67 + 93 = 160$ MHz was sent through a polarisation maintaining fiber to provide light to injection lock [171, 172] a diode laser, see fig. 4.6, which was used to provide light for holographic probing.

To adjust the power in each of the beam pathways, and thus the intensity, the power of the RF signal to each AOM could be adjusted. Furthermore, using a $\lambda/2$ waveplate, the relative transmittance/reflectance at each PBS could be changed. The overall power in the cooling laser pathways could be altered by changing the current supplied to the TA chip. The frequency detuning of any beam was easily adjusted with a change in the AOM RF driving frequency.

4.3.3 Repump and slave lasers

To produce repump light resonant with the $F = 1 \rightarrow F' = 1$ transition in the main and glass cell MOTs, a separate ECDL was used with output frequency approximately

Figure 4.6: Diagram displaying both the repump (green lines) and imaging laser (red lines) beam paths. The repump light was delivered to the cooling laser set-up to co-propagate with the cooling beam. The probe laser also provided light for a pulsed pushing beam to transfer atoms from the main MOT to the glass cell MOT.

6.8 GHz larger than that of the cooling laser (section 4.3.2). A schematic of the optical layout for the repump laser set-up, alongside the slave laser set-up is displayed in fig. 4.6.

As with the cooling laser, an OI was placed near the output of the repump ECDL to minimise optical feedback into the diode. After the optical isolation stage, the beam was split into two pathways using a $\lambda/2$ waveplate and a PBS. The reflected component from the PBS was diverted into a saturated absorption spectroscopy set-up, where the output of the repump ECDL was dither locked [166] to the crossover resonance between the $F = 1 \rightarrow F' = 1$ and $F = 1 \rightarrow F' = 2$ transitions. The transmitted component from the first PBS was further separated with a $\lambda/2$ waveplate - PBS combination. This produced spare repump light coupled into an optical fibre that was $|\Delta| = 78$ MHz detuned from both repump transitions, and repump light with $\Delta = 78$ MHz from the $F = 1 \rightarrow F' = 1$ transition to co-propagate with the cooling laser, see fig. 4.5.

The repump light co-propagated with the cooling beam and both were amplified by the TA. The $m = -1$ diffraction from the main and glass cell MOT AOMs shifted the frequency of the repump light near-resonance ($\Delta = 78 - 80 = -2$ MHz) with the $F = 1 \rightarrow F' = 1$ transition. The Zeeman slower repump light with $\Delta = 78 - 247 = -169$ MHz was sufficient for the requirements of the slower.

Having the repump light co-propagate with the cooling beam reduced the complexity and cost of the optical assembly, since no additional independent optical components were required to steer and manipulate the properties of the repump light. However, after the combination location every beam along the cooling laser pathway was dual frequency. For applications that required a beam with a single frequency such as holographic imaging (chapter 3) the beams needed be separated, or another source of single frequency light created, such as from another diode laser.

The saturation parameter is heavily reduced with off-resonant probing, thus short exposure times with large probe intensities are permitted without saturating the atomic transition. To create a beam for holographic probing of the atomic sample, a diode laser was injection locked [171, 172] using light with $\Delta = 67 + 93 = 160$ MHz from the cooling laser pathway, see fig. 4.5, via a polarisation maintaining optical fibre, thus delivering more power to the probe but also suppressing the repump side band in the cooling light. The seeding light was coupled into the diode by passing the beam into side port of the PBS at the output of the OI, see fig. 4.6. Though the seeding light was dual frequency, the diode laser could be injection locked to either

of the two frequencies by adjusting the temperature/current of the diode. Here the slave laser current was tuned so that the output was locked to the cooling beam, thus its frequency was nearer to resonance with the $F = 2 \rightarrow F' = 3$ transition.

The optically isolated output of the injection locked diode laser was split using a $\lambda/2$ waveplate and a PBS. The reflected component was coupled into an optical fibre. To monitor the line shape and the injection lock, the fiber output was coupled into a Fabry-Perot interferometer [173]. The transmitted component was used to provide light for a pulsed pushing beam to transfer atoms between the main chamber and glass cell MOTs, and to provide light for the holographic probe beam. The $m = -1$ diffraction from an AOM driven at 160 MHz in 80 μs pulses provided resonant light for the pushing beam.

For versatility when probing atomic samples, the holographic probe laser beam needed frequency tunability such that probing could be conducted with blue or red detuning, or near-resonance if desired. The $m = 0$ light from the pushing beam AOM was steered into a double pass AOM set-up driven at 80 MHz, with the $m = -1$ beam providing tunable near-resonant light for holographic probing.

For probe polarisation and alignment stability, the output from the double pass AOM was couple into a single mode polarisation maintaining fiber before being delivered to the experiment. A mechanical shutter placed before the optical fibre coupler, see fig. 4.6, allowed the holographic probe beam to be fully switched off when not probing the sample, thus minimising noise due to light leaked from the AOM at the CCD.

4.3.4 MOT and double source holography assembly

After preparing the detuning of the MOT beamss, it remained to manipulate the output from the optical fibre to achieve six counter-propagating laser beams with the appropriate polarisations as explained in section 2.2.3, and a total intensity such that $s = 10$ (see eq. (2.21)). This was required for both the main chamber MOT and the glass cell MOT independently. Furthermore, optics were arranged to provide the dual point source for DSHM with atomic samples in the glass cell MOT, and for providing the Zeeman slower beam.

In fig. 4.7, a schematic is shown displaying the set-up for the probe beam, main and glass cell MOTs. The main MOT light with $\Delta = -13$ MHz, delivered from the cooling laser set-up (section 4.3.2) via an optical fibre, was collimated and split into six beams using two $\lambda/2$ waveplates and two PBSs. The six beams were steered

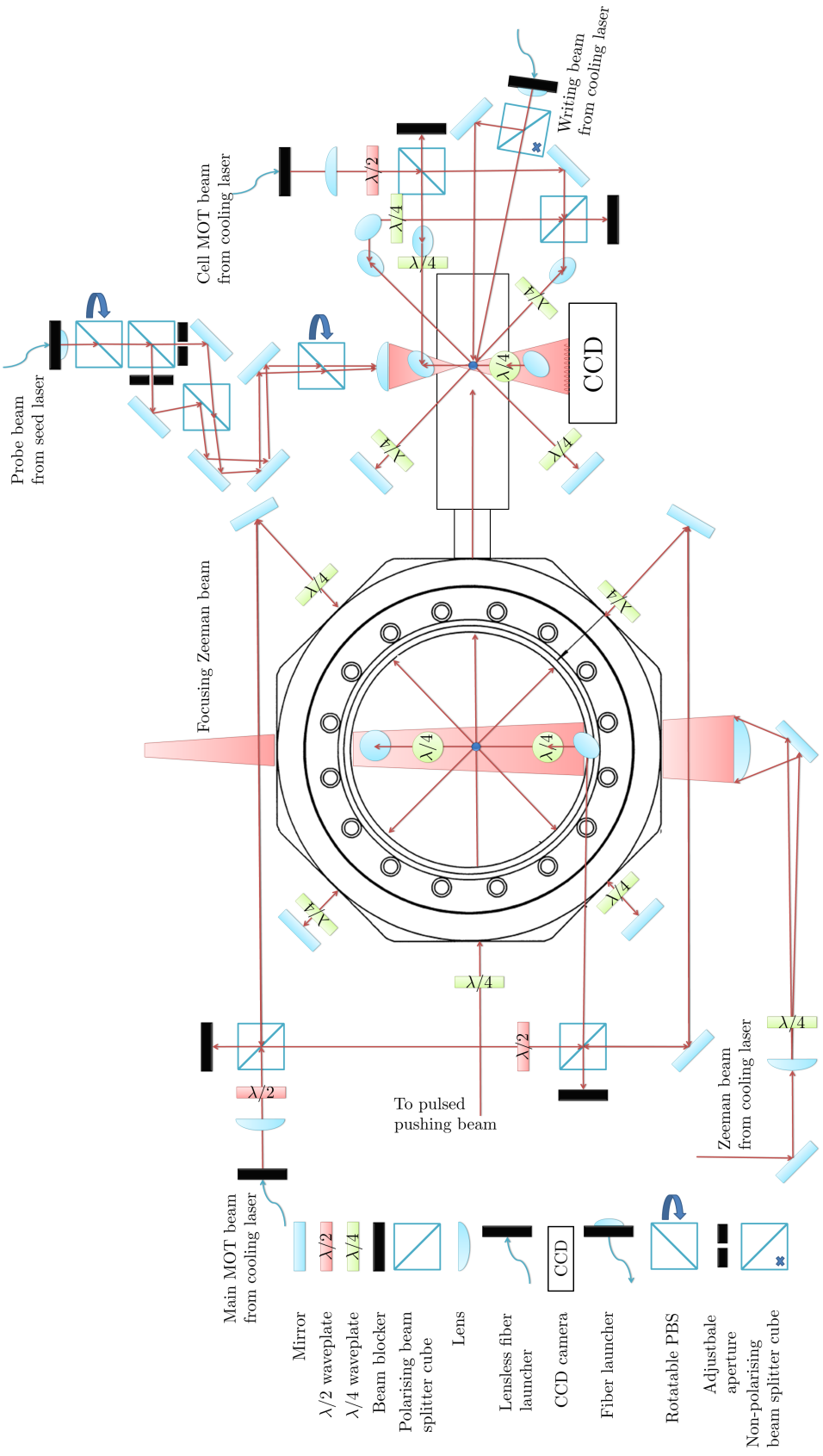

Figure 4.7: A drawing displaying the optical arrangement for the main MOT, glass cell MOT, Zeeman slower, holographic probe and the writing beam.

with optics to propagate orthogonally to each other in the centre of the octagonal chamber with diameters of 20 mm. Before entering the chamber, the polarisation of each of the beams was changed from linearly polarised to circularly polarised with three $\lambda/4$ waveplates. After the beams exited the chamber, second $\lambda/4$ waveplates were placed and a mirror retro-reflected the beams back along their original path. Then the retro-reflected beams had the opposing circularly polarised light to the input beams inside the chamber as required by the MOT (see section 2.2.3).

In a similar fashion to the main MOT, the glass cell MOT beam delivered via a fiber from the cooling laser set-up with $\Delta = -13$ MHz, was collimated with a 20 mm diameter and split into six beams. As with the main MOT, the correct $\sigma^{\pm}$ polarisation for the input and retro-reflected beams was achieved with two $\lambda/4$ waveplates and a retro-reflecting mirror for each input beam. As the repump light co-propagated with the MOT beams, no further optics were needed for alignment of repump light to the MOTs. To improve the available NA for holographic imaging, the MOT beams were adjusted so that along the horizontal plane, their angular separation was not orthogonal, and the MOT formed ≈ 3 mm away from the geometric centre of the glass cell along the holographic probe beam direction.

To transfer atoms from the main MOT to the glass cell MOT, a resonant pulsed pushing beam was aligned to intersect the main MOT. In the glass cell chamber, the pushing beam passed above the glass cell MOT location and did not disturb the atoms. This beam did however intersect the vertical glass cell MOT beam, thus delivered atoms were captured into the glass cell MOT.

As the atoms were slowed, the initial radial velocity coupled with heating from spontaneous emission resulted in an expansion of the beam along the radial directions. To reduce the radial heating and to minimise the expansion, the Zeeman slower laser beam was slightly focusing along the slower, see fig. 4.7. To achieve the focusing of the Zeeman beam, the light delivered from the cooling laser diameter was expanded from 2 mm to 40 mm using a Keplerian telescope. The second lens was positioned to achieve a slight focusing of the beam. The beam delivered from the cooling laser assembly was linearly polarised. To achieve the correct σ polarised light for the Zeeman slower, a $\lambda/4$ waveplate was used before the vacuum window.

To test the resolution of the holographic microscope, structure could be written to the atomic sample using blue detuned light. The writing beam delivered from the cooling laser with $\Delta = 187$ MHz was split into two using a non-polarising beam splitter cube, thus both arms shared the same polarisation. Each arm was adjusted

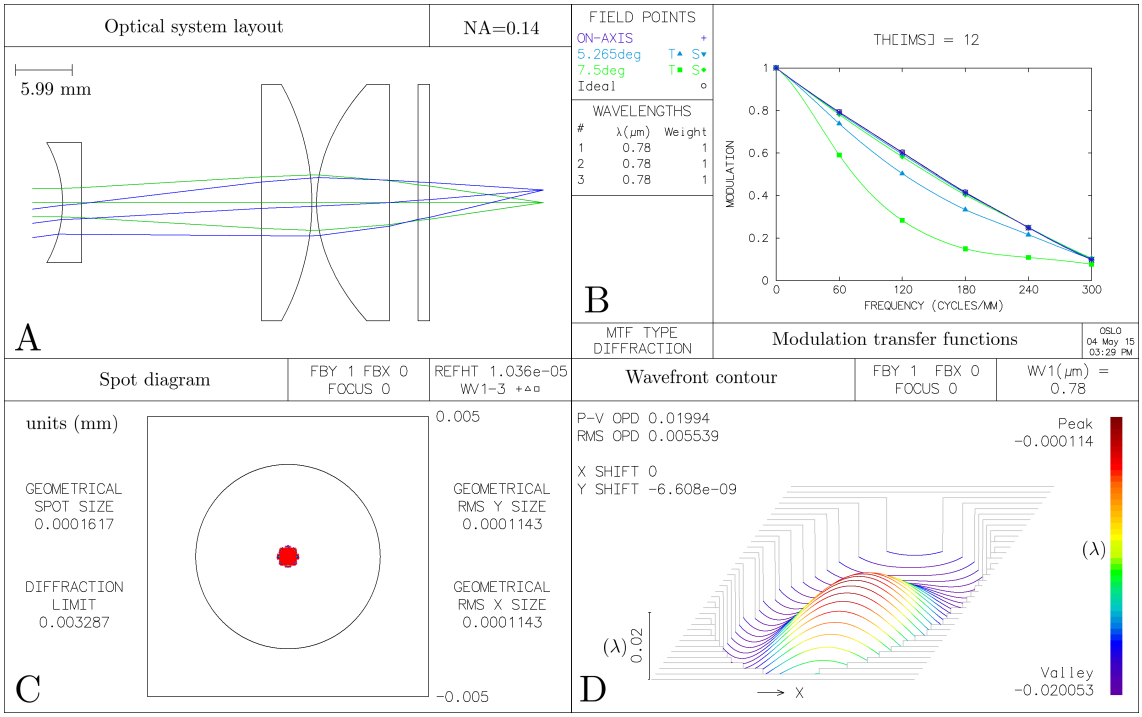

Figure 4.8: (a) OSLO diagram of the point source lens array and the glass cell window. (B) Modulation transfer function, plotted (overlapping) with the ideal modulation transfer function. (C) Geometric spot diagram created by OSLO for the lens array (red dots) with the Airy radius (black circle). (d) Wavefront optical path difference contour plot displayed at the focal point in units of λ.

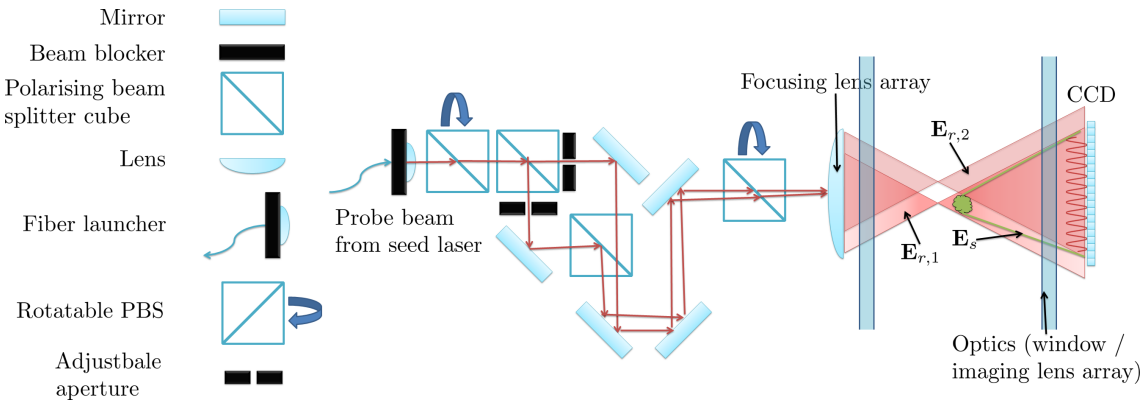

Figure 4.9: Diagram displaying the optical arrangement for using lenses to achieve a double source holographic microscope.

so that they intersected at the MOT location at an angle θ to each other. The mutual polarisation between the two beams resulted in interference fringes at the atoms location with a pancake structure, similar to the design in [174]. When the writing beams were on, atoms were attracted to the regions of destructive interference because of the action of the dipole force (see appendix B). This resulted in a density modulation in the atomic sample with a period matching the that of the interference $\lambda/\sin(\theta)$. By adjusting θ, writing fringe periods of ≈ 20 μm and ≈ 10 μm were written to the sample. The 20 μm fringe was used for testing the resolution in NA=0.07 DSHM, whilst the 10 μm fringe was used for the NA=0.16 version.

4.4 Optics for double source holography

To achieve the diffraction limited point sources for use in DSHM (section 3.2), one approach is to focus laser beams to points that have a waist of the order of λ. In this scenario the light emanating from the points are well described by spherical waves (section 3.1). In this section the optical arrangement for generating a vibrationally stable double point source is presented, then two separate DSHM lens systems are described. The first (section 4.4.2) used a combination of focusing lenses to form the double point sources, and with no imaging lenses achieves a DSHM system with NA = 0.07. The second (section 4.4.3) utilises a higher NA focusing lens system coupled with an array of imaging lenses to remove the aberration from a plane glass window and achieve NA = 0.16 DSHM.

4.4.1 Double point source generation

To achieve a vibrationally stable double point source for use in DSHM, optics were mounted on a single rigid breadboard. Alignment of the holographic probe beam to the atomic sample was achieved by adjusting the breadboard position with a 3D translation stage. The optical layout to achieve the dual source is displayed in figs. 4.7 and 4.9. To minimize the relative power fluctuation in the two sources, a rotatable PBS was used to stabilise the beam polarisation. A second static PBS was used to split the beam into two. Adjustable apertures placed on each arm could be used to control the beam diameter and change the final waist of the focal point. The two beams were made to propagate at an angle to each other upon recombination with another PBS. The angular separation between the two beams was kept small enough that they were both able to encounter the same steering optical elements as they travelled toward the focusing assembly (see section 4.4.2). A second rotatable PBS, rotated by 45° ensured that the two transmitted beams share the same polarisation and thus interfered at the CCD. To remove probe reflections between the CCD chip and the glass cell window, the CCD and the probe light was oriented at an angle to the perpendicular of the glass cell window, such that stray reflections miss the CCD chip.

4.4.2 Point source lens array for NA = 0.07 holographic microscopy

Without imaging lenses, the sample to camera separation was restricted by the MOT beams, see fig. 4.7, to $L - z_0 > 5$ cm. The imaging camera was a pco.pixelfly usb [175] with 1392×1040 square pixels, $x_{\text{pix}} = 6.45$ μm pixel pitch, quantum efficiency $Q = 0.1$ @ 780 nm and a 14 bit dynamic range. Considering the camera chip size and the source separation, the maximum numerical aperture available for imaging was NA ≈ 0.1. To take advantage of the allowable NA, the light from the point sources needed to span an area at least as large as the camera chip at the detection plane. For this the focusing optics were required produce diffraction limited points with NA ≥ 0.1.

The two beams that entered the point source focusing lens array had a diameter ≈ 1.5 mm (measured with a CCD camera). To achieve the required NA, the input beams were expanded before being focused to diffraction limited points inside the chamber. Furthermore, the focusing array compensated for aberrations induced by the glass cell window (1.27 mm thick, silica). A schematic of the focusing array,

Table 4.1: Specifications for the NA= 0.14 lens system and the silica glass cell window for creating diffraction limited point sources for use in DSHM.

Surface number	Radius of curvature (mm)	Thickness (mm)	Material
1	-12.9	2	BK7
2	0	19.02	air
3	0	5.3	BK7
4	-25.8	0.5	air
5	15.51 (Aspheric)	7.7	S-LAH64
6	0	3	air
7	0	1.27	silica
8	0	11.98	vacuum

produced by the optical design software OSLO [147], is displayed in fig. 4.8(a). The design consisted of a plano concave lens (LC1054-B, ⌀ = 12.7 mm, N-BK7, Thorlabs) to expand the beams, and a combination of a plano convex (LA1131-B, ⌀ = 25.4 mm, N-BK7, Thorlabs) and an aspheric lens (AL2520-B, ⌀ = 25.4 mm, S-LAH64, Thorlabs) to focus them to diffraction limited points.

With the MOT location fixed at ≈ 15 mm from the beam entrance window of the glass cell, the design distance from the window to the focal point was fixed to 12 mm to achieve $z_0 \approx 3$ mm. Then using the OSLO built-in GENII ray aberration error function, the air spaces between each of the optical elements were iteratively optimised to achieve diffraction limited focusing with NA=0.14. Given in table 4.1 are the optimised specifications of the lens system, and table F.4 in appendix F gives the aspheric coefficients for the aspheric lens.

To quantify how close the lens array got to achieving diffraction limited spots, the system was evaluated at the location of the minimum on axis spot size. In fig. 4.8(b), the lens system modulation transfer function (MTF) is plotted. The overlap with the ideal MTF indicates a diffraction limited lens design [176, 177]. The spot diagram in fig. 4.8(c) indicates a geometrical spot size smaller than the diffraction limited Airy radius, further corroborating the diffraction limited design of the imaging system. To evaluate the wavefront distortion at the focal point, an optical path difference (OPD) wavefront contour plot is displayed in fig. 4.8(d), The maximum peak to valley (P-V) difference in the plot is well below Rayleigh's quarter wavelength rule [178–180].

Upon assembly of the optical system, the real performance was evaluated by imaging the focal point directly with a CCD camera. To achieve this, light from the holographic probe pathway was passed through the assembled lens system and

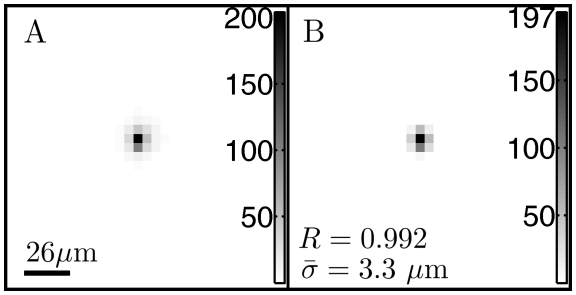

Figure 4.10: (a) Intensity image (photon counts per pixel) recorded at the focus of the point source generating lens system. (b) A 2D Gaussian fit of the intensity image in (a) displaying a mean waist of (3.3 ± 0.6) μm.

imaged by a CCD detector (DCC1545M, $x_{\text{pix}} = 5.2$ μm, Thorlabs). The intensity of the light was adjusted to prevent the CCD pixels saturating. Displayed in fig. 4.10(a) is an image recorded near the focal point. A large fraction of the beam power was contained within a single pixel. A 2D Gaussian fit of the focal point, fig. 4.10(b), indicates that the mean beam waist was $\bar{\sigma} = 3.3$ μm. A focal point of this size was sufficient to fill the detection camera with light at the expected operating distance $L = 5$ cm for holographic imaging.

For use in DSHM, two beams were passed through the imaging system. Adjusting the relative angular displacement between the beams, see fig. 4.7, moves the focal point along the radial direction. The beams were adjusted whilst monitoring them live using the CCD detector. Translation of the CCD back and forth along the propagation direction enabled the adjustment of the alignment so that both beams propagated along the axial direction and had no noticeable distortion to their foci. Once the beams were sufficiently separated and aligned, their separation d was measured by counting the number of camera pixels between the foci $d = (387 \pm 2.6)$ μm.

4.4.3 Focusing and imaging systems for NA = 0.16 holography

In a more recent upgrade to the DSHM set-up to improve the imaging NA compared to that described in section 4.4.2, the focusing lens array in fig. 4.8 was replaced with a higher NA focusing system, see fig. F.1. Then to compensate for the small extent of the CCD chip, an imaging lens array was used to image the hologram on to the camera, see figs. F.2 and F.3. The design of the focusing and imaging arrays were based on a four lens system to account for aberration introduced by a plane window as discussed in [181] and later utilised in [182, 183]. A diagram of these

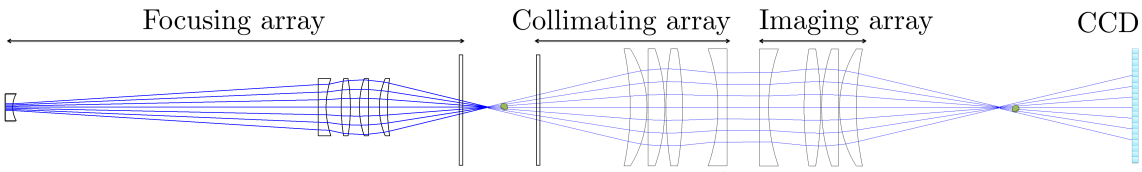

Figure 4.11: Schematic illustrating the design of the imaging system to undertake DSHM with NA = 0.16.

improved focusing and imaging systems that were designed to achieve NA = 0.23 DSHM is presented in fig. 4.11.

To account for aberration introduced into the probe beam by the glass cell windows, the air spacings between the lenses was adjusted. As with the earlier lens design (section 4.4.2), the OSLO built-in GENII ray aberration error function was utilised to minimise the beam aberration by optimising the air spacing between each of the optical elements.

In the previous design (section 4.4.2), the numerical aperture available for imaging was limited by the size of the CCD chip and how close it could be placed to the atomic sample. The two inch diameter imaging array with a magnification factor of approximately one had a larger lateral extent than the CCD chip, thus allowing a larger numerical aperture for imaging.

Though the lens systems discussed in appendix F were designed to accommodate NA = 0.23 imaging, the camera was placed at a location where the reference beams occupied a larger area than the camera chip, thus NA = 0.16 was achieved in the upgraded DSHM system. To achieve NA = 0.16 DSHM, the camera was placed a distance $L = 2.19$ cm away from the image of the point source. When recording a hologram of the compressed MOT with the higher NA DSHM system, the sample was typically located a distance $z_0 = 1$ mm away from the image of the point source. With this microscope geometry a diffraction limited lateral resolution of $R_{\text{lat}} = 5$ μm was expected. To resolve the two source interference fringes with the higher NA DSHM, the source separation was reduced to $d = (229 \pm 2.6)$ μm, since the smaller L reduced the fringe period at the camera.

To minimise the amount of detected stray reflections between the CCD and the final imaging lens, the CCD chip was tilted by 10° with respect to the imaging axis, and aperture was placed in front of the CCD chip to coincide with the image of the point source. This also minimised reflections and stray light from MOT beams and other ambient sources. This modification could permit imaging of atomic samples

while cooling with extended exposure times $\tau_{\text{exp}} \sim 10$ ms, since the stray scattering from the MOT beams into the CCD chip is reduced.

4.5 Experiment timing

Atoms were loaded into the main MOT for a time $\tau_{\text{load}} = 3.2$ ms, then the main MOT beams were switched off using the AOM, and the pushing beam was pulsed for $\tau_{\text{push}} = 80$ μs with a beam intensity I_{push}. To control the delivery of atoms into the glass cell, the intensity I_{push} was tunable, and maximal delivery efficiency occurred when the scattering force was saturated ($\nu = 0$ and $s \gg 1$). To minimise the recapture of pushed atoms back into the main MOT, the cooling beams remained off after the pushing pulse for 100 ms. Increasing τ_{push} or τ_{load} further had no noticeable effect on the loading rate of the glass cell MOT. To control/reduce the loading rate of atoms into the glass cell MOT, I_{push} and/or τ_{push} could be altered. The interaction with the pulsed travelling wave resulted in the atoms being accelerated via the scattering force (see appendix B) in the direction of travel of the pushing beam. With $I_{\text{push}} \gg I_s$ resulting in a constant atomic acceleration at $a \approx a_{\text{max}}/2 = \hbar k\Gamma/4m_{\text{Rb}}$ [46], the atomic trajectory could be easily estimated using the equations of constant linear accelerated motion.

An example of a timing sequence for preparing and holographically probing an atomic sample is illustrated in fig. 4.12. To load atoms into the glass cell MOT, the field gradient near the MOT centre was set to 10 Gcm^{-1} and the MOT beams were switched on with a typical intensity such that $s = 16$ and $\Delta = -13$ MHz. The loading stage typically lasted for a time $\tau_{\text{load}} = 1$ s. To compress the atomic sample after the loading, the field gradient could be linearly ramped to a typical field gradient of $B_2 = 50$ Gcm$^{-}1$, typically during a time $\tau_{\text{compress}} = 250$ μs. To control the sample size and temperature during compression via Sisyphus cooling (see appendix B.0.2), the MOT beam intensity and detuning could be altered to $I_2 \approx I_s$ and $\Delta_2 = 25$ MHz respectively. If desired, atoms could be magnetically trapped by holding the gradient at B_2 for a typical time of $\tau_{\text{hold}} = 20$ ms. Without the fast coil current switch-off times awarded for example by an insulated-gate bipolar transistor (IGBT) switch, a wait time of $\tau_{\text{switch}} = 10$ ms for the field to reduce to negligible values was required if imaging without stray field was a necessity. To image an expanded sample, or to conduct a time-of-flight (TOF see appendix A) experiment [72, 184, 185], the sample could be left to expand for a time τ_{TOF} after the field was switched off. To test the microscope resolution, an atomic density

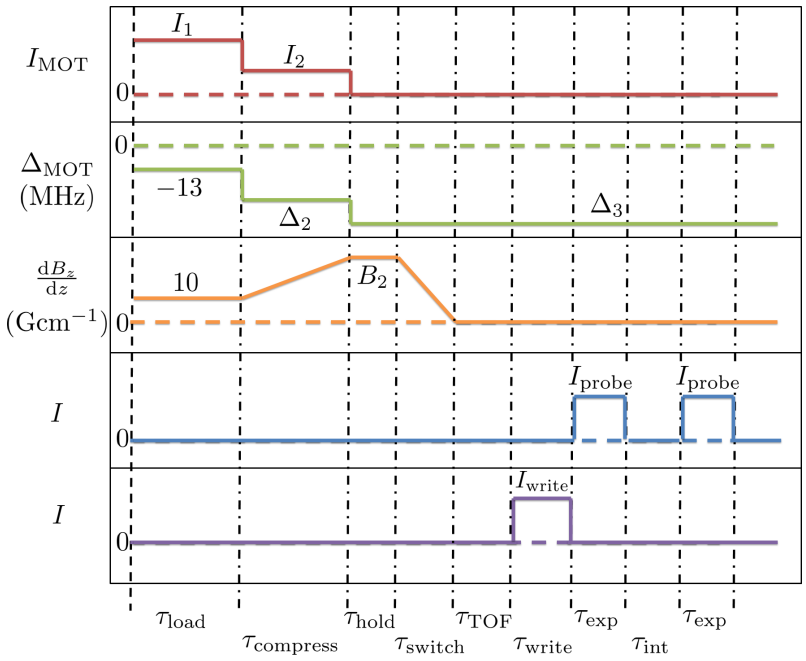

Figure 4.12: Illustration showing an example of a timing sequence for laser beams and field gradient for preparing and imaging a sample with holography. Here I_{MOT}, Δ_{MOT} and $\frac{\mathrm{d}B_z}{\mathrm{d}z}$ refer to the properties of the glass cell MOT laser beams and coils.

modulation could be written to the sample by setting the writing beams intensity to $I_{\mathrm{write}} \sim 100 I_s$ for a typical time $\tau_{\mathrm{write}} = 40$ μs. To preserve the modulation contrast when writing structure to the cloud, the sample was probed immediately after the writing pulse for a typical exposure time of $\tau_{\mathrm{exp}} = 100$ μs to record the hologram H. Before recording the reference intensity H_0 with exposure time τ_{exp}, an inter-frame time $\tau_{\mathrm{int}} = 10$ ms elapsed to allow atoms to disperse from the probe region. A shorter τ_{int} reduced speckle noise in the hologram by reducing the effect of vibration. The camera was set to record two images, one of H, and one of H_0, the timing of the camera exposure was synchronised with the probe pulse. To control the size and number of atoms in the atomic sample, I_1, I_2, Δ_2, τ_{load}, τ_{compress},τ_{hold} and B_2 could be independently adjusted, and this was done on a regular basis. For imaging while cooling, instead of switching the cooling beam off, I_{MOT} would remain at I_2 and the detuning at Δ_2 for the remainder of the imaging sequence.

4.6 Conclusion

The developed apparatus provided a highly controllable MOT conveniently located in a glass cell with ample optical access for holographic probing. A tunable cooling

laser permitted sub-Doppler cooling via polarisation gradient cooling, which coupled with the controllable MOT anti-Helmholtz coils allowed the MOT size, shape and temperature to be easily manipulated, which could be used to load a dipole (see section 7.2.4) or magnetic trap. A phase-stable, detuning and intensity tunable double point source was constructed for holographic probing with DSHM. The two versions of DSHM discussed in this chapter provided lensless imaging at NA = 0.07, as well as an imaging system for NA = 0.16 holographic imaging.

With apparatus for delivering, preparing and holographic imaging of atomic samples constructed, atoms in the glass cell MOT should easily be detected using DSHM. As a coherent imaging technique holography is susceptible to noise sources, particularly speckle noise. Since the glass cell window used to is not anti-reflection coated, difficulties are expected with multiple reflections between optical elements. It remains to describe the imaging/reconstruction procedures to minimise noise levels in reconstructed images. With the constructed apparatus the experimental recording of the hologram and subsequent reconstruction via eq. (3.24) or eq. (3.27) can be analysed and tested against theoretical predictions, as will be demonstrated in chapters 5 to 7.

Chapter 5

Diffraction and shot-noise limited holography with cold atoms

With the apparatus constructed and a sound theoretical understanding of DSHM, it remains to experimentally test the microscope against the theoretical predictions. In this chapter, the procedures to optimally reconstruct images of laser cooled atoms using DSHM including optimal subtraction of background noise, the twin and DC image removal, and speckle field suppression by its inclusion into the reference field estimation will be discussed. The signal to noise ratio of reconstructed images are evaluated against those predicted in sections 3.2.2 and 3.2.3. The performance of the reconstruction algorithm for experimentally recorded data is evaluated against images from numerically generated idealised holograms.

Diffraction limited resolution and shot-noise limited sensitivity are pre-requisites for any imaging technique for precision experiments with cold atoms. To reach the shot-noise limit, other noise sources such as speckle and poor background subtraction must be reduced to levels that are negligible in comparison with shot-noise. Along with an optimal subtraction of multiple background noise sources, the results presented in this chapter demonstrate that in DSHM with iterative twin image removal, the major twin, DC and speckle noise obstacles to applying in-line holographic microscopy to cold atoms can be alleviated. With this consideration, DSHM is proposed for precision quantitative imaging of cold atoms samples with high sensitivity.

The mechanics of hologram recording is discussed in section 5.1. A procedure is described in section 5.1.2 that has been developed to minimise the noise level in the reconstructions and push imaging toward the shot-noise limit. To extract

the complex wave E_H using eq. (3.15), a spherical wave phase was assumed for $\mathbf{E}_1$, which was used to estimate the full reference field $\mathbf{E}_r$ (details of the estimation of $\mathbf{E}_r$ are given in section 6.1.1). Since E_H remained disturbed by the twin and DC image noises, they needed to be removed via eq. (3.27). In section 5.2, the twin image removal performance for experimentally recorded holograms is compared to the performance for numerically generated holograms. It was found that the convergence agrees with the theoretical prediction (see section 3.2.3), and can be faster in DSHM when compared to DIHM. Demonstrations of diffraction limited imaging are given in section 5.3.1 with both versions of DSHM with and without imaging lenses. Then in section 5.3.3 it is shown that the noise levels in the reconstructions reach the expected shot-noise limit. In section 5.4 an algorithm is presented that has been developed for for the suppression of speckle noise. Its performance was demonstrated by considerably suppressing the speckle noise level in an experimentally recorded hologram.

5.1 Holograms and optimal subtraction

A direct subtraction of the reference intensity H_0 does not account for background ambient light or power fluctuations in the probe laser between recording of H and H_0. To reduce the noise level toward the shot-noise limit these effects need to be accounted for. Images of the ambient light background are recorded and subtracted from H. However, a direct subtraction is not precise enough to remove the ambient effects or to account for laser power fluctuations. To account for these effects and a fluorescence background from the atoms, a noise minimisation procedure has been developed and is described in section 5.1.2.

5.1.1 Raw data recording and preliminary subtraction

When holograms were recorded, alignment optimisation was achieved by observing and then centring the diffraction pattern in the subtracted hologram by adjustment of the probe. The atoms were loaded into the MOT for an initial cooling stage. The number of atoms in the sample was controlled by varying the loading time. The size of the atomic sample was controlled by ramping the MOT field from ~ 10 Gcm^{-1} up to a maximum of ~ 60 Gcm^{-1}. The size could be further reduced by decreasing the ratio I/Δ with MOT beam intensity or an increased negative detuning. This secondary cooling stage before ramping the field resulted in a reduced cloud temperature via a Sisyphus cooling mechanism (see appendix B.0.2). The shape of the sample was

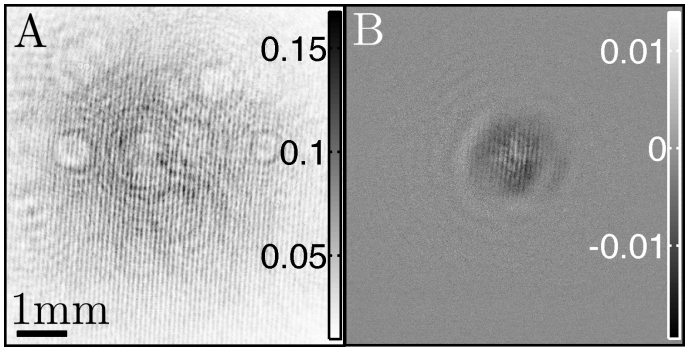

Figure 5.1: (a) Example of a hologram (H) recorded by the camera ($\mathrm{mWcm^{-2}}$). (b) The hologram in (a) after subtraction of the reference intensity $H - H_0$ and ambient background light ($\mathrm{mWcm^{-2}}$). Initially the recorded hologram (a) is heavily disturbed by fringes from speckle noise. After subtraction (b) the speckle fringes still disturb the diffraction pattern from the out-of-focus $\mathbf{E}_s$. Both images share the same spatial size scale bar.

determined predominantly by the alignment of the cooling beams, though fringes could be written to the cloud using the writing beam (see section 5.3.1).

Care was taken during the imaging process to reduce stray ambient light. This was accomplished by switching off all unnecessary lighting when imaging, and by enclosing the camera as much as possible. As it was difficult to completely eliminate the ambient light, two images bk_1 and bk_2 of the ambient intensity were recorded for both H and H_0 respectively, thus it could be removed via subtraction. The hologram H and the subtracted hologram ($H - bk_1 - H_0 + bk_2$) are shown in fig. 5.1, for a sample probed with exposure time $\tau_{\mathrm{exp}} = 0.8$ ms and detuning $\nu = 0.5$. Before subtraction, H is disturbed by significant fringes from speckle sources, fig. 5.1(a). The reason that two images of the background ambient light were recorded was due to the fact that the second exposure time for the pco.pixelfly usb in "double image" mode is fixed at 74 ms [175], thus the image bk_2 could have a significantly different exposure time and ambient background than bk_1.

To reduce speckle noise fluctuation in hologram recording, the optical table was floated on a bed of nitrogen gas, hence suppressing vibration. This was aided by mounting the imaging optics on a rigid platform, so that vibrations were mutually experienced by the imaging optics. Speckle was further reduced by having the probe light and camera at an angle of 10° to the vacuum window surface, so that reflections off the vacuum window (which was not anti-reflection coated) missed the camera chip. This tilting of the camera was not taken into account into the estimation of

the reference field (see section 6.1.1). Reasons for why reconstructing with small errors in the reference field still produced accurate retrievals of the samples optical properties are discussed in section 6.4.

To help with the estimation of the $\mathbf{E}_{r,1}$ and $\mathbf{E}_{r,2}$ parts of the reference field used for reconstruction of $\mathbf{E}_s$ from H (see section 6.1.1), each of the sources was in turn be blocked and an images of $H_1 = |\mathbf{E}_{r,1}|^2$ and $H_2 = |\mathbf{E}_{r,2}|^2$ were recorded with the same probe intensity and τ_{exp} as H and H_0. The reference field $\mathbf{E}_r(L)$ used to reconstruct images in this chapter was estimated using the procedure discussed in section 6.1.1.

5.1.2 Optimisation of the background subtraction

To reach the shot-noise limit, the subtraction $H - H_0$ and the ambient light subtraction for use in eq. (3.3) required a greater level of precision than was awarded from the direct subtraction $(H - bk_1 - H_0 + bk_2)$. In the following a two-step optimization procedure for the subtraction is presented. Each of the images H, H_0, H_1 and H_2 were affected by overall laser power fluctuations, a relative power fluctuation between $\mathbf{E}_{r,1}$ and $\mathbf{E}_{r,2}$, and ambient light, whilst H was also effected by a fluorescence background from the atoms.

Using the double point source interference, the subtraction of the background $H_R^{(0)} = H - bH_0$, was optimised with a parameter b to account for a power fluctuation between each recording. Using the estimation of $\mathbf{E}_r$ (see section 6.1.1) the complex field $\mathbf{E} = H_R^{(0)}/\mathbf{E}_{r,1}^*$, was propagated to the source plane $z = 0$ via $\hat{\mathrm{U}}(-L)\,\mathbf{E}$, where the focal points were observable. The point at $\mathbf{r}_2 = (d, 0, 0)$, corresponding to the real image of the second source $\mathbf{E}_{r,2}$, was isolated, and its residual power $\delta P(b)$ was calculated. At an optimal choice b_{opt}, $\delta P(b)$ was minimised. To prevent the atomic sample from influencing the choice of b_{opt}, a mask was used to block the geometric shadow of the atoms in H and H_0.

Since the optimisation based upon the two source interference fringes cannot account for a relative power fluctuation, ambient light or the atomic fluorescence background, these were accounted for in the second stage with a four parameter $(c_j,\ j = 1, 2, 3, 4)$ optimization,

$$H_R = H - b_{\text{opt}}H_0 - c_1 bk_1 + c_2 bk_2 - c_3 f_{bk} - c_4 P_f. \tag{5.1}$$

Here $P_f = H_{1,f} - H_{2,f}$ accounted for a relative power fluctuation, and f_{bk} was a uniform background to account for atomic fluorescence. Then the complex field $\mathbf{E}(c_j) = H_R(c_j)/\mathbf{E}_{r,1}^*$ was propagated to $z = z_0$ via $\hat{\mathrm{U}}_0\mathbf{E}(c_j)$, where the in-focus

image of the atomic sample $\mathbf{E}_s(z_0)$ was expected, and its out-of-focus twin image. Multiplication with $1-\hat{\mathrm{P}}$ excluded $\mathbf{E}_s$ and some of $\mathbf{E}_s^*$. The remainder of $\mathbf{E}_s^*$ was converted into a real image using the $\hat{\mathrm{U}}_0\hat{\mathrm{C}}\hat{\mathrm{U}}_0^{-1}$ operation as in eqs. (3.24) and (3.27), then it too was excluded using $1-\hat{\mathrm{P}}$. The final image was then nearly free of atomic signal, and it was used to calculate the RMS (root mean squared) noise level $\delta_{\mathrm{rms}}(c_j)$, which was minimised at an optimal choice of $c_{j,\mathrm{opt}}$, and provided the $H_R(c_{j,\mathrm{opt}})$ for use as "$H-H_0$" in eq. (3.3). This typically took 10 minutes with a PC (Intel Core i5- 2400 CPU, 3.1 GHz).

5.2 Removal of the twin image noise

The optimised background subtraction procedure lead to a reduced hologram H_R, that was used to approximate $\mathbf{E}_s$ via eq. (3.3), but it remained disturbed by the twin and DC image noises. To reach the shot-noise limit with double source in-line holography, these noises needed to be eliminated. To remove both of these noise sources, the algorithm presented in eq. (3.27) was also used, and the performance of the removal algorithm is evaluated in this section. To demonstrate the twin image removal with NA = 0.07 DSHM, the convergence of the removal algorithm for experimentally recorded holograms was compared to that for a numerically generated ideal hologram free of speckle noise. In both the NA = 0.16 set-up and the imaging lens free NA = 0.07 microscope, the twin image noise was shown to be suppressed well below the shot-noise level.

5.2.1 Finding the focal plane

The twin image removal algorithm assumes that the sample is contained with in a finite support at the object focal plane, thus accurate knowledge of the object focal plane location is required for both extracting reliable information from hologram reconstructions, and for efficient twin and DC noise removal via eq. (3.27), since ϵ is minimized at z_0, see eq. (3.26). The density modulation in the atomic sample provided by the writing beams (see section 4.3.4), gave structure that was used to determine the focal plane.

The writing beams were pulsed with $s \gg 1$ and $\nu = 31$ for approximately 40 μs prior to and during the recording of H so that a clear density modulation formed in the sample. The wavefront from the sample $\mathbf{E}_s$ was extracted using eq. (3.27) and it could be propagated via $\hat{\mathrm{U}}_0$ to the expected focal plane. The propagation was scanned over z values, and at each z value, a sum of 1D Fourier transforms along the perpendicular axis to the written fringes in the $|\mathbf{E}_s(z)|$ image provided information

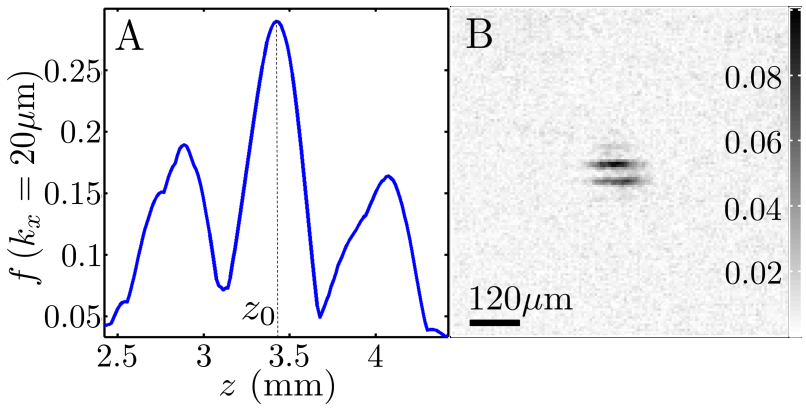

Figure 5.2: (a) The maximum value of the Fourier spectrum corresponding to a spatial frequency of 20 μm, extracted from experimental data, with the atomic sample probed with detuning $\nu = 1.9$, $\tau_{\text{exp}} = 20$ μs. (b) Image of $|\mathbf{E}_s(z_0)|$ (mVcm^{-1}) at the z_0 extracted from (a), there fringes are clearly resolved indicating a correct identification of the focal plane (the twin image has been removed in this image.).

on the spatial frequency of the modulation in $|\mathbf{E}_s(z)|$. The maximum value of the Fourier signal at $f(k_x = 20\mu\text{m})$, was used to decide the z_0 to be used for hologram reconstruction. For weak objects, the twin image noise can be small enough that the identification of the focal plane can be achieved prior to twin image removal (see section 5.2), but larger objects may require that the twin image noise be removed.

5.2.2 Twin image removal with double source holography

Although imaging very small atomic samples (with a small spatial extent, such that the Fresnel number $N_f \ll 1$) with a high NA holographic microscope, results in a negligible twin image and DC disturbance (see section 3.1.3), this assumption becomes invalid when imaging a MOT-sized atomic sample where the Fresnel number $N_f \gtrsim 1$. In such a situation, a significant proportion of the out-of-focus twin image overlaps with the real image at its focal plane. The effect of the twin image interference in DSHM for experimental data with source power ratio $\eta < 1$ and sample Fresnel number $N_f \approx 3$ is shown in fig. 5.3(a). The twin image that is in-line with the real image covers a larger area, and causes a significant distortion to $\mathbf{E}_s(z_0)$, as is evidenced in fig. 5.3(a). To remove this twin image noise using eq. (3.27), a mask $\hat{\text{P}}$ was generated once the object spatial location had been determined from the one step reconstruction of $\mathbf{E}_s^{(0)}$. The diameter of the mask was decided so that the real image $\mathbf{E}_s(z_0)$ was well contained within $\hat{\text{P}}$. After twin image removal, the

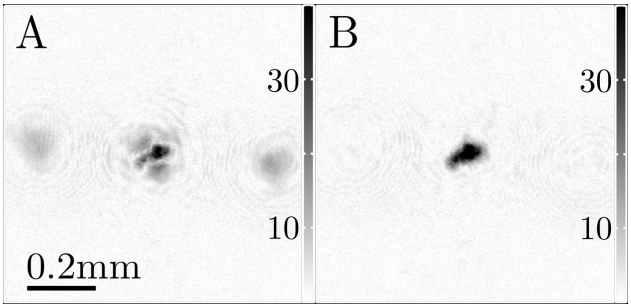

Figure 5.3: (a) [$\nu = -7$, $\tau_{\text{exp}} = 100$ μs]: $|\mathbf{E}_s^{(0)}|$ (mVcm^{-1}) image before removing the twin image noise, for an atomic sample with $N \sim 10^5$. (b) Data from the same hologram as (a) after 165 iterations of the removal algorithm $|\mathbf{E}_s^{(165)}|$, with the twin image noise suppressed.

magnitude of the twin image was reduced to a value well below the background noise level, see fig. 5.3(b).

The plots in fig. 5.4(a) display the convergence for two simulated phase objects with $N_f = 3.8$ and 28, in both the double source and the in-line geometries. The twin and DC image removal algorithm, see eq. (3.27), convergence with $\vartheta = 0.5$ and two different source power ratios ($\eta = 0.17$ and $\eta = 16.7$ respectively), for a real atomic sample with $N_f \approx 3.8$ are shown in fig. 5.4(b). The residual r, defined in eq. (3.25), for the simulated data in the DSHM geometry with $\eta = 0.16$ decayed with a characteristic constant $N_0 = 2.8 \approx -1/\log(1-\eta)^2$, for both $N_f = 3.8$ and $N_f = 28$. In contrast, the in-line case failed to converge within 10^3 iterations, even for $N_f = 3.8$. The non-zero final residual after twin image removal in the DSHM geometry for the simulated object was mainly due to boundary artefacts in the fast Fourier transforms. The choice of $\vartheta = 0.5$ resulted in the convergence speed for the experimental data with $\eta = 0.17$ being twice slower than the simulated case, see fig. 5.4, and with the increased stability, the oscillatory feature in the convergence was suppressed. Similar to the off-axis geometry [122–124], DSHM with $\eta > 1$ achieved almost full real and twin image spatial separation ($\tilde{r} \approx 5 \times 10^{-5}$). A key difference between DSHM and off-axis holography is that DSHM shares the advantage of recording forward scattering at high NA with the in-line geometry (section 3.1). In contrast to the simulated case where the expected $\mathbf{E}_s(z_0)$ was known, the residual $\tilde{r}$ was defined by the difference of $\mathbf{E}_s^{(n)}$ and $\mathbf{E}_s^{(250)}$, with the latter being almost invariant under further iteration.

If $\mathbf{E}_{r,1}$ alone probes the sample, imaging with $\eta > 1$ is not ideal for optimising the SNR and sensitivity of imaging (see section 3.2.1). The increased $\mathbf{E}_{r,2}$ amplitude

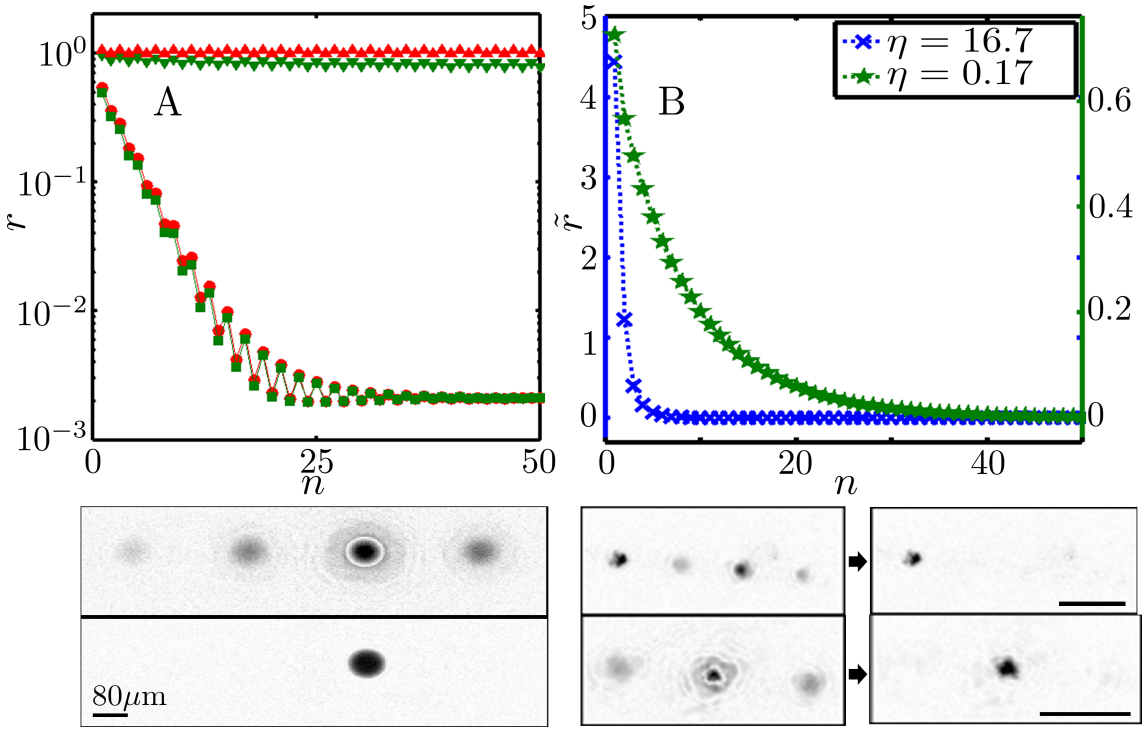

Figure 5.4: (a) Convergence of the twin image removal algorithm for a simulated phase object. The residual r is plotted against iteration number n, for $N_f = 3.8$ and $N_f = 28$ with squares and circles respectively in DSHM with $\eta = 0.16$, and with inverted triangles and triangles respectively in the in-line geometry. (Below) The one-step $\mathbf{E}_s^{(0)}$(top) and the converged $\mathbf{E}_s^{(50)}$ (bottom) for $N_f = 28$ and $\eta = 0.16$ (scale bar is 80μm). (b) Convergence of the twin and DC removal algorithm for DSHM with different source power ratios $\eta = 0.17$ and $\eta = 16.7$, and with $N_f = 3.8$. (Below) The one-step $\mathbf{E}_s^{(0)}$(left) and the converged $\mathbf{E}_s^{(50)}$ (right) images for $\eta = 16.7$ (top) and $\eta = 0.17$ (bottom) (scale bar is $d = 387\mu$m.).

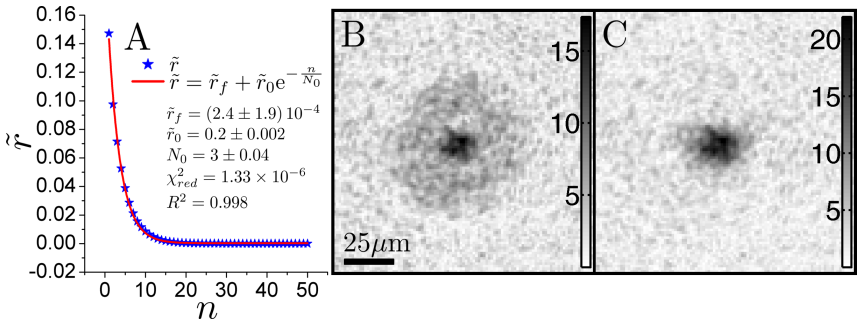

Figure 5.5: (a) Plot showing the decay of the residual $\tilde{r}$ as a function of the removal algorithm iteration number n (Blue stars), alongside a fit of the data to an exponential decay function (Red line). (b) [$\nu = -1.2$, $\tau_{\text{exp}} = 80$ μs]: Image of the scattered wave electric field magnitude before of the atomic sample with $N \approx 270$ before removal of the twin image noise $|\mathbf{E}_s^{(0)}|(\text{mVcm}^{-1})$ from a hologram recorded with the improved NA DSHM. (c) $|\mathbf{E}_s^{(50)}|(\text{mVcm}^{-1})$ extracted from the same hologram as (a) after 50 iterations of the twin image removal algorithm.

does not provide an increase to the SNR because the SNR is only dependant on the number of photons scattered by the sample, see section 3.2.2. To optimally use a cameras bit depth and to optimize the SNR, it is preferable to have the $\mathbf{E}_{r,2}$ amplitude just large enough to assist in the twin image removal using eq. (3.27) (e.g $\eta \sim 0.1$).

Twin image suppression in NA= 0.16 DSHM

To demonstrate the removal of the in-line twin image noise with the improved numerical aperture DSHM, the residual $\tilde{r}$ is plotted against the twin image removal algorithm iteration number n for an atomic sample probed with $\nu = -1.2$ and $\tau_{\text{exp}} = 80$ μs (the residual $\tilde{r}$ is defined as the difference between $\mathbf{E}_s^{(n)}$ and $\mathbf{E}_s^{(250)}$ using eq. (3.25)). The decay of $\tilde{r}$ using eq. (3.27) with $\vartheta = 0.5$ and $\eta \approx 0.4$ follows an exponential form, see fig. 5.5(a). The non-zero value of the final residual $\tilde{r}_f$ was caused by the background noise. Images are displayed before, fig. 5.5(a), and after, fig. 5.5(b), the twin image removal illustrated in fig. 5.5(a) via eq. (3.27). Before twin image removal the out-of-focus in-line twin image was visible in the background above the noise level. After 50 iterations of eq. (3.27) the twin image disturbance was suppressed below the background noise level, see fig. 5.5. Furthermore the magnitude of the $\mathbf{E}_s$ amplitude was increased post twin image removal, thus indicating that a destructive interference effect from the twin on the real image had been lifted.

Discussion

In removing the twin and DC noise, DSHM has simultaneously removed two of the largest noise sources, thus overcomes two of the major obstacles to the application of holography to imaging cold atoms. Before iteration, the image was heavily distorted by the interference from the twin image term and copies of the out-of-focus twin image were visible either side of the real image, see fig. 5.4. After iteration, the twin image noise was no longer visible above the background noise, thus leaving only the real image. Analysis of the noise penalty associated with the twin image removal (see section 3.2.3) indicates that a negligible increase in the noise level is expected except when both $a/z_0 \gg \mathrm{NA}$ and $\eta \ll 1$. This situation is easy to avoid in DSHM when compared to DIHM, since z_0, a and η can be independently adjusted. In the results presented here no noise increase from the iteration is noticeable in the background.

It is shown that the twin image removal speed in DSHM can be much faster than in DIHM (see section 5.2). For an object with $N_f \gg 1$, where twin image removal via eq. (3.24) in DIHM failed, DSHM still removed the twin image. Imaging objects with large N_f allows DSHM to image spatially extended samples such as those in time-of-flight experiments to determine atomic sample temperatures (see appendix A). At high numerical aperture and with $N_f \ll 1$ where the twin image noise is well below the noise level at the focal plane, DSHM may be unnecessary (see chapter 3). Then if required, DSHM can easily be converted into DIHM by blocking or removing the second point source, thus fully alleviating the need for iterative twin image removal. Aside from twin image removal, the iterative method developed in this work can also remove the DC noise term, which becomes significant for samples with large optical thickness $\mathbf{E}_s \sim \mathbf{E}_r$.

5.3 Shot-noise and diffraction limited imaging

In this section images of atomic samples with a known density modulation are utilised to infer that imaging approaches the diffraction limit. To analyse the signal to noise ratio of images produced with DSHM, the noise level in the reconstructions are compared with the expected shot-noise level, and are compared to those from numerically generated idealised holograms. An ideal hologram simply means a numerically generated hologram where the reference field is exactly known, and can be made completely free of laser speckle and/or photon shot-noise if desired. Comparison of the retrievals SNR with the expected signal to shot-noise ratio reveals that DSHM reaches the shot-noise limit for images with a dynamic range SNR $\lesssim 30$.

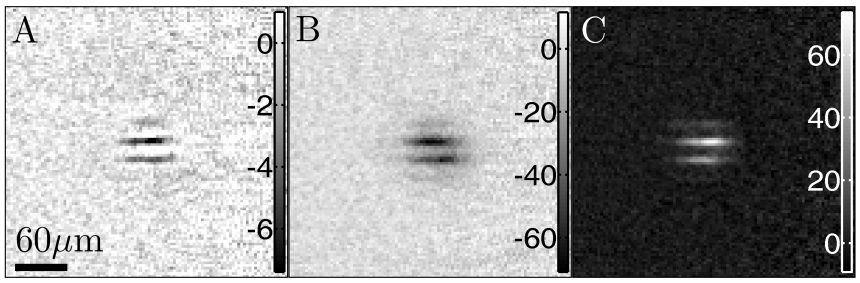

Figure 5.6: Images showing the fractional absorption α_f (%) and phase shift ϕ (mrad) of density modulated atomic samples subjected to a 20 μm spatial period writing lattice. (a) [$\nu = 1.9$, $\tau_{\text{exp}} = 20$ μs]: α_f. (b) ϕ, extracted from the same hologram as (a). (c) [$\nu = -7$, $\tau_{\text{exp}} = 20$ μs]: ϕ, the phase shift has the opposite sign to (b) as expected.

By adding speckle noise sources with 4 % of the $\mathbf{E}_1$ source power to the idealised holograms, it is shown that speckle noise becomes significant for SNR > 30, thus preventing such reconstructions from reaching the shot-noise limit.

5.3.1 Diffraction limited imaging

Writing a structure with a known spatial period of 20 μm, for 40 μs before and during the entire probe exposure time, to the atomic sample with the writing lattice allows verification of the microscope resolution. The sample was probed for a short exposure time $\tau_{\text{exp}} \sim 10$ μs so that the written structure was preserved during imaging. In fig. 5.6(a) and fig. 5.6(c,d) α_f and ϕ images (extracted using the expressions developed in section 3.2.4 with knowledge of the reference field at the atoms location $\mathbf{E}_r(z_0)$, as discussed in section 6.1.1.) of atomic samples subjected to the writing lattice are displayed respectively. The 20 μm density modulation in the atomic sample caused by the writing beams is clearly visible, thus indicating a resolution near the diffraction limited resolution of 10.4 μm. And as expected, fig. 5.6(c,d) display $\text{sgn}(\phi) = \pm 1$ for $\text{sgn}(\nu) = \mp 1$, see fig. 2.4.

Improved imaging resolution

To holographically demonstrate a resolution approaching the diffraction limited value with the modified NA = 0.16 DSHM, a density modulation with 10 μm spatial period was written to the atomic sample using the writing beams. The fringe writing direction has changed since the writing beams were moved to accommodate optics for a dipole trap to be discussed later in section 7.2.4. Column density images (retrieved using eq. (3.34) and knowledge of $\mathbf{E}_r(z_0)$, see section 6.1.1) of the density modulated atomic samples are displayed in fig. 5.7. To preserve the structure in the image,

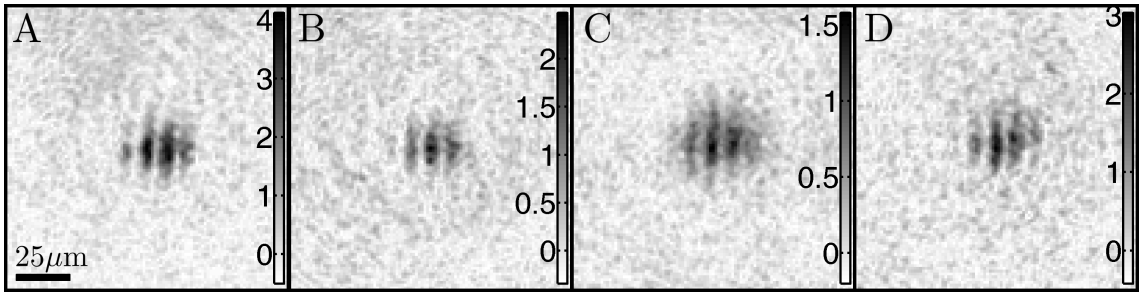

Figure 5.7: Holographically extracted ρ_c images ($1/\mu m^2$) of atomic samples subjected to a 10 μm period density modulation. (a) [$\nu = 5.94$, $\tau_{exp} = 60$ μs]: ρ_c image. (b) [$\nu = 4.34$, $\tau_{exp} = 60$ μs]: ρ_c image. (c) [$\nu = 2.37$, $\tau_{exp} = 60$ μs]: ρ_c image. (d) [$\nu = -5.37$, $\tau_{exp} = 60$ μs]: ρ_c image.

the sample is probed with $\tau_{exp} = 60$ μs. The compensation for lens and window aberration in the lens system design (see appendix F) allowed the 10 μm fringes to consistently resolvable at various differing probe detunings, thus indicating a resolution approaching the diffraction limited value.

5.3.2 Characterising the shot-noise level

The minimum noise level expected for holographic imaging is the counting fluctuation of the photon detector when detecting laser light, otherwise known as photon shot-noise. As detailed in section 3.2.2, the shot-noise level at the image focal plane can be approximated by eq. (3.22). To perform a more precise estimation of the expected shot-noise level, the contributions from H, H_0, bk_1 and bk_2 were considered separately. Due to the high photon counts in the camera recording ($N_{max} \sim 2^{14} - 1$), the 8 count/pixel readout noise of the camera was negligible, and with $\eta \ll 1$ and $a/z_0 \ll$ NA the noise increase due to iteration ($\xi \ll 1$) also contributed negligibly to the noise level (see sections 3.2.2 and 3.2.3).

Measuring image signal and noise levels

Reconstructions can be characterised by comparing their (SNR) with the signal to expected shot-noise ratio ($\overline{\text{SNR}}$). When SNR $\rightarrow \overline{\text{SNR}}$ imaging is near the shot-noise limit, whilst other noise sources such as speckle and poor subtraction via eq. (5.1) dominate when the SNR is noticeably less than $\overline{\text{SNR}}$.

For this work, the signal was defined as the mean value of $|\mathbf{E}_s(z_0)|$ above 60% of its maximum. The noise level was measured in the immediate vicinity of the atomic

image that can be excluded via multiplication with $1 - \hat{\mathrm{P}}$. The noise level is given by

$$\delta \mathbf{E}_{s,\mathrm{meas}}(z_0) = \sqrt{\langle |\mathbf{E}_s(z_0)|^2 \rangle_D}, \tag{5.2}$$

where D is the area of an annulus surrounding $\hat{\mathrm{P}}$ with a ring width equal to the characteristic sample size a. A choice of a large ring width can lead to an inaccurate measurement of the noise level, since the noise level at the atomic plane is not expected to be uniform if $A_r < A_p$ due to a focusing effect on the shot-noise field under propagation (see section 3.2.3).

5.3.3 Reaching the shot-noise limit

To compare the experimental data with theoretical predictions, holograms of simulated pure phase objects were recorded, each producing a different phase shift. To simulate the presence of speckle noise, point source wavefronts were generated from random locations with intensities approximately 4% that of the reference. These wavefronts were ignored in the generation of the reference field for reconstruction. For the simulated data it is easy to determine the number of photons scattered by the sample N_s. Then, in fig. 5.8(a), the measured SNR (see section 5.3.2) is plotted against the theoretical predication of the shot-noise limited signal to noise ratio, see eq. (3.23). For the data simulated with no speckle noise, the reconstructions were always shot-noise limited, as expected. Images reconstructed in the presence of speckle noise approached the shot-noise limit for SNR $\lesssim 30$.

Ignoring speckle noise in the reference field results in multiple copies of $\mathbf{E}_s$, whose focal locations are shifted by the corresponding distance between the $\mathbf{r}_{1,2}$ focal points and the source of each speckle noise. This has the effect of decreasing the energy in the true $\mathbf{E}_s(z_0)$, and adding the lost energy to the background. The out-of-focus faint copies of $\mathbf{E}_s$ are visible in fig. 5.8(a), as circular structures in the background above the shot-noise level. The circular structures are displayed along with a characteristic reconstruction for SNR < 30.

In fig. 5.8(b), the SNR is plotted against $\overline{\mathrm{SNR}}$ for an unbiased collection of reconstructions of $|\mathbf{E}_s(z_0)|$ from experimentally recorded holograms. The holograms were recorded during or after cooling, with various values of τ_{exp} and ν, and intensities such that optimal use was made of the cameras bit depth with minimal pixel saturation. Similar to the simulated data, fig. 5.8(a), experimental reconstructions frequently reached the shot-noise limit (SNR $\approx \overline{\mathrm{SNR}}$) for SNR $\lesssim 30$, for both imaging during and after cooling, see fig. 5.8(b). The $\overline{\mathrm{SNR}}$ in fig. 5.8(b) corresponds

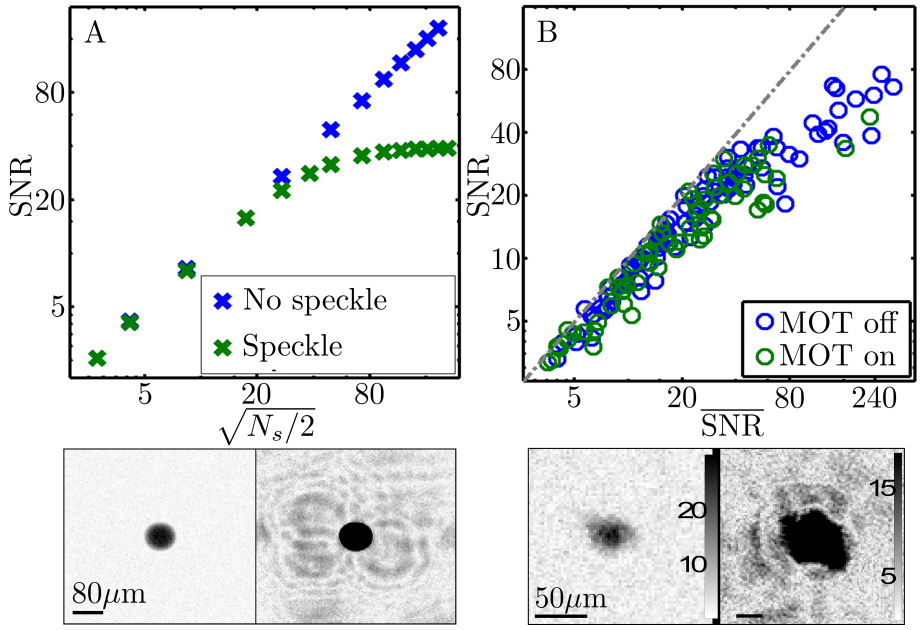

Figure 5.8: (a) SNR of the converged $|\mathbf{E}_s^{(n)}|$ from a collection of simulated phase objects versus $\sqrt{N_s/2}$, in the presence of shot-noise (blue crosses) and of both speckle and shot-noise (green crosses). (below): The converged $|\mathbf{E}_s^{n=50}|$ for a strong (right, SNR > 30) and weak (left, SNR < 30) phase object in the presence of the same speckle noise. (b) SNR versus $\overline{\text{SNR}}$ for an unbiased collection of reconstructions with the MOT on or off. (below): The converged $|\mathbf{E}_s^{n=50}|$ (mVcm^{-1}) for a large (right, SNR > 30) and a small (left, SNR < 30) atomic sample.

to the theoretical prediction of the shot-noise limited signal to noise ratio $\sqrt{N_s/2}$ in fig. 5.8(a). As with the simulated case, for SNR > 30, speckle noise is non negligible and the SNR is less than $\overline{\text{SNR}}$. The inset of fig. 5.8(b) displays the speckle noise induced blurring of $\mathbf{E}_s$ in the background, visible above the shot-noise level for a representative reconstruction with SNR > 30. Though it is noted here that the effect of speckle noise can be suppressed using a method detailed later in section 5.4.

Discussion

The results presented in this section are the first demonstration of shot-noise and diffraction limited imaging of cold atoms with holographic microscopy. Shot-noise limited imaging is needed for precision measurement and accurate determination of atom number with cold atom clouds. However shot-noise limited imaging is not always sufficient, as shot-noise limited imaging is relatively easy to achieve for a camera with a low bit depth, since the low pixel count (e.g. $N_{\text{max}} = 2^8 - 1$) means shot-noise can easily dominate other noise sources such as speckle. Imaging cold atoms with precision requires a camera with larger bit depth such as the one used in this work ($N_{\text{max}} = 2^{14} - 1$). Under such conditions shot-noise limited imaging (with $N_p \sim N_{\text{max}}$) becomes more difficult, since the shot-noise scales with $1/\sqrt{N_{\text{max}}}$ it is smaller relative to N_{max} and other noise sources such as speckle must be further reduced below this level. Furthermore, the unwanted scattering from cooling beams makes it more challenging to achieve shot-noise limited imaging while cooling. Remarkably, in this work shot-noise limited imaging was demonstrated for weak samples with a range of probe detunings, and there was no noticeable effect on the quality of images reconstructed when there was additional scattering from the MOT beams into the camera if imaging while cooling. In addition to careful placement of the camera to minimise unwanted cooling beam scatter, the subtraction optimisation procedure (section 5.1.2) developed in this work was critical for suppressing noise.

Numerical hologram generation

To compare experimental reconstruction in the presence of noise sources such as ambient and speckle noise, holograms were generated numerically. Noise sources such as speckle and/or shot-noise were simulated and added to the holograms. Twin image removal and the retrieved SNR of reconstructions in the presence of these noise sources was simulated and compared to experimental values.

The first step in the numerical generation of a hologram was to generate the effect of an object on a probing point source reference field at the object plane, and then

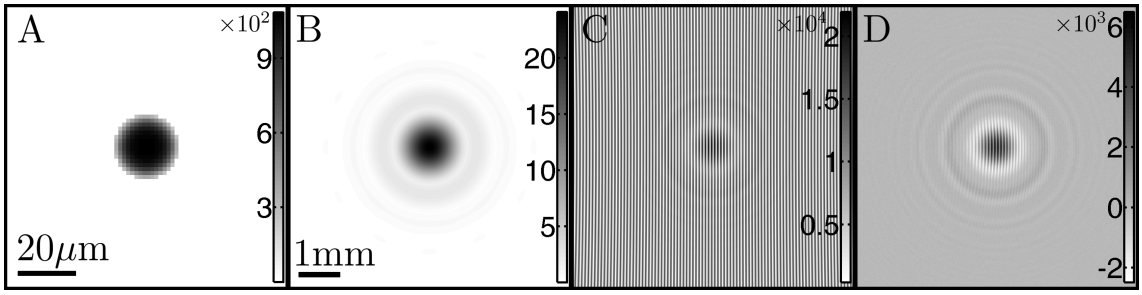

Figure 5.9: (a) Absolute value of the scattered wave electric field at the object plane $|\mathbf{E}_s(z_0)|$ (arb). (b) $|\mathbf{E}_s(L)|$ after propagation of (a) to the detection plane (arb). (c) The numerically generated hologram $H = |\mathbf{E}_r(L) + \mathbf{E}_s(L)|^2$, with simulated shot-noise added to each pixel (arb). (d) The hologram after subtraction of the reference intensity $H - H_0$ (arb).

to generate the resultant scattered wavefront at the camera plane $\mathbf{E}_s(L)$. It was assumed that the object was only probed by one of the two point sources ($\mathbf{E}_{r,1}$), and the other ($\mathbf{E}_{r,2}$) passed around the object without interacting with it. Since it was a requirement that the object be generated on a grid with finer pixel size than the hologram itself, as the microscope resolution was not limited by the pixel size of the camera (see section 3.1.2), the process for constructing $\mathbf{E}_s(L)$ was carried out on a grid with pixel size $x_{\text{pix}} < \lambda/2\text{NA}$. After extraction of $\mathbf{E}_s(L)$, it was resized to the desired hologram dimension and pixel size (e.g. to match the dimensions of a camera).

To mimic the expected position distribution of the atomic sample, the phase shift or optical depth was generated with a 2D Gaussian profile in the object plane,

$$G = A \exp\left(-\frac{(x-x_0)^2}{2\sigma_x^2} - \frac{(y-y_0)^2}{2\sigma_y^2}\right), \tag{5.3}$$

where (x_0, y_0) is the object centre (x, y) coordinate, A is an amplitude factor that for object generation was fixed to be $A = 1$, and σ_x and σ_y are the object width along the x and y dimensions respectively. The phase shift and optical depth produced by an object, which at its centre has has a peak phase shift and optical depth of $\phi_{\max}$ and $OD_{\max}$ respectively, are given respectively by $\phi(x,y) = \phi_{\max} G$ and $OD(x,y) = OD_{\max} G$. The size, aspect ratio, OD and ϕ produced by the simulated object was controlled by tuning the $\sigma_x, \sigma_y, OD_{\max}$ and $\phi_{\max}$ parameters.

With the spatial distribution of the phase shift and optical depth at the object plane $z = z_0$ known, generation of $\mathbf{E}_s(z_0)$ using eq. (2.43), requires knowledge of

$\mathbf{E}_{r,1}(z_0)$. In the point source geometry $\mathbf{E}_{r,1}(z_0)$ is simply given by eq. (3.1) with $|\mathbf{R}| = \left((x+x_1)^2 + (y+y_1)^2 + z_0^2\right)^{1/2}$, where $\mathbf{r}_1 = (x_1, y_1, 0)$ is the spatial coordinate of the $\mathbf{E}_{r,1}$ point source. The object plane scattered wavefront is displayed in fig. 5.9(a). With $\mathbf{E}_s(z_0)$ known, it can be propagated to the camera plane $z = L$ using $\hat{\mathrm{U}}(z_0 - L)$ as in eq. (3.6), thus $\mathbf{E}_s(L) = \hat{\mathrm{U}}(z_0 - L)\,\mathbf{E}_s(z_0)$, see fig. 5.9(b).

Generation of the double point source reference field $\mathbf{E}_r = \mathbf{E}_{r,1} + \mathbf{E}_{r,2}$ at the camera plane was achieved with eq. (3.1). Replacing z_0 with L in the above expression for $\mathbf{R}$ for generation of $\mathbf{E}_{r,1}$ and replacing $\mathbf{r}_1$ with $\mathbf{r}_2$, for generation of $\mathbf{E}_{r,2}$, the hologram was created using the element-wise multiplication $H = |\mathbf{E}_r(L) + \mathbf{E}_s(L)|^2$, see fig. 5.9(c), and the background was generated as $H_0 = |\mathbf{E}_r(L)|^2$. To simulate the effect of a real camera, H and H_0 was resized to the desired hologram dimension (e.g. a hologram generated with pixel size $x_{\mathrm{pix}} = 3.225$ μm can be resized to the real camera size $x_{\mathrm{pix}} = 6.45$ μm by averaging 4 neighbouring pixels into one.). The background reference intensity was subtracted away, thus revealing the interference fringes caused by the presence of $\mathbf{E}_s$, see fig. 5.9(d).

Shot-noise was numerically generated for H and H_0 by adding a random number to each pixel that followed the Poisson distribution with centre given by each pixel value. Speckle noise was added to H and H_0 by generating multiple additional point sources with random positions. These point sources were not included into the $\mathbf{E}_r$ used for reconstructing $\mathbf{E}_s(z_0)$ from H, thus mimicking the effect of real speckle noise.

5.4 Speckle noise suppression

The results presented in section 5.3.3 show that the consequence of ignoring speckle noise in the estimation of $\mathbf{E}_r$ for reconstruction results in a degradation of the dynamic range for shot-noise limited detection. To suppress the effect of speckle noise in the reconstruction of $\mathbf{E}_s$, its effect must be included into the estimation of the reference field $\mathbf{E}_r$. To achieve this, the reference intensity H_0 can itself be used as a hologram for speckle noise. The speckle field free estimation of the reference field is discussed thoroughly in section 6.1.1. In the following an iterative method of adding the speckle field to the initial $\mathbf{E}_r$ estimation is presented.

5.4.1 Algorithm

Using the estimation of the reference field $\mathbf{E}_{r,a}^{(0)} = \mathbf{E}_r(a_{1,\mathrm{opt}}, a_{2,\mathrm{opt}}, \phi_{r,\mathrm{opt}})$ (see section 6.1.1), a reference intensity $H_{0,\mathrm{ref}}^{(n)} = |\mathbf{E}_{r,a}^{(n)}|^2$ was generated for H_0. Upon subtraction $H_{\mathrm{sub}} = H_0 - H_{0,\mathrm{ref}}^{(0)}$, the double source interference fringes in the hologram

are removed as $H^{(0)}_{0,\mathrm{ref}}$ was generated from the estimation of the two point source wavefronts. The subtracted hologram $H^{(0)}_{\mathrm{sub}}$ then only contained the circular interference fringes from the point-like sources of the speckle noise. The wavefronts from all of the speckle sources were estimated by $\mathbf{E}^{(0)}_{\mathrm{sub}} = H^{0}_{\mathrm{sub}}/\mathbf{E}^{(0)*}_{r,a}$. However, the estimation $\mathbf{E}_{\mathrm{sub}}$ contained both the real and twin images of the speckle sources, which needed to be distinguished from each other.

To locate a source of speckle noise, $\mathbf{E}_{\mathrm{sub}}$ was propagated via $\hat{\mathrm{U}}\mathbf{E}_{\mathrm{sub}}$ to a range of values of z. Due to the point like nature of the speckle sources, at the focal plane of a particular speckle source, its intensity was maximized, thus making its coordinate $\mathbf{r}^{(n)}_{\mathrm{s}} = \left(x^{(n)}_s, y^{(n)}_s, z^{(n)}_s\right)$ easy to identify. Recording the coordinates of a total of n_{spot} scattering sources, masks $\hat{\mathrm{P}}^{(n)}$ were generated to isolate each source at its focal plane. Knowledge of each source coordinate $\mathbf{r}^{(n)}_{\mathrm{s}}$ allowed a one step propagation to the focal plane via $\hat{\mathrm{U}}^{(n)}_s\mathbf{E}^{(n)}_{\mathrm{sub}}$, where $\hat{\mathrm{U}}^{\pm(n)}_s = \hat{\mathrm{U}}\left(\pm\left(L - z^{(n)}_s\right)\right)$. The speckle source wavefront was isolated and propagated back to the camera plane with the $\hat{\mathrm{U}}^{-1(n)}_s\hat{\mathrm{P}}^{(n)}\hat{\mathrm{U}}^{(n)}_s\mathbf{E}^{(n)}_{\mathrm{sub}}$ operation (see algorithm 1, step 9), where it was added to the estimation of the reference field $\mathbf{E}^{(n)}_{r,a}$. Similar to the extraction of $\mathbf{E}_r\left(a_{1,\mathrm{opt}}, a_{2,\mathrm{opt}}, \phi_{r,\mathrm{opt}}\right)$ in section 6.1.1, inclusion of the speckle field could be optimised by minimising the difference $|H_0 - |\mathbf{E}^{(n)}_{r,a}|^2|$ with two amplitude parameters for the speckle field and $\mathbf{E}^{(0)}_{r,a}$ respectively and a phase parameter for the speckle field.

To identify whether or not the extracted speckle wavefront was a real image and not a random fluctuation in $\mathbf{E}^{(n)}_{\mathrm{sub}}$, an updated estimation $\mathbf{E}^{(n)}_{r,b} = \sqrt{H_0}\mathrm{e}^{\mathrm{i}\arg\left(\mathbf{E}^{(n)}_{r,a}\right)}$ (with knowledge of the amplitude from H_0) was used to reconstruct an image of the atomic sample using H and eqs. (3.3) and (3.6) (see algorithm 1, steps 10 and 11). As ignorance of speckle noise distorts the atomic wavefront ($\mathbf{E}_s$) and adds noise to the background, inclusion of a real speckle noise wavefront into $\mathbf{E}^{(n)}_{r,b}$ was expected to reduce the background noise level $\delta\mathbf{E}^{(n)}_{s,\mathrm{meas}}$ (see algorithm 1, step 12). Inclusion of a twin image of a speckle source should not reduce the background noise level. With this condition in mind, a decision was made to include the extracted speckle wavefront (see algorithm 1, step 13). If the extracted speckle wavefront caused an increase to the background noise level, an attempt was made instead to add its complex conjugate to the reference field using the conjugation operator $\hat{\mathrm{C}}\mathbf{E} = \mathbf{E}^*\mathbf{E}_r/\mathbf{E}^*_r$ (see algorithm 1, steps 14 to 20). If both attempts failed to reduce the background noise level, the source of speckle was regarded as a random noise fluctuation and was ignored it in the estimation of the reference field and it was

Algorithm 1 Speckle field addition to $\mathbf{E}_r$

Require: $\mathbf{r}_s^{(n)} = \left(x_s^{(n)}, y_s^{(n)}, z_s^{(n)}\right)$, an array of n_{spots} speckle coordinates.
$\mathbf{E}_{r,a}^{(0)} = \mathbf{E}_r\left(a_{1,\text{opt}}, a_{2,\text{opt}}, \phi_{r,\text{opt}}\right)$, Reference estimation (section 6.1.1)
$\hat{\mathrm{U}}_s^{(n)} = \hat{\mathrm{U}}\left(L - z_s^{(n)}\right)$, Propagation operator.

$n = 0$
$H_{0,\text{ref}} = |\mathbf{E}_{r,a}^{(n)}|^2$
$\mathbf{E}_{\text{sub}}^{(n)} = \left(H_0 - H_{0,\text{ref}}\right)/\mathbf{E}_{r,a}^{(n)*}$
$\mathbf{E}_{r,b}^{(n)} = \sqrt{H_0}\mathrm{e}^{\,\mathrm{i}\arg\left(\mathbf{E}_{r,a}^{(n)}\right)}$
$\mathbf{E}_s^{(n)} = \hat{\mathrm{U}}_0\left(\left(H - H_0\right)/\mathbf{E}_{r,b}^{(n)*}\right)$
$\delta\mathbf{E}_{s,\text{meas}}^{(n)} = \sqrt{\left\langle |\mathbf{E}_s^{(n)}|^2 \right\rangle_D}$ determine the background noise level, see eq. (5.2).
$n = n + 1$
while $n \leq n_{\text{spots}}$ **do**
    $\mathbf{E}_{r,a}^{(n)} = \mathbf{E}_{r,a}^{(n-1)} + \hat{\mathrm{U}}_s^{-(n)}\hat{\mathrm{P}}^{(n)}\hat{\mathrm{U}}_s^{(n)}\mathbf{E}_{\text{sub}}^{(n)}$
    $\mathbf{E}_{r,b}^{(n)} = \sqrt{H_0}\mathrm{e}^{\,\mathrm{i}\arg\left(\mathbf{E}_{r,a}^{(n)}\right)}$
    $\mathbf{E}_s^{(n)} = \hat{\mathrm{U}}_0\left(\left(H - H_0\right)/\mathbf{E}_{r,b}^{(n)*}\right)$
    $\delta\mathbf{E}_{s,\text{meas}}^{(n)} = \sqrt{\left\langle |\mathbf{E}_s^{(n)}|^2 \right\rangle_D}$
    if $\delta\mathbf{E}_{s,\text{meas}}^{(n)} \leq \delta\mathbf{E}_{s,\text{meas}}^{(n-1)}$ **then**
    else
        $\mathbf{E}_{r,a}^{(n)} = \mathbf{E}_{r,a}^{(n-1)} + \hat{\mathrm{C}}\hat{\mathrm{U}}_s^{-(n)}\hat{\mathrm{P}}^{(n)}\hat{\mathrm{U}}_s^{(n)}\mathbf{E}_{\text{sub}}^{(n)}$
        $\mathbf{E}_{r,b}^{(n)} = \sqrt{H_0}\mathrm{e}^{\,\mathrm{i}\arg\left(\mathbf{E}_{r,a}^{(n)}\right)}$
        $\mathbf{E}_s^{(n)} = \hat{\mathrm{U}}_0\left(\left(H - H_0\right)/\mathbf{E}_{r,b}^{(n)*}\right)$
        $\delta\mathbf{E}_{s,\text{meas}}^{(n)} = \sqrt{\left\langle |\mathbf{E}_s^{(n)}|^2 \right\rangle_D}$
        if $\delta\mathbf{E}_{s,\text{meas}}^{(n)} \leq \delta\mathbf{E}_{s,\text{meas}}^{(n-1)}$ **then**
        else
            $\mathbf{E}_{r,a}^{(n)} = \mathbf{E}_{r,a}^{(n-1)}$
        end if
    end if
    $\mathbf{E}_{\text{sub}}^{(n+1)} = \hat{\mathrm{U}}_s^{-(n)}\left(\hat{\mathrm{U}}_s^{(n)}\mathbf{E}_{\text{sub}}^{(n)} - \hat{\mathrm{P}}^{(n)}\hat{\mathrm{U}}_s^{(n)}\mathbf{E}_{\text{sub}}^{(n)}\right)$
    $n = n + 1$
end while
$\mathbf{E}_{r,\text{final}} = \sqrt{H_0}\mathrm{e}^{\,\mathrm{i}\arg\left(\mathbf{E}_{r,a}^{(n_{\text{spots}})}\right)}$
return $\mathbf{E}_{r,\text{final}}$

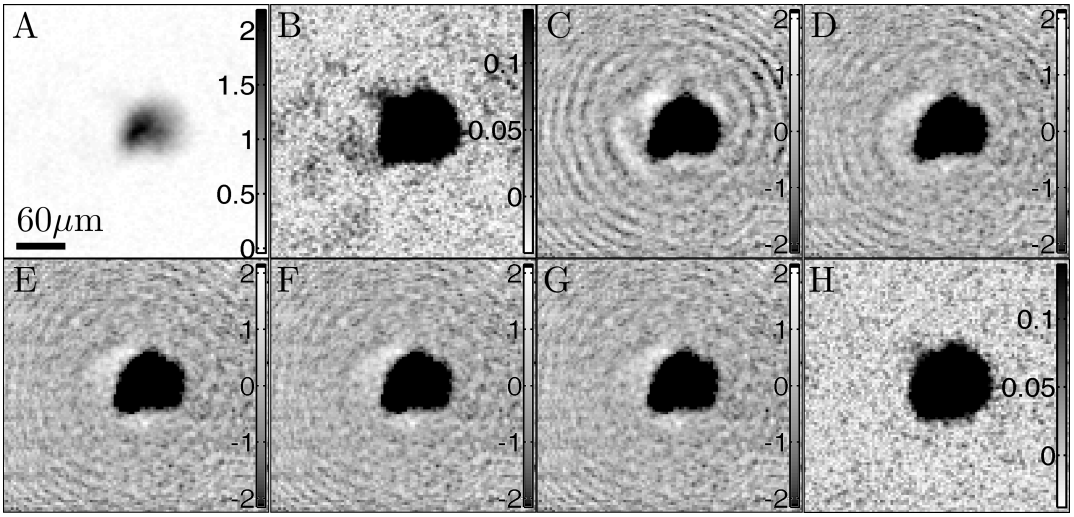

Figure 5.10: A collection of ρ_c (μm^{-2}) and α_f (%) images with [$\nu = 0$, $\tau_{\text{exp}} = 100$ μs], reconstructed from the same hologram with varying numbers of speckle sources included into the estimated $\mathbf{E}_r$. (a) ρ_c image with no speckle sources included in the reference field estimation. (b) Same as (a) but scale changed to display the noise. (c) Same as (b) but showing α_f.
D) α_f with 5 speckle sources. (e) α_f with 20 speckle sources. (f) α_f with 22 speckle sources. (g) α_f with 30 speckle sources. (h) Same as (g) but displaying ρ_c.

removed from $\mathbf{E}_{\text{sub}}$ (see algorithm 1 steps 21 to 24). This process is summarised in algorithm 1, where its output $\mathbf{E}_{r,\text{final}}$ was then used for reconstruction of $\mathbf{E}_s$.

5.4.2 Improved dynamic range

In fig. 5.10, images are displayed showing a reconstruction with no inclusion of speckle noise sources along side reconstructions from the same hologram with the addition of differing numbers of speckle sources into the reference field. Although the initial reconstruction has SNR ≈ 35.7, the noise level is $1.36\delta\mathbf{E}_{s,\text{exp}}$ (see section 5.3.2), because of the spreading of $\mathbf{E}_s$ due to the speckle noise, an effect visible in the background of fig. 5.10(b). When observing a fractional absorption (α_f) or phase shift (ϕ) image, the speckle induced spreading of $\mathbf{E}_s$ manifests its self as a ring structure, see fig. 5.10(c-g), because of the interference of the speckle noise with the spherical reference field. As the noise is easier to visualise in α_f images when compared with ρ_c images, fig. 5.10(b), because of the ring structure, α_f images are used to illustrate the effect of including speckle sources into the reference field. The noise level, initially $\delta\mathbf{E}_{s,\text{meas}} = 1.36\delta\mathbf{E}_{s,\text{exp}}$ is shown to decrease to $\delta\mathbf{E}_{s,\text{meas}} = 1.22\delta\mathbf{E}_{s,\text{exp}}$, $\delta\mathbf{E}_{s,\text{meas}} = 1.19\delta\mathbf{E}_{s,\text{exp}}$, $\delta\mathbf{E}_{s,\text{meas}} = 1.172\delta\mathbf{E}_{s,\text{exp}}$ and $\delta\mathbf{E}_{s,\text{meas}} = 1.168\delta\mathbf{E}_{s,\text{exp}}$ with the

inclusion of 5, 20, 22 and 30 sources of speckle noise respectively. The SNR of these reconstructions changes from SNR= 35.7 to SNR= 39.6, SNR= 40.6, SNR= 40.9 and SNR= 40.7. Here speckle sources were addressed in ascending order of intensity, thus addition of the first sources, see fig. 5.10(c-d), had a larger effect on the background noise level than those added later, see fig. 5.10(f-g). After the addition of 30 speckle sources, the speckle noise was hardly visible in the ρ_c image, fig. 5.10(h).

Whilst $\delta\mathbf{E}_{s,\text{meas}}$ monotonically decreased with addition of speckle sources, the measured SNR did not, see fig. 5.10. The addition of speckle removes noise from the background. The energy from the removed noise is instead converted into the atomic wavefront $\mathbf{E}_s$. As the addition of the field is not necessarily constructive, it can result in a decrease in the measured signal, as observed in the SNR changing from SNR = 40.9 to SNR = 40.7 between the addition of 22 and 30 speckle sources respectively.

Discussion

This development reduces what is the largest difficulty associated with using holography for imaging cold atoms after that of the twin and DC image problems. The reduction in the speckle noise for optically thick atomic samples comes at the expense of an increase in reconstruction time compared to that of twin image removal via eq. (3.27). Numerous additional 2D fast Fourier transforms are required during the propagation to locate speckle sources and include them into the reference field. Reconstruction with the inclusion of ~ 10 speckle sources was completed on a time scale of ~ 1 hour. The reconstruction speed can be improved by processing reconstructions using a GPU. For a single $\hat{\mathrm{U}}_0$ propagation operation (see section 3.2) on a wavefront ($\mathbf{E}$) divided onto 5200×5200 pixels, a factor of 2.6 decrease in processing time from 3.5 s to 1.35 s was observed when comparing CPU (Intel Xenon CPU, E5-2603 0 @ 1.8GHz, 2 processors) to GPU (NVIDIA Tesla C2705) reconstructions respectively. The speckle suppression developed in this work involves reconstruction of the full complex speckle field, thus it should be more accurate and robust when applied to holographic recordings when compared to the speckle suppression technique developed for absorption imaging [186].

Speckle noise is expected to display a larger degradation of image quality for a spatially confined and optically dense sample such as a BEC, since the increased diffraction from such objects makes the strong $\mathbf{E}_s$ fill the entire camera and it can be distorted by more speckle fringes. The development of a method of reducing the speckle noise (see section 5.4), by inclusion of the wavefronts from speckle sources

into the estimation of $\mathbf{E}_r$ is particularly helpful for shot-noise limited imaging of small and optically dense atomic samples such as a BEC.

5.5 Conclusions

By removing the twin and DC image noise, DSHM with iterative twin image removal simultaneously eliminates two of the major obstacles to the application of in-line holography for imaging cold atoms. No noise penalty caused the iteration was observable in the reconstructed images, since as is shown in section 3.2.3 it is expected to be negligible except when both $a/z_0 \gg \mathrm{NA}$ and $\eta \ll 1$. The removal convergence speed in DSHM is faster than that in DIHM, and DSHM can reconstruct extended objects with $N_f \ll 1$ where DIHM fails.

A pre-requisite for a precise imaging technique for cold atoms is that it displays shot-noise limited sensitivity coupled with diffraction limited resolution. This work is the first realisation of shot-noise limited in-line holographic microscopy for cold atoms. This is an impressive result considering that a 14-bit CCD with $N_p \sim N_{\max} = 2^{14} - 1$ is used with the shot-noise level less than 1 %. In addition to the optimised subtraction of background noise, reaching the shot-noise limit was aided by experimental procedures including tilting the probe and CCD with respect to vacuum window to minimise stray reflections (see section 4.4.1) and recording images of the ambient light background for optimal subtraction (see section 5.1.2).

In developing a speckle removal algorithm another major obstacle to in-line holographic microscopy for cold atoms is lifted. In this work with the atoms located in a glass cell with no anti-reflection coating, the dynamic range for shot-noise limited detection was limited to SNR ≈ 35, see figs. 5.8 and 5.10, without speckle noise suppression. With use of the speckle noise suppression, the dynamic range for detection was enhanced to SNR ≈ 41, see fig. 5.10, and the reconstruction quality was comparable to standard focal plane coherent imaging (see section 2.3.2).

The results presented in this chapter could provide the key to opening the door to applying in-line holography to cold atoms, since the major obstacles to its application have been addressed. The major downfall is limited to a modest increase in image reconstruction time, that arises as a result of alleviating the twin, DC and speckle noise problems to reach the shot-noise limit. It is pointed out that the reconstruction time can be improved with more efficient GPU coding.

With a method of determining the reference wavefront at the object plane $\mathbf{E}_r(z_0)$, as is shown in chapter 6, DSHM can be implemented for precise quantitative measure-

ments of cold atoms optical properties. Since the microscope records the point source interference with the out-of-focus diffraction of $\mathbf{E}_s$, the intensity at the recording plane is less than at the object plane. This means that a larger intensity is permitted at the detector, thus more scattering can be collected from the sample for more precise phase shift and absorption retrieval when compared to phase-contrast and absorption imaging, as is shown in chapter 6.

Chapter 6

Precision phase and absorption imaging with holography

Analysis of the resolution and noise in DSHM reconstructions, as in chapter 5, can be conducted entirely with the extracted coherent scattering from the atoms $\mathbf{E}_s$. To connect $\mathbf{E}_s$ with the optical properties of the sample, the probe light is typically assumed to have a uniform intensity so that a dark field image ($|\mathbf{E}_s|^2$) can provide spatial information on the atomic density distribution. Alternatively, if the probing wavefront is a uniform plane wave, then the phase of the transmitted wavefront, $\arg(1 + \mathbf{E}_s/\mathbf{E}_s)$ [26, 109, 114], can be plotted which is equal to the probe light phase shift. The latter technique is common place in biological imaging [26–28, 187]. To the authors knowledge, a method of simultaneously retrieving the probe attenuation and phase shift with the more complex spherical wave illumination is yet to be developed. Such a technique is essential for quantitative analysis in cold atom experiments, see eqs. (6.1) and (6.2).

Precision measurements of ϕ and OD rely on precise knowledge of $\mathbf{E}_r(z_0)$ at the location of the atoms. In this chapter, a method to estimate $\mathbf{E}_r(z_0)$ is discussed, which is consistent with the $\mathbf{E}_r(L)$ estimation to holographically retrieve the complex $\mathbf{E}_s$. Using the estimate of the image plane reference field, precise ϕ and OD measurements with cold atom samples using a near-resonant probe are made. In particular, the detuning dependence of ϕ and OD was measured across an atomic resonance, both in absence and in presence of the dressing MOT lasers. The agreement between the measured detuning dependence of ϕ and OD confirmed the validity of the proposed retrieval.

Shot-noise limited ϕ and OD sensitivities of $\delta\phi = (1.8 \pm 0.17)$ mrad and $\delta\alpha_f = (0.36 \pm 0.034)$ % were consistently demonstrated. Such sensitivity levels are beyond the shot-noise limited values in absorption or phase-contrast imaging by a factor of 8 in this particular experiment, provided that an identical camera is used with magnification of one. This is due to an important, but somewhat overlooked advantage in holographic microscopy. The point-source geometry permits optimal collection of the high spatial frequency interference using the entire CCD chip, thus allowing sensitive phase shift and absorption measurements. The idea relies on the spherical wave illumination geometry, where the probe light intensity at the camera plane can be far less than at the atoms location. The reduction in probe intensity from the atom to camera planes means that for a given probe intensity at the atoms location, a much longer exposure time is permitted for the camera before pixel saturation. Similarly if $s \ll 1$, for a given exposure time the probe intensity can be greatly increased to improve the collection coherent scattered photons from the sample. Such long exposure times result in enhanced phase shift and absorption sensitivities when compared with in-focus coherent imaging methods such as absorption or phase-contrast imaging, see section 2.3.2. Here this holographic enhancement is quantified with a numerical factor $\kappa = |\mathbf{E}_r(z_0)/\mathbf{E}_r(L)|^2$. The implication of the holographic enhancement of sensitivity for precise imaging of cold atoms with off-resonant light is discussed.

6.1 From holography to phase shift/absorption imaging

In a typical point source in-line holographic microscope [26–28], extraction of an approximate $\mathbf{E}_s$ at the camera plane is easy, since a basic estimation of $\mathbf{E}_r(L)$ as a spherical wave with an amplitude given by $\sqrt{H_0}$ is sufficient to observe an image. As was demonstrated in chapter 5, the dual source reference field in DSHM aids in the removal of the twin image noise. However, precision extraction of $\mathbf{E}_s$ in DSHM requires more careful estimation of the reference field, since the double source field is more complex. In section 6.1.1, this issue is addressed with the development of a procedure for estimation of $\mathbf{E}_r(L)$, which is then used to estimate $\mathbf{E}_s(L)$ using eq. (3.15). The developed method of including an additional source is similar to the speckle noise addition algorithm discussed in section 5.4, which was utilised to increase the dynamic range of holographic detection. By comparing the double point source interference pattern with the pre-measured source separation, an accurate

calibration of the source camera separation L was made for accurate estimation of the reference field. To reduce the increase in reconstruction computation time, a GPU is utilised.

Knowledge of the reference field at the atomic location is necessary for extraction of probes phase shift and absorption due to interaction with the sample. In the more complex spherical wave geometry, it is not sufficient to assume a uniform plane wave for the reference field. To maintain consistency in the estimations of $\mathbf{E}_s(z_0)$ and $\mathbf{E}_r(z_0)$, the estimate of $\mathbf{E}_r(L)$ that was used to extract $\mathbf{E}_s(L)$ was propagated to the sample plane as was done to determine $\mathbf{E}_s(z_0)$, thus giving an estimate of $\mathbf{E}_r(z_0)$. With an estimation of $\mathbf{E}_r(z_0)$ and $\mathbf{E}_s(z_0)$, it is easy to extract the probe phase shift and attenuation. Finally, it is mathematically shown that the phase shift and absorption sensitivities in DSHM display holographic enhancement over coherent focal plane imaging thanks to the microscope geometry.

6.1.1 Estimating the reference field at the camera and image planes

The first process in the reconstruction of $\mathbf{E}_s$ from H is to use information about the microscope geometry and the location of the $\mathbf{E}_{r,1}$ point source location to generate an estimate of the total reference field $\mathbf{E}_r$. Once $\mathbf{E}_r$ is known, an estimate of $\mathbf{E}_s$ is extracted using eq. (3.15), and it can be propagated to the focal plane using the propagation operator $\hat{\mathrm{U}}_0$ (see section 3.1.2). To aid in estimation of the full $\mathbf{E}_r$, the $\mathbf{E}_2$ and $\mathbf{E}_1$ sources were removed to record the $H_1 = |\mathbf{E}_1|^2$ and $H_2 = |\mathbf{E}_2|^2$ intensity patterns respectively (see section 5.1.1). This technique was also employed to extract the images presented in chapter 5, but detailed discussion is deferred to this chapter.

To estimate $\mathbf{E}_r$, only the phase of the reference $\phi_{\mathrm{ref}} = \arg(\mathbf{E}_r)$ needed to be estimated, since its amplitude is already given by $|\mathbf{E}_r| = \sqrt{H_0}$, the estimation was $\mathbf{E}_r = \sqrt{H_0}\mathrm{e}^{\mathrm{i}\phi_{\mathrm{ref}}}$. It was assumed that the $\mathbf{E}_{r,j}$ $(j = 1, 2)$ wavefronts at the camera plane originate from point sources located at $\mathbf{r}_j$, and were well approximated by spherical waves $\mathbf{E}_{r,j} \propto \sqrt{H_j}\mathrm{e}^{ik|\mathbf{R}-\mathbf{r}_j|}$, with $\mathbf{R} = (x, y, L)$. Prior to installation of the microscope, the two point sources were measured to have the same z coordinate. For this discussion it is assumed that the corresponding ambient light had been directly subtracted away from each recorded image ($H_0 = H_0 - bk_2$, $H_1 = H_1 - bk_1$ and $H_2 = H_2 - bk_2$) without optimisation of its subtraction.

To extract $\mathbf{E}_{r,1}$, the H_1 intensity profile was centred to the camera, so that it could be fitted with a 2D Gaussian function $H_{1,f}$ with $x_0 = y_0 = 0$. With prior

knowledge of the microscope geometry, an estimate of L was used to generate an estimate of $\mathbf{E}_{r,1}$.

Propagation of $\mathbf{E} = H_0/\mathbf{E}^*_{r,1}$ to the point source focal plane ($z = 0$) using $\hat{\mathrm{U}}\,(L)\,\mathbf{E}$, revealed an image of three points in a line sequentially separated by $|\mathbf{r}_2 - \mathbf{r}_1| = d$ (a value of $d = (387 \pm 2.6)$ μm, was measured with a CCD camera with $x_{pix} = 5.2$ μm before installation for the NA= 0.07 microscope (see section 4.4.2). For the higher NA= 0.16 microscope (see section 4.4.3) $d = (229 \pm 2.6)$ μm was measured.). The centre point source corresponds to the $\mathbf{r}_1$ position, and the other two correspond to the $\mathbf{r}_2$ location, and the location of the focal point of the twin image $\mathbf{E}^*_{r,2}$ at $-\mathbf{r}_2$. With prior knowledge of the orientation of $\mathbf{E}_{r,1}$ and $\mathbf{E}_{r,2}$ with respect to the camera, it was easy to identify which was the real image $\mathbf{E}_{r,2}$. The measurement of d in this reconstruction was calibrated to the pre-measured value by proper choice of L in $\mathbf{E}_{r,1}$.

With the acquired knowledge of L and d providing an estimate of the relative phase ϕ_r between $\mathbf{E}_{r,1}$ and $\mathbf{E}_{r,2}$, and the 2D fit of the H_2 intensity $H_{2,f}$, the total reference field was estimated as $\mathbf{E}_r\,(a_1, a_2, \phi_r) = a_1\sqrt{H_{1,f}}\mathrm{e}^{ik|\mathbf{R}-\mathbf{r}_1|} + a_2\sqrt{H_{2,f}}\mathrm{e}^{ik|\mathbf{R}-\mathbf{r}_2|+\mathrm{i}\phi_r}$. To optimise the estimation, $|H_0 - |\mathbf{E}_r\,(a_1, a_2, \phi_r)\,|^2|$ was minimised to give the improved reference field $\mathbf{E}_r\,(a_{1,\mathrm{opt}}, a_{2,\mathrm{opt}}, \phi_{r,\mathrm{opt}})$. To create the optimum reference field, the phase estimation was extracted as $\phi_{1,2} = \arg\left(\mathbf{E}_r\,(a_{1,\mathrm{opt}}, a_{2,\mathrm{opt}}, \phi_{r,\mathrm{opt}})\right)$ and was used in the final estimation that was used for image reconstruction $\mathbf{E}_r\,(L) = \sqrt{H_0}\mathrm{e}^{\mathrm{i}\phi_{\mathrm{ref}}} \approx \sqrt{H_0}\mathrm{e}^{\mathrm{i}\phi_{1,2}}$.

For extraction of the probe phase shift ϕ and fractional absorption α_f using eqs. (3.32) and (3.33), with the assumption that the atoms are only probed by the $\mathbf{E}_{r,1}$ field, the probing field at the focal plane $\mathbf{E}_{r,1}\,(z_0)$ was extracted by propagating the estimation of $\mathbf{E}_{r,1}\,(L)$ to the focal plane via $\mathbf{E}_{r,1}\,(z_0) = \hat{\mathrm{U}}_0\mathbf{E}_{r,1}\,(L)$. To avoid FFT boundary artefacts, the fitted $\mathbf{E}_{r,1}\,(L) \approx \sqrt{H_{1,f}}\mathrm{e}^{\mathrm{i}k|\mathbf{R}-\mathbf{r}_1|}$ was generated on a larger grid, thus it was well contained within. Then after numerical propagation of $\mathbf{E}_{r,1}\,(L)$ to the atom focal plane, it was resized to match the dimension of $\mathbf{E}_s\,(z_0)$. In the results presented in this chapter, the estimation of $\mathbf{E}_{r,1}$ does not include the effect of speckle noise. To include the speckle noise into $\mathbf{E}_{r,1}\,(z_0)$, the speckles generated between the atoms and the camera need to be isolated and included into the reference field estimation. Such a demonstration is not presented in this work, and is left as a topic for future study.

6.1.2 Holographically enhanced sensitivity

For further comparison of DSHM with in-focus coherent imaging methods such as absorption and phase-contrast imaging, it is instructive to analyse the sensitivity to optical depth and phase shift. A key difference between holographic microscopy and the in-focus techniques (see section 2.3.2) is that holograms can be recorded far from the image focal plane $L \ll z_0$, where the probe intensity can be significantly weaker which has important consequences for the sensitivity.

Extracting the optical depth and phase shift requires knowledge of the reference field $\mathbf{E}_r(z_0)$, as presented in section 6.1.1. As shown in section 3.2.4, but repeated here for convenience, using this estimation of $\mathbf{E}_r$ the sample plane optical depth and phase shift are respectively

$$OD = 2\mathrm{Re}\left[\ln\left(1+\frac{\mathbf{E}_s}{\mathbf{E}_r}\right)\right], \tag{6.1}$$

$$\phi = \mathrm{Im}\left[\ln\left(1+\frac{\mathbf{E}_s}{\mathbf{E}_r}\right)\right]. \tag{6.2}$$

However, here the fractional absorption $\alpha_f = |1+\mathbf{E}_s/\mathbf{E}_r|^2 - 1 \approx -OD$ is used to represent the OD for samples with $OD \ll 1$. Then the absorption sensitivity $\delta\alpha_f \approx \delta OD$.

To derive the shot-noise limited sensitivities, for simplicity DSHM with $\eta \ll 1$ is considered such that $\sqrt{1-\xi^2} \approx 1$ and there is negligible noise increase from twin image removal (see section 3.2.3). Standard cameras have a maximum pixel count $N_{\max}$, at which point pixels become saturated and information is lost from the image. To avoid this, a condition $|\mathbf{E}_r(L)|^2 A_p Q \tau_{\exp}/\hbar\omega \leq N_{\max}$, is imposed on the intensity of the probe beam, which simply means that the number of photons detected by a pixel from the probe cannot exceed the bit depth of the camera. Using this condition and eq. (3.23), it is easy to show that

$$\mathrm{SNR} \leq \sqrt{\frac{|\mathbf{E}_s(z_0)|^2 N_{\max} A_r}{2|\mathbf{E}_r(L)|^2 A_p}}. \tag{6.3}$$

With the probe intensity at the camera plane ($z = L$) differing from that at $z = z_0$ by $|\mathbf{E}_r(L)|^2 = \kappa|\mathbf{E}_r(z_0)|^2$, and considering the limit where SNR$= 1$, it can be shown that $|\mathbf{E}_s(z_0)/\mathbf{E}_r(z_0)| > \sqrt{2\kappa A_p/N_{\max}A_r}$. Then, considering that holographic techniques are sensitive to the full phase shift and half of the optical depth, see

eq. (2.43), the following expressions can be derived

$$\delta\phi = \sqrt{\frac{2\kappa A_p}{N_{\max} A_r}}, \tag{6.4}$$

$$\delta OD = \sqrt{\frac{8\kappa A_p}{N_{\max} A_r}}, \tag{6.5}$$

for the phase shift and optical depth sensitivities respectively. In comparison with phase-contrast and absorption imaging with a magnification of one, effectively $\kappa = 1$ and the sensitivities differ by a factor of $\sqrt{4\kappa}$. In double point source holography with $L \gg z_0$, the intensity at the camera plane can be much smaller than that at the image focal plane, thus $\kappa \ll 1$ and the sensitivity in holography can be much smaller than that of both absorption and phase-contrast imaging. This holographic enhancement of the imaging sensitivity could be exploited for precision detection of weakly phase shifting/absorbing samples such as single atoms.

6.2 Measuring phase shift and absorption

In this section, shot-noise limited retrievals of ϕ and α_f with holographically enhanced sensitivity beyond the sensitivity of regular imaging techniques are demonstrated. By taking advantage of the extracted wavefront at the image focal plane, phase shift and fractional absorption images was obtained. Reconstructed ϕ and α_f images are presented from both the NA = 0.07 and NA = 0.16 versions of DSHM. It is demonstrated that thanks to the factor of $\sqrt{4\kappa}$ holographic enhancement, the absorption and phase shift reconstructions in DSHM display a sensitivity greater than those expected in absorption and phase-contrast imaging by a factor of 8 with NA = 0.16 DSHM. Imaging with the MOT beams on and off, the light shift experienced by the atoms when cooling is inferred (see section 6.3). Furthermore, by varying the probe detuning across the atomic resonance frequency, the detuning dependence of the phase shift and absorption during and after cooling is measured.

6.2.1 Shot-noise limited absorption and phase shift images of cold atoms

To demonstrate holographic enhancement of the imaging sensitivity, characteristic fractional absorption α_f (%) and phase shift ϕ (mrad) images (for SNR $\lesssim$ 30), extracted using the estimation of $\mathbf{E}_{r,1}(z_0)$ (see section 6.1.1) and eqs. (3.32) and (3.33), are displayed in fig. 6.1. With shot-noise limited double point source holographic microscopy, the RMS background noise level was consistently $\delta\phi = (1.8 \pm 0.17)$ mrad

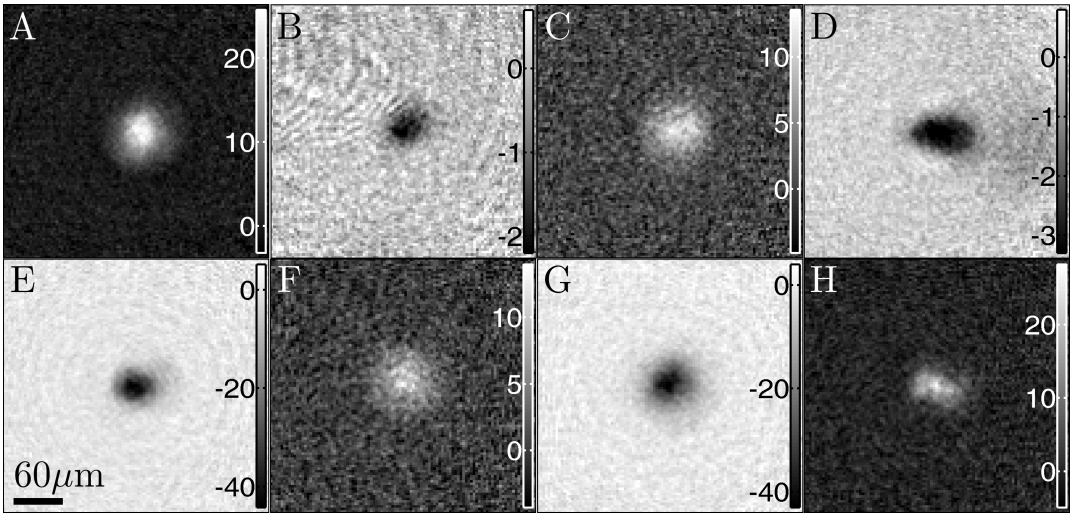

Figure 6.1: Characteristic absorption (α_f, displayed in %) and phase shift (ϕ, mrad) images recorded with NA = 0.07 DSHM. (a) [$\nu = -7$, $\tau_{\text{exp}} = 800$ μs]: ϕ. (b) [$\nu = 0$, $\tau_{\text{exp}} = 800$ μs]: α_f. (c) [$\nu = -7$, $\tau_{\text{exp}} = 400$ μs]: ϕ. (d) [$\nu = 0$, $\tau_{\text{exp}} = 800$ μs]: α_f. (e) [$\nu = 29$, $\tau_{\text{exp}} = 800$ μs]: ϕ. (f) [$\nu = -7$, $\tau_{\text{exp}} = 800$ μs]: ϕ. (g) [$\nu = 29$, $\tau_{\text{exp}} = 100$ μs]: ϕ. (h) [$\nu = -7$, $\tau_{\text{exp}} = 400$ μs]: ϕ, during cooling.

and $\delta\alpha_f = (0.36 \pm 0.034)$ %. Such sensitivity levels were achieved with various values of exposure time τ_{exp} and detuning ν, and even when imaging while cooling, see fig. 6.1(h). As expected from fig. 2.4, for $\text{sgn}(\nu) = \pm 1 \rightarrow \text{sgn}(\phi) = \mp 1$ and $\text{sgn}(\alpha_f) = -1$, see fig. 6.1. The ability to image reliably at negative detuning, see fig. 6.1(a,c,f,h), overcomes previous difficulties with DCI (section 2.3.3). The absorption and phase shift sensitivities in holographic imaging differ from those in standard imaging by $\sqrt{4\kappa}$. With $\kappa \approx 0.01$ here, the expected sensitivities in standard phase-contrast and absorption imaging with similar mean camera counts N_p, an identical camera with magnification of one, and without frame binning or pixel saturation, are $\delta\alpha_f \approx 2$ % and $\delta\phi \approx 10$ mrad. In recording these images with DSHM, see fig. 6.1, $N_p < N_{\text{max}}$, the first reason was to avoid pixel saturation, the second was that a non-zero value of η resulted in an intensity modulation at the camera. Incredibly the sensitivities achieved in DSHM with $N_p < N_{\text{max}}$ are better than those expected in absorption or phase-contrast imaging with $N_p = N_{\text{max}}$ ($\delta\alpha_f = 1.4$ % and $\delta\phi = 7$ mrad respectively.).

To achieve shot-noise limited imaging with the improved NA = 0.16 DSHM, a 1 mm diameter aperture was placed around the image of the point sources, thus minimising ambient light and stray reflections between the camera surface and

Figure 6.2: Absorption (α_f, %) and phase shift (ϕ, mrad) images. (a) [$\nu = -1.45$, $\tau_{\text{exp}} = 500$ μs]: α_f image. (b) ϕ image from the same hologram as (a). (c) [$\nu = 1.26$, $\tau_{\text{exp}} = 500$ μs]: α_f image. (d) ϕ image from the same hologram as (c). (e) [$\nu = -6.93$, $\tau_{\text{exp}} = 500$ μs]: ϕ image. (f) [$\nu = 6.46$, $\tau_{\text{exp}} = 500$ μs]: α_f image. (g) ϕ image from the same hologram as (f). (h) [$\nu = 0$, $\tau_{\text{exp}} = 500$ μs]: α_f image. (i) ϕ image from the same hologram as (h). (j) [$\nu = 7.75$, $\tau_{\text{exp}} = 500$ μs]: ϕ image.

the lenses. This combined with the optimised subtraction procedure discussed in section 5.1.2 allowed imaging to consistently approach the shot-noise limit, provided there was no interference fringe shift between recording of H and H_0.

To demonstrate sensitivity approaching the shot-noise limited value with the modified DSHM, shot-noise limited α_f and ϕ images with $\tau_{\text{exp}} = 500$ μs are displayed in fig. 6.2. The absence of a ring structure as observed in the α_f images displayed in fig. 5.10, indicated that the effect of speckle noise was below the shot-noise level.

To demonstrate imaging where there was positive ϕ and a detectable α_f, α_f and ϕ images of a sample probed with $\nu = -1.45$ are displayed In fig. 6.2(a,b) respectively. A similar scenario but with negative ϕ is shown for a sample probed with $\nu = 1.26$ is displayed in fig. 6.2(c,d). As expected, the sign of the α_f signal did not change between image fig. 6.2(a) and image fig. 6.2(c), while the sign of the corresponding (fig. 6.2(b) and fig. 6.2(d)) ϕ images did.

To show imaging with large detuning at either side of the atomic resonance, ϕ images from a sample of $N \sim 10^3$ atoms are displayed in fig. 6.2(e,j) with $\nu = -6.93$ and $\nu = 7.75$ respectively. A situation where the α_f signal was below the noise level whilst the ϕ signal was detectable is demonstrated in fig. 6.2(f,g) respectively. In fig. 6.2(h,i), the reverse is displayed by probing the atomic sample with $\nu = 0$, thus the α_f is detectable whilst ϕ is not. Shot-noise limited absorption and phase shift sensitivities of $\delta\alpha_f = (3.6 \pm 0.026)$ % and $\delta\phi = (1.8 \pm 0.13)$ mrad were consistently demonstrated, see fig. 6.2(a,c,f,h) and fig. 6.2(b,d,e,g,i) respectively.

Discussion

With knowledge of the reference field $\mathbf{E}_r$, it is easy to extract the sample phase shift ϕ and fractional absorption α_f using the expressions derived in sections 3.2.4 and 6.2.1. Measuring the RMS background noise level in α_f and ϕ images using eq. (5.2) gave an estimation of the sensitivity of the reconstructed images.

With the NA= 0.07 version of DSHM and with SNR$\lesssim$ 30, α_f and ϕ images were consistently reconstructed with shot-noise limited sensitivities of $\delta\alpha_f = (3.6 \pm 0.034)$ % and $\delta\phi = (1.8 \pm 0.17)$ mrad respectively. Despite absorption and phase-contrast imaging possessing a factor of two improvement in signal, thanks to holographic enhancement DSHM can easily outperform both of the techniques in terms of sensitivity. The improved sensitivity displayed by DSHM makes it an alternative for detection of single atoms when compared to single atom absorption [86] and other phase sensitive [55] techniques.

Using the upgraded NA = 0.16 DSHM assembly, similar sensitivities of $\delta\alpha_f = (3.6 \pm 0.026)$ % and $\delta\phi = (1.8 \pm 0.13)$ mrad were observed (the uncertainties are the standard error of the noise levels of the images presented in figs. 6.1 and 6.2). There are two reasons why a lower sensitivity was not observed at NA = 0.16. The first was that the choice of $\eta = 0.4$ resulted in a higher modulation contrast, thus reducing the mean number of counts N_p at the detector. The second was caused by the mean number of counts being further reduced at high NA because of an increased intensity inhomogeneity, with the intensity centred to the CCD, a larger intensity was detected near the centre than at the edge. The combination of the two effects reduced N_p from near the maximum pixel count of $N_{\max} = 2^{14} - 1$ to $N_p \approx 2000$, thus reducing the sensitivity as shown in eq. (6.5). With poor choice of η, such as demonstrated here, the holographic enhancement with $\kappa \approx 0.002$ at NA = 0.16 can be partly cancelled out by a reduction in N_p, though this can easily be avoided by choosing $\eta \ll 1$ in future experiments.

6.3 Detuning-dependent phase shift and absorption of a magneto-optical trap

To experimentally confirm the method of phase shift and absorption extraction, and to demonstrate its accuracy and convenience, it would be convenient to have an object with tunable complex refractive index. Cold atoms are an ideal object to achieve this, thanks to the detuning dependence of the refractive index. In the following, advantage was taken of this fact by scanning the probe detuning across the atomic resonance to retrieve probe phase shift and absorption images at different detunings. Experimental results were then compared with the theoretical prediction for a single two-level atom. This was further investigated by measuring the detuning dependence of probe phase shift and absorption while the atoms were dressed by the cooling light.

The probe detuning was experimentally varied by manipulation of the frequency driving a double-pass AOM (see section 4.3.3). To minimize the distance that atoms travelled during the probe when imaging after cooling, a short exposure time of $\tau_{\text{exp}} = 40$ μs was chosen, thus minimising the effect the moving atomic sample had on the measurement. When imaging while cooling in a MOT, the trapping and cooling permitted imaging for longer exposure times $\tau_{\text{exp}} = 1$ ms. To reduce unwanted effects such as a fringe shift between recording of H and H_0, and laser lock insatiabilities, multiple holograms were recorded at each probe detuning. The extracted ϕ and α_f

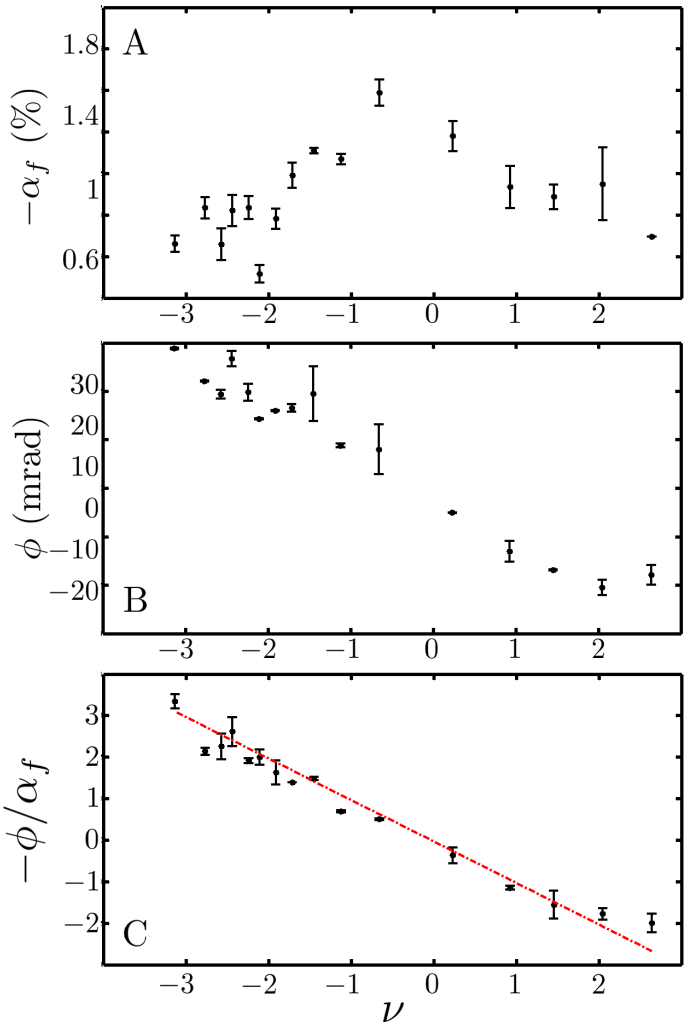

Figure 6.3: Plots displaying the detuning dependence of the fractional absorption, phase shift and phase shift to absorption ratio for an atomic sample probed after cooling for an exposure time of $\tau_{\text{exp}} = 40$ μs. (a) $-\alpha_f$ versus ν (detuning in units of Γ). (b) ϕ versus ν. (c) $\phi/-\alpha_f$ versus ν, along with a red line indicating the theoretical expectation for the gradient. The extracted ϕ and α_f values at each detuning were then the average of at least one reconstructed image and the error bars are given by the statistical standard error in the mean.

values at each detuning were then the average of at least one reconstructed image. Furthermore, images that display a severe fringe shift, or have no atoms present upon reconstruction due to the injection/dither locking becoming unstable were discarded systematically.

The process of measuring ϕ and α_f for each reconstruction was as follows: first a twin image free estimation of $\mathbf{E}_s(z_0)$ was retrieved using the estimation of the reference field and eq. (3.27). Secondly, the pixel indices of a $|\mathbf{E}_s(z_0)|$ image above 60 % of the maximum were recorded. With knowledge of $\mathbf{E}_r(z_0)$, ϕ and α_f images were plotted, and the average was taken for each over the pixel locations extracted from the $|\mathbf{E}_s(z_0)|$ image to give the measured ϕ and α_f values. To measure the phase shift to optical depth ratio, the ratio of the extracted mean values were used $\phi/OD \approx \phi/-\alpha_f$. When imaging after cooling, the two-level atom picture predicts a linear dependence on detuning for the ratio $\phi/OD = -\nu$ (see section 2.1.6). The uncertainty in each ϕ, α_f and $\phi/-\alpha_f$ measurement is given by the statistical standard error of the mean, see eq. (5.2). Since images including those with no atoms present are systematically discarded, at most five data points were averaged to give the measured ϕ and α_f values.

In fig. 6.3 the retrieved mean $-\alpha_f$, ϕ and $\phi/-\alpha_f$ data are plotted against the probe light detuning for a sample probed with $\tau_{\text{exp}} = 40$ μs after cooling in a MOT. For the $-\alpha_f$ (fig. 6.3(a)) data there is a peak near $\nu \approx 0$, whilst the phase shift data changes sign at a similar location (see fig. 6.3(b)). Due to the inability to maintain a constant atom number shot to shot, the α_f and ϕ plots against detuning fluctuate. To address this issue the atom number independent ratio $\phi/-\alpha_f \approx \phi/OD = -\nu$ is plotted in fig. 6.3(c). The dotted red line indicates the theoretical expectation (see chapter 2). The systematic deviation in the $x-$axis intercept to small positive detuning was mainly attributed to the Doppler effect, since the atoms were accelerated to $v \sim 1$ ms^{-1} during probing. A slight shift of approximately -0.5 MHz was also expected in the probe detuning from imperfections in the saturated absorption spectroscopy experiment used to dither lock the cooling laser: the Doppler broadened profile was not subtracted away, thus shifting the centre frequency of the peak used for dither locking (see appendix C).

In fig. 6.4(a,b,c), $-\alpha_f$, ϕ and $\phi/-\alpha_f$ data are plotted against the probe light detuning for an atomic sample probed for an extended $\tau_{\text{exp}} = 1$ ms after cooling in a MOT. In addition to the Doppler shift that arises since the atoms were accelerated during the probe, for such a long probe time with $s \approx 1$, the atoms were expected to

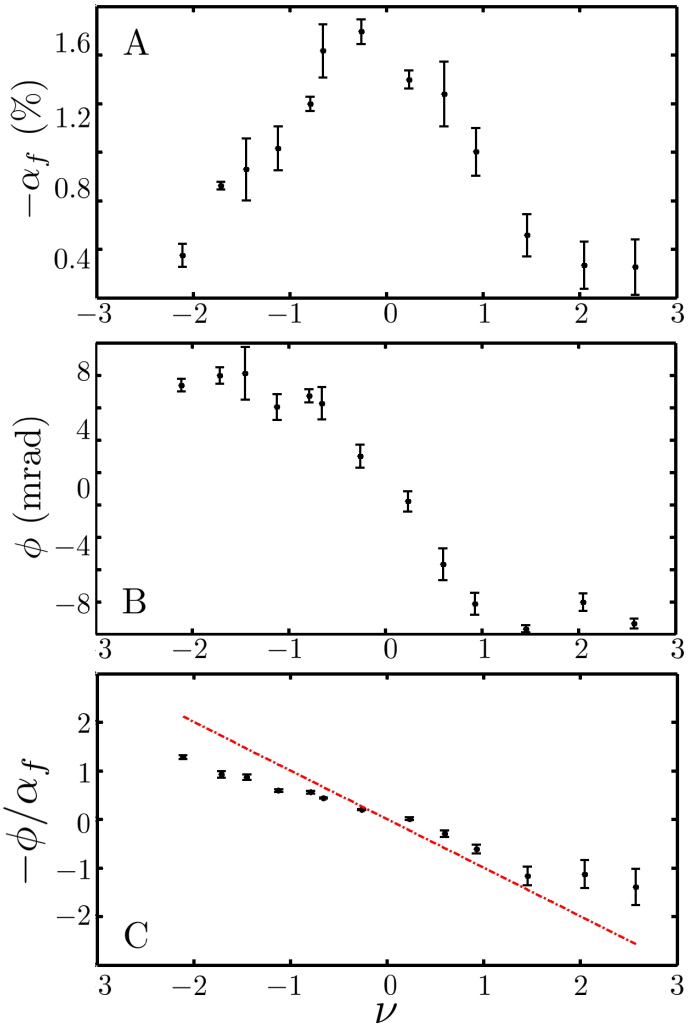

Figure 6.4: Plots displaying the detuning dependence of the fractional absorption, phase shift and phase shift to absorption ratio for an atomic sample probed after cooling for an exposure time of $\tau_{\text{exp}} = 1$ ms. (a) $-\alpha_f$ versus ν. (b) ϕ versus ν. (c) $\phi/-\alpha_f$ versus ν, along with a red line indicating the theoretical expectation for the gradient. The extracted ϕ and α_f values at each detuning were then the average of at least one reconstructed image and the error bars are given by the statistical standard error in the mean.

move ~ 1 mm for a probe with $\Delta < 3\Gamma$. Such distances are much larger than the depth of view of 60 μm in the NA $= 0.16$ DSHM, thus erroneous retrievals of ϕ and α_f were expected. Indeed, in fig. 6.4(c), the gradient from the experimental data deviates from the theoretical prediction of -1 by a factor of approximately 2.

To address this issue of atoms moving in extended exposure time, the sample was probed whilst cooling and trapping in a MOT. The scattering force from the MOT beam reduced the net effect of the force from the probe, thus atoms were held near the MOT centre for longer while probing. However, the introduction of cooling beams modified the atomic responsivity to the probe beam [188]. The probe absorption by the atoms dressed with the MOT cooling beams could no longer longer be described by the simple two-level picture described in section 2.1.6. Figure 6.5 displays $-\alpha_f$, ϕ and $\phi/-\alpha_f$ data plotted against ν for an atomic sample imaged for $\tau_{\text{exp}} = 1$ ms while cooling in a MOT. When plotting $-\alpha_f$ against detuning (see fig. 6.5(a)), two peaks in absorption were observed: one occurred slightly shifted to the blue side the atomic resonance, whilst the second appeared at the same frequency as the MOT beam detuning $\nu \approx -2.2$. The feature at $\nu \approx -2.2$ is also visible in the ϕ versus ν and $\phi/-\alpha_f$ versus ν plots, see fig. 6.5(a,c). The feature in the $\phi/-\alpha_f$ versus ν plot near $\nu \approx -2.2$, demonstrates that the observed feature was not caused by a fluctuation in the atom number and was a result of dressing the atoms with the MOT beams. Such a feature is due to Raman and recoil resonances, as is discussed in the details of [188].

Discussion

In summary, to extract information that matches the predicted theory when imaging after cooling, the sample must be probed with short exposure time to prevent the atomic sample moving out of the depth of field during the probe time. An ^{87}Rb atom probed with $s \gg 1$, near-resonant light and an exposure time of $\tau_{\text{exp}} = 40$ μs will travel ~ 10 μm during the probe, a distance less than the microscope depth resolution $\lambda/(1-\cos(\theta)) \approx 60$ μm. With such a short exposure time the atomic movement cannot be resolved, even with the higher NA $= 0.16$ microscope. However, when probing for $\tau_{\text{exp}} = 1$ ms, the atoms are able to travel a distance of ~ 1 mm, which is much larger than the microscope depth resolution. With atoms travelling such distances during the $\tau_{\text{exp}} = 1$ ms probe it is entirely expected that data recorded with such exposure times would produce erroneous results as demonstrated in fig. 6.4(c). Furthermore, such a problem can be addressed by imaging the atoms

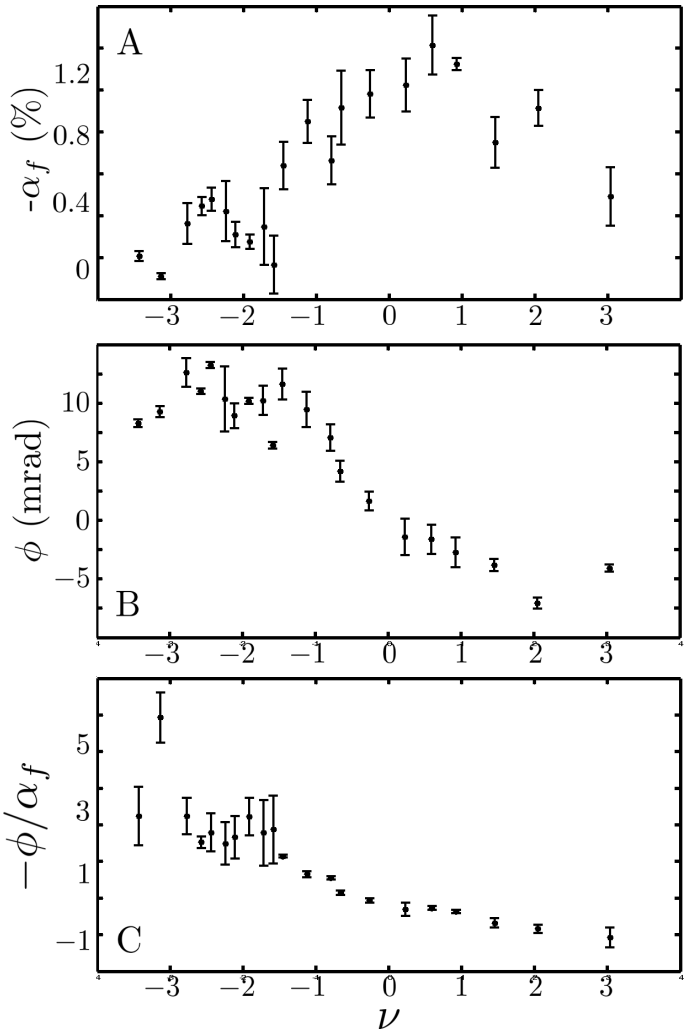

Figure 6.5: Plots displaying the detuning dependence of the fractional absorption, phase shift and phase shift to absorption ratio for an atomic sample probed during cooling for an exposure time of $\tau_{\text{exp}} = 1$ ms. (a) $-\alpha_f$ versus ν. (b) ϕ versus ν. (c) $\phi/-\alpha_f$ versus ν. Each display a feature near $\nu \approx -2.2$. The extracted ϕ and α_f values at each detuning were then the average of at least one reconstructed image and the error bars are given by the statistical standard error in the mean.

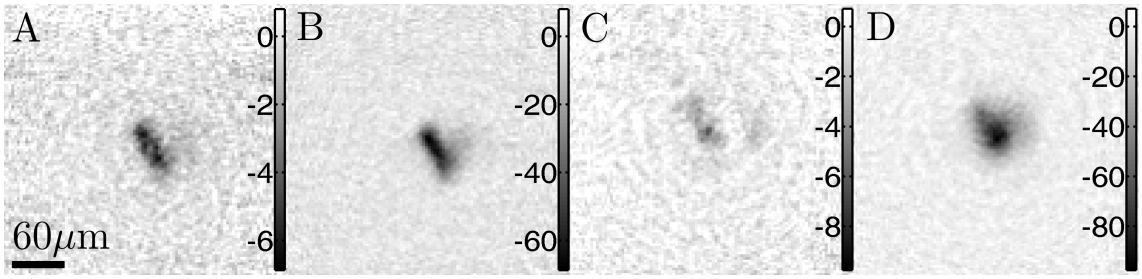

Figure 6.6: α_f (%) and ϕ images taken during and after cooling with $\nu = 1.9$. A) [$\nu = 1.9$, $\tau_{\text{exp}} = 100$ μs]: α_f, taken during cooling. (b) ϕ, extracted from the same hologram as (a). (c) [$\nu = 1.9$, $\tau_{\text{exp}} = 100$ μs]: α_f, taken after cooling. (d) ϕ, extracted from the same hologram as (c).

while trapping and cooling to reduce the atomic motion to values below the depth resolution.

Measuring light shift

Observing the graphs displayed in figs. 6.3 and 6.5, it can be seen that in the presence of the MOT cooling beams, the resonance was shifted by $\nu \approx 1$, due to the light shift of the MOT beams (see section 2.1.1). The change in the phase shift to fractional absorption ratio near the atomic resonance can be utilized to infer the amount of light shift experienced by the atoms as a result of dressing with the cooling light. To demonstrate this a particular example is given in fig. 6.6, where ϕ and α_f reconstructions from holograms recorded during (fig. 6.6(a,b)) and after cooling (fig. 6.6(c,d)) with $\tau_{\text{exp}} = 40$ μs and $\nu = 1.9$ are shown. Analysis of the images revealed that $\phi/\alpha_f \approx 1.1$ when imaging during cooling (see fig. 6.6(a,b)), and $\phi/\alpha_f \approx 1.7$ after cooling (see fig. 6.6(c,d)). The differing absorption to phase shift ratio when imaging with and without cooling inferred a light shift of $1.9\ \Gamma\left(1 - \frac{1.1}{1.7}\right) = 4$ MHz to the cooling transition when cooling, thus shifting the dressed probe nearer to resonance.

6.4 Summary and discussion

The results presented in this chapter are the first demonstration of simultaneous phase shift and absorption imaging of cold atoms with holographic microscopy at the shot-noise and diffraction limits. Fractional absorption and phase shift images are extracted using eqs. (6.1) and (6.2) and the estimate of the reference field at the atomic sample plane $\mathbf{E}_r(z_0)$. Analysis of the mean noise level in the reconstructed ϕ and α_f images revealed that DSHM at NA = 0.16 achieved remarkable phase shift and

optical thickness sensitivities of $\delta\phi = (1.8 \pm 0.13)$ mrad and $\delta\alpha_f = (3.6 \pm 0.026)$ % respectively. Such resolution is beyond that achievable with standard absorption or phase-contrast imaging if an identical camera is used with image magnification of one. The physics behind this demonstrated holographic enhancement in sensitivity is also discussed.

An obvious caveat in this comparison is the assumption that in standard absorption or phase-contrast imaging the magnification is one. Practically, the sensitivities in absorption and phase-contrast imaging can be improved by magnifying the image, thus reducing the ratio A_p/A_r in an effect similar to the holographic enhancement via κ. However, optimising the sensitivity requires that the magnified image maximally fills a significant fraction the CCD chip. The magnified image of the atomic sample is then heavily susceptible to low spatial frequency noise in detection, thus it is difficult to distinguish weak signals from a laser power fluctuation shot to shot or a temperature variation across the camera chip. Holographic recording as in DSHM avoids this difficulty, since signal is recorded in high spatial frequency interference fringes over the entire CCD in a nearly optimal fashion.

The retrieval of ϕ and α relies on precise knowledge of the complex ratio $\mathbf{E}_s(z_0)/\mathbf{E}_r(z_0)$. In this work, the reference field at the image focal plane $\mathbf{E}_r(z_0)$ was decided from the same reference field at the camera plane $\mathbf{E}_r(L)$ that was used to extract $\mathbf{E}_s$, since the focal plane reference could be extracted as a simple propagation $\mathbf{E}_r(L) = \hat{\mathrm{U}}_0\mathbf{E}_r(L)$.

Although error in the estimation was minimized through calibration of L, as discussed in section 6.1.1, substantial ($> \pi$) phase errors in $\mathbf{E}_r$ were still present, which arise predominantly in two ways: The first is an error in the estimation of the x, y spatial coordinate of the source location. The second is caused by speckle noise which results in high spatial frequency interference rings in the hologram that cause a distortion to $\mathbf{E}_s$ upon reconstruction (see chapter 5). In this work both errors in $\mathbf{E}_r(z_0)$ have not been reduced with any precision (e.g. a to phase error $< \pi$). In the following, a basic understanding of why reliable ϕ and OD retrieval was possible in spite of these errors is discussed.

Since the amplitude of the reference field is given by $\sqrt{H_0}$, the error in estimation of $\mathbf{E}_r$ is purely a phase error $\tilde{\mathbf{E}}_r = \mathbf{E}_r e^{i\tilde{\epsilon}}$. The error in the extracted $\mathbf{E}_s$ can then be written as $\mathbf{E}_r(L)^* \mathbf{E}_s(L)/\tilde{\mathbf{E}}_r(L)^* = \mathbf{E}_s(L) e^{i\tilde{\epsilon}}$, thus both wavefront share a common phase error at the camera plane. With $z_0 \ll L$, the two wavefronts originate from a similar location with respect to the detector, thus upon recon-

struction remains approximately the same for both waves. Taking into account the phase error, the ratio $\mathbf{E}_s(z_0)/\mathbf{E}_r(z_0)$ used for extracting ϕ and OD can be written as $\hat{\mathrm{U}}_0\mathbf{E}_s(L)\,\mathrm{e}^{\mathrm{i}\tilde{\epsilon}}/\hat{\mathrm{U}}_0\mathbf{E}_r(L)\,\mathrm{e}^{\mathrm{i}\tilde{\epsilon}} \approx \hat{\mathrm{U}}_0(\mathbf{E}_s(L)+\mathrm{i}\mathbf{E}_s(L)\,\tilde{\epsilon})/\hat{\mathrm{U}}_0(\mathbf{E}_r(L)+\mathrm{i}\mathbf{E}_r(L)\,\tilde{\epsilon})$, for $\tilde{\epsilon} \ll 1$. If $z_0 \ll L$ and the atomic sample is point-like, then both $\mathbf{E}_r$ and $\mathbf{E}_s$ are well described by spherical waves that travel along a similar path, thus encountering similar distortions on their way to the camera. It is believed that such consistency in the estimation of $\mathbf{E}_s(z_0)$ and $\mathbf{E}_r(z_0)$, results in a common mode rejection of the error in the ratio $\mathbf{E}_s(z_0)/\mathbf{E}_r(z_0)$ estimation, which permits an almost error free retrieval of the sample optical properties, in spite of the estimated $\mathbf{E}_r(z_0)$ and $\mathbf{E}_s(z_0)$ being incorrect from the true value.

To add to this discussion, it is pointed out that a small error in the estimation of the source location should lead to a low spatial frequency phase error in the $\mathbf{E}_r$ estimation at the camera plane. Furthermore, the sources of speckle noise are typically imperfections in optics such as vacuum windows that scatter the probe where its intensity is weaker than near the focal point, thus the phase error due to speckle noise is expected to be $\ll \pi$. The smooth distortion from the source location error will have little effect on the relative phase between $\mathbf{E}_r$ and $\mathbf{E}_s$ during propagation, since, as discussed earlier, the distortion is common to the two waves. The speckle noise distortion has a higher spatial frequency but is weaker. Furthermore, the small error can be averaged out when the mean phase shift is evaluated. This effect is similar to passing the object wavefront through weakly patterned glass similar to a bathroom window. In future advantage may be taken of the developed speckle suppression algorithm by inclusion of speckle noise sources into the $\mathbf{E}_r(L)$ used for reconstruction.

Chapter 7

Toward single atom resolution with holographic microscopy

An ultimate goal for optical imaging of cold atoms is to determine atom number at the atom shot-noise limit. An imaging scheme with this ability would permit the measurement of quantum states of many atom systems, as demonstrated in the field of quantum gas microscopy [19–21]. Resolving atom numbers in large atomic quantum gases may be useful in the development of a scalable quantum computer [189, 190].

Imaging optical lattice sites with multiple atom occupancy may be possible with phase sensitive DSHM, since light assisted collisions can be reduced [34]. In contrast to the popular fluorescence imaging method of detecting single atoms [19–21], the sensitivity to atom number in DSHM is independent of the number of atoms detected, see section 7.1, since the shot-noise level is proportional to the square root of the probe intensity and not the number of atoms.

In this chapter, the experimental efforts made during this project toward single atom detection with DSHM are discussed. The chapter begins with a mathematical derivation of the atom number sensitivity per resolution area for DSHM. In addition to the achievement of shot-noise limited holography, see chapter 5, further efforts to achieve this goal are largely divided into two parts: the improvement of imaging resolution by increasing the NA in DSHM, and the attempt of restricting atomic motion to a smaller volume during imaging using a dipole trap. Finally future improvements to the DSHM set-up are suggested, see section 7.3, that should permit off-resonant single atom imaging with a numerical aperture as large as NA = 0.7, and reduce the amount of speckle noise recorded in holograms as a result the

spatial filtering awarded by pinhole sources. Speckle noise can be further reduced by fabricating the pinhole sources into high optical quality mirror surfaces, see section 7.3.1, thus reducing reflection from imperfections in the surface.

7.1 Atom number resolution in holographic microscopy

Thanks to the point source geometry of DSHM, it can display holographic enhancement of the sensitivity to ϕ and OD when compared to the established phase-contrast and absorption imaging, see chapter 6. In this section, to further explore this holographic enhancement over in-focus coherent imaging (see section 2.3.2), the sensitivity of DSHM to atom number δN_{atom} is investigated. Similar to the holographically enhanced phase shift and optical thickness sensitivities, it is shown that if an identical camera is used with image magnification of one, DSHM with $z_0 \ll L$ can display a much better atom number sensitivity per resolution area than standard absorption or phase-contrast imaging.

Similar to the extraction of ϕ and OD discussed in section 6.1.2, accurate determination of atom number in DSHM requires knowledge of the reference field at the image focal plane $\mathbf{E}_r(z_0)$ (see section 6.1.1). To determine the sample atom number distribution, the column density ρ_c is determined after propagation of the extracted $\mathbf{E}_s$ to its focal plane as

$$\rho_c = \frac{|\ln\left(1+\frac{\mathbf{E}_s}{\mathbf{E}_r}\right)|}{|\tilde{\sigma}|}, \tag{7.1}$$

where $\tilde{\sigma}$ is the complex absorption cross section (see chapter 3). The total atom number can be easily determined by summing the column density over the pixels.

For simplicity when deriving the sensitivity to atom number in DSHM, it is assumed that the point source power ratio $\eta \ll 1$, such that $\sqrt{1-\xi^2} \approx 1$ and there is negligible noise increase from removal of the twin image noise (see section 3.2.3). Then using eqs. (2.43), (6.4), (6.5) and (7.1) it is easy to show that the sensitivity to column density is given by

$$\delta\rho_c = \sqrt{\frac{2\kappa A_p}{N_{\max} A_r |\tilde{\sigma}|^2}}. \tag{7.2}$$

The sensitivity to atom number is determined by summing the sensitivity to column density over the smallest resolvable area $\delta N_{\text{atom}} = \delta\rho_c R_{\text{lat}}^2$, which is given by the

microscope resolution (see section 3.1.2) and is a factor of four larger than A_r. Using this, it can be shown that the atom number sensitivity in DSHM is given by

$$\delta N_{\text{atom}} = 4\sqrt{\frac{2\kappa A_p A_r}{N_{\max}|\tilde{\sigma}|^2}}. \tag{7.3}$$

To compare with absorption and phase-contrast imaging with an identical camera and an image magnification factor of one, a similar derivation reveals the sensitivities as $\delta N_{\text{abs}} = 2\sqrt{2\kappa A_p A_r / N_{\max}\sigma_{Im}^2}$ and $\delta N_{\text{PCI}} = 2\sqrt{2\kappa A_p A_r / N_{\max}\sigma_{Re}^2}$ respectively. In comparison with standard absorption and phase-contrast imaging which are only sensitive to the imaginary and real parts of the refractive index respectively (see chapter 2), the atom number sensitivity in DSHM benefits from both the holographic enhancement via κ and a complex absorption cross-section $\tilde{\sigma}$, since holography is sensitive to the full complex refractive index. The factor of two loss in signal for holographic microscopy is taken into account in these derivations.

According to the derived atom number sensitivity, a single atom held within a resolution area during the exposure time will be detectable with a signal to noise ratio $\text{SNR} = 1/\delta N_{\text{atom}}$. To demonstrate the differences in the atom number sensitivity expected in DSHM, absorption and phase-contrast imaging at two different numerical apertures, fig. 7.1 shows plots of the detuning dependence of the SNR for a single atom held within an area R_{lat}^2 during probing for each method. In the calculation a magnification factor of one and $N_{\max} = 2^{14} - 1$ was used for absorption and phase-contrast imaging. To be consistent with the experiments conducted with the NA = 0.16 DSHM, a value of $N_{\max} = 1500$ was chosen for the DSHM calculation, an order of magnitude less than absorption and phase-contrast imaging.

In the numerical example given in fig. 7.1, the atom number sensitivity for DSHM is calculated for a camera with pixel pitch $x_{\text{pix}} = 6.45$ μm, maximum pixel count $N_{\max} = 1500$, 1040×1040 pixels, with probe wavelength $\lambda = 0.78$ μm, resonant absorption cross-section $\sigma_0 = 0.14$ μm^2 and microscope geometrical parameters $L = 23$ mm and $z_0 = 1.03$ mm such that $\kappa = 0.002$ and NA = 0.15, see fig. 7.1(a). The parameters are chosen to be similar to the experimental parameters of the upgraded NA = 0.16 DSHM system developed in this work (although a camera with $N_{\max} = 2^{14} - 1$ is used, $N_{\max} = 1500$ for calculation. This is due to a high fringe contrast ($\eta = 0.4$) and the requirement to avoid the camera saturating.). The corresponding sensitivities in absorption and phase-contrast imaging are determined

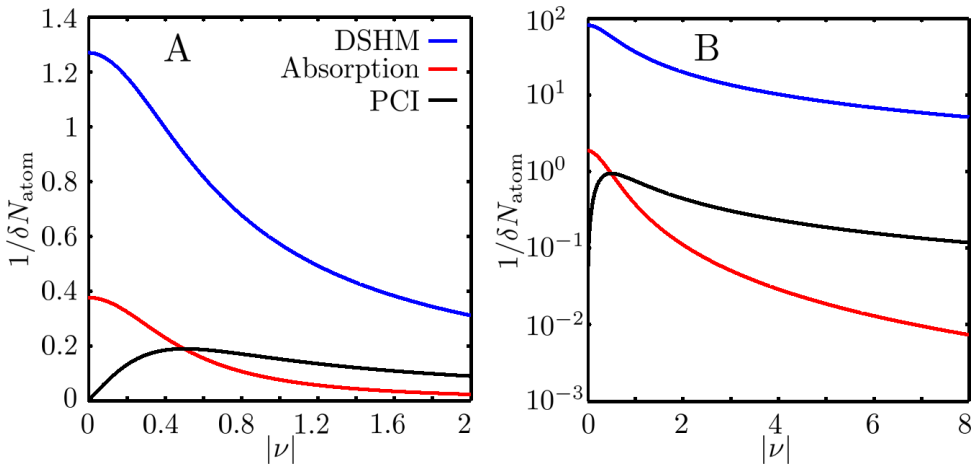

Figure 7.1: Plots displaying the detuning dependence of the signal to noise ratio expected for a single atom held within a resolution area during probing for, (a) DSHM ($\kappa = 2 \times 10^{-3}$ and $N_{\mathrm{max}} = 1500$), absorption and PCI with NA = 0.15 and $N_{\mathrm{max}} = 2^{14} - 1$, and (b) DSHM ($\kappa = 9 \times 10^{-5}$ and $N_{\mathrm{max}} = 11000$), absorption and PCI with NA = 0.7 and $N_{\mathrm{max}} = 2^{14} - 1$.

with consistent values, but with $\kappa = 1$ and $N_{\mathrm{max}} = 2^{14} - 1$. The comparisons between the atom number sensitivity of each technique are displayed in fig. 7.1.

On resonance, the expected SNR for detection of a single atom held within a resolution area with DSHM is SNR = 1.3, whilst absorption imaging demonstrates a value significantly less at SNR = 0.37, see fig. 7.1(a). Furthermore, the sensitivity in DSHM for all values of detuning is consistently better than both absorption and phase-contrast imaging, even if $N_{\mathrm{max}} = 2^{14} - 1$ for the two in-focus imaging methods.

The resonant single atom SNR = 1.3, as achieved experimentally in this work (see section 7.2.2), is too small to accurately determine an atom from a background noise fluctuation. To improve the resonant SNR from 1.3 and unambiguously resolve a single atom from a noise fluctuation, two of the most significant approaches can be pursued independently or simultaneously: the atomic sample can be moved closer to the point source (e.g. by a factor of 3, thus reducing κ by another factor of 9), and/or the numerical aperture can be improved with a reduction in L. Other less significant approaches include, improving the mean number of camera counts with a reduction in η.

Before discussing the experimental progress, to demonstrate the potential of DSHM for lens-free single atom detection, the SNR for a single atom held within a resolution area is calculated for a hypothetical geometry consistent with the

atom chip DSHM geometry proposed in section 7.3.1. For an upgraded camera with $x_{\mathrm{pix}} = 3$ μm, 2048×2048 pixels, in a DSHM geometry with $N_{\mathrm{max}} = 11000$, $\lambda = 0.78$ μm, $\sigma_0 = 0.14$ μm^2, $L = 3.18$ mm and $z_0 = 30$ μm such that $\kappa \approx 9 \times 10^{-5}$ and NA $= 0.7$, the single atom SNR is plotted as a function of detuning, see fig. 7.1(b). Again the calculated SNR in absorption and phase-contrast imaging is consistent but with $\kappa = 1$ and $N_{\mathrm{max}} = 2^{14} - 1$. near-resonance, DSHM displays a single atom SNR ≈ 81, whilst regular absorption imaging only displays a value of SNR ≈ 1.87. With this NA $= 0.7$ version of DSHM, single atom sensitivity with SNR $= 5$ is even expected when probing with off-resonant light with detuning $|\nu| = 8$.

An obvious caveat in this comparison is the assumption that in standard absorption or phase-contrast imaging the magnification is one. Practically, the atom number sensitivities in absorption and phase-contrast imaging can be improved by magnifying the image, thus reducing the ratio A_p/A_r in an effect similar to the holographic enhancement via κ. However, optimising the sensitivity requires that the magnified image maximally fills a significant fraction the CCD chip. The magnified image of the atomic sample is then heavily susceptible to low spatial frequency noise in detection, thus it is difficult to distinguish the weak single atom signal from a laser power fluctuation shot-to-shot or a temperature variation across the camera chip. Holographic recording as in DSHM avoids this difficulty, since the single atom signal is recorded in high spatial frequency interference fringes over the entire CCD in a nearly optimal fashion.

To achieve single atom sensitivity, DSHM must meet a number key requirements: shot-noise and diffraction limited imaging is a pre-requisite, whilst smaller values of z_0 improve the holographic enhancement factor κ. Furthermore, probing near-resonance is optimal for increasing $\tilde{\sigma}$, whilst maximising the available numerical aperture minimises A_r, further improving the sensitivity.

With single atom sensitive DSHM, the atoms must be held within an area given by $R_{\mathrm{lat}}^2 = 4A_r$ during the probe to maximise the sensitivity for observing atom shot-noise. This can only be achieved with a combination of trapping potential to restrict atomic motion, and laser cooling to compensate for probe heating. Practically the trapping potentials available in optical lattices can easily be spatially small enough to contain an atom within an area R_{lat}^2 during imaging.

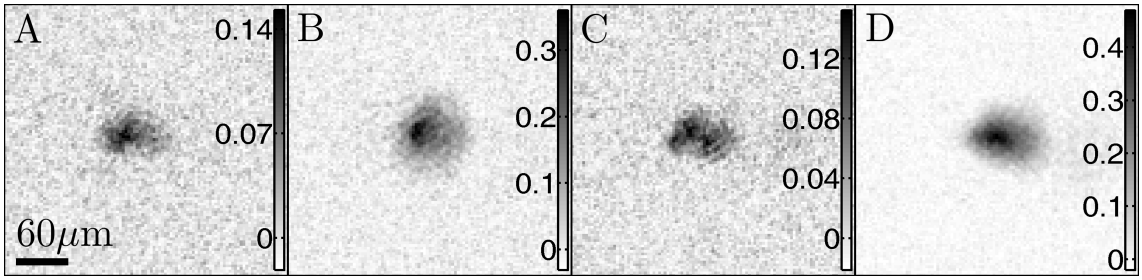

Figure 7.2: A collection of characteristic column density images ($1/\mu m^2$) with varying atom numbers. Each display a sensitivity to column density $\delta\rho_c = 0.025$, thus a single atom sensitivity per resolution area of $\delta N_{\text{atom}} = 2.7$ is expected. (a) [$\nu = 0$, $\tau_{\text{exp}} = 800$ μs]: ρ_c. (b) [$\nu = 0$, $\tau_{\text{exp}} = 400$ μs]: ρ_c. (c) [$\nu = 0$, $\tau_{\text{exp}} = 800$ μs]: ρ_c. (d) [$\nu = 0$, $\tau_{\text{exp}} = 800$ μs]: ρ_c.

7.2 Experimental progress

In this section, the efforts made during this project to push DSHM into the single atom detection regime are discussed. By increasing the microscopes numerical aperture from NA = 0.07 to NA = 0.16 and reducing the holographic enhancement factor κ, an improvement in the expected atom number sensitivity per resolution from $\delta N_{\text{atom}} = 2.7$ to $\delta N_{\text{atom}} = 0.75$ was demonstrated (see sections 7.2.1 and 7.2.2). It was shown that by careful removal of unwanted MOT beam scattering and ambient light sources, shot-noise limited imaging with DSHM can be achieved with extended exposure times (see section 7.2.3). Finally details of an attempt to observe quantised atom numbers with DSHM by restricting atomic motion during imaging is discussed in section 7.2.4. With the impressive sensitivity to atom number displayed by DSHM, it is proposed as an alternative to the popular fluorescence method for number resolving detection of atomic samples.

7.2.1 Sensitivity with NA = 0.07 holography

To determine the imaging sensitivity to atom number, the column density ρ_c is extracted with $\sigma = 0.14$ μm^2 for the non-polarized atomic sample of ^{87}Rb atoms [67]. The RMS noise level $\delta\rho_c$ (calculated in a similar fashion to eq. (5.2)) in the reconstructed ρ_c image was used to determine the atom number noise level $\delta N_{\text{atom}} = \delta\rho_c R_{\text{lat}}^2$. This definition of the atom number sensitivity requires that the atoms be held within a resolution area R_{lat}^2 during the imaging exposure time τ_{exp}. In fig. 7.2, a collection of ρ_c images with varying atom numbers are presented, all were recorded near-resonance to optimize the atom number sensitivity, by maximising the absorption cross-section

$\tilde{\sigma}$. With a diffraction limited resolution area $R_{\text{lat}}^2 = 108.2\ \mu\text{m}^2$ and a RMS noise level of $\delta\rho_c = 0.025$ as in fig. 7.2, a sensitivity to atom number per resolution area of $\delta N_{\text{atom}} = 2.7$ is expected. This predicts that a single atom held within a trap with cross sectional area smaller than R_{lat}^2 during τ_{exp} will produce an image with a signal below the shot-noise level (SNR $= 1/\delta N_{\text{atom}} < 1$) if probed with negligible power broadening such that $\sigma = 0.14\ \mu\text{m}^2$. This SNR is not large enough to distinguish the signal from such a sample from the background. To detect atom shot-noise the atoms must be held within R_{lat}^2 during imaging and δN_{atom} must be improved, for example by reducing A_r with an increased NA.

7.2.2 Improving sensitivity at NA = 0.16

The numerical aperture of the lens free DSHM was limited to NA = 0.07 by the spatial extent of the CCD chip and a constraint on the distance L between the source and the camera. To overcome this limitation, an upgraded imaging system was constructed to achieve NA = 0.16. The upgraded system consisted of a replacement focusing lens array to generate the double diffraction limited point sources for DSHM, and collimating and imaging lens arrays to image the hologram to the camera (see section 4.4.3 and appendix F). The lens system design was based on the four lens design to account for aberration introduced by a plane window [181], and the air spacing between each lens was adjusted to account for the glass cell window aberration. To increase the numerical aperture, 51 mm diameter optics were chosen, since the MOT-lens separation distance was limited to ~ 5 cm. The magnification of the imaging system was chosen to be one. The lenses minimised the aberration but the correction was not perfect. However, holographic microscopy was expected to be tolerant to residual aberration, since $\mathbf{E}_r$ and $\mathbf{E}_s$ share a common optical path [34].

With the increased imaging resolution awarded thanks to the use of imaging lenses, an increase in the predicted atom number sensitivity per resolution area for the upgraded DSHM system was expected when compared to the values presented in section 7.2, since $\delta N_{\text{atom}} = \delta\rho_c R_{\text{lat}}^2$. The column density ρ_c and total number of atoms N in an atomic sample were easily computed in DSHM using the expressions presented in section 3.2.4.

To demonstrate the imaging sensitivity to atom number, atomic samples were probed near-resonance with saturation parameter $s \approx 1.7$. Images of the extracted column densities of the atomic samples are displayed in fig. 7.3. On resonance the

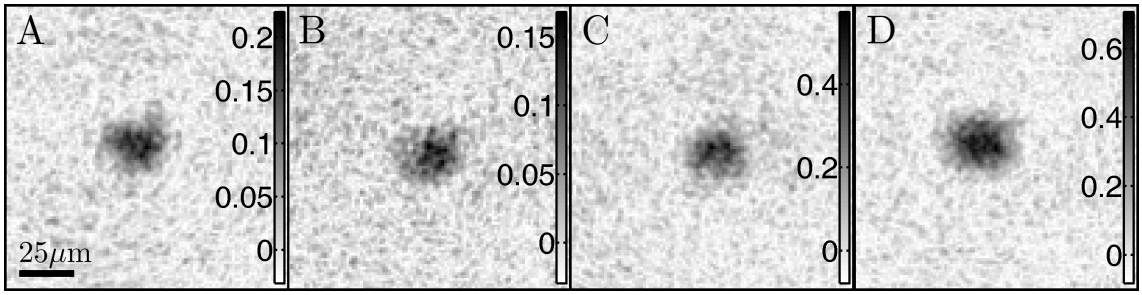

Figure 7.3: Column density images ρ_c (μm^{-2}) with a RMS noise levels of $\delta = \rho_c = 0.03$, thus inferring a sensitivity to atom number per resolution area of $\delta N_{\text{atom}} = 0.75$. (a) [$\nu = 0$, $\tau_{\text{exp}} = 500$ μs]: ρ_c, with $\delta N_{\text{atom}} = 0.8$. (b) [$\nu = 0$, $\tau_{\text{exp}} = 500$ μs]: ρ_c, with $\delta N_{\text{atom}} = 0.75$. (c) [$\nu = 1.25$, $\tau_{\text{exp}} = 500$ μs]: ρ_c, with $\delta N_{\text{atom}} = 2$ (d) [$\nu = -1.45$, $\tau_{\text{exp}} = 500$ μs]: ρ_c, with $\delta N_{\text{atom}} = 2.1$.

RMS noise level was $\delta\rho_c = 0.03$, see fig. 7.3(a,b), thus with the improved resolution area $R^2_{\text{lat}} = 25$ μm^2, the predicted minimum sensitivity to atom number per resolution area was $\delta N_{\text{atom}} = 0.75$. Here power broadening was ignored in the absorption cross-section used. This can be alleviated by combining a weaker probe beam with a longer exposure time. A single atom trapped within a resolution area R^2_{lat} during the exposure time τ_{exp} with negligible power broadening, should produce an image with SNR $= 1/\delta N_{\text{atom}} = 1.3$, consistent with the theoretical prediction in section 7.1. Such a sensitivity is not enough to confidently distinguish the signal from a single atom trapped within a resolution area above the background noise level. With the upgraded DSHM, a sensitivity above the single atom level per resolution area ($\delta N_{\text{atom}} = 2$) was inferred with $|\nu| > 1$ at both sides of the atomic resonance, see fig. 7.3(c,d).

Discussion

A sensitivity to atom number was determined by analysing column density ρ_c images (see section 7.2). Using the RMS noise level in an annulus surrounding the atomic sample to define $\delta\rho_c$, and the resolution area R^2_{lat}, minimum sensitivities to atom number per resolution area of $\delta N_{\text{atom}} = 2.7$ and $\delta N_{\text{atom}} = 0.75$ were predicted with the NA $= 0.07$ and NA $= 0.16$ DSHM systems respectively. This increased sensitivity at higher NA was thanks to a reduction in the resolution area.

The results obtained with the NA $= 0.16$ microscope indicate a sensitivity at the boundary of the single atom level. A single atom held within a resolution area, would produce a reconstruction with a signal to maximum noise level ratio of SNR $= 1.3$. The atomic signal is likely to fill an area on the order of a single pixel

in the reconstructed image, thus it would be difficult to distinguish from a noise fluctuation at this level of signal. By increasing the microscope NA to 0.7 to reduce the resolution area, a sensitivity to atom number per resolution area well below the single atom level ($\delta N_{\text{atom}} = 0.2$) is expected, even with an off-resonant probe at $|\nu| = 8$ (see section 7.1).

The impressive sensitivity to atom number inferred at NA=0.16 coupled with the even more impressive prediction at NA = 0.7, indicates that DSHM may provide an alternative route to number resolving detection of atomic samples [81]. Fluorescence imaging has regularly demonstrated number resolving detection for small ($N \sim 10$) ensembles of atoms [191–193], this has even been shown for $N \approx 1200$ [81]. However, the dependence of the shot-noise level on the square root of atom number means that achieving number resolving detection of larger ensembles becomes more challenging. The atom number sensitivity demonstrated by DSHM, along with the fact that the shot-noise level is proportional to the square root of the probe intensity and not the number of atoms opens up the possibility of DSHM being used for number resolving detection of larger samples ($N > 10^3$). The signal enhancement by collection of the forward scattering [37] inherent to coherent imaging when compared to fluorescence imaging (see section 2.3.1) is retained in DSHM. On the other hand, spatially resolved fluorescence detection of optical lattices [19–21, 190] only determines the number of singly occupied sites, since atom pairs are quickly lost due to light assisted collisions. Detuned probing as with DSHM can reduce the light assisted collisions. This coupled with the promised single atom sensitivity at $|\nu| = 8$, see fig. 7.1(b), may allow three dimensional spatially resolved detection of optical lattice sites with multiple atom occupancy per site [34].

7.2.3 Extended exposure holographic imaging at the shot-noise limit

To demonstrate the NA = 0.07 microscopes potential for imaging while cooling, a collection of images are presented with long exposure times. In all cases $s \ll 1$ for the probe beam, such that scattering force from the MOT cooling beams dominated that from the probe. Figure 7.4 shows images of atoms probed while cooling the sample for $\tau_{\text{exp}} = 10$ ms, fig. 7.4(a,b), and $\tau_{\text{exp}} = 2$ ms, fig. 7.4(c,d), with $\nu = 0$ and $\nu = 29$ respectively. Such long exposure times are impossible to achieve without cooling, since atoms would fall under gravity and be pushed a significant distance by the probe. The noise level in fig. 7.4(a,b), is twice the shot-noise level, due to a large

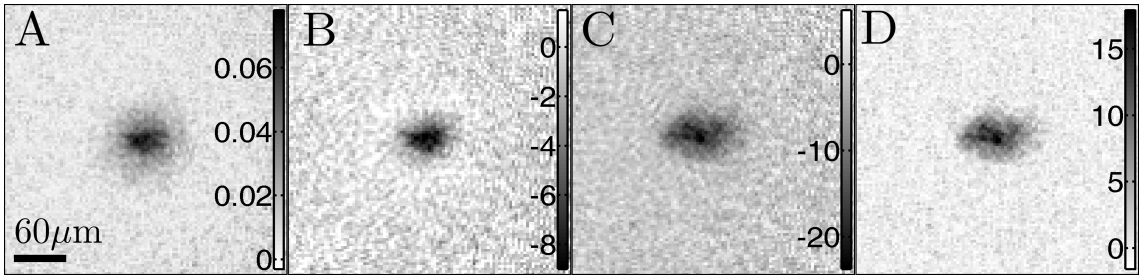

Figure 7.4: Images recorded with a long exposure time ($\tau_{\text{exp}} \gg 100$ μs) during cooling. (a) [$\nu = 0$, $\tau_{\text{exp}} = 10$ ms]: ρ_c. (b) [$\nu = 0$, $\tau_{\text{exp}} = 10$ ms]: α_f (%), extracted the hologram as (a). (c) [$\nu = 29$, $\tau_{\text{exp}} = 2$ ms]: ϕ. (d) [$\nu = 29$, $\tau_{\text{exp}} = 2$ ms]: ρ_c, extracted from the same hologram as (c).

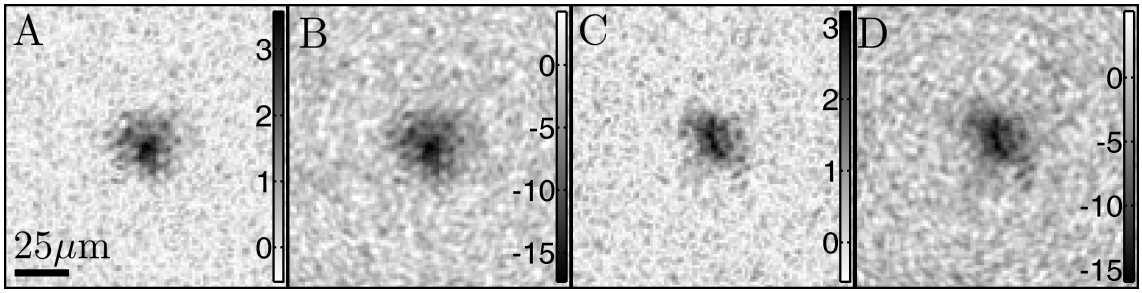

Figure 7.5: Images recorded at the shot-noise limit with the NA = 0.16 DSHM and a long exposure time ($\tau_{\text{exp}} = 10$ ms) while cooling in a MOT. (a) [$\nu = 7.9$, $\tau_{\text{exp}} = 10$ ms]: shot-noise limited ρ_c image. (b) [$\nu = 7.9$, $\tau_{\text{exp}} = 10$ ms]: ϕ image, extracted from the same hologram as (a). (c) [$\nu = 7.9$, $\tau_{\text{exp}} = 10$ ms]: Shot-noise limited ρ_c image. (d) [$\nu = 7.9$, $\tau_{\text{exp}} = 10$ ms]: ϕ image, extracted from the same hologram as (c).

ambient light background from the cooling beam scattering. A shorter exposure time with a detuned probe as in fig. 7.4(c,d), resulted in less destructive imaging with a noise level approaching the shot-noise limit.

With the improved NA = 0.16 DSHM system with an imaging lens, an aperture was located before the camera to coincide with the image of the double point source. The aperture removed the majority of the ambient light and the unwanted scattering from the MOT beams into the camera. This reduction in the noise sources permitted imaging while cooling at the shot-noise limit for extended exposure times. The ability of the NA = 0.16 DSHM to image at the shot-noise limit while cooling with $\tau_{\text{exp}} = 10$ ms is demonstrated in fig. 7.5, where ρ_c and ϕ images of MOTs were retrieved from holograms probed with with $\nu = 7.9$.

With such a large detuning $\nu = 7.9$, the sensitivity to atom number for the reconstructions displayed in fig. 7.5 is $\delta N_{\text{atom}} = 12$, since in this experiment the absorption cross-section was reduced by a factor ~ 16 from the resonant value. With a higher NA microscope and a smaller value of ν, the ability to image while cooling at the shot-noise limit may permit number resolving detection of weakly confined gases over long exposure times [19–21, 190].

7.2.4 Spatial confinement with a dipole trap

It is clear that to take full advantage of the atom number sensitivity in DSHM, the atoms movement during the exposure time must be restricted to within a resolution area R_{lat}^2 (see section 7.1). For micron imaging resolution, such confinement of atoms is impossible to achieve in MOTs or optical molasses since the atoms can diffuse out of a resolution area in a ~ 1 ms time scale. To restrict the atomic motion, experimenters often rely on optical lattices, where the light shifts confine atoms at the anti-nodes of a far-red detuned standing wave. Combining trapping with cooling in the lattice, the atomic motion can be restricted to within each lattice site, thus allowing the atom number to be counted from each site.

In this project, an attempt was made to restrict atomic motion during probing to a smaller volume using a dipole trapping potential while cooling with optical molasses. The dipole trapping light was provided by the output of a ECDL with $\lambda = 783.03$ nm. The $m = -1$ diffraction from a single pass AOM (see appendix D) provided precise and fast control of the dipole beam power. To provide output stability for the dipole trap beam, the output from the ECDL was aligned into an optical fiber before being delivered to the dipole trap focusing optics. At the output of the optical fiber the beam was first expanded and collimated to a diameter of 40 cm, then a focusing array identical to the collimating lens array described in appendix F, was used to focus the dipole trapping beam to a waist $w_0 \approx 2$ μm. For stability and control, the fiber launcher and focusing optics were mounted in a single lens tube which could be manoeuvred with a 3D translation stage. The beam focus was aligned to the MOT location by adjustment of the translation stage. After the beam manipulations $P \approx 7$ mW of power remained for the dipole trap, thus the beam focus had an intensity $I = 2P/\pi w_0^2 \approx 1.1 \times 10^8$ mWcm^{-2}. Such a beam resulted in a trap with depth $T = \hbar\Gamma s_0/8k_B\nu \approx 5$ mK, and a scattering rate of $R_{\text{sc}} = s_0\Gamma/8\nu^2 \approx 3 \times 10^3$ s^{-1}.

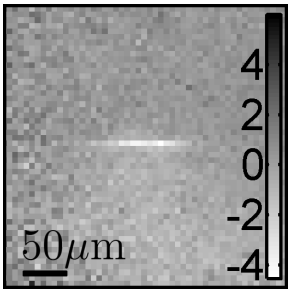

Figure 7.6: Absorption image (%) of a dipole trap retrieved by averaging twenty individual images.

To cool atoms into the dipole trap, atoms were initially loaded into the MOT with field gradient ~ 10 Gcm^{-1}, then the MOT field gradient was reduced to ~ 1 Gcm^{-1} and the MOT detuning was increased from $\Delta = -13$ MHz to $\Delta = -25$ MHz for a stage of polarisation gradient cooling (see appendix B.0.2). After holding the atoms in the dipole trap for ~ 10 ms, an absorption image of the sample was taken, see fig. 7.6, by translating the camera to the location of the in-focus image of the shadow of the dipole trap. Averaging over twenty absorption images the atoms in the trap were visible with ~ 4 % absorption. It was found that the trap loading efficiency was heavily sensitive to small changes in the wavelength of the trapping potential, which was attributed to photoassociation of excited state molecules [194, 195]

In the spherical wave geometry of DSHM, the intensity at the atomic plane is large compared to the camera. Atoms in the trap with an initial temperature of 100 μK probed with resonant light and $s_0 = 1$, have a scattering rate $R_{\text{scat}} = \Gamma/4 \approx 9 \times 10^6$ s^{-1}. With the recoil temperature for ^{87}Rb given by $T_r = 362$ nK [67], the atoms in the trap were heated to temperatures larger than the trap depth within 0.1 ms of probing. Imaging near-resonance to maximise the absorption cross-section also maximises the heating, thus in the long exposure times ~ 10 ms needed to make optimal use of the cameras bit depth, atoms were easily ejected from the trap.

As a consequence, detection of the dipole trap with DSHM requires a higher NA set-up capable of probing off-resonant to reduce heating. This heating must be balanced by cooling into the dipole trap to allow sufficiently long exposure times. Unfortunately due to time constraints with this project, an attempt to image the dipole trapped atoms while cooling with the upgraded NA = 0.16 DSHM was not undertaken. In a future attempt at imaging a dipole trap with DSHM, one may consider trapping atoms at the intersection of two focused beams to compensate for the poor longitudinal

trapping awarded by a single beam trap. In this scheme the atoms could be confined to smaller volume (e.g. $\sim 2\ \mu\text{m}^3$), thus improving the sensitivity to atom number.

7.3 Future Work

To achieve off-resonant single atom detection of optical lattices with DSHM, the most urgent task required is to develop and construct a DSHM system with a higher NA = 0.7. Proposals for such high NA systems are discussed in section 7.3.1. Imaging optical lattice sites with multiple atom occupancy would verify DSHMs ability to reduce the rate of light assisted collisions. Since the heating from the probe can be balanced by cooling, DSHM could be used to probe condensed atomic samples without destroying them. A direct comparison of the images reconstructed with DSHM to those in absorption and phase-contrast imaging would verify the claim made in this work that DSHM is expected to display a greater sensitivity.

7.3.1 Lens-free atom chip DSHM

To fully realise the potential of DSHM for imaging cold atom samples at high NA, in future the microscope could be integrated into an atom chip [196]. In such atom chip devices, a common initial cooling stage for the atoms is via a mirror magneto-optical trap [196–199]. To accommodate the mirror MOT system, the atom chips main surface can fabricated from a reflective metal [196] or dielectric [199], upon which current carrying wires can be fabricated [197] to manipulate the atoms cooled by the mirror MOT.

The proposed design consists of forming a mirror MOT system from a commercially available back side polished metallic/dielectric mirror (e.g. PF10-03-P01P, ⌀1" Back Side Polished, Protected Silver Mirror, Thorlabs). Sub-wavelength diameter pinholes can be fabricated into the reflective layer. A schematic of this set-up is given in fig. 7.7. With a transparent mirror substrate, the pinholes can be illuminated from the back side of the chip. Both pinholes can in principle be illuminated by a single light source on the back side. To improve pinhole transmission, two separate lenses can be used to focus light into each pinhole independently. The spatial filtering awarded by the pinholes removes speckle noise from dust and reflections that originate from optics placed before the back side of the chip. This also relaxes the requirements on the focusing lenses, since aberrations in the illuminating beam are eliminated on the experiment side of the chip. To avoid stray light transmitted through the reflective layer of the mirror, it is proposed that the pinholes be illuminated at an angle to the mirror surface, such that light unintentionally transmitted through the reflective layer

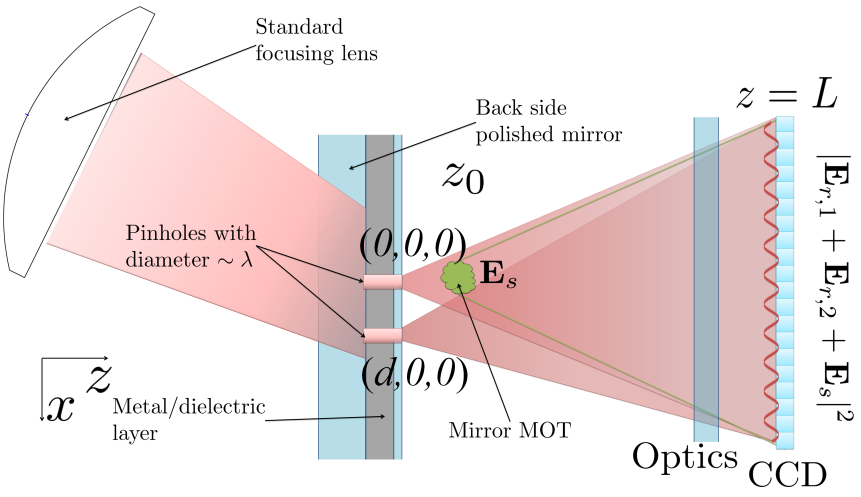

Figure 7.7: Schematic of the proposed atom chip with integrated DSHM. Two backside illuminated holes in a mirror surface form the point sources for use in DSHM. A tilted illumination beam prevents the light that inevitably transmits through the reflective layer from illuminating the camera. Atoms trapped and cooled near the mirror surface can be imaged with high numerical aperture.

misses the CCD chip, whilst the light transmitted via the pinholes travels toward the CCD. This arrangement may be difficult to realize in atom chip experiments where the chip is fabricated on a non transparent substrate, since manufacturing a $\sim 1\mu$m pinhole into a ~ 1 mm thick substrate is challenging with nano-fabrication techniques.

Pinhole fabrication

During this project, some initial efforts toward construction of an atom chip DSHM were pursued. Preliminary work toward achieving such pinhole sources was carried out in 2012-2013, which is described in a Masters Dissertation [106] co-supervised by the author of this work. The work was part conducted at Both Cardiff University and University Collage London, and funding for the work was awarded via the Engineering and Physical Sciences Research Council (EPSRC) Access to Nanoscience and Nanotechnology Equipment programme. To emphasize the ease and flexibility at which nano-fabrication techniques can generate the pinhole sources into thin metal/dielectric layers, in this section a review will be conducted of this effort in particular the recipe developed for fabricating the sub-wavelength sources in a commercially available mirror.

To fabricate the two sub-wavelength pinholes in the mirror surface, focused ion beam (FIB) lithography was employed. Initial investigations into pinhole fabrication

into a commercially purchased mirror surface using FIB yielded promising results, see fig. 7.8. A recipe for the fabrication of pinholes in a mirror surface with FIB was successfully developed. The mirror pinhole device was successfully integrated into a DIHM system for imaging samples on glass microscope slides. Impressively, a nano-fabricated logo was successfully imaged with NA = 0.72 with lens-free DIHM [106].

To prevent a charge build up on the non conductive mirror, and to hold the mirror onto the FIB sample stage a conductive metallic tape was used that was made to contact with the stage and mirror substrate, see fig. 7.8(a). Care must be taken to avoid damaging the mirror surface. Enquires into the specified thickness of the protective layer and the reflective layer were unsuccessful, since the distributors source from multiple manufacturers who each specify a different thickness. To address this issue and determine the thickness of the layers, test holes were drilled with FIB into the mirror surface near the edge of the mirror (away from the centre where the final holes are to be located). With the layer thickness known, a recipe for fabricating holes with any desired diameter was developed. Once a satisfactory pinhole fabrication recipe had been developed, the final holes were fabricated near the centre of the mirror, see fig. 7.8(b).

The images in fig. 7.8 show a collection of FIB fabricated pinholes in the surface of a back side polished mirror. The images were recorded at an angle to the normal of the mirror surface so that the pinhole depth could be measured. In fig. 7.8(c), a fabricated pinhole with diameter = 826 nm and aspect ratio ≈ 1 is displayed. For this particular mirror, the protective and reflective layers were 89 nm and 136 nm thick respectively, see fig. 7.8(d). To ensure that the FIB drills beyond the reflective layer, a hole 71 nm deep was fabricated beyond the reflective layer into the substrate. With a well established recipe, fabricating precision double pinholes with a well defined separation d was simple with FIB, see fig. 7.8(e). And further much more elaborate pinhole arrangements are easily fabricated, see fig. 7.8(f).

If optical access restricts the camera, then the hologram can be imaged to the CCD detector with larger (e.g. 51 mm diameter) high NA optics. Alternatively to improve the microscope NA beyond the NA = 0.16 and to remove plane window aberration, it is proposed that the lens system designed in [183] be used. With a wavelength of $\lambda = 780$ nm, the lens system achieves NA= 0.36 focusing whilst correcting for the aberration introduced by a plane window. If optical access restricts the pinhole camera separation L, this lens array may be used to image the hologram

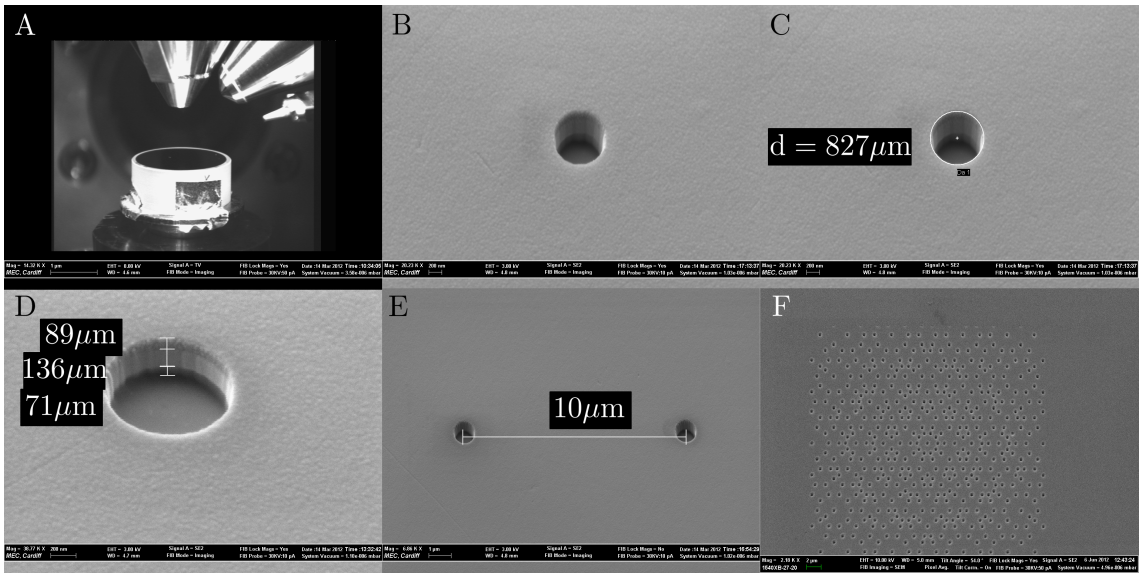

Figure 7.8: Electron microscope images of the pinholes fabricated into a backside polished silver mirror. (a) Image showing the mirror mounted on the stage for undertaking focused ion beam lithography (FIB). (b) and (c) Images of a 827 nm diameter pinhole fabricated into the mirror surface with FIB. (d) View of a pinhole from a 45° angle, showing the 89 μm thick protective SiO_2 layer, the 136 μm thick reflective silver layer and the 71 μm thick cut into the substrate. (e) Image showing two FIB fabricated pinholes separated by 10 μm. (f) Image showing a complex pattern of pinholes easily fabricated with FIB.

on to the camera, thus alleviating the restriction in NA due to optical access. Then the optics shown in fig. 7.7 would represent both the vacuum window and the imaging system. For set-ups that cannot accommodate atom chip DSHM, this lens system could be used as the focusing array for generating point sources (see section 4.4.2).

7.4 Conclusion

In this chapter the prospects of number-resolving detection in point source holographic imaging of cold atoms is discussed. Three key aspects are highlighted for pushing DSHM into the single atom regime: improving the holographic enhancement awarded by minimising the factor κ, increasing the numerical aperture to minimise the resolution area, and restricting the atomic motion to within a resolution area during probing.

An improved κ is easily achieved with a reduction in z_0. Toward improvement of the microscope NA, the improved NA $= 0.16$ DSHM demonstrated a sensitivity near the single atom level $\delta N_{\text{atom}} = 0.75$ with near-resonant probing. Shot-noise limited imaging of cold atoms in a MOT with an extended exposure time $\tau_{\text{exp}} = 10$ ms was shown, thus satisfying a pre-requisite for number resolving detection of weakly confined gases over long exposure times [19–21, 190]. To improve the microscope resolution further, an NA $= 0.7$ integrated atom chip DSHM has been proposed which should be capable of single atom detection even with $|\nu| = 8$. In an attempt to observe quantised atom number with DSHM, a $w_0 \approx 2$ μm waist dipole trap was successfully loaded with $N \sim 100$ atoms. However due to time constraints, an attempt to image the dipole trap has yet to be retrieved with holography.

With a high NA $= 0.7$ DSHM, off-resonant number resolving detection of optical lattice sites with multiple atom occupancy may be possible, since the off-resonant probe can reduce the light assisted collisions. Here a scheme is proposed [34] based on optical shielding [200, 201], where blue detuned light enhances the repulsion between symmetrically excited atom pairs. Atoms can be trapped in single lattice sites with strong x, y confinement. A blue detuned probe and auxiliary cooling beams with polarisation in the x-y plane, switch on adiabatically so that atoms within each site find new equilibrium positions along z. The blue detuned molasses should permit sub-Doppler cooling of the atoms in the lattice, thus permitting continuous shot-noise limited holographic detection for extended exposure times as demonstrated in this work.

Chapter 8

Conclusion

Holographic microscopes have widespread applications from imaging condensed structures with electrons to imaging biological samples with photons. However, the application of holographic microscopy to imaging cold atoms has been so far limited to a few precursory examples. The purpose of this work was to investigate the difficulties involved in applying holography to imaging cold atoms, develop solutions to these difficulties, and then exploit the well known advantages of holographic microscopy for cold atom research. To achieve this, a double point source holographic microscope (DSHM) was theoretically and experimentally developed, along with an experimental apparatus for generating atomic samples with controllable size and temperature for imaging.

The first difficulties preventing direct application of holography to cold atoms are the well known twin image problem, and DC noise problem for optically thick samples. Other attempts at overcoming these problems for imaging cold atoms include; diffraction-contrast imaging [23] that exploits the monomorphous responsivity of atoms, and spatial heterodyne imaging [25] that spatially separates the twin image noise from the real image, whilst temporal heterodyning has been proposed [102, 103] for cold atoms. However, these methods have not seen regular use throughout the cold atom research community due to their complexity and/or constraints, particularly for high numerical aperture imaging at both the shot-noise and diffraction limits. In chapter 5, advantage was taken of the unique characteristics of DSHM discussed in chapter 3 by use of an iterative algorithm to efficiently eliminate both the twin image and DC noise simultaneously, even for large atomic samples or when the recorded hologram is obscured by shot-noise.

The second difficulty is speckle noise, which is common to all imaging techniques to varying degrees of severity. In holographic microscopy, a common technique to alleviate speckle noise is to illuminate the sample with light that has a short coherence length [80]. This method of speckle noise removal is difficult to implement when imaging cold atoms, since the linewidth of the probing laser should be less than the detuning from the atomic transition, and should be less than the linewidth of the transition for near-resonant probing. Therefore in cold atom holography, speckle noise in the recorded hologram can originate from imperfections in optical surfaces meters away from the detector. Speckle noise in standard absorption imaging can result in false absorption signals, this prevents accurate absorption imaging of atomic samples near structured surfaces (such as an atom chip [196]). A holographic method of suppressing speckle noise is presented in chapter 5, where the sources of speckle noise are located, isolated, and then included into the reference field estimation used for image reconstruction, thus suppressing their distortion in the final image. With this speckle noise removal algorithm, an enhancement in the dynamic range for shot-noise limited imaging from SNR = 35 to SNR = 41 was observed, in spite of the reflections from the uncoated vacuum windows. With more careful design of the experimental apparatus, such as generating a double source reference field with sub-wavelength pinhole sources, anti-reflection coating of the vacuum windows, and/or using a wavefront sensing camera to improve the reference field estimation, the dynamic range for shot-noise limited detection should be easily further enhanced.

With the two major problems eliminated, a well known advantage inherent to holography was demonstrated for cold atoms for the first time in chapter 6, by the simultaneous phase shift $\phi(x, y)$ and optical depth $OD(x, y)$ retrieval from a single recorded hologram. A systematic literature review revealed that such retrievals in holographic microscopy are uncommon even outside of the bounds of cold atom research. For the retrievals, a method is developed to consistently estimate the in-line reference field $\mathbf{E}_r$ at the detection plane for extraction of the scattered wavefront $\mathbf{E}_s$, and $\mathbf{E}_r$ at the image focal plane for extraction of ϕ and OD via the complex ratio $\mathbf{E}_s/\mathbf{E}_r$. The precision of this method of retrieval was demonstrated by measuring ϕ and OD with shot-noise limited sensitivity with various detunings across the $F = 2 \rightarrow F' = 3$ cycling transition in ^{87}Rb (see chapter 6).

In addition to the well known advantageous properties of holographic microscopy, such as lens free 3D imaging, an important yet largely overlooked advantage was highlighted. With point source illumination, the intensity at the camera plane where

the out-of-focus diffraction from the sample is recorded can be significantly weaker than the intensity at the samples location, thus a significantly longer exposure time is afforded at the camera before its pixels are saturated compared to focal plane imaging methods such as absorption and phase-contrast imaging. Exploiting this holographic enhancement of signal collection, absorption and phase shift sensitivities as low as $\delta\alpha_f = (0.36 \pm 0.026)$ % and $\delta\phi = (1.8 \pm 0.13)$ mrad were consistently demonstrated, outperforming the expected shot-noise limited sensitivities in the established absorption and phase-contrast imaging by a factor of 8 in this particular experiment. Indeed, the sensitivity of absorption and phase-contrast imaging can in principle be improved by magnification of the image. However, optimising the sensitivity requires that the magnified image fills a significant fraction the camera. The magnified image of the atoms is then more susceptible to low spatial frequency noise in detection, thus leading to difficulties distinguishing signal from noise such as a laser power fluctuation shot-to-shot, or inhomogeneous dark counts due to temperature variations across the CCD. DSHM avoids this difficulty, since the signal can be recorded in a near optimal way by encoding it in high spatial frequency interference fringes over the entire CCD, thus DSHM can display a shot-noise limited sensitivity beyond those of regular techniques.

The holographic enhancement in imaging sensitivity was further explored for number resolving detection of atomic samples (see chapter 7). Similar to the retrieval of ϕ and OD, the column density ρ_c was easily extracted from the complex ratio $\mathbf{E}_s/\mathbf{E}_r$. As shown in chapter 7, the sensitivity to atom number per resolution area δN_{atom} was determined by summing the sensitivity to column density $\delta\rho_c$ over the smallest resolvable area $\delta N_{\text{atom}} = 4\delta\rho_c A_r = 4\sqrt{2\kappa A_p A_r / N_{\max}|\tilde{\sigma}|^2}$. Then it is easy to see that a combination of approaches can be undertaken to improve the atom number resolution with holographic microscopy including, a reduction in A_r with an increased NA, an improvement in the holographic enhancement factor κ, restriction of the atomic motion to within $4A_r$ during imaging, and choosing a camera with a large bit depth.

To pursue the first approach in this work, a sensitivity to atom number of $\delta N_{\text{atom}} = 2.7$ was first demonstrated with NA = 0.07 DSHM, then by improving the NA to 0.16 with lenses, a sensitivity near the single atom level was demonstrated $\delta N_{\text{atom}} = 0.75$ (see chapter 7). An attempt was made to observe quantised atom numbers by restricting atomic motion during the probe with a dipole trap. With atoms successfully loaded into the trap (see chapter 7), the next step is to pursue

imaging of the trapped atoms while cooling with the NA = 0.16 DSHM. In addition, imaging a MOT for an extended exposure time of 10 ms at the shot-noise and diffraction limits (see chapter 7) was demonstrated, a pre-requisite for number resolving detection of weakly confined gases over long exposure times [19–21, 190].

Further advantages intrinsic to holographic microscopy include, the possibility of 3D imaging and the ability to image lens and/or aberration free, the latter of which is demonstrated with modest NA = 0.07 and NA = 0.16 DSHM (see chapter 5). A continuing goal of the research group is to pursue the advantage of 3D imaging for imaging all occupied sites of a 3D optical lattice.

Outlook and evaluation

The author hopes that by addressing the noise problems in cold atom holography and demonstrating precise imaging of cold atoms at the shot-noise and diffraction limits, the work described in this thesis will open the doorway to regular use of holographic microscopy in cold atom research, particularly for retrieving 3D information with arbitrary probe detuning. Furthermore, this preliminary work has demonstrated the relatively unknown holographically enhanced sensitivity in measuring probe phase shift and attenuation, which may permit off-resonant imaging with single atom sensitivity.

Off-resonant probing with the developed holographic microscope may be exploited to alleviate difficulties associated with near-resonant absorption imaging of optically dense clouds, such as resonant dipole-dipole interactions inhibiting simple retrieval of the probe absorption by dense clouds via Beer's law [39] and multiple photon scattering in dense gases leading to a deviation in the expected absorption cross-section [40–42].

Increasing the complexity in the reference field $\mathbf{E}_r$, as demonstrated in this work, may be useful for twin image removal outside the bounds of cold atom research, such as in holography of biological samples [26, 202] and x-ray holography [121, 203]. Furthermore, the increased reference field complexity offers the possibility of probing the sample with both sources simultaneously, and could be explored to permit sub-diffraction limited resolution via structured illumination [204].

Improving the NA further to 0.7 with atom chip DSHM as discussed in section 7.3.1, should permit off-resonant ($\Delta = 8\Gamma$) DSHM with single atom sensitivity (see chapter 7). Taking advantage of the lensless nature of DSHM, diffraction limited and high resolution [80] imaging of cold atom samples will be possible without lens aberration. At high NA with sparse objects, such as single atoms in a 3D optical

lattice, three dimensional DSHM can be conducted with holographic depth of field without imaging lenses (see section 7.3.1). Utilising the benefits DSHM promises for off-resonant detection of atoms in an optical lattice is a research avenue demanding further attention, since single atom sensitive holographic microscopy may permit precise phase imaging of optical lattice sites with multiple atom occupancy, and extend the range of observables in quantum gas microscopy [19–22]. Furthermore, 3D resolving of optical lattices with large atom numbers and single atom sensitivity may pave the way to a scalable quantum computer [189, 190].

Appendix A

Temperature determination via the time of flight technique

A standard technique used with absorption imaging to determine the temperature of cold atom samples is the the time of flight (TOF) technique [166, 205–207]. This method was used in the first experiment to measure a cold atom gas with a temperature below the Doppler limit (eq. (B.7)) [72].

The expansion of an atomic cloud is recorded over time. From this expansion the temperature of the cloud can be deduced. With $j = x, y, z$, the j-axis velocity (v_j) for atoms in a atomic sample obey a Maxwellian distribution

$$f\left(v_j\right) = \left(\frac{m_a}{2\pi k_B T_j}\right)^{1/2} \mathrm{e}^{-\frac{m_a v_j^2}{2k_B T_j}}, \tag{A.1}$$

where m_a is the atomic mass and T_j the temperature along the j-axis. Equation (A.1) has the form of a Gaussian, as does the position distribution given by,

$$P\left(j\right) = \frac{1}{\sigma_j\left(t\right)\sqrt{2\pi}} \mathrm{e}^{-\frac{j^2}{2\left(\sigma_j(t)-\sigma_j(0)\right)}}, \tag{A.2}$$

where the parameter $\sigma_j\left(t\right)$ is the standard deviation of the distribution and $\sigma_j\left(0\right)$ is the standard deviation at a time $t = 0$. Equating the exponents of eqs. (A.1) and (A.2), the expansion of the cloud as a function of time follows,

$$\sigma_j\left(t\right) = \sqrt{\sigma_j\left(0\right) + \frac{k_B T_j}{m_a} t^2}. \tag{A.3}$$

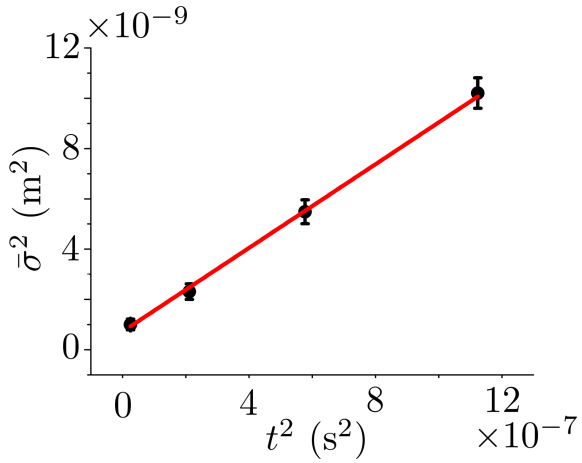

Figure A.1: Time of flight graph, with $\bar{\sigma}^2$ plotted against t^2. The red line is a linear fit to the data, the temperature extracted from this graph is 87 μK.

.

To extract the temperature using absorption imaging, images of the atomic position distribution can be recorded at different times t after the release of the atomic sample. Fitting each image with a 2D Gaussian allows identification of $\sigma_j(t)$ for each one. A plot of $\sigma_j(t)^2$ versus t^2 results in a straight line graph with gradient $G = k_B T_j / m_a$ and a y-axis intercept of $\sigma_j(0)$. Extracting G with a linear fit, the temperature is determined using

$$T_j = \frac{m_a G}{k_B}. \tag{A.4}$$

To demonstrate the ability of DSHM to image atomic samples with $N_f > 1$, a TOF experiment to determine the MOT temperature was conducted, see fig. A.1. With a compressed MOT of ^{87}Rb atoms to reduce the sample spatial extent prior to imaging, a MOT temperature of 87 μK was determined using eq. (A.4), below the Doppler temperature of 146 μK for ^{87}Rb [67].

Appendix B

Additional discussions on laser cooling

The forces that arise upon an atom at rest in a one dimensional radiation field along the z-axis can be calculated using the Ehrenfest theorem, which states that the force is given by the negative expectation value of the gradient of the Hamiltonian,

$$F = -\left\langle \frac{\partial \hat{H}}{\partial z} \right\rangle = -\operatorname{Tr}\left(\hat{\rho} \frac{\partial \hat{H}}{\partial z} \right). \tag{B.1}$$

This expression is analogous to the classical description of a force being the negative derivative of a potential. Using eq. (B.1) and invoking the rotating wave approximation [46–48], the force depends on the coherences of the density matrix,

$$F = \hbar \left(\frac{\partial \Omega}{\partial z} \rho_{12}^{*} + \frac{\partial \Omega^{*}}{\partial z} \rho_{12} \right). \tag{B.2}$$

The derivative of the Rabi frequency is split into its real and imaginary parts, $\partial\Omega/\partial z = (q_r + \mathrm{i}q_i)\,\Omega$. The real part describes the spatial gradient of the field amplitude whilst the imaginary part corresponds to the phase gradient. Using the steady state solution of eqs. (2.17) to (2.20) for ρ_{12},

$$F = \frac{\hbar s}{1+s} \left(-\Delta q_r + \frac{\Gamma q_i}{2} \right). \tag{B.3}$$

When an atom is illuminated with a single plane beam of light (a travelling wave) its amplitude is constant but the phase is not so $q_r = 0$ and $q_i = k$, where k is the wave

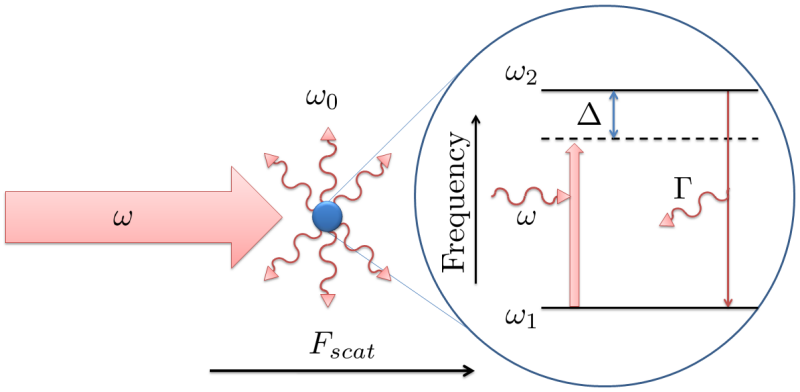

Figure B.1: A single beam of radiation excites the transition in a two level atom resulting in a radiation force F_{scat} along the beam direction. Each spontaneous emission event is random and the recoil momentum received by the atom averages to zero over many events.

number. When it is illuminated with two beams of light with equal amplitude in opposing directions (a standing wave) the phase is constant but the amplitude is not, hence in this regime $q_r = -k\tan(kz)$ and $q_i = 0$. Using these two situations, the expression for the force can be split into two separate constituent parts, a dissipative scattering force and a conservative dipole force. An atom in a radiation field can spontaneously emit a photon, resulting in a force acting upon it. During absorption of light from a travelling radiation field there is a transfer of momentum to the atom. Following this absorption, the atom can spontaneously emit a photon, thus there is further momentum transfer in a random direction. This random momentum transfer due to spontaneous emission averages to zero over many emissions. Thus using eq. (2.26) and eq. (B.3) the magnitude of the scattering force exerted by the radiation field is given by

$$F_{\text{scat}} = \hbar k \Gamma \rho_{22} = \hbar k \frac{\Gamma}{2} \frac{s_0}{1 + s_0 + (2\Delta/\Gamma)^2}. \tag{B.4}$$

This is simply a product of the momentum transfer per photon scattered $\hbar k$, the excited decay rate Γ and the probability to be in the excited state ρ_{22}. This force corresponds to the second term in eq. (B.3), which is non-zero in travelling wave illumination and zero in a standing wave. At large intensities and with detuning near resonance ($s \gg 1$), the atomic transition saturates and the excited state population $\rho_{22} \to 1/2$, see eq. (2.26). Hence under these conditions the force reaches a maximum value $F_{\text{max}} = \hbar k \Gamma/2$. As this force relies on the spontaneous scattering of light out of

the radiation field, it is a dissipative force, since the reverse of spontaneous emission is impossible [46]. This dissipation of energy via the scattering force is used as a mechanism for cooling atomic samples.

In a standing wave of two equal opposing plane waves the scattering force vanishes as the momentum received from a beam propagating in one direction is equal to that received by a beam propagating in the opposing direction. Leaving only the force known as the dipole force, which corresponds to the first term in eq. (B.3). When $|\Delta| \gg \Gamma, \Omega$, this dipole force approaches the negative derivative of the light shift, see eq. (2.11),

$$F_{\text{dip}} \simeq -\frac{\partial\left(\hbar\delta\omega_{\text{a.c}}\right)}{\partial z} = \frac{\hbar\Omega}{2\Delta}\frac{\partial\Omega}{\partial z}. \tag{B.5}$$

The light shift acts as a potential in which the atoms move. For $\Delta < 0$ the potential is attractive with respect to intensity and has a minimum where the intensity is largest (i.e. atoms are attracted the the anti-nodes of a standing wave.). For $\Delta > 0$ the reverse is true and the atoms are repelled from the anti-nodes. The dipole force that is proportional to the gradient of the light shift does not saturate at large intensities as in the case of the intensity dependant scattering force. However it cannot be directly used to cool as it is conservative. It can be used in conjunction with spontaneous emission to trap and cool atomic samples [73, 74].

B.0.1 The Doppler cooling limit

The isotropic nature of spontaneous emission results in the atoms receiving a momentum kick in a random direction after each emission. For an atom in a standing wave it is assumed that the scattering rate is twice that of a single beam, and the effect of the optical force on the atoms is ignored momentarily. For atoms undergoing spontaneous emission the atomic velocity undergoes a random walk in a time t, and the mean square velocity increases along the $z-$axis as $\bar{v^2}_{z(\text{scat})} = 2v_r^2\Gamma\rho_{22}t/3$. Here v_r is the recoil velocity and the factor of $1/3$ is the angular average for isotropic emission. This only accounts for the spontaneous emission from one of the standing waves, thus the true value is three times larger. Before a spontaneous emission a photon is absorbed. The number of photons absorbed from a single standing wave in each time period t is not constant. This results in a one dimensional random walk of the mean square velocity, $\bar{v^2}_{z(\text{abs})} = v_r^2 2\Gamma\rho_{22}t$, with all photons being absorbed along the same axis. Including these additional fluctuation terms and accounting for the effect of the mean optical force eq. (2.51), the rate of change of the kinetic energy is

given by,

$$\frac{1}{2}m\frac{d\bar{v^2}_z}{dt} = 2mv_r^2\Gamma\rho_{22} - \alpha\bar{v^2}_z. \tag{B.6}$$

With the recoil energy given by $\mathrm{E}_r = \frac{1}{2}mv_r^2$, and using eq. (B.6) it can be shown that in steady state $\bar{v^2}_z = 4E_r\Gamma\rho_{22}/\alpha$. The velocity along the $z-$axis is related to the temperature by $\frac{1}{2}m\bar{v^2}_z = \frac{1}{2}k_BT$. Substituting for α and ρ_{22}, and with $s_0 \ll 1$ so it can be ignored in the denominator of eq. (2.26),an expression for the temperature that is at its minimum T_D when $\Delta = -\Gamma/2$ can be found,

$$T_\mathrm{D} = \frac{\hbar\Gamma}{2k_B}. \tag{B.7}$$

This Doppler temperature was thought to be the limiting temperature for the optical molasses technique. But the two level treatment is too simple and there are mechanisms that allow cooling beyond T_D such as the linear-perpendicular-linear Sisyphus cooling mechanism operated on atoms with degenerate ground states (see appendix B.0.2). The optical molasses technique produces a force that is dependent on the atomic velocity, as this is not a position dependent force it is not a trap for atoms and they are easily able to diffuse out of the overlap region of the beams.

B.0.2 Sisyphus cooling

The Doppler limit was soon seen as an inadequate limit for laser cooling of cold atoms when a temperature of 43 ± 20 μK was measured in an optical molasses of Sodium atoms [72] using the time of flight technique (see appendix A), well below the predicted Doppler limit of $T_D \approx 240$ μK. This observation led to the discovery of new cooling mechanisms that can explain the low temperature. Sisyphus cooling describes a group of cooling schemes that involve an atom travelling in a spatially varying potential. In general, if an atom exists in a state which expends a large amount of kinetic energy as it travels up a potential gradient and can be switched to a state which receives less kinetic energy as it travels down the gradient, it will slow down over many cycles in a process reminiscent of the Greek Sisyphus myth. For ease of discussion, one of the more simpler realisations of Sisyphus cooling are covered, which is a well established sub-Doppler cooling mechanism.

Linear-perpendicular-linear polarisation gradient cooling

As the name suggests, linear-perpendicular-linear polarisation gradient cooling is a type of Sisyphus cooling that consists of creating a standing wave from two opposing beams with linear polarisation. The method utilises the differing effect

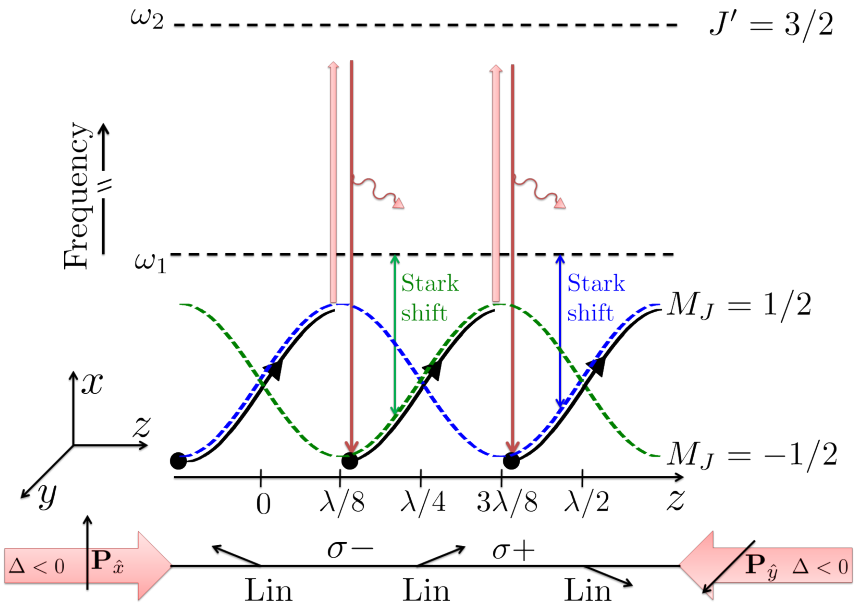

Figure B.2: The effect of the varying polarisation $\mathbf{P}$ along a standing wave formed by two counter-propagating beams with linear polarisation on the magnetic sub-states states of a $J = 1/2$ to $J = 3/2$ transition in a multilevel atom. The solid black lines displays a "trajectory" that an atom can undertake in such a standing wave. The varying polarisation allows the atoms to switch ground states after a spontaneous emission, as the light shifts of the sub-levels are out of phase with each other the atom can be made to perpetually travel up potential gradients, with the kinetic energy that was converted into potential energy while travelling up the potential carried away by the spontaneous emission.

of the polarisation on the light shift of different magnetic sub-levels [74]. Two counter-propagating plane waves with linear polarisation produce a standing wave with polarisation at a particular distance along the wave depending on the relative phase of the two beams, see fig. B.2. The simplest case where this cooling mechanism works requires an atom with ground and exited state angular momenta of $J = 1/2$ and $J = 3/2$ respectively. The ground state has two magnetic sub-levels $M_J = \pm 1/2$, whilst the excited state has four $M'_J = \pm 1/2, \pm 3/2$. For more complex atomic structures than the two level atom, the a.c. Stark shift of the two ground states depends on the polarisation of the light through the Clebsch-Gordan coefficient C_{12}, which describes the coupling between the atom and the radiation [47],

$$\delta\omega_{\mathrm{a.c.}} = \frac{\Delta s_0 {\mathrm{C}_{12}}^2}{1 + (2\Delta/\Gamma)^2}. \tag{B.8}$$

The light shift of the ground $M_J = 1/2$ magnetic sub-level is three times larger than that of the $M_J = -1/2$ ground sub-state when the polarisation of the resultant light field is σ^+, and vice versa for σ^-.

Consider the situation in fig. B.2, an atom begins with all the population in the $M_J = 1/2$ ground state at $z = -\lambda/8$. At this location the polarisation of the light field is σ^+ and the strongest transition the light will excite is the cycling transition to the $M'_J = 3/2$ state, which can only decay back to the $M_J = 1/2$ ground state resulting in no loss of kinetic energy. As the atom travels along the standing wave, the $M_J = 1/2$ state travels up a potential gradient as the polarisation changes with z. When it reaches $z = \lambda/8$, the light field polarisation is σ^- and the coupling to the $M'_J = -1/2$ state is at its strongest. From this excited state the atom can spontaneously emit a photon, after which the entire population can decay to either of the $M_J = \pm 1/2$ ground states. If the atom decays to the $M_J = -1/2$ state it looses more energy than if it were to decay to the $M_J = 1/2$ state, since at this σ^- polarisation the the light shift is larger for the $M_J = -1/2$ sub-level. With the atom now in the $M_J = -1/2$ sub-level, the atom is at a location where the polarisation is σ^- and the transition with the strongest coupling is the cycling transition to the $M'_J = -3/2$ excited state. As the atom travels further along the standing wave, the polarisation continues to change and the $M_J = -1/2$ state travels up a potential gradient until it reaches $z = 3\lambda/8$ where the light is σ^+. Now the coupling to the $M'_J = -1/2$ state is at its strongest, and after a spontaneous emission from this excited state the entire population can decay to either of the ground states, thus

the process can continue. If there is a switch of the ground state sub-level after spontaneous emission, the kinetic energy the atom converts into potential energy as it travels up a potential gradient is taken away by the spontaneous emission. If there is no switch of the ground state then there is no change in the kinetic energy. Over many averages of this Sisyphus mechanism the atomic kinetic energy will reduce, since depending on the decay channel the atom either looses kinetic energy or exhibits no change in kinetic energy after each spontaneous emission.

The energy that is carried away by each photon when there is a switch of the ground states is equal to the difference in light shift between the two ground states U_0. When the atoms kinetic energy is below U_0 it can no longer reach the top of the potential, thus cooling will cease. As the light shift is proportional to $I/|\Delta|$, then so is the temperature,

$$k_B T \simeq U_0 \propto I/|\Delta|. \tag{B.9}$$

This method of Sisyphus cooling requires initial Doppler cooling of atoms, for example in an MOT (section 2.2.3), as the capture velocity v_c, related to the population transfer rate Γ_{trans} between the ground states after a spontaneous emission, is small compared to the capture velocity of the MOT. If $|\Delta| \gg \Gamma$ in the standing wave, then Γ_{trans} can be calculated from eq. (2.26) as $\Gamma_{\text{trans}} = s_0\Gamma^3/4\Delta^2$. The mechanism works best for atoms that have velocity $v = \lambda\Gamma_{\text{trans}}/4$ such that they are likely undergo a ground state population transfer each time they travel a distance equal to $\lambda/4$. This discussion has ignored the effect of stray magnetic field on the cooling scheme for example the Earths magnetic field at $\sim 5 \times 10^{-4}$ T produces a Zeeman shift comparable to the light shift required to cool to sub μK temperatures. This limits cooling to ~ 10 μK, thus stray magnetic fields are often eliminated in laser cooling labs with compensation coils. Other types of Sisyphus cooling include σ^+-σ^- polarisation gradient cooling [47, 73] and magnetically induced laser cooling [47, 208]. However reducing the the factor $I/|\Delta|$ in eq. (B.9) toward zero does not reduce the temperature toward zero, since the recoil from random nature of spontaneous emission results in a temperature limit to this cooling mechanism known as the recoil limit (see appendix B.0.3).

B.0.3 The recoil limit

Naively one would think that simply by reducing the factor $I/|\Delta|$ in eq. (B.9), the atomic kinetic energy could be reduced toward zero for the linear-perpendicular-linear polarisation gradient cooling scheme. However, when an atom undergoes a

spontaneous emission it receives a random momentum kick that increases the kinetic energy by the recoil energy E_r, when this recoil energy balances the energy lost by climbing up a potential gradient $U_0 = \mathrm{E}_r$, there will be no net loss of energy and Sisyphus cooling will cease. A thorough investigation into the cooling limit of the Sisyphus mechanism was presented in [209] where they find the minimum kinetic energy to be a few tens of times the recoil energy. The recoil temperature T_r associated with the recoil energy can be found using $\frac{1}{2}k_B T_r = E_r$, with a substitution for E_r,

$$T_r = \frac{m v_r^2}{k_B} = \frac{\hbar^2 k^2}{k_B m}. \tag{B.10}$$

Atomic species with larger mass have a lower recoil temperature than lighter ones. As an example, the recoil temperature for ^{87}Rb is $v_r = 5.89$ mm/s whilst for the lighter ^{11}Na the recoil velocity is $v_r = 2.95$ mm/s.

Appendix C

Saturated absorption spectroscopy

The resolution of standard absorption spectroscopy at room temperature is limited by the effect of Doppler broadening on the spectral lines. In saturated absorption spectroscopy, the effect of Doppler broadening is eliminated by use of an intense pump beam that is counter-propagating to a weaker probe beam used to measure the absorption of a gas of atoms often contain within a glass vapour cell.

C.1 Absorption Spectroscopy

The standard set up for absorption spectroscopy using a glass vapour cell is to have a probe laser beam pass through the cell and hence through the vapour of atoms contained within. The absorption of the probe beam as it passes through the vapour cell is described using Beer's law [46]. A Schematic of the set-up for absorption spectroscopy is displayed in fig. C.1.

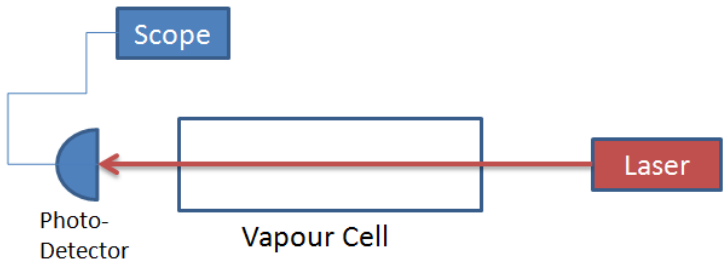

Figure C.1: Displayed is a schematic of the set up required to acquire an absorption spectrum. Inside the vapour cell would be a gas of atoms for (for example Rubidium). The frequency of the laser can be controlled, so that the laser frequency can be scanned over a certain time frame.

Consider the case where the atoms in the vapour cell are two level atoms. The difference in energy between these two levels is $E = hf_0$, where f_0 is the resonant frequency. In the absence of any external radiation the population of the excited state will decay to the ground state with a mean lifetime τ. The Uncertainty principle

$$\Delta E \Delta t = \hbar, \tag{C.1}$$

results in a broadening of the line with a full width at half maximum (FWHM) given by $\Gamma = \frac{1}{\tau}$, this is known as the natural line width of the transition, and this process is often referred to as natural broadening. However, this is not the only broadening mechanism. Consider that the atoms within the vapour cell have a temperature T, thus they will have a distribution of velocities within the vapour cell. As the lasers frequency is scanned it can interact with a larger number of atoms in the vapour cell. Each atom absorbs radiation at an angular frequency $\omega_0 = 2\pi f_0$ in its rest frame, thus atoms moving at a velocity v see the incoming laser beam with a frequency shifted by the Doppler effect. these atoms are most likely to absorb radiation from the beam when,

$$\Delta = kv. \tag{C.2}$$

The fraction of atoms in the vapour cell with a velocity in the range v to $v + dv$ is,

$$F(v)\,\mathrm{d}v = \sqrt{\frac{m_a}{2\pi k_B T}} \exp\left(-\frac{m_a v^2}{2k_B T}\right) \mathrm{d}v, \tag{C.3}$$

Where m_a is the mass of the atom [46] and T the temperature. Using equation eq. (C.2), it can be shown that $v = c\left(\frac{f-f_0}{f_0}\right)$ and $dv = \frac{c}{f_0} df$, thus,

$$g(f)\,\mathrm{d}f = \frac{c}{f_0}\sqrt{\frac{m_a}{2\pi k_B T}} \exp\left(-\frac{m_a C^2 (f-f_0)^2}{2k_B T f_0^2}\right) \mathrm{d}f. \tag{C.4}$$

When the incident laser beam is at the resonant frequency f_0, the above Gaussian line shape function reaches a maximum. When $f - f_0 = 0$, the exponential term becomes one, thus the maximum of the line shape is,

$$g(f_0) = \frac{c}{f_0}\sqrt{\frac{m_a}{2\pi k_B T}}. \tag{C.5}$$

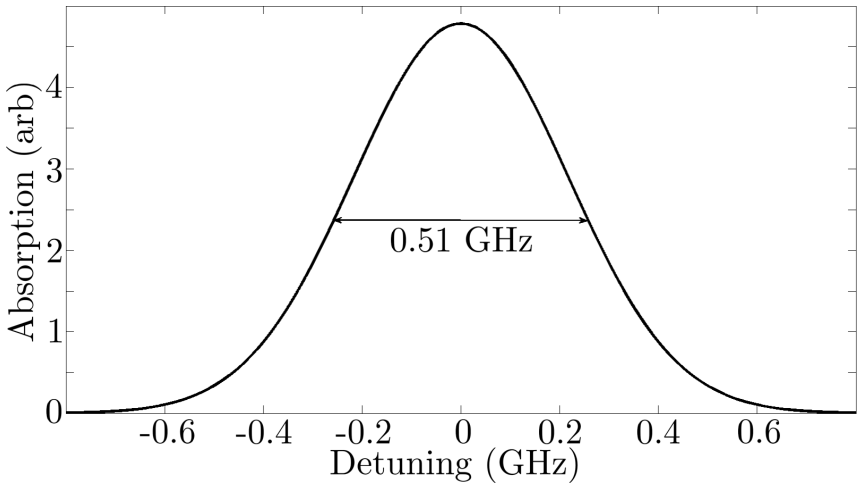

Figure C.2: This is a plot of theline shape given by equation eq. (C.4), as can be seen here the FWHM of the peak is 0.5 GHz for ^{87}Rb in a vapour cell at a temperature of 300K.

The FWHM of this Gaussian line shape occurs when $g(f) = \frac{g(f_0)}{2} = g(f_0)\exp(-\ln(2))$, thus using equation eq. (C.4),

$$-\ln(2) = -\frac{m_a C^2 (f_D - f_0)^2}{2k_B T f_0^2}, \tag{C.6}$$

where f_D is the frequency of the laser at half the maximum peak value. Then rearranging for $f_D - f_0$,

$$f_D - f_0 = \sqrt{\frac{2\ln(2)\, k_B T f_0^2}{m_a C^2}} = \frac{1}{\lambda_0}\sqrt{\frac{2\ln(2)\, k_B T}{m_a}}. \tag{C.7}$$

With the knowledge that the distribution is symmetrical about the maximum, the Doppler broadened line width is,

$$\Delta f_D = 2(f_D - f_0) = \frac{2}{\lambda_0}\sqrt{\frac{2\ln(2)\, k_B T}{m_a}} = 2\ln(2)\frac{u}{\lambda_0}, \tag{C.8}$$

where $u = \sqrt{\frac{2k_B T}{m_a}}$ is the most probable speed for the atoms. The fractional width is thus,

$$\frac{\Delta f_D}{f_0} = 2\ln(2)\frac{u}{c}. \tag{C.9}$$

This Doppler broadening mechanism causes a problem in terms of the resolution.

Take the example of the ^{87}Rb isotope with $T = 300$ K, the Doppler broadened line width is 0.51 GHz as shown in fig. C.2. This width is larger than the hyperfine splitting between all of the hyperfine levels in the $5P_{3/2}$ state which is ≈ 494 MHz. This method would not resolve the hyperfine structure, thus the true spectra would be hidden in the Doppler broadened line. The true line shape is a Voigt, which is a convolution between the Lorentzian natural line shape and the Doppler broadened Gaussian line shape. If the width of the Gaussian line shape is much larger than the natural line width then this line shape is well approximated by a Gaussian.

C.2 Saturated Absorption Spectroscopy

In saturated absorption spectroscopy a weak probe beam is passed through the glass vapour cell as would occur in regular absorption spectroscopy. Except a strong pump beam is also sent through the vapour cell in such a way that it is counter propagating to the probe beam and overlaps the probe beam inside the vapour cell. Both the pump and probe beams originate from the same laser, thus have the same frequency f. Using the optical Bloch equations (see chapter 2), the exited state has a population given by eq. (2.26). When $I \gg I_s$, the transition saturates and $\rho_{22} \to 1/2$ (see chapter 2). At these intensities power broadening [46] becomes important, which leads to an increased linewidth given by,

$$\Gamma' = \Gamma \left(1 + \frac{I}{I_s}\right)^{1/2}. \tag{C.10}$$

This power broadening occurs because the saturation effect of the transition at high laser intensities reduces the absorption near f_0, further from the resonant frequency the absorption changes little [46].

The experimental set-up for saturated absorption spectroscopy is displayed in fig. C.3. Both the pump and probe beams have the same frequency f. When the lasers frequency is scanned, the frequency of the pump and probe beams are scanned in the same way. If the pump beam is blocked before it enters the vapour cell, then the same result would be observed as for absorption spectroscopy. If the pump beam in unblocked, it passes through the vapour cell and can interact with atoms that have a velocity,

$$v = (f - f_0)\,\lambda. \tag{C.11}$$

This is because atoms moving with this velocity will see the laser beam Doppler shifted into resonance. And due to the power broadening effects it will also interact

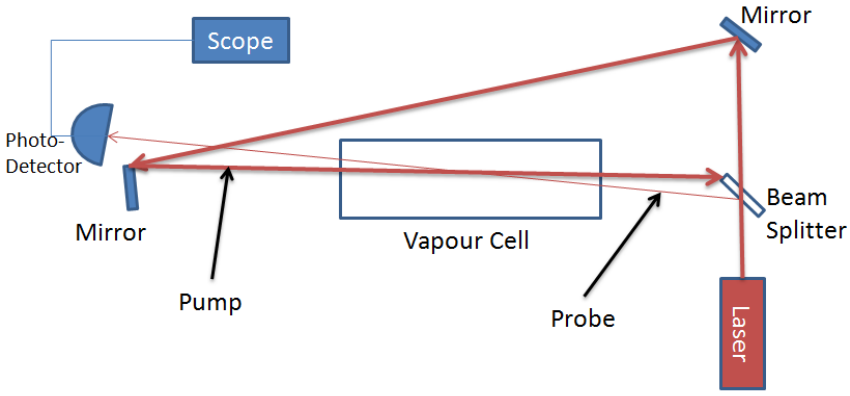

Figure C.3: Displayed is the apparatus required to achieve saturated absorption spectroscopy. The laser beam from is split into two separate beams by a beam splitter, the probe beam is much weaker than the pump beam.

with a few velocity classes surrounding the value of v given by equation eq. (C.10). The atoms that lie within this velocity range are excited to the upper state, thus reducing the ground state population of the atoms moving at these velocities. This process is often referred to as "hole burning" (i.e. a hole is burned in the ground state population of the atoms). As the pump beam intensity $I > I_s$, these atoms transitions become saturated. Consider the scenario where $v/\lambda \gg \Gamma$, the probe beam interacts with atoms moving with the same speed as those interacting with the pump beam but in the opposing direction $(-v)$, since this beam is counter-propagating to the pump. As the pump beam interacts with a different velocity class to the probe it has no effect on the probes interaction. However, there is a scenario where both the pump and probe beams can interact with the same velocity class at the same time. Consider the scenario where frequency of the pump and probe beams are equal to the atomic resonant frequency $f = f_0$, then both beams will interact with the same velocity class ($v = 0$) as equation eq. (C.11) becomes zero. Now the pumps interaction with the atoms can have a significant effect on the absorption of the probe. In the overlap region with the probe, the pump saturates the transitions of the atoms moving at $v = 0$. When the probe passes through the overlap region with the pump, it sees atoms that have their transitions saturated by the pump, thus the probe will have a reduction in its absorption. Due to stimulated emission processes the probe can be amplified as it interacts with the saturated atoms. The detector will record a higher light intensity for the probe when it has a frequency around f_0 when compared to frequencies where $|f - f_0| \gg \Gamma'$. From the point of

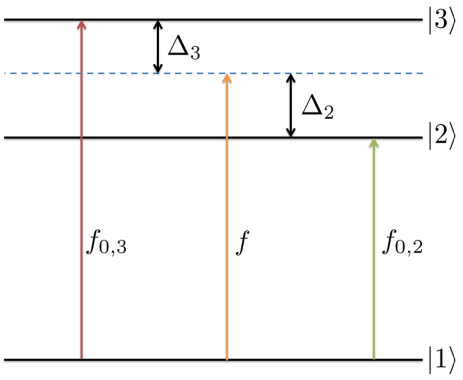

Figure C.4: Displayed is a drawing of a simple three level system with a single ground state $|1\rangle$ and two excited states $|2\rangle$ and $|3\rangle$.

view of the detector, as the lasers frequency is scanned, for frequencies $f \neq f_0$ the same Doppler broadened absorption profile as with regular absorption spectroscopy will be observed. The pump beam and probe beam interact with different velocity classes and do not effect one and other. On top of this Doppler broadened Gaussian absorption line shape, a reduction in the absorption about $f = f_0$ will be observed. This reduction appears as a peak with Lorentzian line shape that is broadened by the power broadening mechanism with a width given by equation eq. (C.10).

C.2.1 Cross-over Resonances

In real spectra obtained by saturated absorption spectroscopy, more peaks than are explained in appendix C.2 are observed. Additional decreases in absorption are seen exactly half way between the peak locations that correspond to the atomic resonances. This is due to the fact that real atoms are not well described by the two-level system. The simplest system that can be considered where these additional cross-over resonances occur is the three level system. Consider a three level atom that has one ground state and two excited states as depicted in fig. C.4. The frequency of the pump and probe beam is again given by f whilst the resonant frequency of the transitions from state $|1\rangle$ to $|2\rangle$ and $|1\rangle$ to $|3\rangle$ are $f_{0,2}$ and $f_{0,3}$ respectively. The detuning of the pump and probe lasers from the $|1\rangle$ to $|2\rangle$ and $|1\rangle$ to $|3\rangle$ transitions are Δ_2 and Δ_3 respectively. As before, the pump and probe can interact with the atoms moving at zero velocity when $f = f_{0,2}$ or when $f = f_{0,3}$ and absorption can be reduced for the probe beam as described in section appendix C.2. In the three level system there are two further situations where the pump and probe laser beams can interact with the same velocity class of atoms at the same time. Consider the

situation where the probe and pump beams have frequency $f_{0,2} < f < f_{0,3}$. The probe beam is blue detuned with respect to the $|1\rangle$ to $|2\rangle$ transition, thus it will excite this transition in atoms that have a velocity

$$v_{\text{probe}} = \frac{f - f_{0,2}}{\lambda}. \tag{C.12}$$

As $f > f_{0,2}$, the velocity is negative and the probe excites the $|1\rangle$ to $|2\rangle$ transition in atoms moving away from its source. The pump can interact with the atom, by exciting the $|1\rangle$ to $|3\rangle$ transition this occurs when,

$$v_{\text{pump}} = \frac{f - f_{0,3}}{\lambda}. \tag{C.13}$$

As $f < f_{0,3}$ the velocity is positive, thus the pump can interact with atoms moving toward its source. Then at the same time the probe interacts with atoms moving in the direction of its propagation, the pump interacts with atoms moving against its direction of propagation, thus both beams interact with atoms moving in the same direction. The two velocity classes that these beams interact with can become the same if $v_{\text{probe}} = v_{\text{pump}}$. Under this condition the frequency of the pump and probe beam reqired is,

$$f = \frac{f_{0,3} - f_{0,2}}{2}. \tag{C.14}$$

When this condition is met the pump and probe beams are interacting with the same velocity class of atoms, but with two different transitions within the atoms. The significance of this is much the same as if they were interacting with the same transition for atoms moving at zero velocity as described in section appendix C.2. The pump will interact with the $|1\rangle$ to $|3\rangle$ transition and saturate the atoms it interacts with. In the crossover region between the pump and probe beams in the vapour cell, the probe will see atoms that have been saturated by the pump on the $|1\rangle$ to $|3\rangle$ transition. Then the probe beam will see a reduction its absorption in this crossover region with the pump beam.

Yet there is another velocity class of atoms, for which the above is true. If the transitions that each beam interact with are reversed compared to the previous treatment, the probe now excites the $|1\rangle$ to $|3\rangle$ transition and the pump the $|1\rangle$ to $|2\rangle$ transition. The probe beam is red detuned from the $|1\rangle$ to $|3\rangle$ transition and it

will excite this transition in atoms moving at a velocity,

$$v_{\text{probe}} = \frac{f - f_{0,3}}{\lambda}. \tag{C.15}$$

Now $f < f_{0,3}$ and $v_{\text{probe}} > 0$, the probe excites this transition in atoms moving toward its source. At the same time the pump can excite the $|1\rangle$ to $|2\rangle$ transition in atoms moving with a velocity,

$$v_{\text{pump}} = \frac{f - f_{0,2}}{\lambda}. \tag{C.16}$$

Now $f > f_{0,2}$, thus $v_{\text{pump}} < 0$ and the pump excites atoms moving away from its source. As before these two velocity can be equal and the frequency at which this occurs is again exactly the same frequency given by equation eq. (C.14). The probe beam will see atoms that have their $|1\rangle$ to $|2\rangle$ transitions saturated by the pump beam in the overlap region between the two beams in the vapour cell. the probe will see a reduction in the absorption at this frequency. When the pump and probe have a frequencies given by equation eq. (C.14), the pump and probe beams can interact with two separate velocity classes of atoms simultaneously. The probe beam will see an even larger decrease in absorption in the vapour cell as it can interact with twice the amount of atoms (i.e. the velocity class at v and $-v$ simultaneously). These peaks that occur half way between two resonant frequencies of two transitions within the atom are called cross-over resonances. This decrease in absorption can give an even larger decrease in absorption than the case of the pump and probe interacting with the same transition for atoms moving at $v = 0$, since larger numbers of atoms interact with the pump and probe beams. Larger peaks in the saturated absorption spectrum are expected for cross over resonances. Experimenters often prefer to dither lock [166] their lasers to these larger peaks, since they provide a more defined frequency reference.

C.2.2 Experimentally Observed Spectra

Using the relations and information discussed in the previous sections, what is observed in saturated absorption spectra obtained experimentally can be interoperated. The spectrum displayed in fig. C.6 was obtained using Rb vapour in a vapour cell in a set up similar to that displayed in fig. C.3. Rb is predominantly composed of two isotopes, the stable ^{85}Rb, and the radioactive ^{87}Rb with a half life of about 49 billion years. ^{87}Rb has a 28% abundance with the rest composed of mainly ^{85}Rb.

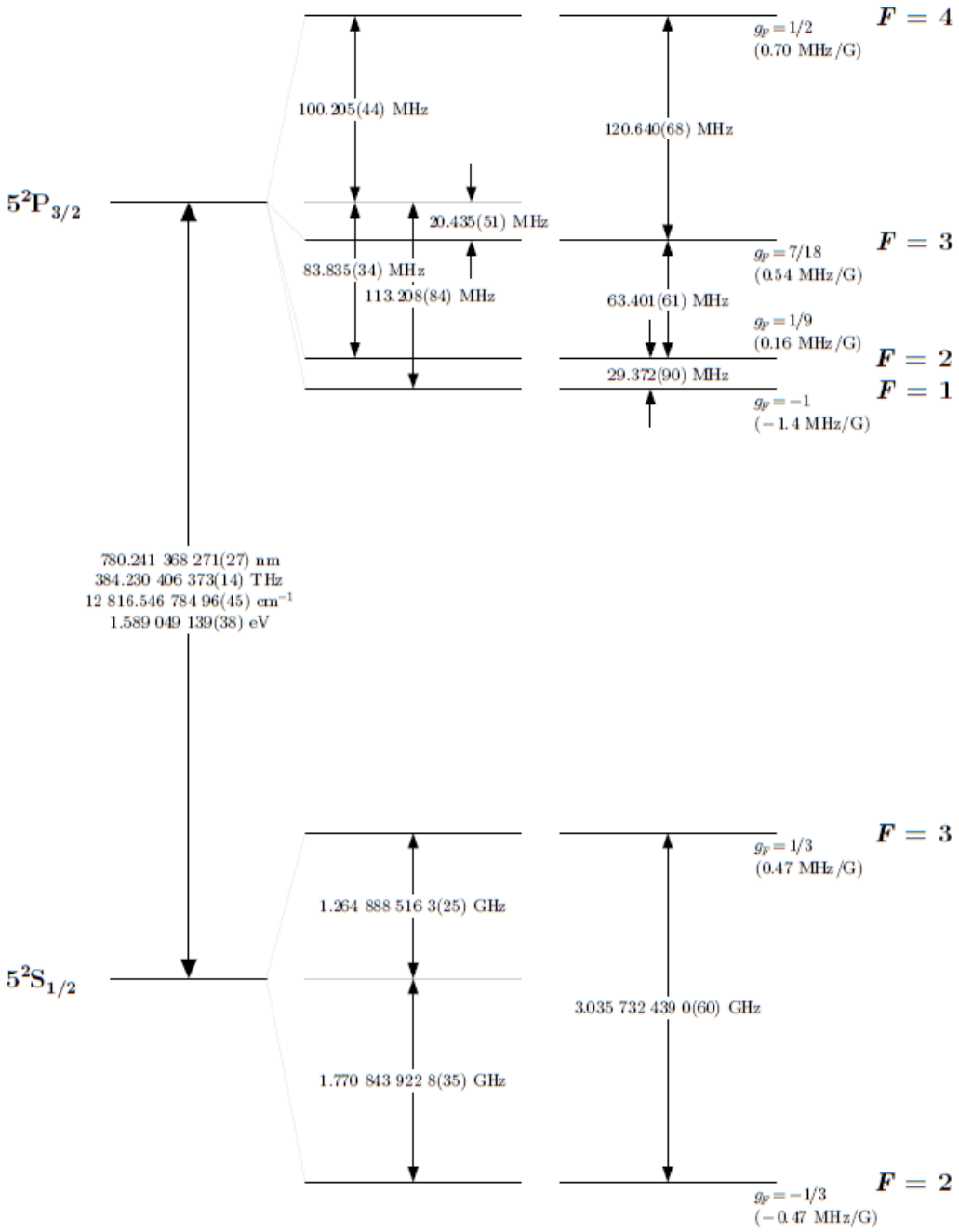

Figure C.5: Schematic taken from [210] showing the hyperfine energy levels of the ^{85}Rb D_2 line with the frequency splitting between the levels. The approximate Lande g_F factors for the levels are given, with the corresponding Zeeman splitting between adjacent magnetic sublevels.

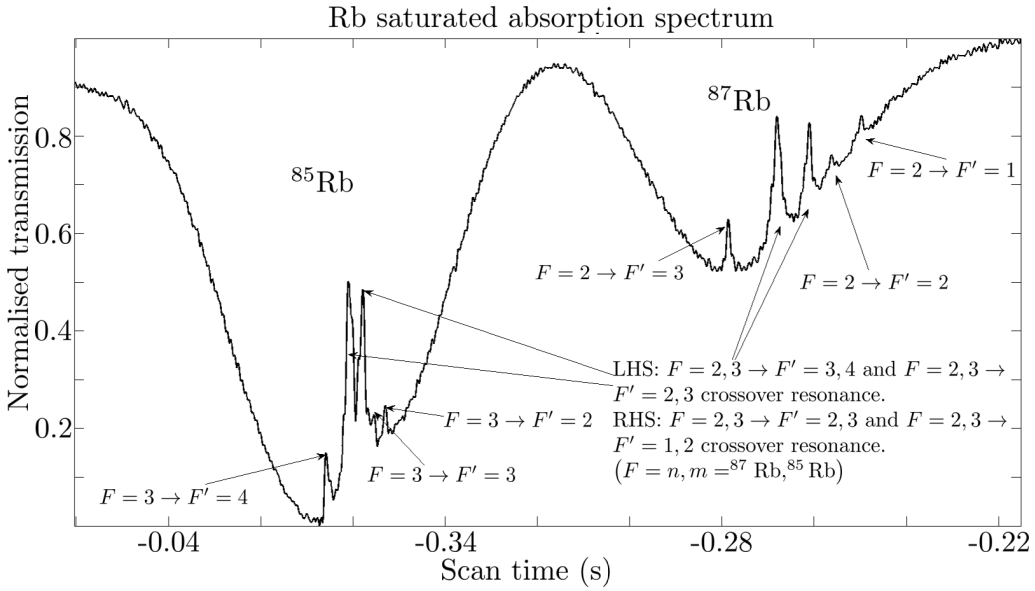

Figure C.6: The spectrum on the left is that obtained for the D_2 line in ^{85}Rb. The spectrum on the right is from ^{87}Rb it has the same peak structure as ^{85}Rb but the peaks have a larger spacing between them.

The ground state of Rb is the $5S_{1/2}$ state. The atom can be excited to the 5P sate by either going from $5S_{1/2} \rightarrow 5P_{1/2}$, which is called the D_1 transition, or by the D_2 transition $5S_{1/2} \rightarrow 5P_{3/2}$. This discussion will focus on the D_2 transition. The hyperfine splitting arises due to the coupling of the total angular momentum and the nuclear spin [46].

For ^{87}Rb, a schematic of the D_2 transition is displayed in fig. 4.4, whilst a schematic the ^{85}Rb D_2 line displayed in fig. C.5. looking at the D_2 line in ^{87}Rb, and considering the transition from $F = 2 \rightarrow F' = 1, 2, 3$, first peaks should be observed in the saturated absorption spectrum corresponding to the laser beam interacting with each of the three transitions when the atoms have zero velocity. As well as the three resonance peaks, crossover resonances are expected half way between each of the transitions. The same is expected for ^{85}Rb, except the separation between the peaks is less, since the hyperfine splitting is smaller. Considering the relative abundance of ^{85}Rb compared to ^{87}Rb, a larger signal is expected from ^{85}Rb, since there are more atoms there for the beam to interact with. Larger peaks are expected for crossover resonances, since the beams interact with larger numbers of atoms. The spectrum displayed in fig. C.6 was obtained by scanning the frequency of an ECDL [164, 165] by adjusting the voltage to a piezoelectric transducer that adjust

the orientation of a grating placed in front of the output of the laser. Looking at fig. C.6, two large Doppler broadened absorption profiles can be seen. The larger profile (to the left) is due to ^{85}Rb, and the smaller profile (on the right) is due to ^{87}Rb. This difference in the two absorption profiles is expected from their relative abundance. Inside the Doppler broadened absorption profiles peaks can be seen in the normalised transmission. These peaks corresponds to the transitions between the hyperfine levels in the D_2 line. The transitions shown in this spectrum are all excited from the ground $F = 2$ state. The $F = 2 \rightarrow F' = 1$ peak is unresolvable as it weaker than the nearest crossover peak. Using the simple theory presented in the previous sections predictions of the structure of the saturated absorption spectrum can be made. These peaks can be used to generate an error signal, which is essentially the derivative of the line of the peak. this error signal can be used in a PID (Proportional Integral Derivative) control system to dither lock [166] the frequency of the laser to one of the transitions or to one of the crossover resonances if desired.

Appendix D

Acousto-optic modulators

Acousto-Optic Modulators (AOM's) are devices that use sound waves to diffract light. The diffracted light experiences a frequency shift corresponding to an integer multiple of the sound frequency. AOM's consist of a piezoelectric transducer and a crystal, through which the sound waves propagate. The AOM is used widely in the field of laser cooling and atomic physics for high speed manipulation of the frequency and intensity of laser light.

D.1 Theory

Inside an AOM, sound waves propagate at the velocity of sound in the crystal (v_s). The sound waves are essentially pressure waves that increase and decrease the density of the crystal periodically, thus periodically altering the refractive index of the crystal. This acts as if there multiple moving interfaces within the crystal. What the light 'sees' when it propagates through the crystal is a diffraction grating moving at velocity v_s.

D.1.1 Bragg's Law

Considering the case where there are multiple interfaces within the crystal each separated by a distance λ_s, which is analogous to the description of atoms in a crystal lattice. A ray of light impinging on one of the interfaces with an angle of incidence θ, will be reflected with the same angle of reflection. A proportion of the beam will be transmitted through the interface, where it can be reflected by the next interface a distance λ_s from the first. This results in two rays being reflected off successive interfaces within the crystal, see fig. D.1. The condition that the two rays undergo constructive interference is known as the Bragg's condition. For this to hold, the

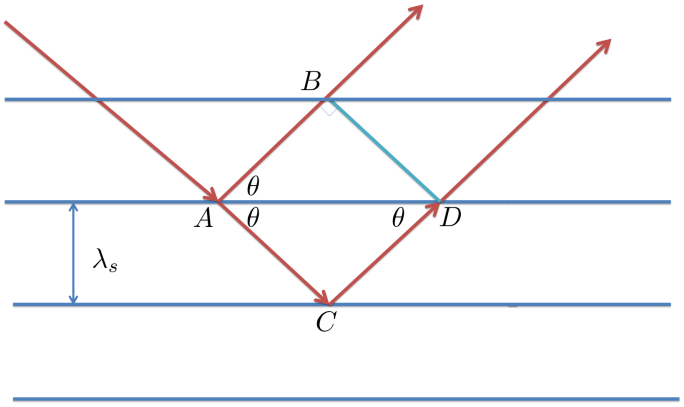

Figure D.1: Bragg diffraction off periodic interfaces.

path difference between the two rays must equal an integer value of the wavelength of light (λ),

$$(AC + CD) - (AB) = n\lambda, \tag{D.1}$$

where AC, CD and AB represent the distance between the points A, B, C, or D, see fig. D.1. Looking at the geometry in fig. D.1 it can be shown that,

$$AC = CD = \frac{\lambda_s}{\sin\theta}, \tag{D.2}$$

$$AD = \frac{2\lambda_s}{\tan\theta}. \tag{D.3}$$

Using eqs. (D.2) and (D.3), an expression for AB can be found as,

$$AB = AD \cdot \cos\theta = \frac{2\lambda_s}{\tan\theta}\cos\theta = \frac{2\lambda_s}{\sin\theta}\cos^2\theta. \tag{D.4}$$

Substitution of eqs. (D.2) to (D.4) into equation eq. (D.1) gives Bragg's law [211],

$$n\lambda = \frac{2\lambda_s}{\sin\theta}\left(1 - \cos^2\theta\right) = 2\lambda_s \sin\theta. \tag{D.5}$$

D.1.2 Propagating sound wave

Considering the case where a sound wave is propagated through a crystal, the travelling pressure wave causes the crystal to have a periodic density modulation matching the period and speed of the sound. This density change also causes the refractive index of the crystal to alter periodically. This effectively introduces multiple

moving interfaces in the crystal that propagate in tandem with the sound wave. Once the sound wave reaches the end of the crystal it is prevented from reflecting back toward its origin using an acoustic absorber, which is usually an angled cut of the crystal. The light ray would observe a similar situation as in appendix D.1.1, except now the periodic interfaces would be moving at the velocity of the sound wave, see fig. D.2. Taking the example in shown in fig. D.2, the incoming light ray with frequency f sees the periodic interfaces traveling toward it at a velocity v_s. The zeroth order ($m = 0$) diffracted ray will pass through the crystal unaffected. The first order diffracted beam ($m = 1$) will be Doppler shifted because of the motion of the interfaces. The frequency of the first order diffracted ray f_1 is Doppler shifted by the frequency of the sound wave f_s,

$$f_1 = f + f_s, \tag{D.6}$$

or more generally,

$$f_m = f + mf_s. \tag{D.7}$$

This frequency change can be thought of as the absorption of a phonon by the light from the crystal. Or in the reverse process the creation of a phonon in the crystal due to the interaction with the light field. The change in the laser beam frequency is then given by,

$$\delta f = mf_s, \tag{D.8}$$

where δf corresponds to the frequency shift experienced by the light ray, hmf_s is the energy of the phonon absorbed or created and h is Planck's constant. $m < 0$ corresponds to the creation of a phonon whilst $m > 0$ corresponds to absorption [212].

The frequency shift is required by energy and momentum conservation. Another consequence of momentum conservation is that each order of diffraction m will only appear at specific angles of incidence to the direction of propagation of the sound wave. The frequency of sound typically used in AOM's is ~ 100 MHz. Compared with the frequency of a near infra red laser ~ 400 THz, the frequency of the sound is orders of magnitude smaller. This means that the magnitude of the momentum vectors k_0 and k_1(shown in fig. D.3) are approximately equal, and $\theta_1 \approx \theta_2 \approx \theta_3$. These conditions must be satisfied to observe the diffracted beam of any order.

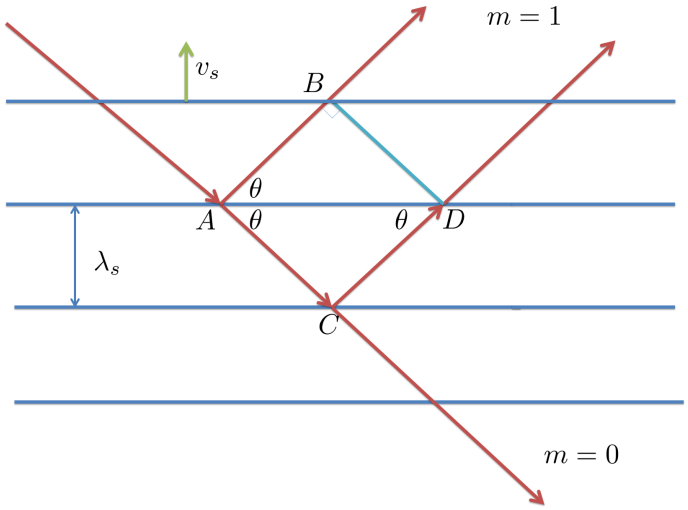

Figure D.2: Bragg diffraction off moving periodic interfaces.

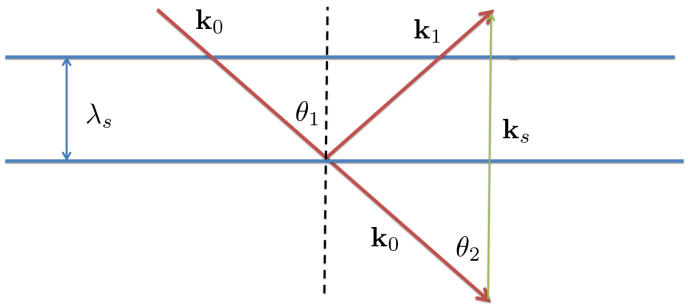

Figure D.3: The momentum vectors of the zeroth and first orders of light, and the sound momentum in the AOM.

This frequency shifting effect is often used in laser cooling experiments to gain precise frequency control of lasers [213]. The intensity of the diffracted rays can be varied by altering the intensity of the sound waves in the crystal using an AOM [214]. The AOM benefits from a switching speed that is limited by the time it takes a sound wave to propagate through the diameter of the incident beam (D), $\tau \approx D/v_s \sim 10$ ns. The switching speed, intensity and frequency control makes the AOM an essential tool for for experiments with atoms.

D.1.3 Importance of the acoustic absorber

In AOM's, an acoustic absorber is used to prevent the sound waves from reflecting back toward their origin, this absorber is usually an angled cut at the end of the crystal. The acoustic absorber is important, since if it were not present a standing wave would form in the crystal. A ray of light passing through the crystal could

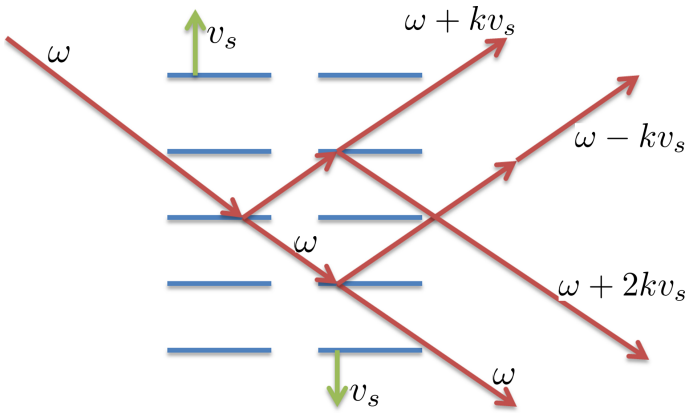

Figure D.4: Frequency shifts that occur when light ray interacts with a standing sound wave.

interact with both sound waves that form the standing wave, thus resulting in some unwanted effects. Displayed in fig. D.4 are the effects that can occur. Considering only the $m = -1, 0, 1$ orders of diffraction, since at a certain angle only one order of diffraction will be favoured, thus only these orders will contribute to the situation being considered. A ray incoming to the crystal with angular frequency ω will interact with the first sound wave (velocity upward in fig. D.4). The zeroth order will pass through unaffected. The first order will be diffracted and have its angular frequency shifted by $\omega + kv_s$, where k is the wavenumber of the sound wave. This first order ray can then interact with the second sound wave (velocity downward in fig. D.4) and again either be transmitted (zeroth order) without a frequency shift or diffracted (first order) and frequency shifted by $\omega + 2kv_s$. The zeroth order ray from the interaction with the first sound wave (i.e with angular frequency ω) can also interact with the second sound wave. It can zeroth order diffract again, or it can negative first order diffract off the sound wave, thus resulting in a ray frequency shifted by $\omega - kv_s$. The result is that the two beams that leave the crystal are both composed of two separate frequencies. A photo detector placed in the path of these beams would observe the beat frequency (i.e the difference between the component frequencies).

D.2 Operation

The simplest way to use an AOM is in the single pass configuration, see fig. D.5. An amplified output from a radio frequency (RF) signal generator is connected to the AOM, with RF power large enough to power the AOM efficiently. Typical

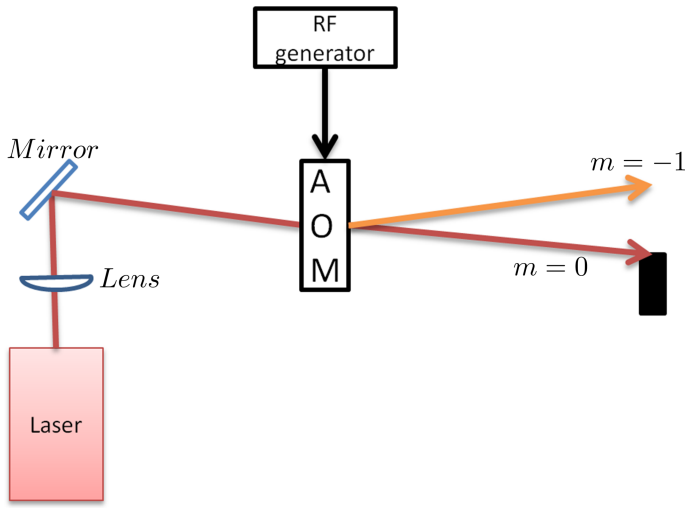

Figure D.5: Schematic diagram for a single pass AOM set up, the lens is used to optimize the beam shape entering the AOM for increased diffraction efficiency. The zeroth ($m = 0$) order is blocked by a beam blocker.

operating power and frequency of AOM's for use in laser cooling are ~ 2 mW and ~ 100 MHz respectively. The RF signal causes the Piezoelectric transducer in the AOM to vibrate at the RF frequency, which causes a sound wave at that frequency to propagate through the crystal. The laser beam shape and angle of incidence to the AOM is adjusted to optimize for the positive or negative first order diffraction, since the first order diffracted beams have a higher diffraction efficiency than those of higher order [212].

The frequency shift of the output light in this configuration is given by eq. (D.7). A disadvantage of this design is that when the frequency of the sound wave is altered the diffraction angle changes, thus altering the beam direction. This can hamper experiments that require high precision alignment and frequency modulation.

D.2.1 Double Pass AOM

Another common AOM configuration is the double pass, Again the negative or positive first order diffracted beams are most commonly used. A diagram of the set up is displayed in fig. D.6. The input laser beam with initial frequency f is sent through a polarizing beam splitter (PBS), thus making it linearly polarized. Here the beam input angle is adjusted to favour the $m = +1$ order of diffraction. The $m = 0$ beam is blocked by a beam blocker, whilst the $m = +1$ sent through a lens and a $\lambda/4$ wave plate. At the focal point of the lens a mirror is placed, thus the beam is retro reflected back along its original path through the $\lambda/4$ wave plate

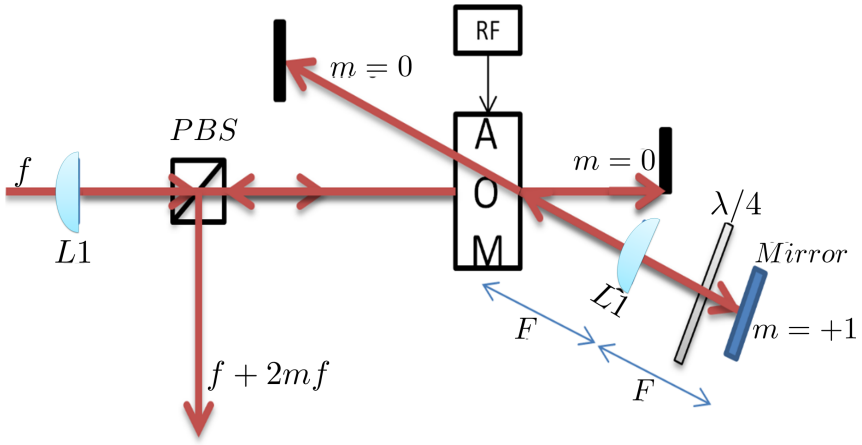

Figure D.6: Double Pass AOM

and the lens in the reverse direction. The AOM is placed a distance equal to the focal length of the lens (F) away from the lens, thus the retro reflected beam will re enter the AOM optimally. The first pass through the $\lambda/4$ wave plate changes the lights polarization from linear to circular. The second pass changes the polarization from circular back to linear but orthogonal to the initial polarization. The light then travels back through the AOM where it is diffracted for a second time. The zeroth order can be blocked by a second beam blocker if unwanted. Whatever order was collected and retro reflected on the first pass through the AOM must again be selected on the second pass[1]. This second passed beam should travel back along the reverse direction of the initial input laser beam, but now is has a polarization that is orthogonal to the initial beam. When this beam interacts with the PBS it will be reflected away, see fig. D.6, thus separating it from the input. And as it has passed twice through the AOM, it has acquired twice the frequency shift of a single pass,

$$f_{DP} = f + 2mf_s, \tag{D.9}$$

where f_{DP} represents the frequency of the output. Similar to selecting the second order diffraction in the single pass set up, this design can be useful if larger frequency shift are required, since it gives twice the shift of the first order in the single pass configuration. However this set up is advantageous compared to the single pass configuration since adjusting the sound frequency does not adjust the output direction

[1]If on the first pass the $m = +1$ order was retro reflected back then, on the second pass through the AOM the same order must be selected

of the double passed beam, thus making alignment of output beam much more stable and reliable [212].

Appendix E

Hybrid broadband-Zeeman slowing

In this section an attempt at building an atomic beam slower for delivering atoms to experiments such as a MOT will be discussed. The design consists of combining the established Zeeman [1, 4, 65, 66] and broadband [70, 71] slowing techniques. The goal of the proposed slower is to create an efficient mechanism of delivering large quantities (e.g. 10^{12} s^{-1}) of slow atoms to a MOT without the need for water cooling of the Zeeman coils or large laser power for broadband cooling.

A strong magnetic field ($|B| \approx 341$ G) is required in a Zeeman slower to compensate for the Doppler shift experienced by an ^{87}Rb atom in an atomic beam travelling with the most probable velocity ($v = 266$ ms^{-1} see section 2.2.1). Capturing a large fraction of the atomic velocity distribution requires Copper coils that carry large currents. The resistive heating from coils running high currents often require heat dissipation in the form of water cooling. An alternative to Zeeman slowing that avoids the need for water cooling of the coils is broadband slowing [70, 71]. However broadband slowing requires a high power light source to have sufficient power to slow at each frequency component.

To counteract the problem of requiring cooling for Zeeman coils and to relax the laser power demand of a broadband slower, a hybrid slower consisting of an initial broadband section and a second Zeeman slower section was proposed, see fig. E.1. A Zeeman slower in the reverse configuration [46] uses a Zeeman slowing beam with $\Delta = -180$ MHz to slow atoms from $v \approx 140$ ms^{-1} at the beginning of the Zeeman section to $v \sim 5$ ms^{-1} at the entrance of the MOT. The Zeeman slower beam is slightly focusing along the slower tube to compensate for radial heating. The Zeeman

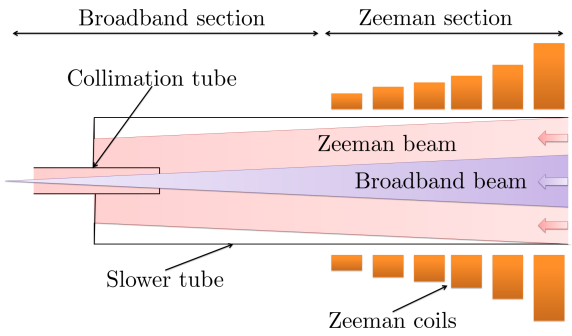

Figure E.1: Schematic of the hybrid broadband-Zeeman slower design.

coils here are the same as those described in section 4.2.1, and require a maximum field ~ 100 G. The field produced with these coils require a current small enough that the resistive heating in the coils can be dissipated by air cooling. With this Zeeman slower only capable of slowing atoms that have velocity $v \lesssim 140$ ms^{-1}, a significant fraction of ^{87}Rb atoms leaving the oven at T =370 K are not slowed.

To slow atoms that travel too fast for the Zeeman slower to capture, a broadband laser beam can be used to slow atoms in the broadband section, see fig. E.1, to $v \approx 140$ ms^{-1} by the entrance of the Zeeman section. To achieve the broadband beam, an EOM modulated with a sine wave with $\sim$1 V amplitude and ~ 10 MHz frequency is used. The modulated output from the EOM is used as a seeding beam with a central frequency detuning of $\Delta \sim 250$ MHz. The EOM modulation produces frequency spikes displaced by integers of the sine wave frequency mirrored either side of the central detuning. To achieve significant laser power, the modulated broadband beam is used as seeding light for injection locking a diode laser. The broadband output of the locked laser has a power ~ 30 mW. This beam is kept narrower than the Zeeman beam to preserve its intensity. And similar to the Zeeman beam it is focused along the broadband slower section to a diameter ~ 1 cm at the exit of the collimation pipe to compensate for radial heating. When the EOM modulates with a sufficient amplitude sine wave, at least one frequency component has a smaller detuning than that of the Zeeman beam $|\Delta| < 180$ MHz. The broadband frequency then spans $\Delta f \sim 140$ MHz, hence the largest velocity that the broadband beam can slow is $v = \lambda|\Delta_{\max}| \approx 250$ ms^{-1}. To prevent the atoms from falling into a dark state with respect to the broadband and Zeeman slower beams, significant repump light resonant to the $F = 1 \rightarrow F' = 2$ transition in ^{87}Rb co-propagates with both beams along the slower tube.

With the Zeeman beam and coils switched on, atoms are delivered to the MOT as expected (As described in chapter 4). However when the broadband beam is switched on there is a reduction in the MOT fluorescence by ~ 10 %. Numerous attempts at adjusting the central frequency and frequency span of the broadband beam failed to noticeably increase the MOT fluorescence. After much discussion, it was realised that the broadband beam has frequency components with $\Delta = -266$ MHz that are resonant with the $F = 2 \rightarrow F' = 2$ transition, see fig. 4.4, for atoms in the MOT, since they have small velocities. With components at this frequency the broadband beam may blow atoms out of the MOT. In an attempt to counteract this the broadband beam was realigned to avoid the MOT location. However even with the realignment no noticeable increase in the MOT fluorescence could be observed.

This may be due to the broadband beam components with $\Delta \approx -266$ MHz causing significant de-pumping of atoms moving at slow velocities near the end of the Zeeman slower section into the $F = 1$ ground state, hence preventing efficient slowing. Another possible reason is that there is insufficient power in the broadband beam for slowing over such a large frequency span.

To counteract the problem of de-pumping atoms, it is proposed here that the D_1 transition in ^{87}Rb [67] be addressed with the broadband beam. If addressing the $F = 2 \rightarrow F' = 2$ transition in the D_1 line, a detuning approaching -816 MHz is possible before the broadband beam can come into resonance with the $F = 2 \rightarrow F' = 2$ transition for low velocity atoms. With sufficient repump light co-propagating with the broadband beam resonant with either of the $F = 1 \rightarrow F' = 1, 2$ transitions, the broadband slowing section should slow atoms to the Zeeman section. And with a frequency significantly different from that of the Zeeman beam, the broadband slower should not degrade the performance of the Zeeman section.

Appendix F

Upgraded imaging system specifications

In this section the details of the upgraded lens system for achieving higher numerical aperture (NA ≈ 0.23) imaging with DSHM is discussed. To validate the assumption that the $\mathbf{E}_1$ part of the reference field is well described by a spherical wave (see section 3.1), the imaging system described in section 4.4.3 must be diffraction limited and minimise aberrations introduced by the lenses and the glass cell vacuum windows. Due to a limitation imposed by the version of OSLO used in this work [147], the number of optical interfaces that can be modelled must be less than 10. To counteract this the lens system is split into three sections that are coined, the focusing array, the collimating array and the imaging array. Each section has fewer than ten interfaces, and provided that each part of the system is diffraction limited, it is assumed that the final system (all parts combined) is too diffraction limited.

In a cautious improvement to the earlier NA = 0.07 point source generating lens array described in section 4.4.2, the focusing array here is designed to achieve diffraction limited focusing with NA ≈ 0.23. The focusing lens system, see fig. F.1(a), is based upon the design discussed in [181] and later modified in [182, 183], where a 4-lens combination of commercially available lenses consisting of a plano-concave lens(LC1582-B N-BK7 Plano-Concave Lens, Thorlabs), bi-convex lens (LB1901-B N-BK7 Bi-Convex Lens, Thorlabs), a plano-convex lens (LA1608-B N-BK7 Plano-Convex Lens, Thorlabs) and a positive meniscus lens (LE1234-B ⌀ 1", N-BK7 + Meniscus Lens, Thorlabs) account for aberration introduced by a plane window.

Due to a lack of optical access, the focusing array lens diameters are restricted to 1". To minimise the aberration in the system the air spacings are varied using the

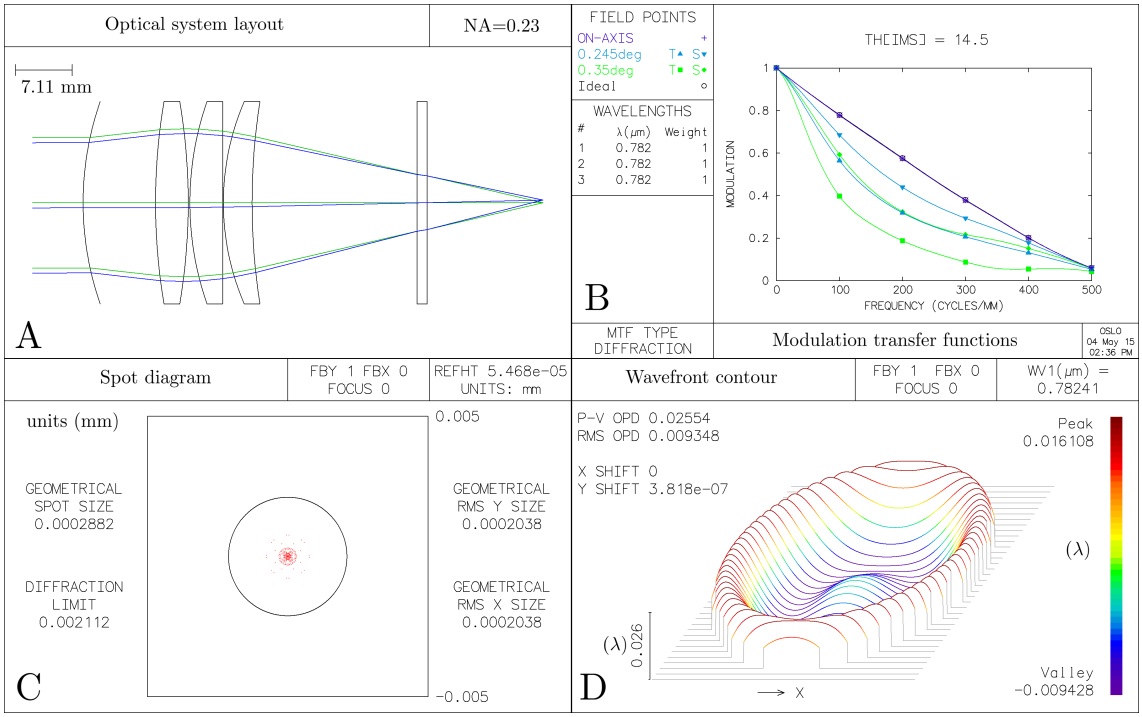

Figure F.1: Lens diagnostics for the NA≈ 0.23 focusing lens array. (a) lens system drawing produced by OSLO. (b) Modulation transfer function for the lens system in (a). (c) Diffraction limited spot diagram. (d) Wavefront contour plot in units of λ.

Table F.1: Specifications for the NA ≈ 0.23 focusing lens system and the silica glass cell window.

Surface number	Radius of curvature (mm)	Thickness (mm)	Material
1	0	3.5	BK7
2	-38.6	9.01	air
3	76.6	4.1	BK7
4	-76.6	0.2	air
5	38.6	4.1	BK7
6	0	0.1	air
7	32.1	3.6	Bk7
8	82.2	20.7	air
9	0	1.27	silica
10	0	14.53	vacuum

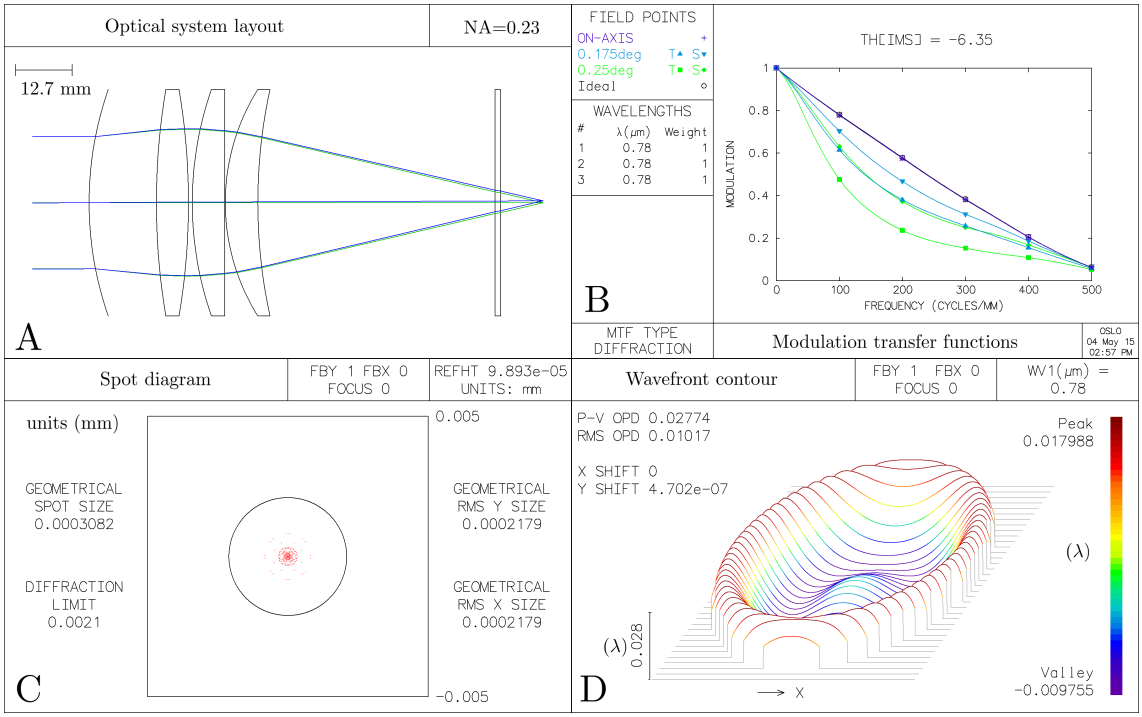

Figure F.2: Lens diagnostics for the NA≈ 0.23 collimating lens array. (a) lens system drawing produced by OSLO. (b) Modulation transfer function for the lens system in (a). (c) Diffraction limited spot diagram. (d) Wavefront contour plot in units of λ.

OSLO [147] built in GENII ray aberration function. The final optimal spacings in the lens system are given in table F.1. To verify that the design is diffraction limited, in fig. F.1(b) the systems modulation transfer function MTF is plotted for a selection of field angles. Near the optical axis the system closely follows the ideal MTF. The spot size diagram fig. F.1(c) indicates a spot size limited by diffraction. Whilst the wavefront contour plot in fig. F.1(d) indicates a distortion to the wavefront well below Lord Rayleigh's quarter wavelength rule [178–180].

To collimate the light from the focusing array on the opposing side of glass cell as illustrated in fig. 4.11, a similar 4-lens array but with 2" diameter is used, with each lens commercially available from the distributor Thorlabs. A schematic produced by OSLO of the collimating lens array is displayed in fig. F.2. The OSLO optimised air spacings (see table F.2) in the system are designed to correct for the aberration introduced by the second glass cell window. With such optimisation, the MTF, fig. F.2(b), spot diagram, fig. F.2(c) and wavefront contour analysis, fig. F.2(d), indicate a diffraction limited imaging system on axis.

Table F.2: Specifications for the NA ≈ 0.23 collimating lens system and the silica glass cell window.

Surface number	Radius of curvature (mm)	Thickness (mm)	Material
1	0	4	BK7
2	77.2	15.5	air
3	153.3	7.2	BK7
4	-153.3	0.5	air
5	77.3	7.3	BK7
6	0	0.5	air
7	47.9	7.3	Bk7
8	119.3	53	air
9	0	1.27	silica
10	0	9.5	vacuum

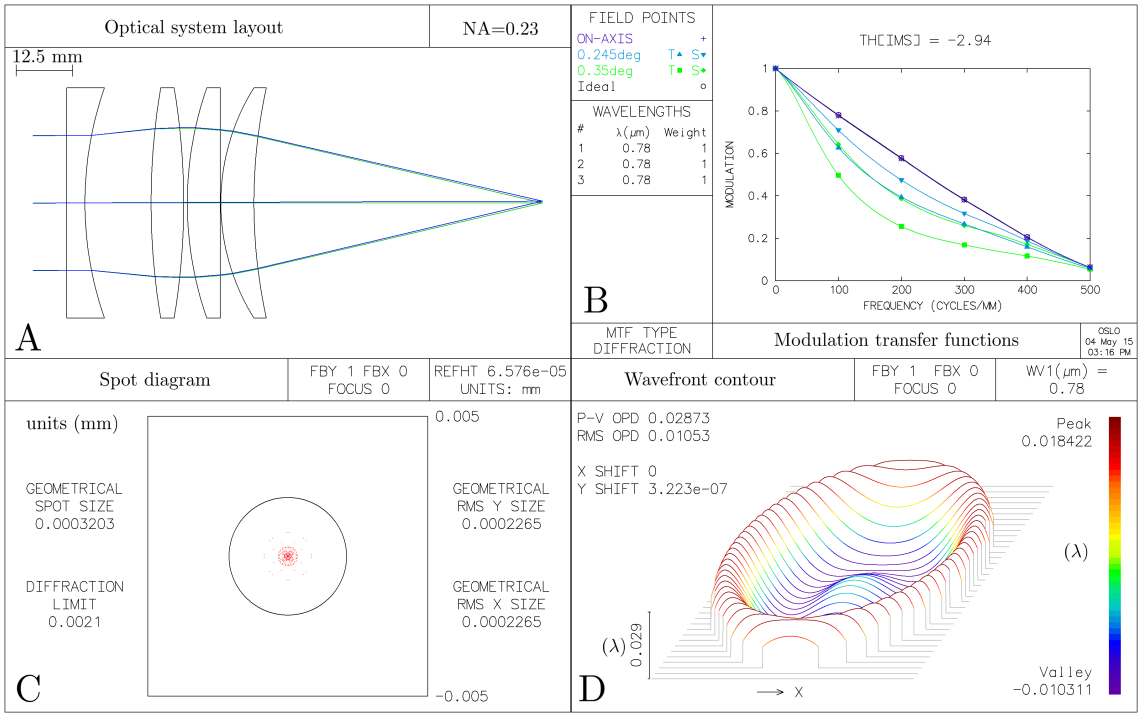

Figure F.3: Lens diagnostics for the NA≈ 0.23 imaging lens array. (a) Lens system drawing produced by OSLO. (b) Modulation transfer function for the lens system in (a). (c) Diffraction limited spot diagram. (d) Wavefront contour plot in units of λ.

Table F.3: Specifications for the NA ≈ 0.23 imaging lens system.

Surface number	Radius of curvature (mm)	Thickness (mm)	Material
1	0	4	BK7
2	77.2	14.6	air
3	153.3	7.2	BK7
4	-153.3	0.8	air
5	77.3	7.3	BK7
6	0	0.1	air
7	47.9	7.3	Bk7
8	119.3	66.5	air

Table F.4: Aspheric coeficients for the aspheric lens (surface 5 in table 4.1).

Aspheric lens (surface 5) coefficients	
Conic/Toric	-1.35
A_4	$2.361\,813\,4 \times 10^{-5}$
A_6	$-1.130\,307\,9 \times 10^{-8}$
A_8	$-1.111\,390\,6 \times 10^{-11}$
A_{10}	$-2.398\,171\,4 \times 10^{-14}$
A_{12}	$3.035\,791 \times 10^{-17}$
A_{14}	$1.366\,081\,5 \times 10^{-19}$
A_{16}	$-1.888\,158\,7 \times 10^{-22}$

To image the light collimated by the collimating lens array, see fig. F.2, the 4-lens collimating lens array is repeated but with the air spacing between the lenses optimised to account for the aberration introduced by the lenses themselves, since there is no glass cell window to account for. In fig. F.2 an OSLO schematic of the imaging lens array is shown along with plots of the MTF, the spot diagram and a wavefront contour plot indicating a diffraction limited imaging system.

The collimating and imaging systems discussed in this section form an $f-2f-f$ imaging system. Such an imaging system can be used in other imaging techniques for cold atoms such as absorption, PCI, fluorescence and DGI. The design discussed here may be useful for removing aberration from plane windows to in cold atom experiments using alternative imaging techniques.

Aside, table 4.1 gives the aspheric coeficients for the aspheric lens used in creating the diffraction limited point sources for the NA= 0.07 DSHM set up (see section 4.4.2).

Bibliography

[1] Daniel A Steck. Rubidium 87 D line data, 2001. xvi, 18, 85, 86, 152, 158, 172, 203

[2] Jun Ye, Steve Swartz, Peter Jungner, and John L Hall. Hyperfine structure and absolute frequency of the 87Rb 5P3/2 state. *Opt. Lett.*, 21(16):1280–1282, August 1996. xvi, 85

[3] S Bize, Y Sortais, M S Santos, C Mandache, A Clairon, and C Salomon. High-accuracy measurement of the 87 Rb ground-state hyperfine splitting in an atomic fountain. *EPL (Europhysics Letters)*, 45(5):558, 1999. xvi, 85

[4] Daniel A Steck. Rubidium 85 D Line Data, 2013. xxiii, 189

[5] William D Phillips. Nobel Lecture: Laser cooling and trapping of neutral atoms. *Rev. Mod. Phys.*, 70(3):721–741, July 1998. 1, 18, 19, 201

[6] Steven Chu. Nobel Lecture: The manipulation of neutral particles. *Rev. Mod. Phys.*, 70(3):685–706, July 1998. 1

[7] Claude N Cohen-Tannoudji. Nobel Lecture: Manipulating atoms with photons. *Rev. Mod. Phys.*, 70(3):707–719, July 1998. 1

[8] William D Phillips and Harold Metcalf. Laser Deceleration of an Atomic Beam. *Phys. Rev. Lett.*, 48(9):596–599, March 1982. 1, 18, 19, 201

[9] Steven Chu, L Hollberg, J E Bjorkholm, Alex Cable, and A Ashkin. Three-dimensional viscous confinement and cooling of atoms by resonance radiation pressure. *Phys. Rev. Lett.*, 55(1):48–51, July 1985. 1, 20

[10] E. L Raab, M. Prentis, Alex Cable, Steven Chu, and D. E. Pritchard. Trapping of Neutral Sodium Atoms with Radiation Pressure. *Physical Review Letters*, 59(23):2631–2634, 1987. 1, 22

[11] CC Bradley, CA Sackett, JJ Tollett, and RG Hulet. Evidence of Bose-Einstein condensation in an atomic gas with attractive interactions. *Physical Review Letters*, 75(9):1687–1691, 1995. 1

[12] M H Anderson, J R Ensher, M R Matthews, C E Wieman, and E a Cornell.

Observation of bose-einstein condensation in a dilute atomic vapor. *Science (New York, N.Y.)*, 269(5221):198–201, July 1995. 1, 31

[13] KB Davis, MO Mewes, and MR Andrews. Bose-Einstein condensation in a gas of sodium atoms. *Physical review ...*, 75(November):3969–3973, 1995. 1, 31

[14] D S Jin, J R Ensher, M R Matthews, C E Wieman, and E A Cornell. Collective Excitations of a Bose-Einstein Condensate in a Dilute Gas. *Phys. Rev. Lett.*, 77(3):420–423, July 1996. 1, 31

[15] B DeMarco and D S Jin. Onset of Fermi Degeneracy in a Trapped Atomic Gas. *Science*, 285(5434):1703–1706, 1999. 1

[16] J Estève, C Gross, A Weller, S Giovanazzi, and M K Oberthaler. Squeezing and entanglement in a Bose-Einstein condensate. *Nature*, 455(7217):1216–1219, October 2008. 1

[17] R Wynands and S Weyers. Atomic fountain clocks. *Metrologia*, 42(3):S64, 2005. 1

[18] Mark A Kasevich, Erling Riis, Steven Chu, and Ralph G DeVoe. rf spectroscopy in an atomic fountain. *Phys. Rev. Lett.*, 63(6):612–615, August 1989. 1

[19] B J Bloom, T L Nicholson, J R Williams, S L Campbell, M Bishof, X Zhang, W Zhang, S L Bromley, and J Ye. An optical lattice clock with accuracy and stability at the 10(-18) level. *Nature*, 506(7486):71–5, 2014. 1

[20] Jordan. M. Gerton, Dmitry Strekalov, Ionut Prodan, and Randall. G. Hulet. Direct observation of growth and collapse of a BoseEinstein condensate with attractive interactions. *Nature*, 408:692–695, 2000. 1

[21] L E Sadler, J M Higbie, S R Leslie, M Vengalattore, and D M Stamper-Kurn. Spontaneous symmetry breaking in a quenched ferromagnetic spinor Bose-Einstein condensate. *Nature*, 443(7109):312–315, 2006. 1

[22] Nathan Gemelke, Xibo Zhang, Chen-Lung Hung, and Cheng Chin. In situ observation of incompressible Mott-insulating domains in ultracold atomic gases. *Nature*, 460(7258):995–998, 2009. 1

[23] Waseem S Bakr, Jonathon I Gillen, Amy Peng, Simon Fölling, and Markus Greiner. A quantum gas microscope for detecting single atoms in a Hubbard-regime optical lattice. *Nature*, 462(7269):74–7, November 2009. 1, 2, 29, 43, 53, 55, 72, 147, 155, 157, 163, 168, 169

[24] Jacob F Sherson, Christof Weitenberg, Manuel Endres, Marc Cheneau, Immanuel Bloch, and Stefan Kuhr. Single-atom-resolved fluorescence imaging of an atomic Mott insulator. *Nature*, 467(7311):68–72, September 2010. 1, 2, 29,

43, 53, 55, 147, 155, 157, 163, 168, 169

[25] Elmar Haller, James Hudson, Andrew Kelly, Dylan A. Cotta, Bruno Peaudecerf, Graham D. Bruce, and Stefan Kuhr. Single-atom imaging of fermions in a quantum-gas microscope. *Arxiv:1503.02005v2*, page 6, 2015. 1, 2, 29, 43, 53, 55, 147, 155, 157, 163, 168, 169

[26] Lawrence W Cheuk, Matthew A Nichols, Melih Okan, Thomas Gersdorf, Vinay V Ramasesh, Waseem S Bakr, Thomas Lompe, and Martin W Zwierlein. Quantum-Gas Microscope for Fermionic Atoms. *Phys. Rev. Lett.*, 114(19):193001, May 2015. 1, 2, 29, 43, 53, 55, 169

[27] LD Turner, K Domen, and RE Scholten. Diffraction-contrast imaging of cold atoms. *Physical Review A*, 72(3):031403, September 2005. 2, 13, 37, 40, 43, 165

[28] LD Turner. *Holographic imaging of cold atoms*. PhD thesis, University of Melbourne, 2004. 2, 34, 36, 37, 39, 40, 43

[29] S Kadlecek, J Sebby, R Newell, and T G Walker. Nondestructive spatial heterodyne imaging of cold atoms. *Optics letters*, 26(3):137–9, February 2001. 2, 13, 37, 38, 39, 61, 165

[30] M H Jericho and H J Kreuzer. Point Source Digital In-Line Holographic Microscopy. In Pietro Ferraro, Adam Wax, and Zeev Zalevsky, editors, *Coherent Light Microscopy*, volume 46 of *Springer Series in Surface Sciences*, chapter Point Sour, pages 3–30. Springer Berlin Heidelberg, Berlin, Heidelberg, 2011. 2, 44, 53, 129, 130, 168

[31] Jorge Garcia-Sucerquia, Wenbo Xu, Stephan K Jericho, Peter Klages, Manfred H Jericho, and H Jürgen Kreuzer. Digital in-line holographic microscopy. *Appl. Opt.*, 45(5):836–850, February 2006. 2, 48, 53, 129, 130

[32] H J Kreuzer, M J Jericho, I A Meinertzhagen, and Wenbo Xu. Digital in-line holography with photons and electrons. *Journal of Physics: Condensed Matter*, 13(47):10729, 2001. 2, 48, 53, 129, 130

[33] Conor P McElhinney, Bryan M Hennelly, and Thomas J Naughton. Twin-image reduction in inline digital holography using an object segmentation heuristic, 2008. 2

[34] Thomas M Kreis and Werner P O Juptner. Suppression of the dc term in digital holography. *Optical Engineering*, 36(8):2357–2360, 1997. 2, 51, 55

[35] Yimo Zhang, Qieni Lü, and Baozhen Ge. Elimination of zero-order diffraction in digital off-axis holography. *Optics Communications*, 240(46):261–267, 2004.

2, 51, 55

[36] Gu-Liang Chen, Ching-Yang Lin, Ming-Kuei Kuo, and Chi-Ching Chang. Numerical suppression of zero-order image in digital holography. *Opt. Express*, 15(14):8851–8856, July 2007. 2, 51, 55

[37] Choongsang Cho, Byeongho Choi, Hoonjong Kang, and Sangkeun Lee. Laplace operation-based DC noise reduction in digital holography. *IEEE Photonics Technology Letters*, 25(12):1188–1191, 2013. 2

[38] James Paul Sobol and Saijun Wu. Imaging cold atoms with shot-noise and diffraction limited holography. *New Journal of Physics*, 16(093064):16, 2014. 2, 33, 34, 40, 55, 147, 153, 155, 163

[39] Ye Pu and Hui Meng. Intrinsic speckle noise in off-axis particle holography. *Journal of the Optical Society of America A*, 21(7):1221, 2004. 2, 27

[40] M. Kanka, R. Riesenberg, and H. J. Kreuzer. Reconstruction of high-resolution holographic microscopic images. *Optics Letters*, 34(8):1162, April 2009. 2, 46, 47, 51

[41] W. Ketterle, D. S. Durfee, and D. M. Stamper-Kurn. Making, probing and understanding Bose-Einstein condensates. *Fermi summer school on Bose-Einstein condensation in Varenna, Italy*, April 1999. 2, 30, 31, 32, 33, 54, 155

[42] Marshall T DePue, Colin McCormick, S Lukman Winoto, Steven Oliver, and David S Weiss. Unity Occupation of Sites in a 3D Optical Lattice. *Phys. Rev. Lett.*, 82(11):2262–2265, March 1999. 2, 29, 32, 43, 55, 72

[43] L Chomaz, L Corman, T Yefsah, R Desbuquois, and J Dalibard. Absorption imaging of a quasi-two-dimensional gas: a multiple scattering analysis. *New Journal of Physics*, 14(5):055001, May 2012. 2, 32, 54, 168

[44] Steffen P. Rath, Tarik Yefsah, Kenneth J. Günter, Marc Cheneau, Rémi Desbuquois, Markus Holzmann, Werner Krauth, and Jean Dalibard. Equilibrium state of a trapped two-dimensional Bose gas. *Physical Review A*, 82(1):013609, July 2010. 2, 32, 34, 43, 168

[45] Tarik Yefsah, Rémi Desbuquois, Lauriane Chomaz, Kenneth J. Günter, and Jean Dalibard. Exploring the Thermodynamics of a Two-Dimensional Bose Gas. *Physical Review Letters*, 107(13):130401, September 2011. 2, 28, 32, 55, 168

[46] Edmundo R Sánchez Guajardo, Meng Khoon Tey, Leonid A Sidorenkov, and Rudolf Grimm. Higher-nodal collective modes in a resonantly interacting Fermi

gas. *Phys. Rev. A*, 87(6):63601, June 2013. 2, 168

[47] D Gabor. A new microscopic principle. *Nature*, 161(4098):777–778, 1948. 3, 37, 44

[48] D Gabor. Microscopy by Reconstructed Wave-Fronts. *Proceedings of the Royal Society of London. Series A. Mathematical and Physical Sciences*, 197(1051):454–487, 1949. 3, 37, 44

[49] D Gabor. Microscopy by Reconstructed Wave Fronts: II. *Proceedings of the Physical Society. Section B*, 64(6):449, 1951. 3, 37, 44

[50] C. J. Foot. *Atomic physics*. Oxford master series in physics. Oxford University Press, 2005. 9, 10, 11, 18, 19, 20, 26, 80, 81, 83, 86, 101, 173, 175, 181, 182, 184, 190, 201

[51] H J Metcalf and P van der Straten. *Laser Cooling and Trapping*. Graduate Texts in Contemporary Physics. Springer New York, 1999. 9, 10, 11, 12, 15, 19, 26, 78, 86, 173, 178, 179

[52] M Weidemüller and C Zimmermann. *Cold Atoms and Molecules*. Physics textbook. Wiley, 2009. 9, 10, 173

[53] J. Dalibard and C. Cohen-Tannoudji. Dressed-atom approach to atomic motion in laser light: the dipole force revisited. *Journal of the Optical Society of America B*, 2(11):1707, November 1985. 10

[54] Rudolf Grimm, Matthias Weidemüller, and Yurii B. Ovchinnikov. Optical Dipole Traps for Neutral Atoms. *Advances In Atomic, Molecular, and Optical Physics*, 42:95–170, 2000. 10, 11

[55] K Blum. *Density Matrix Theory and Applications*. Springer Series on Atomic, Optical, and Plasma Physics. Springer, 2012. 11

[56] L Allen and J H Eberly. *Optical Resonance and Two-Level Atoms*. Dover Books on Physics. Dover Publications, 2012. 12

[57] C Cohen-Tannoudji, J Dupont-Roc, and G Grynberg. *Atom-Photon Interactions: Basic Processes and Applications*. A Wiley-Interscience publication. Wiley, 1998. 13, 14

[58] C Roychoudhuri, A F Kracklauer, and K Creath. *The Nature of Light: What is a Photon?* Optical Science and Engineering. CRC Press, 2008. 13, 14

[59] A Jechow, B G Norton, S Händel, V Blums, E W Streed, and D Kielpinski. Controllable Optical Phase Shift Over One Radian from a Single Isolated Atom. *Phys. Rev. Lett.*, 110(11):113605, March 2013. 13, 39, 137

[60] P. S. Light, C. Perrella, and a. N. Luiten. Phase-sensitive imaging of cold

atoms at the shot-noise limit. *Applied Physics Letters*, 102(17):171108, 2013. 13, 37, 38, 39

[61] M Pappa, P C Condylis, G O Konstantinidis, V Bolpasi, a Lazoudis, O Morizot, D Sahagun, M Baker, and W von Klitzing. Ultra-sensitive atom imaging for matter-wave optics. *New Journal of Physics*, 13(11):115012, November 2011. 13, 29, 35, 36, 37

[62] Gregory O Konstantinidis, Melina Pappa, Gustav Wikström, Paul C Condylis, Daniel Sahagun, Mark Baker, Olivier Morizot, and Wolf von Klitzing. Atom number calibration in absorption imaging at very small atom numbers. *Central European Journal of Physics*, 10(5):1054–1058, July 2012. 13, 35

[63] GERT WRIGGE. *Coherent and Incoherent Light Scattering in the Resonance Fluorescence of a Single Molecule*. Phd, Albert Ludwigs Universitat, Freiburg, 2008. 14

[64] D J Griffiths. *Introduction to Electrodynamics*. Pearson international edition. Prentice Hall, 1999. 14, 16

[65] Graham Thomas Purves. *Absorption And Dispersion In atomic Vapours: Applications To Interferometry*. PhD thesis, Durham University, 2006. 15

[66] W Ertmer, R Blatt, J L Hall, and M Zhu. Laser Manipulation of Atomic Beam Velocities: Demonstration of Stopped Atoms and Velocity Reversal. *Phys. Rev. Lett.*, 54(10):996–999, March 1985. 18

[67] John Prodan, Alan Migdall, William D Phillips, Ivan So, Harold Metcalf, and Jean Dalibard. Stopping Atoms with Laser Light. *Phys. Rev. Lett.*, 54(10):992–995, March 1985. 18

[68] F B Dunning and R G Hulet. *Atomic, Molecular, and Optical Physics: Atoms and Molecules: Volume 29B: Atomic, Molecular, And Optical Physics*. Experimental Methods in the Physical Sciences. Elsevier Science, 1996. 18, 19

[69] Yuri B Ovchinnikov. A Zeeman slower based on magnetic dipoles. *Optics Communications*, 276(2):261–267, 2007. 18, 19, 201

[70] P Cheiney, O Carraz, D Bartoszek-Bober, S Faure, F Vermersch, C M Fabre, G L Gattobigio, T Lahaye, D Guéry-Odelin, and R Mathevet. A Zeeman slower design with permanent magnets in a Halbach configuration. *Review of Scientific Instruments*, 82(6):–, 2011. 18, 19, 201

[71] R Gaggl, L Windholz, C Umfer, and C Neureiter. Laser cooling of a sodium atomic beam using the Stark effect. *Phys. Rev. A*, 49(2):1119–1121, February 1994. 19

[72] J R Yeh, B Hoeling, and R J Knize. Longitudinal and transverse cooling of a cesium atomic beam using the D1 transition with Stark-effect frequency compensation. *Phys. Rev. A*, 52(2):1388–1393, August 1995. 19

[73] M Zhu, C W Oates, and J L Hall. Continuous high-flux monovelocity atomic beam based on a broadband laser-cooling technique. *Phys. Rev. Lett.*, 67(1):46–49, July 1991. 19, 201

[74] S N Atutov, R Calabrese, R Grimm, V Guidi, I Lauer, P Lenisa, V Luger, E Mariotti, L Moi, A Peters, U Schramm, and M Stö\ssel. "White-light" Laser Cooling of a Fast Stored Ion Beam. *Phys. Rev. Lett.*, 80(10):2129–2132, March 1998. 19, 201

[75] Paul D Lett, Richard N Watts, Christoph I Westbrook, William D Phillips, Phillip L Gould, and Harold J Metcalf. Observation of Atoms Laser Cooled below the Doppler Limit. *Phys. Rev. Lett.*, 61(2):169–172, July 1988. 22, 101, 171, 176

[76] A Aspect, J Dalibard, A Heidmann, C Salomon, and C Cohen-Tannoudji. Cooling Atoms with Stimulated Emission. *Phys. Rev. Lett.*, 57(14):1688–1691, October 1986. 24, 175, 179

[77] J. Dalibard and C. Cohen-Tannoudji. Laser cooling below the Doppler limit by polarization gradients: simple theoretical models. *Journal of the Optical Society of America B*, 6(11):2023, November 1989. 24, 175, 178

[78] Steven Chu, J E Bjorkholm, A Ashkin, and A Cable. Experimental Observation of Optically Trapped Atoms. *Phys. Rev. Lett.*, 57(3):314–317, July 1986. 24

[79] C Salomon, J Dalibard, A Aspect, H Metcalf, and C Cohen-Tannoudji. Channeling atoms in a laser standing wave. *Phys. Rev. Lett.*, 59(15):1659–1662, October 1987. 25

[80] Immanuel Bloch. Ultracold quantum gases in optical lattices. *Nature Physics*, 1(1):23–30, October 2005. 25, 29, 43, 53

[81] Alan L Migdall, John V Prodan, William D Phillips, Thomas H Bergeman, and Harold J Metcalf. First Observation of Magnetically Trapped Neutral Atoms. *Phys. Rev. Lett.*, 54(24):2596–2599, June 1985. 25

[82] Naoto Masuhara, John M Doyle, Jon C Sandberg, Daniel Kleppner, Thomas J Greytak, Harald F Hess, and Greg P Kochanski. Evaporative Cooling of Spin-Polarized Atomic Hydrogen. *Phys. Rev. Lett.*, 61(8):935–938, August 1988. 26

[83] Mario Kanka, Rainer Riesenberg, Paul Petruck, and Christian Graulig. High

resolution (NA = 0.8) in lensless in-line holographic microscopy with glass sample carriers. *Optics letters*, 36(18):3651–3, September 2011. 27, 50, 54, 166, 168

[84] D B Hume, I Stroescu, M Joos, W Muessel, H Strobel, and M K Oberthaler. Accurate Atom Counting in Mesoscopic Ensembles. *Phys. Rev. Lett.*, 111(25):253001, December 2013. 29, 72, 155

[85] Igor Teper, Yu-Ju Lin, and Vladan Vuleti\ifmmode \acutec\else ć\fi. Resonator-Aided Single-Atom Detection on a Microfabricated Chip. *Phys. Rev. Lett.*, 97(2):23002, July 2006. 29

[86] Max Berek. Grundlagen der Tiefenwahrnehmung im Mikroskop. *Marburger Sitzungsberichte*, 61:189–223, 1927. 29, 33

[87] H Schnitzler and Klaus-Peter Zimmer. Advances in stereomicroscopy. *Proc. SPIE 7100, Optical Design and Engineering III*, 7100:71000P–71000P–12, 2008. 29, 33

[88] David A Smith, Simon Aigner, Sebastian Hofferberth, Michael Gring, Mauritz Andersson, Stefan Wildermuth, Peter Krüger, Stephan Schneider, Thorsten Schumm, and Jörg Schmiedmayer. Absorption imaging of ultracold atoms on atom chips. *Optics express*, 19(9):8471–85, April 2011. 30, 31

[89] Erik. W. Streed, Andreas Jechow, Benjamin. G. Norton, and David Kielpinski. Absorption imaging of a single atom. *Nature communications*, 3:933, 2012. 31, 137

[90] R. Meppelink, R. a. Rozendaal, S. B. Koller, J. M. Vogels, and P. van der Straten. Thermodynamics of Bose-Einstein-condensed clouds using phase-contrast imaging. *Physical Review A*, 81(5):053632, May 2010. 31, 32, 33, 54

[91] F Zernike. Phase contrast, a new method for the microscopic observation of transparent objects. *Physica*, 9(7):686–698, 1942. 33

[92] F Zernike. Phase contrast, a new method for the microscopic observation of transparent objects part {II}. *Physica*, 9(10):974–986, 1942. 33

[93] Fritz Zernike. How I Discovered Phase Contrast. *Nobel lecture*, 1953. 33

[94] ROBERT BARER. Refractometry and Interferometry of Living Cells. *J. Opt. Soc. Am.*, 47(6):545–556, June 1957. 33, 34, 35, 72

[95] M R Andrews, D M Kurn, H.-J. Miesner, D S Durfee, C G Townsend, S Inouye, and W Ketterle. Propagation of Sound in a Bose-Einstein Condensate. *Phys. Rev. Lett.*, 79(4):553–556, July 1997. 33

[96] C C Bradley, C A Sackett, and R G Hulet. Bose-Einstein Condensation of Lithium: Observation of Limited Condensate Number. *Phys. Rev. Lett.*, 78(6):985–989, February 1997. 33

[97] H.-J. Miesner, D M Stamper-Kurn, M R Andrews, D S Durfee, S Inouye, and W Ketterle. Bosonic Stimulation in the Formation of a Bose-Einstein Condensate. *Science*, 279(5353):1005–1007, 1998. 33

[98] S Inouye, M. R. Andrews, J. Stenger, H.-J. Miesner, D. M. Stamper-Kurn, and Wolfgang Ketterle. Observation of Feshbach resonances in a BoseEinstein condensate. *Nature*, 392(6672):151–154, 1998. 33

[99] R Onofrio, D S Durfee, C Raman, M Köhl, C E Kuklewicz, and W Ketterle. Surface Excitations of a Bose-Einstein Condensate. *Phys. Rev. Lett.*, 84(5):810–813, January 2000. 33

[100] C Raman, J R Abo-Shaeer, J M Vogels, K Xu, and W Ketterle. Vortex Nucleation in a Stirred Bose-Einstein Condensate. *Phys. Rev. Lett.*, 87(21):210402, November 2001. 33

[101] A. H. Bennett, H. Osterberg, H. Jupnik, and O. W. Richards. *Phase microscopy; principles and applications*. Wiley & Sons, New York USA, 1951. 34, 35, 72

[102] M. R. Andrews, M.-O. Mewes, N. J. van Druten, D. S. Durfee, D. M. Stamper-Kurn, and W. Ketterle. Direct, Nondestructive Observation of a Bose Condensate. *Science*, 273(5271):84–87, 1996. 35

[103] Gregory O Konstantinidis. *Diffractive Dark-Ground Imaging of Ultra-Low Atom-Numbers in a MOT*. Phd, University of Crete, 2011. 35

[104] Aaron Reinhard, Jean-Félix Riou, Laura A Zundel, and David S Weiss. Dark-ground imaging of high optical thickness atom clouds. *Optics Communications*, 324(0):30–33, 2014. 35

[105] Tzu-Ping Ku, Chi-Yuan Huang, Bor-Wen Shiau, and Dian-Jiun Han. Phase shifting interferometry of cold atoms. *Optics express*, 19(4):3730–41, March 2011. 38, 39, 52, 165

[106] Chih-Yuan Huang, Hung-Shiue Chen, Chih-Yuan Liu, Chin-Han Chen, and D. J. Han. Lens-free phase shifting imaging for cold atoms. *Journal of the Optical Society of America B*, 31(1):87, December 2013. 38, 39, 52, 165

[107] Ichirou Yamaguchi and Tong Zhang. Phase-shifting digital holography. *Opt. Lett.*, 22(16):1268–1270, August 1997. 39, 51, 52

[108] A N Tikhonov and V I A Arsenin. *Solutions of ill-posed problems*. Scripta series in mathematics. Winston, 1977. 40

[109] B. J. Knight-Gregson. *High-efficiency, holographic detection of weak scatterers*. Mphys, Swansea University, 2012. 40, 160, 161

[110] Dennis Gabor. Dennis Gabor - Nobel Lecture: Holography, 1948-1971, 1971. 44

[111] U Schnars and W Jüptner. Direct recording of holograms by a CCD target and numerical reconstruction. *Appl. Opt.*, 33(2):179–181, January 1994. 45

[112] Ulf Schnars and Werner P O Jüptner. Digital recording and numerical reconstruction of holograms. *Measurement Science and Technology*, 13(9):R85, 2002. 45, 46, 47, 129

[113] Dayong Wang, Jie Zhao, Fucai Zhang, Giancarlo Pedrini, and Wolfgang Osten. High-fidelity numerical realization of multiple-step Fresnel propagation for the reconstruction of digital holograms. *Appl. Opt.*, 47(19):D12—-D20, July 2008. 46

[114] Fucai Zhang, Giancarlo Pedrini, and Wolfgang Osten. Reconstruction algorithm for high-numerical-aperture holograms with diffraction-limited resolution. *Opt. Lett.*, 31(11):1633–1635, June 2006. 46

[115] J W Goodman. *Introduction to Fourier Optics*. McGraw-Hill physical and quantum electronics series. Roberts & Company, 2005. 46, 47, 49, 64

[116] M Kanka, A Wuttig, C Graulig, and R Riesenberg. Fast exact scalar propagation for an in-line holographic microscopy on the diffraction limit. *Opt. Lett.*, 35(2):217–219, January 2010. 46, 47, 51

[117] Weijuan Qu, Dean Liu, Yanan Zhi, and Liren Liu. Digital holographic interferometry and the angular spectrum method applied to measuring the domain inversion in ferroelectric crystal, 2007. 46, 47, 129

[118] A Lipson, S G Lipson, and H Lipson. *Optical Physics*. Cambridge University Press, 2010. 48

[119] J. P. Allebach, N. C. Gallagher, and B. Liu. Aliasing error in digital holography. *Applied Optics*, 15(9):2183–2188, 1976. 49

[120] Mathieu Leclercq and Pascal Picart. Digital Fresnel holography beyond the Shannon limits. *Opt. Express*, 20(16):18303–18312, July 2012. 49

[121] Damien P Kelly, Bryan M Hennelly, Nitesh Pandey, Thomas J Naughton, and William T Rhodes. Resolution limits in practical digital holographic systems. *Optical Engineering*, 48(9):95801–95813, 2009. 49

[122] Christoph Wagner, Sönke Seebacher, Wolfgang Osten, and Werner Jüptner. Digital recording and numerical reconstruction of lensless Fourier holograms in

optical metrology. *Appl. Opt.*, 38(22):4812–4820, August 1999. 49

[123] W. L. BRAGG and G. L. ROGERS. Elimination of the Unwanted Image in Diffraction Microscopy. *Nature*, 167(4240):190–191, February 1951. 51

[124] G L Rogers. In-line soft-x-ray holography: the unwanted image. *Opt. Lett.*, 19(1):67, January 1994. 51, 168

[125] EMMETT N LEITH and JURIS UPATNIEKS. Wavefront Reconstruction with Continuous-Tone Objects. *J. Opt. Soc. Am.*, 53(12):1377–1381, December 1963. 51, 52, 54, 111

[126] EMMETT N LEITH and JURIS UPATNIEKS. Wavefront Reconstruction with Diffused Illumination and Three-Dimensional Objects. *J. Opt. Soc. Am.*, 54(11):1295–1301, November 1964. 51, 52, 54, 111

[127] G W Stroke, D Brumm, A Funkhouser, A Labeyrie, and R C Restrick. On the absence of phase-recording or 'twin-image' separation problems in 'Gabor' (in-line) holography. *British Journal of Applied Physics*, 17(4):497, 1966. 51, 111

[128] D GABOR and W P Goss. Interference Microscope with Total Wavefront Reconstruction. *J. Opt. Soc. Am.*, 56(7):849–856, July 1966. 51

[129] Songcan Lai, Brian King, and Mark A Neifeld. Wave front reconstruction by means of phase-shifting digital in-line holography. *Optics Communications*, 173(16):155–160, 2000. 51

[130] J B Tiller, A Barty, D Paganin, and K A Nugent. The holographic twin image problem: a deterministic phase solution. *Optics Communications*, 183(14):7–14, 2000. 51

[131] Michael Reed Teague. Deterministic phase retrieval: a Green's function solution. *J. Opt. Soc. Am.*, 73(11):1434–1441, November 1983. 51

[132] R W Gerchberg and W Owen Saxton. A practical algorithm for the determination of the phase from image and diffraction plane pictures. *Optik*, 35:237–246, 1972. 51

[133] J R Fienup. Reconstruction of an object from the modulus of its Fourier transform. *Opt. Lett.*, 3(1):27–29, July 1978. 51

[134] J R Fienup. Phase retrieval algorithms: a comparison. *Appl. Opt.*, 21(15):2758–2769, August 1982. 51

[135] G Koren, F Polack, and D Joyeux. Twin-image elimination in in-line holography of finite-support complex objects. *Opt. Lett.*, 16(24):1979–1981, December 1991. 51, 52, 53, 55, 56, 62

[136] Gabriel Koren, François Polack, and Denis Joyeux. Iterative algorithms for twin-image elimination in in-line holography using finite-support constraints. *J. Opt. Soc. Am. A*, 10(3):423–433, March 1993. 51, 52, 53, 55, 56, 62

[137] David Monaghan Bryan M. Hennelly, Damien P. Kelly, Nitesh Pandey. Review of Twin Reduction and Twin Removal Techniques in Holography. In Adam Christopher Winstanley, editor, *CIICT 2009: Proceedings of the China-Ireland Information and Communications Technologies Conference*, pages 241–245. National University of Ireland Maynooth, Maynooth, 2009. 51, 52

[138] Myung K Kim. Principles and techniques of digital holographic microscopy. *Journal of Photonics for Energy*, pages 18005–18050, 2010. 51

[139] X.M.Henry Huang, J M Zuo, and John C H Spence. Wavefront reconstruction for in-line holograms formed by pure amplitude objects. *Applied Surface Science*, 148(34):229–234, 1999. 52

[140] G Liu and P D Scott. Phase retrieval and twin-image elimination for in-line Fresnel holograms. *J. Opt. Soc. Am. A*, 4(1):159–165, January 1987. 52

[141] Iwao Kodama, Masahiro Yamaguchi, Nagaaki Ohyama, Toshio Honda, Kunio Shinohara, Atsushi Ito, Tatsuya Matsumura, Katsuyuki Kinoshita, and Keiji Yada. Image reconstruction from an in-line X-ray hologram with intensity distribution constraint. *Optics Communications*, 125(13):36–42, 1996. 52

[142] A L Bleloch, A Howie, and E M James. Amplitude recovery in Fresnel projection microscopy. *Applied Surface Science*, 111(0):180–184, 1997. 52

[143] Tatiana Latychevskaia and Hans-Werner Fink. Solution to the Twin Image Problem in Holography. *Phys. Rev. Lett.*, 98(23):233901, June 2007. 52

[144] Lu Rong, Yan Li, Shuo Liu, Wen Xiao, Feng Pan, and Dayong Wang. Iterative solution to twin image problem in in-line digital holography. *Optics and Lasers in Engineering*, 51(5):553–559, May 2013. 52

[145] JOHN B DEVELIS, J R GEORGE B. PARRENT, and BRIAN J THOMPSON. Image Reconstruction with Fraunhofer Holograms. *J. Opt. Soc. Am.*, 56(4):423–427, April 1966. 53

[146] J. Lye, J. Hope, and J. Close. Nondestructive dynamic detectors for Bose-Einstein condensates. *Physical Review A*, 67(4):043609, April 2003. 61

[147] J. Hope and J. Close. Limit to Minimally Destructive Optical Detection of Atoms. *Physical Review Letters*, 93(18):180402, October 2004. 61

[148] J. Hope and J. Close. General limit to nondestructive optical detection of atoms. *Physical Review A*, 71(4):043822, April 2005. 61

[149] M Gross and M Atlan. Digital holography with ultimate sensitivity. *Opt. Lett.*, 32(8):909–911, April 2007. 61

[150] OSLO LT edition 6.1. Sinclair Optics Inc, palmyra Road, Fairport, NY 14450. Free download from www.sinopt.com., 2001. 75, 98, 205, 207

[151] Umakant D Rapol, Ajay Wasan, and Vasant Natarajan. Loading of a Rb magneto-optic trap from a getter source. *Phys. Rev. A*, 64(2):23402, June 2001. 76

[152] Samuel Pollock. *Integration of Magneto Optical Traps in Atom Chips*. Phd thesis, Imperial Collage London, 2010. 78

[153] Pfeiffer vacuum. Working with Turbopumps: Introduction to high and ultra high vacuum production., 2003. 78

[154] Pfeiffer Vacuum. *The Vacuum Technology Book, Volume II, Part 1: Vacuum Solutions from a Single Source.* Pfeiffer Vacuum GmbH, Asslar, 2013. 78

[155] Pfeiffer vacuum. *The Vacuum Technology Book, Volume II, Part 2: Know how book.* Pfeiffer Vacuum GmbH, Asslar, 2013. 78, 79

[156] Walter Umrath et al. Fundamentals of Vacuum Technology, 2007. 78

[157] Phil Danielson. How To Use Getters and Getter Pumps. *A Journal of Practical and Useful Vacuum Technology, R&D Magazine.*, 2001. 79

[158] Granville-Phillips. Introduction to Bayard-Alpert Ionization Gauges, 1999. 79

[159] Karl Jousten. PRESSURE MEASUREMENT WITH IONIZATION GAUGES. 79

[160] O Chubar, P Elleaume, and J Chavanne. Radia, 1997. 81

[161] M Inguscio and L Fallani. *Atomic Physics: Precise Measurements and Ultracold Matter*. OUP Oxford, 2013. 84

[162] S S Sané, S Bennetts, J E Debs, C C N Kuhn, G D McDonald, P A Altin, J D Close, and N P Robins. 11 W narrow linewidth laser source at 780nm for laser cooling and manipulation of Rubidium. *Opt. Express*, 20(8):8915–8919, April 2012. 86

[163] L Ricci, M Weidemüller, T Esslinger, A Hemmerich, C Zimmermann, V Vuletic, W König, and T W Hänsch. A compact grating-stabilized diode laser system for atomic physics. *Optics Communications*, 117(56):541–549, 1995. 86

[164] K B MacAdam, A Steinbach, and C Wieman. A narrowband tunable diode laser system with grating feedback, and a saturated absorption spectrometer for Cs and Rb. *American Journal of Physics*, 60(12), 1992. 86

[165] Carl E Wieman and Leo Hollberg. Using diode lasers for atomic physics.

Review of Scientific Instruments, 62(1), 1991. 87, 190

[166] M Fleming and A Mooradian. Spectral characteristics of external-cavity controlled semiconductor lasers. *Quantum Electronics, IEEE Journal of*, 17(1):44–59, January 1981. 87, 190

[167] Kevin J Weatherill. *A CO2 Laser Lattice Experiment for Cold Atoms*. PhD thesis, Durham University, 2007. 87, 91, 171, 188, 191

[168] Jayampathi C B Kangara, Andrew J Hachtel, Matthew C Gillette, Jason T Barkeloo, Ethan R Clements, Samir Bali, Brett E Unks, Nicholas A Proite, Deniz D Yavuz, Paul J Martin, Jeremy J Thorn, and Daniel A Steck. Design and construction of cost-effective tapered amplifier systems for laser cooling and trapping experiments. *American Journal of Physics*, 82(8), 2014. 87

[169] Yihan Xiong, Sytil Murphy, J L Carlsten, and Kevin Repasky. Design and characteristics of a tapered amplifier diode system by seeding with continuous-wave and mode-locked external cavity diode laser. *Optical Engineering*, 45(12):124205, 2006. 87

[170] Andrew C Wilson, Johnathan C Sharpe, Callum R McKenzie, Peter J Manson, and Donald M Warrington. Narrow-linewidth master-oscillator power amplifier based on a semiconductor tapered amplifier. *Appl. Opt.*, 37(21):4871–4875, July 1998. 87

[171] R A Nyman, G Varoquaux, B Villier, D Sacchet, F Moron, Y Le Coq, A Aspect, and P Bouyer. Tapered-amplified antireflection-coated laser diodes for potassium and rubidium atomic-physics experiments. *Review of Scientific Instruments*, 77(3):–, 2006. 87

[172] R Lang. Injection locking properties of a semiconductor laser. *Quantum Electronics, IEEE Journal of*, 18(6):976–983, June 1982. 89, 91

[173] C I Laidler and S Eriksson. Microwave sidebands for atomic physics experiments by period one oscillation in optically injected diode lasers. *EPL (Europhysics Letters)*, 96(5):53001, 2011. 89, 91

[174] M Vaughan. *The Fabry-Perot Interferometer: History, Theory, Practice and Applications*. Series in Optics and Optoelectronics. Taylor & Francis, 1989. 92

[175] Mathias Neidig. *A realization of a two-dimensional Fermi gas in a standing wave trap*. Masters dissertation, University of Heidelberg, 2013. 96

[176] Pco. pco.pixelfly usb manual, 2014. 97, 107

[177] G D Boreman. *Modulation Transfer Function in Optical and Electro-optical Systems*. SPIE tutorial texts. Society of Photo Optical, 2001. 98

[178] Michael Bass, Eric W Van Stryland, David R Williams, and William L Wolfe, editors. *Handbook of optics*. McGraw-Hill , Inc ., 2nd edition, 1995. 98

[179] R Shannon. *Applied Optics and Optical Engineering*. Elsevier Science, 2012. 98, 207

[180] M Born, E Wolf, A B Bhatia, D Gabor, A R Stokes, A M Taylor, P A Wayman, and W L Wilcock. *Principles of Optics: Electromagnetic Theory of Propagation, Interference and Diffraction of Light*. Cambridge University Press, 2000. 98, 207

[181] W T Welford. *Aberrations of Optical Systems*. Series in Optics and Optoelectronics. Taylor & Francis, 1986. 98, 207

[182] Wolfgang Alt. An objective lens for efficient fluorescence detection of single atoms. *Optik*, 113(3):142–144, 2001. 99, 153, 205

[183] P Baranowski, J Zacks, G Hechenblaikner, and C J Foot. Testing and design of a lens system for atom trapping and fluorescence detection. *arXiv:physics/0412126*, page 14, 2004. 99, 205

[184] L M Bennie, P T Starkey, M Jasperse, C J Billington, R P Anderson, and L D Turner. A versatile high resolution objective for imaging quantum gases. *Optics express*, 21(7):9011–6, 2013. 99, 161, 205

[185] Herbert Crepaz. *Trapping and cooling rubidium atoms for quantum information*. Phd, University of Innsbruck, 2006. 101

[186] P D Lett, W D Phillips, S L Rolston, C E Tanner, R N Watts, and C I Westbrook. Optical molasses. *J. Opt. Soc. Am. B*, 6(11):2084–2107, November 1989. 101

[187] C F Ockeloen, A F Tauschinsky, R J C Spreeuw, and S Whitlock. Detection of small atom numbers through image processing. *Phys. Rev. A*, 82(6):61606, December 2010. 125

[188] S. L. Pu, D. Allano, B. Patte-Rouland, M. Malek, D. Lebrun, and K. F. Cen. Particle field characterization by digital in-line holography: 3D location and sizing. *Experiments in Fluids*, 39(1):1–9, 2005. 129

[189] G Grynberg and C Robilliard. Cold atoms in dissipative optical lattices. *Physics Reports*, 355(56):335–451, 2001. 142

[190] Ivan H. Deutsch, Gavin K. Brennen, and Poul S. Jessen. Quantum Computing with Neutral Atoms in an Optical Lattice. *Fortschritte der Physik*, 48(9-11):925–943, September 2000. 147, 169

[191] Karl D. Nelson, Xiao Li, and David S. Weiss. Imaging single atoms in a

three-dimensional array. *Nature Physics*, 3(8):556–560, June 2007. 147, 155, 157, 163, 168, 169

[192] Z Hu and H J Kimble. Observation of a single atom in a magneto-optical trap. *Opt. Lett.*, 19(22):1888–1890, November 1994. 155

[193] Wolfgang Alt, Dominik Schrader, Stefan Kuhr, Martin Müller, Victor Gomer, and Dieter Meschede. Single atoms in a standing-wave dipole trap. *Phys. Rev. A*, 67(3):33403, March 2003. 155

[194] T Grunzweig, A Hillard, M McGovern, and M.F. Andersen. Near-deterministic preparation of a single atom in an optical microtrap. *Nature Physics*, 6(12):951–954, 2010. 155

[195] A Wakim, P Zabawa, and N P Bigelow. Photoassociation studies of ultracold NaCs from the Cs 62P3/2 asymptote. *Phys. Chem. Chem. Phys.*, 13(42):18887–18892, 2011. 158

[196] P Zabawa, A Wakim, A Neukirch, C Haimberger, N P Bigelow, A V Stolyarov, E A Pazyuk, M Tamanis, and R Ferber. Near-dissociation photoassociative production of deeply bound NaCs molecules. *Phys. Rev. A*, 82(4):40501, October 2010. 158

[197] Ron Folman, Peter Krüger, Donatella Cassettari, Björn Hessmo, Thomas Maier, and Jörg Schmiedmayer. Controlling Cold Atoms using Nanofabricated Surfaces: Atom Chips. *Phys. Rev. Lett.*, 84(20):4749–4752, May 2000. 159, 166

[198] J Reichel, W Hänsel, and T W Hänsch. Atomic Micromanipulation with Magnetic Surface Traps. *Phys. Rev. Lett.*, 83(17):3398–3401, October 1999. 159

[199] S. Wildermuth, P. Krüger, C. Becker, M. Brajdic, S. Haupt, A. Kasper, R. Folman, and J. Schmiedmayer. Optimized magneto-optical trap for experiments with ultracold atoms near surfaces. *Physical Review A - Atomic, Molecular, and Optical Physics*, 69(3):030901–1, 2004. 159

[200] Hoon Yu, Lim Lee, Kyung Hyun Lee, and Jung Bog Kim. A magneto-optical trap below a dielectric coated mirror surface. *Journal of the Optical Society of Korea*, 13(2):223–226, 2009. 159

[201] Kalle-Antti Suominen, Murray J Holland, Keith Burnett, and Paul Julienne. Optical shielding of cold collisions. *Phys. Rev. A*, 51(2):1446–1457, February 1995. 163

[202] V A Yurovsky and A Ben-Reuven. Incomplete optical shielding in cold atom traps: three-dimensional Landau-Zener theory. *Phys. Rev. A*, 55(5):3772–3779,

May 1997. 163

[203] J. Garcia-Sucerquia, Wenbo Xu, M. H. Jericho, and H. J. Kreuzer. Immersion digital in-line holographic microscopy. *Optics Letters*, 31(9):1211, 2006. 168

[204] Huaidong Jiang, Rui Xu, Chien-Chun Chen, Wenge Yang, Jiadong Fan, Xutang Tao, Changyong Song, Yoshiki Kohmura, Tiqiao Xiao, Yong Wang, Yingwei Fei, Tetsuya Ishikawa, Wendy L Mao, and Jianwei Miao. Three-Dimensional Coherent X-Ray Diffraction Imaging of Molten Iron in Mantle Olivine at Nanoscale Resolution. *Phys. Rev. Lett.*, 110(20):205501, May 2013. 168

[205] M G Gustafsson. Surpassing the lateral resolution limit by a factor of two using structured illumination microscopy. *Journal of microscopy*, 198(Pt 2):82–7, May 2000. 168

[206] Tomasz M Brzozowski, Maria Maczynska, Michal Zawada, Jerzy Zachorowski, and Wojciech Gawlik. Time-of-flight measurement of the temperature of cold atoms for short trap-probe beam distances. *Journal of Optics B: Quantum and Semiclassical Optics*, 4(1):62, 2002. 171

[207] Tadas Pyragius. Developing and building an absorption imaging system for Ultracold Atoms. *arXiv: 1209.3408 [physics.ins-det]*, September 2012. 171

[208] Aidan Arnold. *Preparation and Manipulation of an 87Rb Bose-Einstein Condensate*. PhD thesis, University of Sussex, 1999. 171

[209] Jean Dalibard, C Salomon, A Aspect, E Arimondo, R Kaiser, N Vansteenkiste, and C Cohen-Tannoudji. New schemes in laser cooling. In *Atomic Physics XI*, page 199, 1989. 179

[210] Y. Castin, J. Dalibard, and C. Cohen-Tannoudji. The limits of Sisyphus cooling. In L. Moi, S. Gozzini, C. Gabbanini, E. Arimondo, and F. Strumia, editors, *Light induced kinetic effects on atoms ions and molecules*, pages 5–24. ETS Editrice, Pisa, 1991. 180

[211] A Yariv. *Quantum Electronics*. Wiley, 1989. 194

[212] D J McCarron. A guide to acousto-optic modulators. Technical report, Technical report, Durham University, 2007. 195, 198, 200

[213] E. A. Donley, T. P. Heavner, F. Levi, M. O. Tataw, and S. R. Jefferts. Double-pass acousto-optic modulator system. *Review of Scientific Instruments*, 76(6):6, 2005. 196

[214] Stefan Bernet, Markus K Oberthaler, Roland Abfalterer, Jörg Schmiedmayer, and Anton Zeilinger. Coherent Frequency Shift of Atomic Matter Waves. *Phys. Rev. Lett.*, 77(26):5160–5163, December 1996. 196